Measurement of Higgs couplings using the diphotons channel and EFT interpretation, with the ATLAS experiment using the Run 2 data of LHC. Calibration of the electromagnetic calorimeter

Oleksii Lukianchuk

université PARIS-SACLAY

Measurement of Higgs couplings using the diphoton channel and EFT interpretation with the ATLAS experiment using the full Run 2 data of LHC. Calibration of the electromagnetic calorimeter.

Mesure des couplages du Higgs dans le canal en paire de photons et interprétation EFT, auprès de l'expérience ATLAS avec le Run 2 du LHC. Calibration du calorimètre électromagnétique.

Thèse de doctorat de l'université Paris-Saclay

École doctorale n° 576 Particules, hadrons, énergie et noyau : instrumentation, imagerie, cosmos et simulation (PHENIICS)
Spécialité de doctorat: Physique des particules
Graduate School : Physique
Référent : Faculté des sciences d'Orsay

Thèse préparée dans l'unité de recherche **IJCLab** (Université Paris-Saclay, CNRS), sous la direction de **Marc Escalier**, Chargé de recherche

Thèse soutenue à Paris-Saclay, le 27 septembre 2023, par

Oleksii LUKIANCHUK

Composition du jury

Samira Hassani Directrice de recherche, IRFU, CEA Saclay, Université Paris-Saclay, Saclay, France	Présidente
Barbara Clerbaux Professeure, Université Libre de Bruxelles, Bruxelles, Belgium	Rapportrice & Examinatrice
Marco Delmastro Directeur de recherche, LAPP, CNRS, Université Savoie-Mont-Blanc, Annecy, France	Rapporteur & Examinateur
Nicolas Berger Directeur de recherche, LAPP, CNRS, Université Savoie-Mont-Blanc, Annecy, France	Examinateur
Adam Falkowski Directeur de recherche, IJCLab, CNRS, Université Paris-Saclay, Orsay, France	Examinateur
Jean-Baptiste de Vivie Directeur de recherche, LPSC, CNRS, Université Grenoble-Alpes, Grenoble, France	Examinateur

THESE DE DOCTORAT
NNT : 2023UPASP080

université PARIS-SACLAY

ÉCOLE DOCTORALE
Particules, hadrons, énergie et noyau : instrumentation, imagerie, cosmos et simulation (PHENIICS)

Titre: Mesure des couplages du Higgs dans le canal en paire de photons et interprétation EFT, auprès de l'expérience ATLAS avec le Run 2 du LHC. Calibration du calorimètre électromagnétique.
Mots clés: Higgs, STXS, EFT, ATLAS, photon, LAr
Résumé: La découverte du boson de Higgs en 2012 a ouvert une nouvelle ère de mesures précises dans le secteur du Higgs. Avec l'ensemble des données du Run 2, la précision des mesures des couplages du Higgs atteint un niveau de dix pour cent au mieux. Dans cette thèse, une analyse STXS du canal de désintégration $H \to \gamma\gamma$ avec l'ensemble des données du Run 2 est réalisée. Ce canal est l'un des plus sensibles. Les résultats sont présentés sous différentes granularités, de la force de signal inclusive aux mesures STXS.

La combinaison des mesures STXS par différents canaux de Higgs est interprétée dans une théorie EFT avec la symétrie top du formalisme SMEFT ainsi que dans différents modèles 2HDM et MSSM. Pour le cas spécifique de la combinaison des canaux $H \to \gamma\gamma$ et $H \to 4\ell$, la contrainte des paramètres EFT est comparée entre l'utilisation des observables STXS et celles des section-efficaces différentielles. Les mesures SMEFT sont réalisées dans une approche avec PCA pour sélectionner les directions d'ajustement les plus sensibles.

La thèse presente également une méthode alternative de la calibration in-situ du calorimètre électromagnétique d'ATLAS à partir de la variable E_T/p_T, comme approche complémentaire à la méthode classique de forme m_{ee}.

Title: Measurement of Higgs couplings using the diphotons channel and EFT interpretation, with the ATLAS experiment and the Run 2 of LHC. Calibration of the electromagnetic calorimeter.
Keywords: Higgs, STXS, EFT, ATLAS, photon, LAr
Abstract: The discovery of the Higgs boson in 2012 opened an era of precise measurements in the Higgs sector. With the full Run 2 data, the precision on the measurements of the Higgs couplings reaches a level of ten per cent for the most precisely determined ones. In this thesis, an STXS analysis of the $H \to \gamma\gamma$ decay channel with full Run 2 data is made, which is one of the most sensitive channels. Results are presented in various granularities, from the inclusive signal strength to the STXS stage 1.2 measurement.

A combination of STXS measurement from various Higgs channels is interpreted in an EFT, with the top-scheme symmetry of the SMEFT framework, and in 2HDM and MSSM models. For the specific case of $H \to \gamma\gamma$ and $H \to 4\ell$ combination, the constraining power on EFT models from STXS inputs is compared to the one from differential cross-sections. SMEFT measurements are also performed in a PCA basis, selecting the most sensitive fit directions.

This thesis also presents an alternative method for the in-situ calibration of the ATLAS electromagnetic calorimeter using the distribution of E_T/p_T variable, complementary to the classical m_{ee} lineshape method.

Contents

Acknowledgements

It would be unfair to say that there is someone from the numerous people mentioned below (and many not-mentioned) who has not contributed to the creation of this manuscript and to the process behind throughout these three years of a PhD, preceded with an internship and countless years before, everyone has constituted a part of a huge joint support-team.

First, I would like to express my highest gratitude to my supervisor, Marc Escalier, for his unbelievable patience and permanent support and for the possibility to learn not only some scientific methods and their applications in Higgs physics but also about the necessity of constant rigorousness and accuracy. It was a great pleasure working with you. Before the beginning of the internship, I had no idea what these magic words like "background" or "efficiency" meant; hence, it would be fair to say that my progress is due to you, Marc. Thank you for your patient explanations of such basic terms, not even mentioning long discussions concerning more sophisticated and advanced topics about the science and the world around us. And an independent thank you for teaching me one of the most essential principles: all complicated things can be handled, the point is to keep trying every day, with only growing enthusiasm.

Speaking of the lab and our ATLAS group, one of the first people to come to mind is Louis Fayard, due to his immense expertise in various fields, starting from the design of the ATLAS EM calorimeter and Higgs physics to the latest exposition at Centre Pompidou, and for the remarkable charism, which motivates keeping discovering the miracles of the universe.

Thank you to the entire ATLAS IJCLab group for hosting me during these three years and for allowing me to work with you, attend various seminars and learn from all of you. Additionally, thank you for all the Zoom meetings during the Covid, which was especially crucial at the very beginning of the lockdown.

Thank you to the HGam group, especially the Couplings sub-group, who were careful and patient enough to let me learn and contribute to the STXS analysis. There were many people I am grateful for the help, discussions and advice. In addition, I want to thank a couple of people, Davide Mungo and Shuo Han, for the technical support and discussions.

Thank you for the Higgs combination group and many people we have been digging Higgs physics with, especially Eleonora Rossi and Rahul Balasabramanian, for countless interactions, discussions, patience, and understanding.

Thank you to all the jury members who have agreed to do it, for all your valuable comments and discussions. Independently, thank you to Nicolas Berger, for all the statistical lectures I occasionally listened to at two summer schools, where we randomly met without knowing that. And thank you for the interesting lunch discussions there, particularly around Marseille.

There is an invaluable acknowledgement to all the friends we have been interacting with at M2 and during the PhD: Lera, Polina, Andrii, Vidya, Juan, Arnaud, Yuya and Julien (do not try to find a quest in the order of your names, it is not present, but who knows...). Thank you for all the "plenary meetings" conducted, which were so crucial, especially during the Covid. Thank you for always being around.

It is impossible not to mention you, Linghua Guo, and numerous discussions during coffee breaks, and for all the time apart from that. Thank you, Oleksii Kurdysh, for all the lunches at the "kids canteen" we have gone to. Thank you, Egor Vereshaka and Olexandr Hryhorenko, for all the trips and help.

Finally, I would like to express my profound gratitude and gracefulness to my parents and sister for all the support and presence. Thank you to my girlfriend, Kristel, for always being around, for the immense support, keeping peace in my soul and permanently inspiring me to follow my dreams.

Résumé étendu en français

Après la découverte du boson de Higgs en 2012, la précision sur les mesures s'est accrue, permettant de déterminer précisément les paramètres décrivant les interactions du Higgs avec les autres particules. De nouvelles méthodes ont été développées pour sonder l'existence potentielle d'une nouvelle physique avec une approche dite théorie effective des champs (EFT pour Effective field Theory).

Le document est organisé comme suit.

Le chapitre 1 donne les concepts mathematiques utilisés pour construire le Modèle Standard de la physique des particules. En particulier, il décrit le mécanisme de Higgs et sa phénoménologie, ainsi que les modes de production et les canaux de désintégration.

Le chapitre 2 décrit le complexe expérimental du CERN : l'accélerateur LHC et le détecteur ATLAS, utilisés pour obtenir les données analysées. Les caractéristiques et la performance attendues sont presentées.

Le chapitre 3 décrit la première partie du travail effectuée pendant la thèse, relative à l'étalonnage du système calorimètre, avec une nouvelle méthode et une comparison de sa performance avec la méthode classique dit template m_{ee}.

Le chapitre 4 présente les mesures des couplages du boson de Higgs avec le canal de désintégration $H \to \gamma\gamma$. Le chapitre 5 présente les interprétations EFT (chapitre 5). L'appendice A introduit les méthodes statistiques utilisés par les différentes parties de l'analyse.

Une conclusion achève le manuscript.

Etalonnage du calorimètre électromagnétique

Le calorimètre électromagnétique est utilisé pour reconstruire les particules qui déposent leur énergie par interaction électromagnétique, comme les électrons et photons. Un étalonnage corrige les biais entre l'énergie des particules réelles et celle de la simulation. Elle consiste a réduire les biais sous forme de décalage entre l'énergie réelle et celle reconstruite et les effets de résolution se manifestant comme une différence entre les queues de distribution du spectre en énergie.

La méthode usuelle est basée sur la distribution de masse invariante de e^+e^- provenant de désintégrations du boson Z. La nouvelle méthode consiste à utiliser la variable E_T/p_T, ou E_T est l'énergie mesurée par le calorimètre et p_T l'impulsion mesurée par le trajectographe. La distribution de E_T/p_T est plus piquée que celle pour E_T ou p_T indépendants. La modélisation de la cinématique du boson Z n'étant pas très précise en raison des corrections QCD, les résultats peuvent être améliorés en appliquant une correction. Cette correction applique des pondérations 2D (dans le plan $p_T^Z \times y_Z$) aux échantillons genérés. L'application de cette

correction améliore l'accord entre les résultats de la méthode classique (m_{ee}) et celle étudiée dans cette thèse (E/p), bien que cette dernière y soit peu sensible.

Comme l'impulsion est mesurée par le trajectographe, la distribution de E_T/p_T est sensible aux problèmes de calibration des traces. Compte tenu du fait que la précision sur l'impulsion diminue avec $|\eta|$, la variable E_T/p_T devient moins sensible au delà de la région centrale du detecteur ($|\eta| > 1.0$). De plus, les résultats E_T/p_T deviennent sensibles à tous les biais du trajectographe, où il existe deux types de biais : le biais sagital et d'échelle. En supposant que la seule différence entre les résultats nominaux et ceux de E_T/p_T provient du mauvais étalonnage du trajectographe, on peut estimer ces biais.

La méthode E_T/p_T permet d'estimer le bias sagital. De plus, l'application des corrections de biais améliore l'accord entre les résultats de m_{ee} et E_T/p_T.

En général, la méthode E_T/p_T peut être utilisée dans les regions centrales du detecteur et sa performance est similaire à celle de la méthode classique (m_{ee}). Au delà, la performance de la méthode est limitée par la précision du trajectographe et la statistique disponible.

Mesure des couplages du boson de Higgs dans le canal de désintegration en paire de photons

La signature expérimentale du canal de désintégration du Higgs en paire de photons est un pic étroit de type gaussien avec une largeur approximative de 2 GeV émergeant par-dessus un fond de continuum décroissant, composé de processus $\gamma\gamma$ irréductibles et γj et jj réductibles, où un ou deux jets sont identifiés à tort comme des photons.

L'analyse développe 101 categories et cible 29 sections efficaces STXS (Simplified Template Cross-Section), qui dépendent de la cinématique et des modes de production du Higgs. La catégorisation consiste en deux étapes : la première est basée sur l'utilisation d'un arbre de décision binaire multiclasses (pour séparer les signaux entre classes) et la deuxième utilise un arbre de décision binaire (un pour chaque classe) séparant les signaux de zones STXS différentes et du bruit.

La modélisation du signal utilise la forme analytique dite DSCB (Double-sided Crystal Ball). La modélisation du bruit est basée sur les données (data-driven) où toutes les composantes reductibles (jj et γj) sont obtenues par repondération du spectre $\gamma\gamma$ pour correspondre à celui des bandes latérales de données.

L'estimation des incertitudes liées à la modélisation du signal est effectuée en utilisant la méthode de signal spurieux : un modèle de bruit de fond est ajusté par une fonction ayant deux composantes : signal et bruit. Pour cet ajustement du spectre $m_{\gamma\gamma}$, le signal est testé pour diverses masses autour du signal de Higgs réel. Pour le bruit, quelques formes de fonctions ont été testées : exponentiel, polynomial, fonction de Bernstein avec divers degrés de liberté. Parmi toutes les résultats d'ajustement passant les critères, le faux signal obtenu dans cet ajustement ne doit pas être supérieur à 10% du signal nominal et à 20% de l'incertitude prévue de signal dans cette catégorie. Celui avec le plus faible signal spurieux est choisi et considéré comme l'incertitude de la modélisation du bruit.

La mesure des sections efficaces est effectuée pour la production totale du boson de Higgs et individuellement pour chaque mode de production. En outre, les mesures sous forme de STXS sont obtenues. Il n'y a pas de déviation par rapport à la prédicion du Modèle Standard. L'interprétation des résultats en EFT et en kappa-framework est également présentée.

Les interprétations en EFT et BSM (2HDM et hMSSM)

Comme des expériences le suggèrent, le Modèle Standard peut ne pas être l'ultime modèle de la nature. Si une nouvelle physique existe à des énergies élevées non atteintes par le LHC, il est toujours possible d'y accéder par le biais des distributions à basses énergies. Une approche classique souvent utilisée pour sonder l'hypothétique nouvelle physique est appelée SMEFT (Standard Model Effective Field Theory). Dans cette théorie, le lagrangien du Modèle Standard est étendu par toutes les combinaisons possibles des opérateurs du Modèle Standard formant des termes de dimension six en énergie. Les coefficients de cette expansion sont connus sous le nom de coefficients de Wilson. Les termes de puissance impairs sont omis car ils provoquent des violations du nombre de leptons et de baryons et donc ne sont pas pertinents dans cette analyse. Une contribution potentielle des termes de dimension huit peut être estimée en comparant les contributions des termes croisés (venant de l'interférence entre les coefficients de Wilson) et les termes linéaires (interférence entre le Modèle Standard et la nouvelle physique, décrite par les coefficients de Wilson).

L'analyse utilise une combinaison des données de désintégration du boson de Higgs dans différents canaux, notamment $H \to \mu\mu$ et $H \to \tau\tau$, qui aident à contraindre les coefficients de Wilson liés aux couplages entre le Higgs et les particules individuelles. Les canaux sont combinés pour obtenir les résultats STXS.

Indépendamment, les performances des mesures STXS et des sections efficaces différentielles sont comparées en utilisant les mêmes données des canaux $H \to \gamma\gamma$ et $H \to 4\ell$. La performance de la méthode STXS est légèrement meilleure grâce à sa conception : les modes de production sont séparés et la définition des intervalles cinématiques est créée pour optimiser la sensibilité à une nouvelle physique potentielle.

Pour obtenir la paramétrisation de la puissance des signaux de STXS en termes des coefficients de Wilson, il faut paramétriser la section efficace de la production ($pp \to H$), le rapport d'embranchement, l'acceptance et l'efficacité du détecteur. Pour cela, des échantillons ont été générés avec MadGraph avec SMEFTsim3.0.

Compte tenu du fait qu'il n'est pas possible de contraindre tous les coefficients de Wilson en même temps, la technique de PCA (Principal Component Analysis) est adoptée. Cela permet en outre de réduire le nombre de paramètres d'intérêt en éliminant ceux pour lesquels la vraisemblance est plate et de minimiser les corrélations entre les directions obtenues.

Les résultats sont présentés pour le modèle linéaire et quadratique des coefficients de Wilson dans la base du PCA. Pour chaque direction, les intervalles de confiance à 68% et 95% sont présentés. Pour la majorité des paramètres d'intérêt, l'incertitude dominante provient de la

statistique.

En dehors des interprétations en EFT, des modèles 2HDM (Two-Higgs Doublet Model) et hMSSM (minimal supersymmetric Standard Model) sont sondés. Pour le 2HDM, sept scénarios sont étudiés, qui diffèrent par les couplages entre les doublets de Higgs et les autres particules ainsi que par leurs masses. De plus, les performances de l'interprétation directe et du matching (interprétation additionnelle des résultats de l'EFT dans le 2HDM) sont comparées et leurs performances sont similaires.

Contributions de l'auteur

Au niveau des études du groupe de calibration, la contribution relève d'une tâche de qualification (QT) décrite au chapitre 3. L'auteur est le contributeur pour l'étalonnage du calorimètre électromagnétique avec une nouvelle méthode utilisant la variable E_T/p_T et le processus de $Z \to e^+e^-$.

La contribution à l'aspect des analyses est composée de deux parties : l'analyse de STXS dans les canaux $H \to \gamma\gamma$ et l'analyse d'interprétation EFT des données combinées du boson de Higgs. Dans la première partie ($H \to \gamma\gamma$), l'auteur a contribué à la modélisation des signaux et du bruit (estimation du signal spurieux), au calcul des efficacités et des purités de STXS, ainsi qu'aux mesures statistiques : forces des signaux, sensibilités expérimentales, interprétation des observations des différents modes de production et limite sur la force du signal du mode de production tH.

Dans la deuxième partie (interprétations EFT et BSM), l'auteur a contribué à la vérification des paramétrisations SMEFT, aux résultats statistiques de la combinaison des canaux $H \to \gamma\gamma$ et $H \to 4\ell$ en STXS : vérification des valeurs d'ajustement et construction des profils de vraisemblance pour tous les paramètres dans la base du PCA. Pour la combinaison des sections efficaces différentielles, l'auteur a également contribué aux ajustements et à la vérification des résultats. Enfin, l'auteur a effectué une analyse des paramètres de nuisance pour les modèles statistiques décrits ci-dessus.

Pour les deux analyses, l'auteur a présenté ces analyses lors de réunions éditoriaux (EB).

Personal Contributions

The contributions of the author on the scientific aspects of this thesis are described below. The performance aspect is a qualification task (Section 3), prospecting for a potential novel method of calibration of the electromagnetic calorimeter using E_T/p_T variable and the $Z \to e^+e^-$ process. The author is the principal and the only contributor to this study.

The analysis aspect is composed of two parts. The first part is the $H \to \gamma\gamma$ analysis (Section 4), aiming to probe the STXS cross-sections. The contributions of the author are:

- Signal modelling (Section 4.7)
- Computation of the STXS efficiencies and purities (Section 4.8)
- Background modelling (Section 4.9), including:
  - Background reweighting (Section 4.9.2)
  - Spurious signal estimation (Section 4.9.4)
- Statistical results:
  - signal strength cross-check, sensitivity, significance of the production modes, limit on tH (Sections 4.11.1, 4.11.2, 4.11.3).
  - Nuisance parameter ranking plots cross-checks (Section 4.27)

The results from $H \to \gamma\gamma$ analysis are used in a combination with other channels. This combination is further interpreted in an EFT approach. The contributions of the author are:

- SMEFT parametrisation cross-check (Section 5.3)
- Statistical results:
  - STXS $H \to 4\ell$ and $H \to \gamma\gamma$ simultaneous and one-at-a-time combination (Section 5.6):
    * Cross-check of fits
    * Likelihood scans cross-check
  - Differential cross-section simultaneous and one-at-a-time combination (Section 5.5.2):
    * fits
    * likelihood scans and their plots
  - Nuisance parameters ranking plots

The contributions of the author correspond to the following documents :

- ATLAS Collaboration, publication, *Measurement of the properties of Higgs boson production at $\sqrt{s} = 13$ TeV in the $H \to \gamma\gamma$ channel using 139 fb^{-1} of p p collision data with the ATLAS experiment*, JHEP 07 (2023) 088, arXiv:2207.00348, CERN-EP-2022-094.
- Support document for publication: Nicolas Berger et al., *Measurements of Higgs boson coupling properties in the diphoton decay channel using full Run 2 pp collision data at $\sqrt{s} = 13$ TeV with the ATLAS detector*, ATL-COM-PHYS-2021-180.

- ATLAS Collaboration, conference note, *Measurement of the properties of Higgs boson production at $\sqrt{s} = 13$ TeV in the $H \to \gamma\gamma$ channel using 139 fb^{-1} of p p collision data with the ATLAS experiment*, ATLAS-CONF-2020-026.
- Supporting document for publication: Nicolas Berger et al., *Measurements of Higgs boson coupling properties in the diphoton decay channel using full Run 2 pp collision data at $\sqrt{s} = 13$ TeV with the ATLAS detector*, ATL-COM-PHYS-2020-202.

- ATLAS Collaboration, publication, *Interpretations of the measurements of Higgs boson production and decay rates and differential cross-sections*, ATLAS-CONF-2023-052.
- Support document: Eleonora Rossi et al., *Interpretation of Higgs boson measurements in terms of Standard Model Effective Field Theory and specific theories beyond the Standard Model*, ATL-COM-PHYS-2022-890.

Introduction

Since the discovery of the Higgs boson in 2012, the current precision of the measurements allows performing precise determination of its properties for a given production mode or cross-section measurements in various kinematic regions of the phase-space. Moreover, to probe anomalous Higgs couplings potentially caused by new physics, more sophisticated methods (as EFT measurements) started to be used to extend existing ones (for example, kappa-framework).

The document is organised as follows:

Chapter 1 gives the main mathematical concepts used to build the modern theory of particle physics. In particular, it describes the Higgs mechanism and its phenomenology, as well as various production modes and decay channels involved in precision measurement of Higgs sector. The current knowledge on properties of the Higgs boson is given.

Chapter 2 describes the CERN experimental complex used to obtain the data analysed, that is the LHC accelerator and the ATLAS detector, in particular the electromagnetic calorimeter that is used for the electron/photon calibration of following chapter. The subdetectors characteristics and expected performances are given.

Chapter 3 describes the first part of the work done during the PhD, related to the $e\gamma$ calibration of the electromagnetic calorimeter, which introduces the method used for the calibration and comparison of its performance to the classical so-called m_{ee} template method. This method uses distribution of E/p variable, where the energy E is measured in the electromagnetic calorimeter and the momentum p is determined in the tracker. Estimation of the tracker biases is made by comparing the nominal m_{ee} method and the E/p one.

Chapter 4 contains information on measurements of the Higgs boson couplings in the diphoton channel in various granularities: from the inclusive cross-section measurement to the 28 STXS 1.2. regions. Detailed information on the signal and background modelling is provided, that is crucial for precision analyses.

Chapter 5 is devoted to the EFT interpretations of the combined Higgs dataset in a general SMEFT and a given set of 2HDM scenarios models using STXS measurements. Further, a comparison of the sensitivities of the differential cross-section and STXS analyses for SMEFT measurements is made, using $\gamma\gamma$ and 4ℓ final states.

The document then follows with a conclusion.

Appendix A introduces statistical methods and their application used in the thesis. The following Appendix B describes an extract of information on the gamma-matrices and their representations often used in the mathematical formulation of the SM. In the last Appendix C, auxiliary information to the EFT analysis is provided: input STXS measurements, impact of Wilson coefficients on cross-sections for various productions modes, likelihood scans for the linear and linear plus quadratic parametrisations and others.

1 - Standard Model (SM) of Particle Physics

This chapter describes the formalism used in particle physics, in particular in the Higgs sector. The reader could find more information in Refs [1, 2, 3, 4, 5, 6].

1.1 Basics of Quantum Field Theory (QFT)

1.1.1 Quantum Field Theory

Classical Mechanics and Field Theory

According to classical equations [7], the dynamics of a mechanical system can be characterised by a few dynamical quantities: generalised coordinates q (for example, position or angle) and their time derivatives[1] $\dot{q}$. Evolution of a system can be described by the Euler-Lagrange equation:

$$\frac{\partial \mathscr{L}}{\partial q} = \frac{d}{dt}\frac{\partial \mathscr{L}}{\partial \dot{q}}, \tag{1.1}$$

where $\mathscr{L}$ is the Lagrangian of the system (difference of the kinetic and potential energies), This equation is a realisation of the principle of least action, stating that trajectories of a system are the stationary points of the functional of action S defined as:

$$\mathcal{S} = \int \mathscr{L}(q, \dot{q}, t)\mathrm{d}t. \tag{1.2}$$

In the nature, we observe various fields everywhere: temperature, velocities in fluids, electromagnetic fields and so on. Fields extend throughout space affecting every point of the space-time. This intrinsic property necessitates their characterisation as infinite systems, given that the field's value at each space-time point is a degree of freedom. Therefore, for a general field ϕ (which is, in general a function of time and space) described by a Lagrangian density $\mathcal{L}(\phi, \dot{\phi})$, it is more convenient to introduce the Lagrangian density $\mathcal{L}(\phi(\mathbf{x}, t), \dot{\phi}(\mathbf{x}, t), t)$, which yields the Lagrangian function $\mathscr{L}(t)$ after integrating it over the entire space:

$$\mathscr{L}(t) = \int \mathcal{L}(\phi(\mathbf{x}, t), \dot{\phi}(\mathbf{x}, t), t)\mathrm{d}\mathbf{x}, \tag{1.3}$$

Therefore, for a field ϕ, action S takes form:

$$\mathcal{S} = \int \mathcal{L}(\phi(x, t), \dot{\phi}(x, t), t)\mathrm{d}\mathbf{x}\mathrm{d}\mathbf{t}, \tag{1.4}$$

where one sees that the time and the spatial coordinates play equivalent roles, which allows natural space-time unification imposed in relativistic mechanics.

Quantum Field Theory

To generalise field theory to relativistic quantum mechanics, one has to accommodate for the quantum origin of the matter and interactions[2], therefore to take into account essentially new

[1] The coordinates and their time derivatives are treated as independent variables.

[2] Quantum fields are, generally, not commuting, which requires

property of the particles, not present in classical physics, such as spin. Quantification of the fields depends on the field's spin. Thus, before building a comprehensive quantum field theory, one has to study the underlying mathematical concepts.

1.2 Mathematical language of symmetry

One of the most essential concept, guiding modern math and physics, is the symmetry. In the most general words, a symmetry is a law according to which a pattern is left unchanged under a certain transformation. In math, two general classes of symmetries are considered:

- discrete. It states that there is a limited number of states during transitions, among which the system remains the same. An example is an equilateral triangle: if we rotate it on $2\pi/3$, $4\pi/3$ or 2π in the plane, it will remain the same.
- continuous symmetry. It stands to an unlimited number of transformations one may hold, under which the system remains the same[3]. An example is a circle, which we can rotate on any angle in a plane, and no difference will be disclosed.

In order to wrap the context of symmetries, it is suitable to use the language of the group theory. Mathematically speaking, a group $\mathcal{G}$ is a combination of two types of objects: a set of elements $g \in \mathcal{G}$ and an operation to be applied between the elements. Also, a few additional conditions are implied:

- Closure: $\forall g_1,\, g_2 \in \mathcal{G},\, g_1 g_2 = g_3 \in \mathcal{G}$.
- Associativity: $\forall g_1,\, g_2,\, g_3 \in \mathcal{G},\, g_1\,(g_2\; g_3) = (g_1\; g_2)\; g_3$.
- Existence of identity e: $\exists e \in \mathcal{G} \mid \forall g \in \mathcal{G}, eg = ge = g$.
- Existence of an inverse element g^{-1} to g: $\forall g \in \mathcal{G},\, \exists g^{-1} \in \mathcal{G} \mid g^{-1}g = gg^{-1} = e$.
- If $\forall g_1, g_2 \in \mathcal{G},\, g_1 g_2 = g_2 g_1$, then the group is commutative, also called Abelian.

1.2.1 Representation theory

Usually, a group is an abstract object, however, it is particularly interesting to investigate groups properties regarding a particular representation, meaning identifying all the groups elements with some existing mathematical objects. Often, the matrix representation is used: all group elements are identified with matrices (linear operators).

Generally speaking, $D(x)$ is a representation of a group $\mathcal{G}$, if:

$$\begin{aligned} \forall x \in \mathcal{G}, \exists \text{ matrix operator } D(x) \mid & \\ D(x) \cdot D(y) &= D(x \cdot y) \\ D(x^{-1}) &= (D\,(x))^{-1}\,. \end{aligned} \tag{1.5}$$

For one group, one can have multiple representations: $D(x)$, $D'(x)$. It is said that these two representations are equivalent if and only if exist a constant transition matrix S, such that:

$$D'(x) = SD(x)S^{-1}. \tag{1.6}$$

[3]Often, to study continuous symmetries, one considers an infinitesimal transformation. Therefore, sometimes in books, people refer to continuous symmetries as to a symmetry under infinitesimal transformations.

If $D(x)$ is block-diagonalisable, then this representation is called reducible. Moreover, there exists a basis in which it takes a block-diagonal form:

$$D'(x) = SD(x)S^{-1} = \begin{pmatrix} D'_1(x) & 0 \\ 0 & D'_2(x) \end{pmatrix}, \tag{1.7}$$

where $D'_1(x)$, and $D'_2(x)$ are two orthogonal subspaces. In the contrary, if $D(x)$ is not diagonalisable, it is called irreducible.

Among all the representations, there are two particularly interesting ones:

- *Fundamental representation*: the smallest irreducible (with no invariant sub-spaces) and non-trivial representation.
- *Adjoint representation*: the matrices $D(x)$ are composed of the structure constants of the group which will be discussed later.

1.2.2 Lie groups in physics

Among the final-dimensional groups, a particular interest is in the Lie groups, which describe continuous unitary transformation, given by a form:

$$U = \mathrm{e}^{i\theta_\alpha T_\alpha}, \tag{1.8}$$

with θ_α being rational parameters ($\alpha = 1, 2, ..., N$, N - dimension of the group) and T_α being generators. To study the properties of these groups, one may refer to the third Lie theorem [8], stating that for any final-dimensional group, there is only one corresponding Lie algebra, which spans the tangent space of the identity. Hence, in the vicinity of identity, consider the following product:

$$P = \mathrm{e}^{i\lambda T_b}\mathrm{e}^{i\lambda T_a}\mathrm{e}^{-i\lambda T_b}\mathrm{e}^{-i\lambda T_a}, \tag{1.9}$$

given vicinity to the identity $\mathbb{I}$:

$$P = \mathbb{I} + \lambda^2 [T_a, T_b] + ..., \tag{1.10}$$

where λ is infinitesimal and $[a, b]$ denotes a *commutator*: $[a, b] = a \cdot b - b \cdot a$. Further on, an *anti-commutator* $\{a, b\}$ will be used: $\{a, b\} = a \cdot b + b \cdot a$. Using the closure property, this product can be expressed as another group element:

$$P = \mathrm{e}^{i\alpha_c T_c} = 1 + i\alpha_c T_c + ... \tag{1.11}$$

After comparison of them, up to the order λ^2:

$$\lambda^2 [T_a, T_b] = i\alpha_c T_c. \tag{1.12}$$

Defining $\alpha_c = \lambda^2 f_{abc}$, the following relation appears:

$$[T_a, T_b] = i f_{abc} T_c, \tag{1.13}$$

which defines a Lie algebra for the group $\mathcal{G}$. The f_{abc} quantities are called structure constants[4]. In the adjoint representation, usually denoted as $\mathbf{ad}_a$, elements of the matrix D are composed of the structure constants in the following way:

$$(D_a)_{bc} \equiv -i f_{abc}. \tag{1.14}$$

[4]For example, for the $\mathrm{SU}(2)$ algebra, given that $[J_i, J_j] = \epsilon_{ijk}$, $f_{abc} = \epsilon_{ijk}$.

1.2.3 Particular groups

As it will be seen later, in particle physics, an important role is devoted to a few particular groups: $\mathrm{U}(1)$, $\mathrm{SU}(2)$ and $\mathrm{SU}(3)$. Hence, in this chapter their overview is given.

$\boldsymbol{U(1)}$ is the simplest unitary group, composed by elements of the type:

$$U(H) = \mathrm{e}^{iH}, \tag{1.15}$$

with H being real numbers. From this definition, it is seen that the group is abelian (commutator $[H_1, H_2] = 0$). Rank of $U(1) = 1$ and it has no creation or destruction operators.

$\boldsymbol{SU(N)}$ stands for special unitary group, which may be represented by unitary $N \times N$ traceless hermitian matrices with a unit discriminant. Therefore, they have $N^2 - 1$ free parameters, usually denoted as α_a. Rank of $\mathrm{SU}(N)$ is $N - 1$. Groups of this type are non-commutative, which manifests to self-interaction of the vector-bosons and gluons in the SM. Any group element U of $\mathrm{SU}(N)$ can be written as:

$$U = \mathrm{e}^{i\alpha_a T^a}, \tag{1.16}$$

where T^a are generators, having shape of traceless hermitian $N \times N$ matrices.

Such groups have $N - 1$ H_i operators (hermitian diagonal) and $N(N - 1)$ operators of creation and destruction.

$\boldsymbol{SU(2)}$ is one of the most often used groups in particle physics. This group is spanned by the three generators J^i (which are Pauli matrices σ^i, $i \in \{1,2,3\}$[5] scaled by one half):

$$\begin{aligned} J_1 &= \frac{1}{2}\sigma^1 \\ J_2 &= \frac{1}{2}\sigma^2 \\ J_3 &= \frac{1}{2}\sigma^3 \end{aligned} \tag{1.17}$$

Following the general facts described in Section 1.2.3, we may deduce that there exists one H operator (usually referred as J_3) and one pair of creation and destruction operators ($J_\pm$ respectively):

- H: J_3.
- J_+: $\dfrac{1}{\sqrt{2}}(J_1 + iJ_2)$
- J_-: $\dfrac{1}{\sqrt{2}}(J_1 - iJ_2)$

It can be shown that for a general state $|m\rangle$ in the irreducible representation of $\mathrm{SU}(2)$ (each state is characterised by only one number m):

$$\begin{aligned} J_3|m\rangle &= m|m\rangle \\ J_3 J_\pm|m\rangle &= (m \pm 1)J_\pm|m\rangle \end{aligned} \tag{1.18}$$

[5] Definition of the Pauli matrices is given by eq. 1.3.2.

Hence, $J_\pm|m\rangle$ has eigenvalues $(m \pm 1)$. This means that the $J_\pm$ operator indeed raises (lowers) the eigenvalue of a state.

The Casimir operator $\mathcal{C}$ for $\mathrm{SU}(2)$ is:

$$\mathcal{C} = \vec{J}^2 = J_+J_- + J_-J_+ + J_3^2 \tag{1.19}$$

with eigenvalues:

$$\mathcal{C}|m_{max}\rangle = \left(J_+J_- + J_-J_+ + J_3^2\right)|m_{max}\rangle = m_{max}\left(m_{max}+1\right)|m_{max}\rangle = J\left(J+1\right)|m_{max}\rangle \tag{1.20}$$

$\boldsymbol{SU(3)}$ Usually, for this group, generators in the adjoint representation are given in the Gell-Mann basis:

$$T_a = \frac{1}{2}\lambda_a, \tag{1.21}$$

with λ_a:

$$\begin{aligned}
\lambda_1 &= \begin{pmatrix} 0 & 1 & 0 \\ 1 & 0 & 0 \\ 0 & 0 & 0 \end{pmatrix} \lambda_2 = \begin{pmatrix} 0 & -i & 0 \\ i & 0 & 0 \\ 0 & 0 & 0 \end{pmatrix} \qquad \lambda_3 = \begin{pmatrix} 1 & 0 & 0 \\ 0 & -1 & 0 \\ 0 & 0 & 0 \end{pmatrix} \\
\lambda_4 &= \begin{pmatrix} 0 & 0 & 1 \\ 0 & 0 & 0 \\ 1 & 0 & 0 \end{pmatrix} \lambda_5 = \begin{pmatrix} 0 & 0 & -i \\ 0 & 0 & 0 \\ i & 0 & 0 \end{pmatrix} \\
\lambda_6 &= \begin{pmatrix} 0 & 0 & 0 \\ 0 & 0 & 1 \\ 0 & 1 & 0 \end{pmatrix} \lambda_7 = \begin{pmatrix} 0 & 0 & 0 \\ 0 & 0 & -i \\ 0 & i & 0 \end{pmatrix} \quad \lambda_8 = \frac{1}{\sqrt{3}} \begin{pmatrix} 1 & 0 & 0 \\ 0 & 1 & 0 \\ 0 & 0 & -2 \end{pmatrix}
\end{aligned} \tag{1.22}$$

Given that the rank of $\mathrm{SU}(3)$ is 2, any eigenstate $|m, y\rangle$ which is fully characterised by two quantum numbers (m, y), there are two hermitian diagonal operators, denoted as I_3 and Y:

$$\begin{aligned}
I_3 &= \frac{1}{2}\lambda_2 \\
Y &= \frac{1}{\sqrt{3}}\lambda_8
\end{aligned} \tag{1.23}$$

each of them given a respective eigenvalue of a state:

$$\begin{aligned}
I_3|m, y\rangle &= m|m, y\rangle \\
Y|m, y\rangle &= y|m, y\rangle
\end{aligned} \tag{1.24}$$

Operators of creation and destruction are given by:

$$\begin{aligned}
I_\pm &= \frac{1}{2}\left(\lambda_1 \pm i\lambda_2\right) \\
V_\pm &= \frac{1}{2}\left(\lambda_4 \pm i\lambda_5\right) \\
U_\pm &= \frac{1}{2}\left(\lambda_6 \pm i\lambda_7\right)
\end{aligned} \tag{1.25}$$

Using commutator relations:

$$\begin{aligned}
[I_3, I_\pm] &= \pm I_\pm \\
[I_3, V_\pm] &= \pm\frac{1}{2} V_\pm \\
[I_3, U_\pm] &= \pm\frac{1}{2} U_\mp \\
[Y, I_\pm] &= 0 \\
[Y, V_\pm] &= \pm V_\pm \\
[Y, U_\pm] &= \pm U_\pm
\end{aligned} \tag{1.26}$$

it can be shown the action of the creation and destruction operators on a eigenstate $|m, y\rangle$:

$$\begin{aligned}
I_\pm|m, y\rangle &= |m \pm 1, y\rangle \\
V_\pm|m, y\rangle &= |m \pm \frac{1}{2}, y \pm 1\rangle \\
U_\pm|m, y\rangle &= |m \mp \frac{1}{2}, y \pm 1\rangle
\end{aligned} \tag{1.27}$$

Often I_3 is referred to as isospin and Y as hypercharge.

The Casimir operator $\mathcal{C}$ for a state with maximal eigenvalues $|m_{max}, y_{max}\rangle$ has eigenvalue:

$$\mathcal{C}|m_{max}, y_{max}\rangle = \left(I_3^2 + 2I_3 + \frac{3}{4}Y^2\right)|m_{max}, y_{max}\rangle, \tag{1.28}$$

where:

$$\begin{aligned}
I_3|m_{max}, y_{max}\rangle &= m_{max}|m_{max}, y_{max}\rangle \\
Y|m_{max}, y_{max}\rangle &= y_{max}|m_{max}, y_{max}\rangle
\end{aligned} \tag{1.29}$$

SO(n)

The physical laws of the nature do not depend on the position and on the orientation of an experimentalist, thus they need to satisfy the translational and rotational symmetry. Mathematically, rotational symmetry is described by the SO(n) group, which is the symmetry group of an n-dimensional sphere. Given the Lorentz structure of the space-time, having (1, 3)[6] signature (since the metric tensor has the $diag(+---)$ signature), the space-time symmetries are described by the $O(1,3)^+$ group (Section 1.3).

Behaviour of particles wave-functions essentially depends on their spin, affecting the transformation properties of the wave-function. Hence, a few groups of objects exists, depending on the representation that they span:

- scalar representation. Examples: Higgs boson or π mesons.
- spinor representation. It is the case for all fermions, such as: electron, muon, neutrinos and so on.
- vector representation. Mediators of the SM interactions (gluon, photon, vector bosons) and hypothetical graviton.

[6] Or, as it often used in particle physics, (3, 1) signature, which is also used in this document.

1.3 Poincaré group as hometown for particles

One of the most important group in particle physics is the Poincaré group, which represents all its possible transformations (isometries) leaving the space-time invariant. Such transformations consist of two independent kinds: 4D translations and 4D-rotations (3D rotations and Lorentz boosts, described by the proper (no mirroring) orthochronous (direction of time is preserved) subpart of the Lorentz group $O(1,3)^{\uparrow}_{+}$). Translations are described by the four Abelian generators P^{μ} and the 4D rotations are defined by J^{μ}, including the 3D rotation generators as the space-components.

Poincaré group is a direct sum: $SO(3,1) = SO(3) \oplus SO(3)$. In this way, there are two Casimir operators, independently for each sub-group. Hence, the labelling of the representations $((j_1, j_2))$ is done by stating the two values of the Casimir element: one for each sub-group [3].

1.3.1 Scalar representation $(0,0)$

Under this representation transformation of objects is trivial and the corresponding generators N_i and Q_i are equal to zero.

1.3.2 Weyl (spinor) representation $\left(\frac{\mathbf{1}}{\mathbf{2}}, 0\right)$

In this representation (and the $\left(0, \frac{\mathbf{1}}{\mathbf{2}}\right)$), objects are two-dimensional and they are called Weyl spinors:

$$\psi_L \in \left(\tfrac{\mathbf{1}}{\mathbf{2}}, 0\right) \quad \psi_R \in \left(0, \tfrac{\mathbf{1}}{\mathbf{2}}\right).$$

This representation comes from the $SO(3)$ and $SU(2)$ homomorphism, hence the generators Q_i (in the case of $\left(\left(\frac{\mathbf{1}}{\mathbf{2}}, 0\right)\right)$ or N_i (for the $\left(0, \frac{\mathbf{1}}{\mathbf{2}}\right)$ case) can be represented using the Pauli matrices:

$$Q_i = \frac{\sigma_i}{2} \quad N_i = \frac{\sigma_i}{2}$$

where the Pauli matrices are:

$$\sigma_1 = \begin{pmatrix} 0 & 1 \\ 1 & 0 \end{pmatrix} \quad \sigma_2 = \begin{pmatrix} 0 & -i \\ i & 0 \end{pmatrix} \quad \sigma_3 = \begin{pmatrix} 1 & 0 \\ 0 & -1 \end{pmatrix}.$$

To distinguish between the $(\frac{\mathbf{1}}{\mathbf{2}}, 0)$ and $(0, \frac{\mathbf{1}}{\mathbf{2}})$ indexes, one uses dotted indexes $\dot{\alpha}$ for ψ_L and normal ones for ψ_R: $(\psi_L)_{\dot{\alpha}}$, $(\psi_R)_{\alpha}$.

1.3.3 Dirac (bi-spinor) representation $(\frac{1}{2}, \frac{1}{2})$

In this representation, a generic element can be written as a pair of $\left(\frac{\mathbf{1}}{\mathbf{2}}, 0\right)$ and $\left(0, \frac{\mathbf{1}}{\mathbf{2}}\right)$ objects:

$$\psi = \left((\psi_L)_{\dot{\alpha}}, (\psi_R)_{\beta}\right). \tag{1.30}$$

1.3.4 Tensor representation

A tensor structure can be straight-forwardly decomposed into the direct sum, showing that such representation is reducible. An example is the decomposition of a generic $\mathbf{4} \otimes \mathbf{4}$ tensor $T^{\mu\nu}$:

$$\mathbf{4} \otimes \mathbf{4} = \underbrace{\mathbf{1}}_{T} \oplus \underbrace{\mathbf{6}}_{A^{\mu\nu}} \oplus \underbrace{\mathbf{9}}_{S^{\mu\nu}}, \tag{1.31}$$

with scalar T (scalar, thus invariant under group transformation), anti-symmetric part $A^{\mu\nu}$ and symmetric traceless part $S^{\mu\nu}$, defined as:

$$T = T^{\mu\nu}T_{\mu\nu} \tag{1.32}$$

$$A^{\mu\nu} = \frac{T^{\mu\nu} - T^{\nu\mu}}{2} \tag{1.33}$$

$$S^{\mu\nu} = \frac{T^{\mu\nu} + T^{\nu\mu}}{2} - \frac{\delta^{\mu\nu}}{4}T. \tag{1.34}$$

Any higher-dimensional tensor representation can be decomposed in a similar way by removing all traces, and by applying symmetrisation or antisymmetrisation over all pairs of indexes.

1.3.5 Particle Content of the SM

Particle content of the SM is shown in Fig. 1.1. It consists of three generations of leptons with progressively growing masses, which participate only in the EM, weak and gravitational interactions[7]. Quarks also take part in the strong interaction. The EM interaction is mediated by photon, the weak occurs via the weak gauge bosons and the strong interaction is carried by gluons. Higgs boson field is responsible for the non-zero masses of particles, after the electro-weak symmetry breaking.

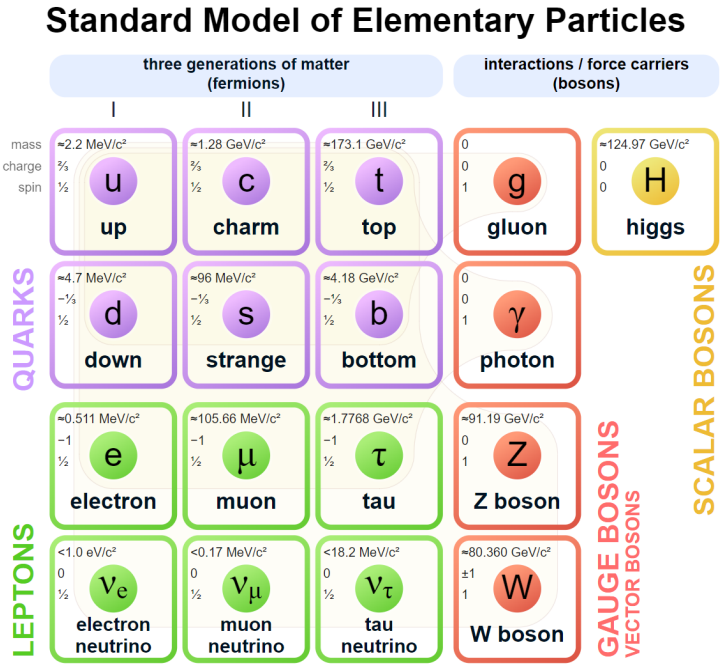

Figure 1.1: Particle content of the SM. Source: [9].

SM is based on the local $\mathrm{SU}(3)_c \times \mathrm{SU}(2)_L \times \mathrm{U}(1)_Y$ gauge symmetry group[8], which stand for the colour symmetry in the QCD sector, symmetry of the left-handed particles in the electro-weak interactions and a hypercharge Y symmetry. Detailed description of each of these groups is given in the following text.

[7] Neutrinos are electromagnetically neutral, thus do not participate in the EM interaction.

[8] The choice of the symmetry group is based on the experiment: such a group choice describes well the observed properties, such as: the number of QCD colours, weak bosons and others.

1.4 Equations of motion

Equations of motion of a free field essentially depend on its spin and space-time transformation properties. In this section, the following Lorentz transformation (see Appendix B) is considered:

$$x'^{\mu} = \Lambda^{\mu}_{\nu} x^{\nu} \tag{1.35}$$

Scalar (pseudo-scalar) field $\phi(x)$

For a scalar field ϕ and pseudo-scalar field ϕ_p, which transform under the Lorentz transformation as:

$$\begin{aligned} \phi'(x') &= \phi(x) \\ \phi'_p(x') &= \phi(x) \det \Lambda \end{aligned} \tag{1.36}$$

the equations of motion (known as Klein-Gordon equation [6]) are:

$$\left(\Box + m^2\right) \phi = 0 \tag{1.37}$$

The corresponding Lagrangian is:

$$\mathcal{L}_{\text{Klein-Gordon}} = \partial_\mu \phi^* \partial^\mu \phi - m^2 \phi^* \phi \tag{1.38}$$

Spinor field $\psi(x)$

For a spinor field $\psi(x)$ and its Dirac-adjoint one $\bar{\psi}(x)$ (see appendix B about the gamma-matrices and Dirac-adjoint), Lorentz transformations are[9]:

$$\begin{aligned} \psi'_\sigma(x') &= L_{\sigma\rho} \psi'_\rho(x) \\ \bar{\psi}'_\sigma(x') &= \bar{\psi}'_\rho(x) L^{-1}_{\rho\sigma} \end{aligned} \tag{1.39}$$

The equation of motion (Dirac equation) is:

$$\left(i\partial\!\!\!/ - m\right) \psi = 0, \tag{1.40}$$

where $\partial\!\!\!/ = \gamma^\mu \partial_\mu$. More details about the solutions of Dirac equation are given in appendix B.

The corresponding Lagrangian is:

$$\mathcal{L}_{\text{Dirac}} = \bar{\psi} \left(i\partial\!\!\!/ - m\right) \psi \tag{1.41}$$

Vector field $A^\mu(x)$

A vector field $A^\mu(x)$, transforming under the Lorentz transformations as:

$$A'^{\mu}(x') = \Lambda^{\mu}_{\nu} A^{\nu}(x) \tag{1.42}$$

The corresponding equations of motion (Proca equation) is:

$$\left(\Box + m^2\right) A^\mu = 0, \tag{1.43}$$

[9] See Appendix B about the L and Λ matrices.

which in the case of a massless particle (photon, for example) can be expressed as:

$$\partial_\mu F^{\mu\nu} = 0 \tag{1.44}$$

The corresponding Lagrangian is:

$$\mathcal{L}_{Proca} = -\frac{1}{4} F_{\mu\nu} F^{\mu\nu} - m^2 A^\mu A_\mu, \tag{1.45}$$

with $F_{\mu\nu} = \partial_\mu A_\nu - \partial_\nu A_\mu$

1.5 Particles

1.5.1 Quarks

Under the assumption that masses of the first three quarks u, d, s are the same, it is possible to consider a symmetry between them, described by a $\mathrm{SU}(3)$ group[10]. It is said that these three quarks have different *flavours*, therefore this symmetry group is often called $\mathrm{SU}(3)_{flavour}$. In this case, each real physical state (observed particle) is a higher-order representation of this group. Therefore, out of these three lightest quarks, one can compose two types of composite, observed, particles:

- Baryons: they are bound states of three quarks, hence they span the $\mathbf{3} \otimes \mathbf{3} \otimes \mathbf{3}$ representation. It can be reduced to the following direct sum of irreducible ones:

  $$\mathbf{3} \otimes \mathbf{3} \otimes \mathbf{3} = \mathbf{10} \oplus \mathbf{8} \oplus \mathbf{8} \oplus \mathbf{1} \tag{1.46}$$

  yielding 27 particles[11] split out into one decuplet, two octets and a singlet. More details are given later on.

- Mesons are made of a quark and anti-quark. Denoting as $\bar{\mathbf{3}}$ representation of anti-quarks:

  $$\mathbf{3} \otimes \bar{\mathbf{3}} = \mathbf{8} \oplus \mathbf{1}. \tag{1.47}$$

  one octet and one singlet arises.

An example of the decuplet is given by Table 1.1.

Taking into account the remaining three flavours of quarks: c, b and t, breaks the symmetry assumption, since their masses are not generally negligible any more.

Colour

Discovery of the delta baryon Δ^{++} (uuu quarks) raised a problem: since spin of Δ^{++} is $\frac{3}{2}$, all the quarks must be aligned. Therefore, all of them must have the same quantum numbers, which is prohibited by QM. The simplest solution was to add a new quantum number, *colour* allowing these three u quarks to be in distinguishable quantum states. This new theory called *Quantum Chromodynamics (QCD)* [2] is based on a few axioms:

[10] More details on the properties of this group are given in 1.2.3.

[11] This calculation shows the number of the lowest mass hadrons, since no possible excitation is taken into account.

Particles	Quark composition
$\Delta^{++}(uuu)$	uuu
$\Delta^{+}(uud)$	$\frac{1}{\sqrt{3}}(uud + udu + duu)$
$\Delta^{0}(udd)$	$\frac{1}{\sqrt{3}}(udd + dud + ddu)$
$\Delta^{-}(ddd)$	ddd
$\Sigma^{*+}(uus)$	$\frac{1}{\sqrt{3}}(uus + usu + suu)$
$\Sigma^{*0}(uds)$	$\frac{1}{\sqrt{6}}(uds + dsu + sud + usd + sdu + du.s)$
$\Sigma^{*-}(dds)$	$\frac{1}{\sqrt{3}}(dds + dsd + sdd)$
$\Xi^{*0}(uss)$	$\frac{1}{\sqrt{3}}(uss + sus + ssu)$
$\Xi^{*-}(dss)$	$\frac{1}{\sqrt{3}}(dss + sds + ssd)$
$\Omega^{-}(sss)$	sss

Table 1.1: Particle composition of the $\mathrm{SU}(3)$ decuplet, composed from u, d, s quarks.

- Existence of the three *colours*, formally called *Red*, *Green*, *Blue*. So that, each quark, is in one of these states. Hence, an additional $\mathrm{SU}(3)_c$ symmetry[12]

- Any observable state is *colourless* (singlet of $\mathrm{SU}(3)_c$), hence physical states should belong to $\mathbf{1}$. For the 2-quark particles (mesons), this implies symmetry of the wave function under colour transformations. In contrary, for the 3-quarks particles (baryon), the wave function must be anti-symmetric.

This additional symmetry is *local*: any transformation (change of colour) depends on a space-time position. In other words, for a quark, to change its colour, it is necessary to interact with other ones[13]. This interaction is carried out by new particles: *gluons* (Section 1.6.2 on the strong interaction).

Quarks wavefunctions

Introduction of the colour, requires adding an additional multiplicative factor to the hadron wave function:

$$\psi = \psi_{space-time} \cdot \psi_{spin} \cdot \psi_{flavour} \cdot \psi_{colour} \tag{1.48}$$

Given that a baryonic wavefunction ψ must change sign after a parity transformation, the colour component ψ_{colour} must be anti-symmetrical:

$$\psi_{colour}^{baryon} = \frac{1}{\sqrt{6}}(RGB + BRG + GBR - RBG - BGR - GRB) \tag{1.49}$$

and for a meson, it must be symmetrical:

$$\psi_{colour}^{meson} = \frac{1}{\sqrt{3}}(R\bar{R} + G\bar{G} + B\bar{B}) \tag{1.50}$$

[12] c stands for *colour*.

[13] As an analogy, for an electron, to change its electromagnetic phase, it needs to emit or absorb a photon.

1.5.2 Leptons

Leptons, contrary to quarks, are not entangled and therefore can be observed. There exists three generations of lepton families, each consistent of a neutral light particle (neutrino) and its charged counter-part: electron, muon and taon families. Under electroweak interaction, they are undistinguishable, since they differ only in mass.

1.6 Interactions in the SM

1.6.1 Electromagnetic $\mathrm{U}(1)$

Equations of a motion for a free electron, described by Lagrangian[14]:

$$\mathcal{L}_{free} = i\bar{\psi}\gamma^{\mu}\partial_{\mu}\psi - m\bar{\psi}\psi \tag{1.51}$$

can be made invariant under an arbitrary $\mathrm{U}(1)$ local phase transformation:

$$\psi(x) \to \psi(x)' = \mathrm{e}^{i\alpha(x)}\psi(x), \tag{1.52}$$

with $\alpha(x)$ being real scalar field. Though, the Lagrangian itself is not invariant under these transformation. To preserve it, one may consider the following modification of the derivatives:

$$\partial_{\mu} \to D_{\mu} \equiv \partial_{\mu} - ieA_{\mu}, \tag{1.53}$$

where A_{μ} is an arbitrary vector field, transformed under the given $\mathrm{U}(1)$ symmetry as:

$$A_{\mu} \to A_{\mu} + \frac{1}{e}\partial_{\mu}\alpha \tag{1.54}$$

Therefore, it can be checked that the modified Lagrangian:

$$\mathcal{L}_{QED} = i\bar{\psi}\gamma^{\mu}D_{\mu}\psi - \bar{\psi}\psi = i\bar{\psi}\gamma^{\mu}\partial_{\mu}\psi + e\bar{\psi}\gamma^{\mu}\psi A_{\mu} - m\bar{\psi}\psi \tag{1.55}$$

is invariant under the underlying $\mathrm{U}(1)$ transformation. This additional vector field A_{μ} required to preserve the theory invariant under $\mathrm{U}(1)$ transformation is called *gauge field*. It is coupled to the matter field ψ via the $e\bar{\psi}\gamma^{\mu}\psi A_{\mu}$ term. From which, one may define a current of matter $j^{\mu} \equiv \bar{\psi}\gamma^{\mu}\psi$. This new field A_{μ} can be associated with a physical photon field, by adding a dynamical term to the Lagrangian[15]:

$$\mathcal{L}_{A} = -\frac{1}{4}F_{\mu\nu}F^{\mu\nu}, \tag{1.56}$$

with $F_{\mu\nu}$:

$$F_{\mu\nu} = \partial_{\mu}A_{\nu} - \partial_{\nu}A_{\mu} \tag{1.57}$$

The complete Lagrangian of the electromagnetic interaction is written as:

$$\mathcal{L}_{QED} = \underbrace{\bar{\psi}\left(i\gamma^{\mu}\partial_{\mu} - m\right)\psi}_{\text{Dynamics of matter}} + \underbrace{e\bar{\psi}\gamma^{\mu}\psi A_{\mu}}_{\text{EM interaction}} - \underbrace{\frac{1}{4}F_{\mu\nu}F^{\mu\nu}}_{\text{Dynamics of EM field}} \tag{1.58}$$

[14] By Lagrangian, one should understand the Lagrangian density throughout the document.

[15] another form of a dynamical term: $\frac{1}{2}m^2A_{\mu}A^{\mu}$ is not allowed, since it would violate the underlying gauge invariance.

1.6.2 Strong $\mathrm{SU}(3)$

As mentioned in Section 1.5.1, solving the problem of the existence of double-charged baryons, required the introduction of a new quantum number: colour, which brought up a new gauge group $\mathrm{SU}(3)_c$ to accommodate for local colour conservation. Following arguments from the group theory on $\mathrm{SU}(3)$ (see Section 1.2.3), this group is spanned by 8 generators (for an $\mathrm{SU}(N)$, N^2-1), which may be chosen in the Gell-Mann basis (eq. 1.22). These eight generators give a rise to eight *gluons*, particles assuring local gauge invariance. To study properties of the strong interaction, one needs to study the corresponding Lagrangian, which is a particular case of a *Yang-Mills* theory [2], which describes a general dynamics of a gauge field $\mathcal{F}$, associated with a symmetry group $\mathrm{SU}(N)$. In the coordinates, the Lagrangian takes the following form:

$$\mathcal{L}_{Yang-Mills} = -\frac{1}{4}\mathcal{F}^{\alpha}_{\mu\nu}\mathcal{F}^{\mu\nu\alpha}, \tag{1.59}$$

where $\mathcal{F}^{\alpha}_{\mu\nu}$ is the field strength tensor (curvature tensor), defined as:

$$\mathcal{F}^{\alpha}_{\mu\nu} = \partial_\mu A^{\alpha}_{\nu} - \partial_\nu A^{\mu\alpha} + g f^{\alpha\beta\gamma} A^{\beta}_{\mu} A^{\gamma}_{\nu}, \tag{1.60}$$

with $f^{\alpha\beta\gamma}$ being structure constants of the underlying $\mathrm{SU}(N)$. The corresponding covariant derivative D_μ is:

$$D_\mu \equiv \partial_\mu - igT^{\alpha}A^{\alpha}_{\mu}, \tag{1.61}$$

where T^α are the generators of $\mathrm{SU}(N)$. And the equations of motion for the $\mathcal{F}$ field are:

$$\begin{aligned} (D_\mu \mathcal{F}^{\mu\nu})^{\alpha} &= \mathcal{J}^{\nu\alpha} \\ \left(D_\mu \tilde{\mathcal{F}}^{\mu\nu}\right)^{\alpha} &= 0 \end{aligned} \tag{1.62}$$

where the $\mathcal{J}^{\nu\alpha}$ is the external current of matter and $\tilde{\mathcal{F}}^{\mu\nu}$ is the *dual-strength-tensor*:

$$\tilde{\mathcal{F}}^{\mu\nu} \equiv \frac{1}{2}\epsilon^{\mu\nu\rho\sigma}\mathcal{F}_{\rho\sigma} \tag{1.63}$$

The existence of the product of $if^{\alpha\beta\gamma}A^{\beta}_{\mu}A^{\gamma}_{\nu}$ terms leads to the field self-interaction (term $\mathcal{F}^{\alpha}_{\mu\nu}\mathcal{F}^{\mu\nu\alpha}$ contains products of three and four A^{α}_{μ} fields, hence allowing three- and four-gluon interactions[16]).

1.6.3 Electro-Weak $\mathrm{SU}(2)_L \times \mathrm{U}(1)_Y$

Weak interaction

Developing the successful four-fermion weak theory by Fermi, introduced the following Lagrangian:

$$\mathcal{L}_{weak} = \mathcal{L}_{ch} + \mathcal{L}_{n}, \tag{1.64}$$

which describe the charged and neutral interactions, respectively[17]:

$$\begin{aligned} \mathcal{L}_{ch} &= \frac{G}{\sqrt{2}}\mathcal{J}^{+}_{\mu}\mathcal{J}^{-\mu} \\ \mathcal{L}_{n} &= \frac{G\rho}{\sqrt{2}}\mathcal{J}^{0}_{\mu}\mathcal{J}^{0\mu} \end{aligned} \tag{1.65}$$

[16] The three gluons part of the Lagrangian is proportional to $\partial_\mu AAA$, hence the corresponding vertex is proportional to the gluons momentum, while the four-gluon term is proportional to $AAAA$, hence is not dependent on the gluon-momentum.

[17] In SM, $\rho = 1$.

With currents $\mathcal{J}^\mu$:

$$\mathcal{J}^\mu = \bar{\psi}_f \gamma^\mu (1 - \gamma^5) \psi_i, \tag{1.66}$$

where ψ_i and ψ_f are Dirac bispinors of the initial and final state, respectively. This theory is known as *V-A* (vector-axial vector) interaction[18]. In the definition for the weak current defined by the eq. 1.66, the interaction operator $\mathcal{O} \equiv \gamma^\mu(1 + \gamma^5)$ can be expressed as:

$$\mathcal{J}^\mu = \gamma^\mu(1 - \gamma^5) = \frac{1}{2}\left(1 - \gamma_5\right)\gamma^\mu\left(1 + \gamma_5\right) \tag{1.67}$$

One can notice that $\left(\frac{1-\gamma_5}{2}\right)$ is a chiral projector P_L on the left-handed state ψ_L:

$$\frac{1 - \gamma_5}{2}\psi = \psi_L. \tag{1.68}$$

Hence, in the expression for the current $\mathcal{J}_\mu$ obtained in the eq. 1.67, the operator $\mathcal{O}$ acts as a chiral projector of the initial and final states on their left-components:

$$\mathcal{J}^\mu = 2\bar{\psi}_{fL}\gamma^\mu\psi_{iL} \tag{1.69}$$

Showing that only left-handed components of the fields take part in the weak interaction.

With the observation of weak bosons [10, 11, 12, 13, 14], all the allowed weak currents are:

- Charged currents $J^\pm$ carried out by the $W^\pm$ bosons. It couples quarks of the same generation but with different electronic charges ($u - d$,$c - s, t - b$). In the lepton sector, it allows interaction of a lepton-neutrino pair of the same flavour ($e - \nu_e, \mu - \nu_\mu, \tau - \nu_\tau$).
- Neutral current J^0 is carried out by the Z-boson. It couples pairs of a particle and its anti-particle ($q - \bar{q}, \ell - \bar{\ell}$, where q is any quark and ℓ is any lepton, including neutrinos).

Weak interaction can be described by a $\mathrm{SU}(2)$ symmetry. All particles are classified according to the projection of their weak isospin I_3^w:

- doublets with $I_3^w = \frac{1}{2}$:

$$\begin{pmatrix} I_3^W = & \frac{1}{2} \\ I_3^W = & -\frac{1}{2} \end{pmatrix} = \begin{pmatrix} \nu_e \\ e \end{pmatrix}_L, \ldots \begin{pmatrix} u \\ d \end{pmatrix}_L, \ldots \tag{1.70}$$

- singlets with $I_3^W = 0$:

$$\nu_{eR}, e_R, .., u_R, d_R, ... \tag{1.71}$$

Components of all doublets differ by their electric charge on $\Delta Q = 1$, hence it's possible to define weak hypercharge Y^W so that:

$$Q = I_3^W + \frac{Y^W}{2}, \tag{1.72}$$

where $Y^W = -1$ for lepton doublets, $Y^W = -2$ for right-handed electrons and $Y^W = 0$ for right-handed neutrinos (which do not exist in the SM) (Table 1.2).

[18] γ^μ is the vector part and $\gamma^\mu\gamma^5$ is the axial part.

Salam-Weinberg model of electroweak interaction

In the 1960s various models [15, 16, 17, 18] were proposed to accommodate for existence of experimentally observed masses of the weak bosons. There are four boson mediator of interactions in the electroweak theory: γ, W^+, W^-, Z^0, however, there exists no simple group with four generators. A simplest solution is to use a composed group $\mathrm{SU}(2)_L \times \mathrm{U}(1)$, where $\mathrm{U}(1)$ is not the electromagnetic gauge group. To study properties of the theory with a gauge invariant group $\mathrm{SU}(2)_L \times \mathrm{U}(1)$, one needs to modify the derivatives by the covariant ones to account for the new interactions available. For simplicity, one could consider a theory with only one generation of leptons: one left-handed electron e_L, its neutrino ν_L, right-handed electron e_R and its anti-neutrino ν_R. One could denote a doublet of left leptons as L:

$$L = \begin{pmatrix} \nu_L \\ e_L \end{pmatrix}, \tag{1.73}$$

fields associated with $\mathrm{SU}(2)$ and $\mathrm{U}(1)$ as W_μ^α (α enumerates generators: $\alpha = 1,2,3$) and B_μ respectively. Charges of the particles under these groups are listed in Table 1.2.

(Component)	Y_w	T_3
$L = \begin{pmatrix} \nu_L \\ e_L \end{pmatrix}$	-1	1/2
e_R	-2	0
ν_R	0	0

Table 1.2: $SU(2) \times \mathrm{U}(1)$ charges of the particle content in the Salam-Weinberg model. Quarks are omitted for simplicity. Y_w is the weak hypercharge, and T_3 is the projection of the weak isospin.

Lagrangian of this theory is given by:

$$-\frac{1}{4} W_{\mu\nu}^\alpha W^{\mu\nu\alpha} - \frac{1}{4} B_{\mu\nu} B^{\mu\nu} + i\bar{L} \not{D} L + i\bar{e_R} \not{D} e_R + i\bar{\nu_R} \not{D} \nu_R, \tag{1.74}$$

with field strength tensors:

$$\begin{aligned} W_{\mu\nu}^\alpha &\equiv \partial_\mu W_\nu^\alpha - \partial_\nu W_\mu^\alpha + g\epsilon^{\alpha\beta\gamma} W_\mu^\beta W_\nu^\gamma \\ B_{\mu\nu} &\equiv \partial_\mu B_\nu - \partial_\nu B_\mu \end{aligned} \tag{1.75}$$

Covariant derivative of the fields under these symmetry groups is:

$$D_\mu \equiv \partial_\mu - ig\vec{T}\vec{W}_\mu - ig'\frac{Y}{2} B_\mu \tag{1.76}$$

where g and g' are the couplings of $\mathrm{SU}(2)$ and $\mathrm{U}(1)$, respectively. $\vec{T}$ is the $\mathrm{SU}(2)$ generator[19] $T \cdot \vec{\sigma}$, where T is the corresponding charge and $\vec{\sigma}$ are the Pauli matrices. For all the particles in the model, it takes different form, depending on their charges under the $\mathrm{SU}(2)_L$ and $\mathrm{U}(1)$ groups:

[19] The $\mathrm{U}(1)$ generator is trivial, unity.

- L with $T = 1/2, Y_w = -1$:

$$D_\mu = \partial_\mu - ig\frac{\vec{\sigma}}{2}\vec{W}_\mu + i\frac{g'}{2}B_\mu \tag{1.77}$$

- e_R with $T = 0, Y_w = -2$:

$$D_\mu = \partial_\mu + ig'B_\mu \tag{1.78}$$

- ν_R with $T = 0, Y_w = 0$:

$$D_\mu = \partial_\mu \tag{1.79}$$

To find out couplings of the matter fields with the gauge fields in this theory, one needs to extract the interaction terms from the total Lagrangian.

For the $\bar{L}i\not{D}L$ term:

$$\frac{1}{2}\begin{pmatrix}\bar{\nu}_L & \bar{e}_L\end{pmatrix}\begin{pmatrix}gW_\mu^3 - g'B_\mu & g(W_\mu^1 - iW_\mu^2)\\ g(W_\mu^1 + iW_\mu^2) & -gW_\mu^3 - g'B_\mu\end{pmatrix}\gamma^\mu\begin{pmatrix}\nu_L\\ e_L\end{pmatrix} \tag{1.80}$$

Denoting:

$$\begin{aligned} Z_\mu &\equiv \frac{gW_\mu^3 - g'B_\mu}{\sqrt{g^2+g'^2}}\\ A_\mu &\equiv \frac{g'W_\mu^3 + gB_\mu}{\sqrt{g^2+g'^2}}\\ W_\mu^+ &\equiv \frac{1}{\sqrt{2}}\left(W_\mu^1 - iW_\mu^2\right)\\ W_\mu^- &\equiv \frac{1}{\sqrt{2}}\left(W_\mu^1 + iW_\mu^2\right) \end{aligned} \tag{1.81}$$

which yields the following substitution for B_μ and W_μ^3:

$$\begin{aligned} B_\mu &= \frac{gA_\mu - g'Z_\mu}{\sqrt{g^2+g'^2}}\\ W_\mu^3 &= \frac{g'A_\mu + gZ_\mu}{\sqrt{g^2+g'^2}} \end{aligned} \tag{1.82}$$

one obtains:

$$\frac{1}{2}\begin{pmatrix}\bar{\nu}_L & \bar{e}_L\end{pmatrix}\begin{pmatrix}-\frac{gg'}{\sqrt{g^2+g'^2}}Z_\mu & \sqrt{2}W_\mu^+\\ \sqrt{2}W_\mu^- & -2\frac{gg'}{\sqrt{g^2+g'^2}}A_\mu - \frac{g^2-g'^2}{\sqrt{g^2+g'^2}}Z_\mu\end{pmatrix}\gamma^\mu\begin{pmatrix}\nu_L\\ e_L\end{pmatrix} \tag{1.83}$$

Multiplying matrices and grouping out terms, one finds:

$$\begin{aligned}
&\underbrace{-\frac{gg'}{\sqrt{g^2+g'^2}}A_\mu\bar{e}_L\gamma^\mu e_L}_{\text{left electrons with } A_\mu} \underbrace{-\frac{g^2-g'^2}{2\sqrt{g^2+g'^2}}Z_\mu\bar{e}_L\gamma^\mu e_L}_{\text{left electrons with } Z_\mu} \\
&\underbrace{-\frac{\sqrt{2}}{2}W^+_\mu\bar{\nu}_L\gamma^\mu e_L}_{\text{left leptons with } W^+_\mu} \underbrace{-\frac{\sqrt{2}}{2}W^-_\mu\bar{e}_L\gamma^\mu\nu_L}_{\text{left leptons with } W^-_\mu} \\
&\underbrace{+\frac{\sqrt{g^2+g'^2}}{2}Z_\mu\bar{\nu}_L\gamma^\mu\nu_L}_{\text{left neutrinos with } Z_\mu}
\end{aligned} \tag{1.84}$$

The coefficient of the $A_\mu\bar{e}_L\gamma^\mu e_L$ term can be associated with the electromagnetic charge e:

$$e \equiv \frac{gg'}{\sqrt{g^2+g'^2}} \tag{1.85}$$

Interactions of the right particles in this theory are given by taking a look onto the interaction part of the $i\bar{e}_R\not{D}e_R$ term:

$$\bar{e}_R i\left(ig'B_\mu\gamma^\mu\right)e_R = \underbrace{-eA_\mu\bar{e}_R\gamma^\mu\bar{e}_R}_{\text{right electrons with } A_\mu} + \underbrace{\frac{g'^2}{\sqrt{g^2+g'^2}}Z_\mu\bar{e}_R\gamma^\mu\bar{e}_R}_{\text{right electrons with } Z_\mu} \tag{1.86}$$

Introducing the following notation[20]:

$$\sin\theta_W \equiv \frac{g'}{\sqrt{g^2+g'^2}} \quad \cos\theta_W \equiv \frac{g}{\sqrt{g^2+g'^2}} \tag{1.87}$$

and grouping out electromagnetic current:

$$\mathcal{J}^{em}_\mu \equiv -\bar{e}_L\gamma_\mu e_L + \bar{e}_R\gamma_\mu e_R \tag{1.88}$$

and current of the third component of weak isospin $\mathcal{J}^3$:

$$\begin{aligned}
\overrightarrow{\mathcal{J}}_\mu &\equiv \bar{L}\gamma_\mu\frac{1}{2}\overrightarrow{\tau}L \\
\mathcal{J}^3_\mu &= \frac{1}{2}\left(\bar{\nu}\gamma_\mu\nu - \bar{e}_L\gamma_\mu e_L\right)
\end{aligned} \tag{1.89}$$

one obtains the following parts of the Lagrangian associated with the neutral and charged currents:

$$\begin{aligned}
\mathcal{L}^N &= e\mathcal{J}^{em}_\mu A^\mu + \frac{g}{\cos\theta_W}\left(\mathcal{J}^3_\mu - \sin^2\theta_W\mathcal{J}^{em}_\mu\right)Z^\mu \\
\mathcal{L}^C &= -\frac{g}{\sqrt{2}}\left(\bar{\nu}\gamma^\mu\frac{1-\gamma_5}{2}e\right)W^+_\mu + h.c.
\end{aligned} \tag{1.90}$$

In this model, all the weak interactions appear naturally. However, discoveries that the weak bosons have masses require an additional mechanism, which is discussed further (Section 1.6.5).

[20] parameter θ_W is called Weinberg angle.

1.6.4 Quarks in the Electroweak interaction

To describe electroweak interaction of quarks, one needs to identify their Y_W and T_3 charges under $\mathrm{SU}(2)_L \times \mathrm{U}(1)$ symmetry group, which describes the interaction itself. Given the relation between the hypercharge, weak isospin and electric charge:

$$Y_w = 2(Q - T_3), \tag{1.91}$$

The Y_w and T_3 charges for the quark sector are described by Table 1.3.

(Component)	Y_w	T_3
$Q = \begin{pmatrix} u_l \\ d_L \end{pmatrix}$	1/3	1/2
u_R	4/3	0
d_R	-2/3	0

Table 1.3: $SU(2) \times \mathrm{U}(1)$ charges of quarks in the Salam-Weinberg model. Quarks are omitted for simplicity. Y_w is the weak hypercharge and T_3 is the projection of the weak isospin.

Hence, the covariant derivative eq. (1.76) takes the following forms:

- Q with $T = 1/2, Y_w = 1/3$:

$$D_\mu = \partial_\mu - ig\frac{\vec{\tau}}{2}\vec{W}_\mu - i\frac{g'}{6}B_\mu \tag{1.92}$$

- u_R with $T = 0, Y_w = 4/3$:

$$D_\mu = \partial_\mu - \frac{2ig'}{3}B_\mu \tag{1.93}$$

- d_R with $T = 0, Y_w = -2/3$:

$$D_\mu = \partial_\mu + \frac{ig'}{3}B_\mu \tag{1.94}$$

The quark part of the electroweak Lagrangian[21]:

$$\mathcal{L}^{EW}_{quarks} = i\bar{Q}\not{D}Q + i\bar{u_R}\not{D}u_R + i\bar{d_R}\not{D}d_R \tag{1.95}$$

Taking a look on the interaction parts of these terms reveals details on the interaction of quarks and electroweak bosons[22]:

[21] mass terms are omitted.
[22] terms with ∂_μ are omitted.

- $\bar{Q}\not{D}Q$:

$$\begin{aligned}\bar{Q}\not{D}Q &= \begin{pmatrix}\bar{u}_L & \bar{d}_L\end{pmatrix}(-\frac{i}{2})\begin{pmatrix} gW_\mu^3+\frac{g'}{3}B_\mu & g\sqrt{2}W_\mu^- \\ g\sqrt{2}W_\mu^+ & -gW_\mu^3+\frac{g'}{3}B_\mu\end{pmatrix}\begin{pmatrix}u_L\\ d_L\end{pmatrix} \\ &= \underbrace{\frac{2}{3}eA_\mu\bar{u}_L\gamma^\mu u_L}_{u \text{ EM interaction}} - \underbrace{\frac{1}{3}eA_\mu\bar{d}_L\gamma^\mu d_L}_{d \text{ EM interaction}} \\ &+ \underbrace{\frac{g^2-g'^2/3}{2\sqrt{g^2+g'^2}}Z_\mu\bar{u}_L\gamma^\mu u_L}_{u-Z^0 \text{ weak interaction}} - \underbrace{\frac{g^2+g'^2/3}{2\sqrt{g^2+g'^2}}Z_\mu\bar{d}_L\gamma^\mu d_L}_{d-Z^0 \text{ weak interaction}} \\ &+ \underbrace{\frac{\sqrt{2}}{2}g\bar{u}_L W_\mu^- d_L}_{d-u-W^- \text{ weak interaction}} + \underbrace{\frac{\sqrt{2}}{2}g\bar{d}_L W_\mu^+ u_L}_{d-u-W^+ \text{ weak interaction}}\end{aligned} \tag{1.96}$$

- $\bar{u}_R\not{D}u_R$:

$$\begin{aligned}i\bar{u}_R\left(\frac{-2ig'}{3}B_\mu\right)u_R = \\ = \underbrace{\sqrt{g^2+g'^2}u_R^\dagger A_\mu u_R}_{u\bar{u} \text{ EM interaction}} + \underbrace{\sqrt{g^2+g'^2}u_R^\dagger Z_\mu u_R}_{u\bar{u} \text{ weak interaction}}\end{aligned} \tag{1.97}$$

- $\bar{d_R}\not{D}d_R$:

$$\begin{aligned}-i\bar{d}_R\left(\frac{ig'}{3}B_\mu\right)d_R = \\ = \underbrace{\frac{\sqrt{g^2+g'^2}}{2}d_R^\dagger A_\mu d_R}_{d\bar{d} \text{ EM interaction}} + \underbrace{\frac{\sqrt{g^2+g'^2}}{2}d_R^\dagger Z_\mu d_R}_{d\bar{d} \text{ weak interaction}}\end{aligned} \tag{1.98}$$

1.6.5 Spontaneous Symmetry Breaking and Higgs boson

Given that three fields (W^+, W^-, Z^0) out of four have a mass, one requires adding new degrees of freedom to the model[23]. The simplest way is to introduce an additional doublet of scalar fields ϕ:

$$\phi = \begin{pmatrix}\phi^+\\ \phi^0\end{pmatrix}, \tag{1.99}$$

with weak hypercharge $Y_W = 1$ and weak isospin $T_3 = 1/2$, described by a Lagrangian:

$$\mathcal{L} = (D_\mu\phi)^\dagger (D^\mu\phi) + V(\phi), \tag{1.100}$$

where $V(\phi)$ is the potential energy term (eq. 1.114, Section 1.6.5). It is coupled to the fermions via the Yukawa term:

$$\mathcal{L}_{Yukawa} = \lambda_{\alpha\beta}\bar{L}_\alpha^\dagger\phi e_{r\ \beta} + \lambda_{\alpha\beta}\bar{Q}_L^\alpha\phi d_r^\beta h.c., \tag{1.101}$$

[23] Explicit mass term of the form $m^2\psi\psi^\dagger$ violates Lorentz-invariance and is therefore forbidden.

where α and β enumerate generations of leptons and quarks, $\lambda_{\alpha\beta}$ is the Yukawa coupling ($\lambda = \sqrt{2}\frac{m_f}{v}V_{\alpha\beta}$), and $V_{\alpha\beta}$ is an element of the CKM matrix for quarks and PMNS matrix for leptons (Section 1.6.6).

Its covariant derivative under the $\mathrm{SU}(2)_L \times \mathrm{U}(1)$ transformation, defined by eq. (1.76) is:

$$D_\mu = \partial_\mu - ig\frac{\vec{\sigma}}{2}\vec{W}_\mu - i\frac{g'}{2}B_\mu \tag{1.102}$$

Using allowed symmetries, it is possible to perform a gauge transformation to a coordinate system, where the ϕ field has components:

$$\phi(x) = \begin{pmatrix} 0 \\ \frac{v+h(x)}{\sqrt{2}} \end{pmatrix} \tag{1.103}$$

where v is the ground state energy: $\langle 0|\phi|0\rangle = v$ (Section 1.6.5). This gives $D_\mu\phi$:

$$\begin{aligned} D_\mu\phi &= \partial_\mu\phi - \frac{i}{2}\begin{pmatrix} gW_\mu^3 + g'B_\mu & g\sqrt{2}W_\mu^+ \\ g\sqrt{2}W_\mu^- & -gW_\mu^3 + g'B_\mu \end{pmatrix}\begin{pmatrix} 0 \\ \frac{v+h}{\sqrt{2}} \end{pmatrix} = \\ &= \partial_\mu\phi - \frac{i}{2}\begin{pmatrix} 2\frac{gg'}{\sqrt{g^2+g'^2}}A_\mu + \frac{g^2-g'^2}{\sqrt{g^2+g'^2}}Z_\mu & g\sqrt{2}W_\mu^+ \\ g\sqrt{2}W_\mu^- & -\sqrt{g^2+g'^2}Z_\mu \end{pmatrix}\begin{pmatrix} 0 \\ \frac{v+h}{\sqrt{2}} \end{pmatrix} = \\ &= \partial_\mu\phi - i\frac{v+h}{2\sqrt{2}}\begin{pmatrix} \sqrt{2}gW_\mu^+ \\ -\sqrt{g^2+g'^2}Z_\mu \end{pmatrix} \end{aligned} \tag{1.104}$$

In the expansion of $(D_\mu\phi)^\dagger (D^\mu\phi)$, one has two similar types of expressions: $v \cdot V_\mu^\dagger V^\mu$ and $h \cdot V_\mu^\dagger V^\mu$, where V_μ can be W_μ^+, W_μ^-, Z_μ. Since v is not a dynamic field, but a constant value, the first kind of terms represents the dynamics of the V_μ fields[24], while the other ones descrive the interaction between the gauge bosons V_μ with the field ϕ.

Masses of weak bosons

The interaction ϕVV ($V = W$ or Z) part of $(D_\mu\phi)^\dagger (D^\mu\phi)$ is[25]:

$$\mathcal{L}_{\phi VV} = -\frac{v^2}{8}\left(W_\mu^- W^{-\mu\dagger} + W_\mu^- W^{+\mu\dagger} + \left(g^2+g'^2\right)Z_\mu^\dagger Z^\mu\right) \tag{1.105}$$

These three terms resemble mass terms for the weak bosons $m^2 V_\mu^\dagger V^\mu$. Hence, one can associate:

- $m_Z = \frac{v\sqrt{g^2+g'^2}}{2}$ is mass of the Z-boson;
- $m_W = \frac{vg}{2}$ is the mass of $W^\pm$-bosons;
- $m_A = 0$ is the absent term, standing for the photon field mass.

[24] In QFT, dynamic terms, which describe the mass term of a free field ψ are: $m\psi^\dagger\psi$.
[25] using $W_\mu^{+\dagger} = W_\mu^-$

Fermion masses

Masses of the fermions are given by the $L\phi e$ interaction term in the Lagrangian:

$$\begin{aligned}\mathcal{L}_{L\phi e} &= \lambda \bar{L}^{\dagger} \phi e_R + h.c. \\ &= \lambda \begin{pmatrix} \bar{\nu} & \bar{e}_R \end{pmatrix} \begin{pmatrix} 0 \\ \frac{1}{\sqrt{2}}(v) \end{pmatrix} e_R + h.c. \\ &= \underbrace{\frac{\lambda v}{\sqrt{2}} \left(\bar{e}_L e_R + \bar{e}_R e_L \right)}_{\text{fermion mass of electrons}}\end{aligned} \tag{1.106}$$

Therefore, masses of fermions m_f are related to the Yukawa coupling $\lambda = \sqrt{2}\frac{m_f}{v}$ and the amplitude is linearly proportional to the mass. One can notice that in the SM, there are as many free parameters as fermion masses.

Quark masses

Masses of the down-quarks are given by the $Q\phi d_R$ interaction term in the Lagrangian:

$$-\lambda_{\alpha\beta} \bar{Q}_L^{\alpha} \phi d_R^{\beta}, \tag{1.107}$$

where the α and β indices enumerate quarks generations and $\lambda_{\alpha\beta}$ is an element of the Yukawa coupling matrix between those indices.

For the up-quarks, to preserve quantum numbers, a charge-conjugated Higgs field is used:

$$\phi^C \equiv -i\sigma^2 \phi^* \tag{1.108}$$

and the interaction terms, yielding to the up-quarks masses:

$$-\lambda_{\alpha\beta} \bar{Q}_L^{\alpha} \phi^c d_R^{\beta} \tag{1.109}$$

Higgs boson interaction

Assume an excitation of the Higgs field ϕ:

$$\phi = \frac{1}{\sqrt{2}} \begin{pmatrix} 0 \\ v + h(x) \end{pmatrix} \tag{1.110}$$

with $h(x)$ being infinitesimally small. Then, it will yield to similar terms in the Lagrangian as the mass terms, but with replacing v by $h(x)$. Hence, the strength of the Higgs boson interaction with other particles is proportional to their mass.

Lagrangian of the interaction of the Higgs boson with the other SM particles is:

$$\mathcal{L}_{Higgs} = g_{H\bar{f}f} \bar{f} f H + \frac{g_{HHH}}{6} H^3 + \frac{g_{HHHH}}{24} H^4 + \delta_V V_\mu V^\mu \left(g_{HVV} H + \frac{g_{HHVV}}{2} H^2 \right), \tag{1.111}$$

where g_* are the couplings of the Higgs boson with various particles:

$$\begin{aligned} g_{H\bar{f}f} &= \frac{m_f}{v} \\ g_{HVV} &= \frac{2m_v^2}{v} \\ g_{HHVV} &= \frac{2m_v^2}{v^2} \\ g_{HHH} &= \frac{3m_H^2}{v} \\ g_{HHHH} &= \frac{3m_H^2}{v^2} \end{aligned} \tag{1.112}$$

and δ_V:

$$\begin{aligned} \delta_W &= 1 \\ \delta_Z &= \frac{1}{2} \end{aligned} \tag{1.113}$$

Higgs potential

After the electroweak spontaneous symmetry breaking, the Higgs boson field acquires a non-zero ground-state energy v, around which the potential energy profile is no more symmetric. The new field configuration has only one remaining degree of freedom, out of the four initial ones. Three out of them are absorbed by the electroweak bosons, giving them masses. The last degree of freedom (Higgs boson) corresponds to a *Goldstone boson* [19, 20], which should be massless, but having a non-zero vev (vacuum expectation energy), implies a finite mass for the Higgs boson. The Higgs potential $V(\phi)$ is:

$$V(\phi) = \mu^2 \left(\phi^\dagger \phi\right) + \lambda \left(\phi^\dagger \phi\right)^2 \tag{1.114}$$

In the case of a negative value of μ^2, the potential takes a form with a minimum at a non-zero value (Fig. 1.2)

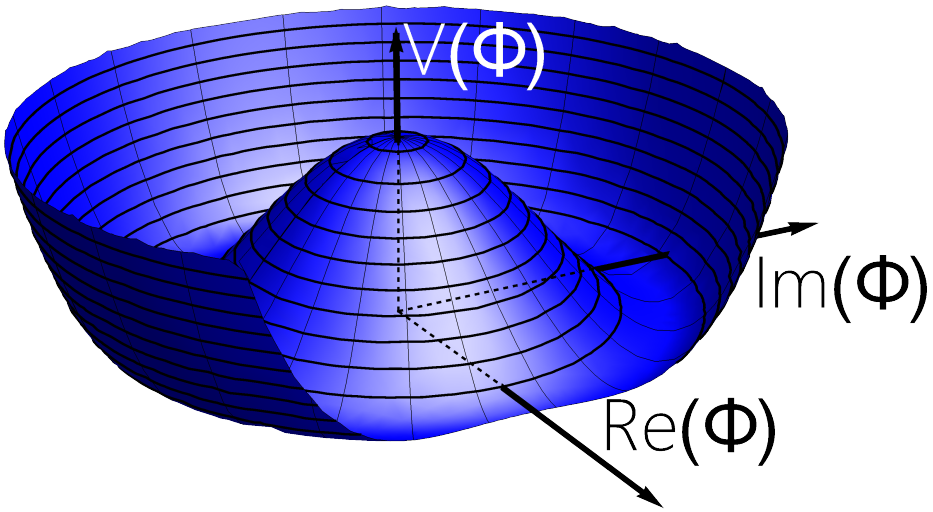

Figure 1.2: Illustration of the Higgs potential.

Therefore, the Higgs field, contrary to the other SM fields, has a non-zero vacuum (ground) energy:

$$\langle 0|H|0\rangle = v \tag{1.115}$$

In QFT, a particle is an excitation of the corresponding field around the vacuum state $|0\rangle$. Hence, for the Higgs field, an excitation with one particle takes the form:

$$\phi(x) = v + h(x) \tag{1.116}$$

1.6.6 Mixing of leptons and quarks

Studies of flavour-changing processes among quarks and leptons have revealed that in electroweak processes, particles are coupled not to the eigenstates of the strong and electromagnetic interactions, but to a combination of them. Mixing between the generations of quarks (leptons) is described by the CKM (for Cabibbo-Kobayashi-Maskawa), Cabibbo-Kobayashi-Maskawa [21, 22] and PMNS (for Pontecorvo-Maki-Nakagawa-Sakata [23]) matrices for quarks and leptons, respectively. They serve as a pivotal components of the electroweak theory and provide an elegant mathematical formulation of the flavour mixing. In the nutshell, a matrix element $V_{\alpha\beta}$ describes a probability of a particle of a flavour α transit to the flavour β.

Cabibbo-Kobayashi-Maskawa (CKM) matrix

In the theory proposed by Cabibbo-Kobayashi-Maskawa [22], objects coupling to the up-type quarks via charged-current interactions, are a mixture of various physical flavours of quarks:

$$\begin{aligned} |d'\rangle &= V_{ud}|d\rangle + V_{us}|s\rangle + V_{ub}|b\rangle \\ |s'\rangle &= V_{cd}|d\rangle + V_{cs}|s\rangle + V_{cb}|b\rangle \\ |b'\rangle &= V_{td}|d\rangle + V_{ts}|s\rangle + V_{tb}|b\rangle \end{aligned} \tag{1.117}$$

which can be written in the matrix notation as:

$$\begin{pmatrix} d' \\ s' \\ b' \end{pmatrix} = \begin{bmatrix} V_{ud} & V_{us} & V_{ub} \\ V_{cd} & V_{cs} & V_{cb} \\ V_{td} & V_{ts} & V_{tb} \end{bmatrix} \begin{pmatrix} d \\ s \\ b \end{pmatrix} \tag{1.118}$$

The down-type quarks, by convention, are not modified.

The most precise up-to-date measurement of the CKM matrix elements [24] gives:

$$\begin{bmatrix} |V_{ud}| & |V_{us}| & |V_{ub}| \\ |V_{cd}| & |V_{cs}| & |V_{cb}| \\ |V_{td}| & |V_{ts}| & |V_{tb}| \end{bmatrix} = \begin{bmatrix} 0.97373 \pm 0.00031 & 0.2243 \pm 0.0008 & 0.00382 \pm 0.00020 \\ 0.221 \pm 0.004 & 0.975 \pm 0.006 & 0.0408 \pm 0.0014 \\ 0.0086 \pm 0.0002 & 0.0415 \pm 0.0009 & 1.014 \pm 0.029 \end{bmatrix} \tag{1.119}$$

From this values, one can find that the measured values of this matrix has tension with the SM. For example, the first row elements show some deviation form unitarity:

$$|V_{ud}|^2 + |V_{us}|^2 + |V_{ub}|^2 = 0.9985 \pm 0.0007 \tag{1.120}$$

which is $2.2\ \sigma$ different from unity.

Pontecorvo–Maki–Nakagawa–Sakata (PMNS) matrix

Similarly to quarks, one has mixing between the generations of neutrinos, described by the PMNS matrix [23]:

$$\begin{pmatrix} \nu_e \\ \nu_\mu \\ \nu_\tau \end{pmatrix} = \begin{bmatrix} U_{e1} & U_{e2} & U_{e3} \\ U_{\mu 1} & U_{\mu 2} & U_{\mu 3} \\ U_{\tau 1} & U_{\tau 2} & U_{\tau 3} \end{bmatrix} \begin{pmatrix} \nu_1 \\ \nu_2 \\ \nu_3 \end{pmatrix} \tag{1.121}$$

The most precise up-do-date measurement of the $3\ \sigma$ ranges of the PMNS values are:

$$\begin{bmatrix} |U_{e1}| & |U_{e2}| & |U_{e3}| \\ |U_{\mu 1}| & |U_{\mu 2}| & |U_{\mu 3}| \\ |U_{\tau 1}| & |U_{\tau 2|} & |U_{\tau 3}| \end{bmatrix} = \begin{bmatrix} 0.803 \sim 0.845 & 0.514 \sim 0.578 & 0.142 \sim 0.155 \\ 0.233 \sim 0.505 & 0.460 \sim 0.693 & 0.630 \sim 0.779 \\ 0.262 \sim 0.525 & 0.473 \sim 0.702 & 0.610 \sim 0.762 \end{bmatrix} \tag{1.122}$$

1.7 Higgs boson phenomenology and experimental overview

1.7.1 Production

At the LHC, the Higgs boson is produced in the collision of protons composed of three valence[26] quarks and a set of virtual particles[27] and gluons, all of them may take part in the interaction. Distributions of all these particles depends on the so-called Bjorken scale, which is the fraction x of the total proton energy carried out by a particle[28]. This distribution is called Parton Distribution Function (PDF). Two examples are given in Fig. 1.3.

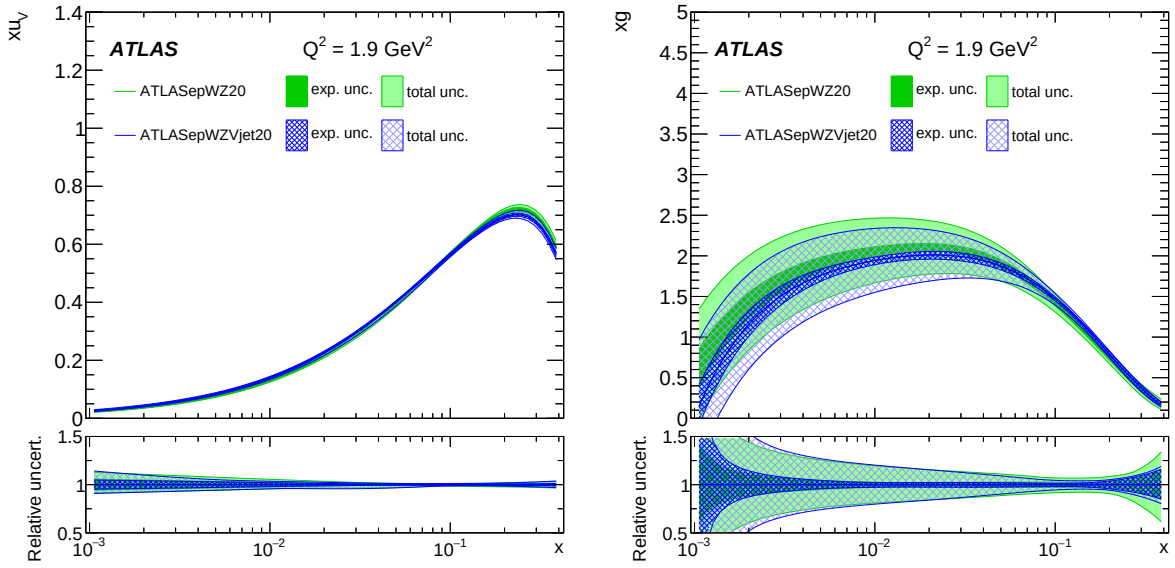

(a) (b)

Figure 1.3: Parton distribution function times x (Bjorken scale) of (a) valence up-quark and (b) gluon as a function of x. Source: [25].

Therefore, in a proton-proton collision, for any process, the cross-section σ of a process $p + p \to X$ is given by:

$$\sigma_{pp\to X} = \sum_{a,b} \int_0^1 \mathrm{d}x_1 f^{a,p}(x_1|\mu_F^2) \int_0^1 \mathrm{d}x_2 f^{b,p}(x_2|\mu_F^2) \hat{\sigma}_{ab\to X}\left(x_1 p_1, x_2, p_2, \alpha_S(\mu_R^2)\right) \quad (1.123)$$

where a and b are partons inside protons, x_i is the fraction of the total momentum of the proton carried out by the corresponding parton, $\mu_R(\mu_F)$ is the renormalisation (factorisation) scale.

[26] Quarks responsible for the quantum numbers of a particle. Usually, the valence quarks carry the biggest part of a proton momentum.

[27] Due to the quantum vacuum, any particle can be created for a short period of time.

[28] This variable is defined as $x = \frac{Q^2}{2p\cdot q}$, where $Q^2 = -q^2$, q is the transferred momentum (is negative), p is the proton 4-momentum. This variable is independent of a frame. In the rest frame, it corresponds to the fraction of energy.

The dominant production modes (Fig. 1.4) for the Higgs boson in proton-proton collisions are: ggF (gluon-gluon fusion), VBF (vector boson fusion), VH (associated production with a weak boson W or Z), ttH and bbH (associated production with a pair of top-quarks or bottom quarks), tH (single top production).

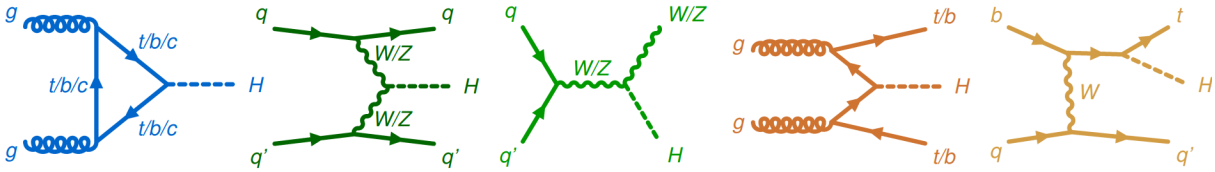

Figure 1.4: Feynman diagrams for the dominant production modes of Higgs boson at LHC: ggF, VBF, VH (WH/ZH), ttH and tH. Source: [26].

Illustration of the typical cross-section of these production modes at the energy of 13 TeV is given in Fig. 1.5.

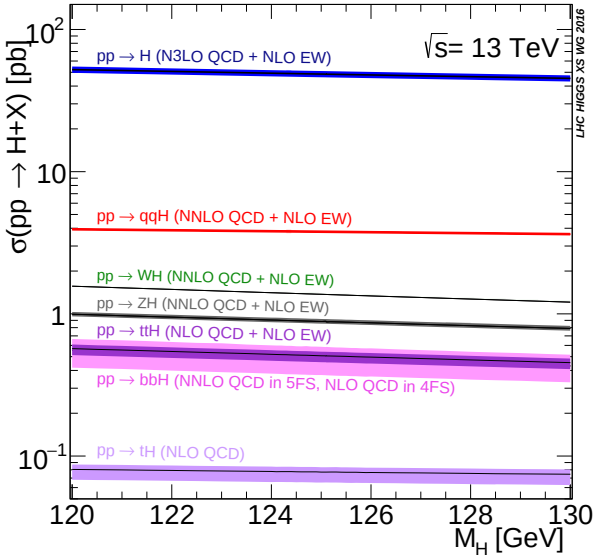

Figure 1.5: Cross-sections of various production modes for the Higgs boson as a function of its mass. The best-known measured value of the mass is $\approx 125.11 \pm 0.11$ [27]. Source: [28].

1.7.2 Decay

Higgs boson couplings depend on the fermion and gauge-boson masses, according to eq. 1.111. Dependencies of the Higgs boson branching ratios (illustrated in Fig. 1.6), depending on its mass are given in Fig. 1.7.

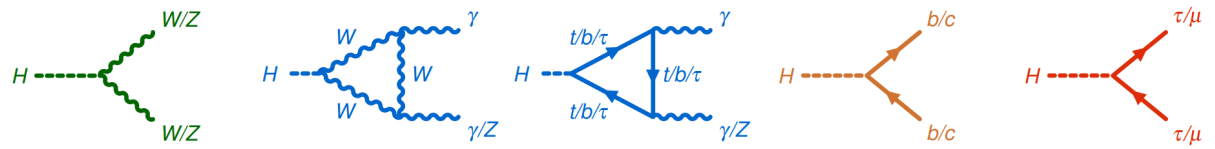

Figure 1.6: Feynman diagrams for the dominant decay modes of Higgs boson. Source: [26].

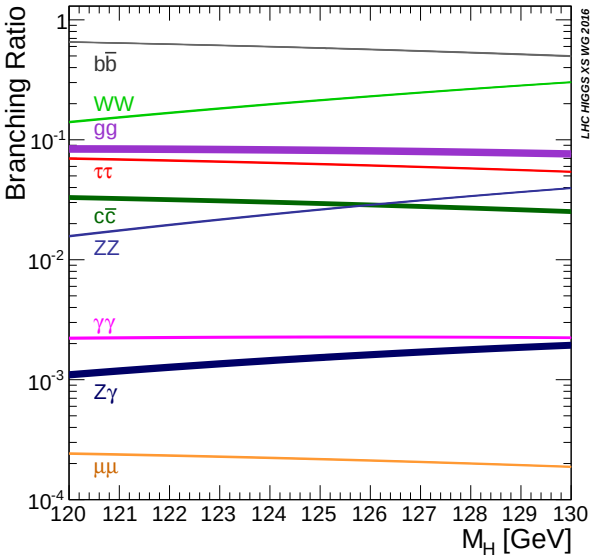

Figure 1.7: Various branching ratios of the Higgs boson as a function of its mass. The best-known measured value of the mass is $\approx 125.11 \pm 0.11$ [27]. Source: [29].

Decay of the Higgs boson to a pair of photons occurs via a loop, since photons are massless. For various studies, sometimes this loop is treated as a point-like interaction and in this case this loop is called effective. Contrary, if the loop is treated as it is, the term resolved loop is used.

1.7.3 Mass and width

The most recent and precise measurement of the Higgs boson mass at the ATLAS is done with the combination of $H \to \gamma\gamma$ and $Z \to 4\ell$ [30] channels with 139 fb^{-1} and gives:

$$m_H = 125.11 \pm 0.11 \text{ GeV} = 125.11 \pm 0.09 \text{ (stat)} \pm 0.06 \text{ (syst) GeV}. \quad (1.124)$$

The most precise single channel measurement is obtained with $H \to \gamma\gamma$ channel by ATLAS [27] with 139 fb^{-1} luminosity:

$$m_H = 125.22 \pm 0.14 \text{ GeV} = 125.22 \pm 0.11 \text{ (stat)} \pm 0.09 \text{ (syst) GeV}. \quad (1.125)$$

The latest combination from CMS [31] from $H \to \gamma\gamma$ and $Z \to 4\ell$ channels with 138 fb^{-1} data gives:

$$m_H = 125.38 \pm 0.14 \text{ GeV} = 125.98 \pm 0.09 \text{ (stat)} \pm 0.11 \text{ (syst) GeV} \quad (1.126)$$

The ATLAS and CMS Run 1 combination [32] gives:

$$m_H = 125.09 \pm 0.24 \text{ GeV} = 125.09 \pm 0.21 \text{ (stat)} \pm 0.11 \text{ (syst) GeV}. \quad (1.127)$$

The width measurement [33] at ATLAS is performed via the comparison of the off-shell [34] and on-shell [35] Higgs boson production in the $Z \to 4\ell$ channel with 139 fb^{-1} luminosity and gives:

$$\Gamma_H = 4.6^{+2.6}_{-2.5} \text{ MeV}. \quad (1.128)$$

A similar measurement of the Higgs width by CMS [36] (with 138 fb^{-1} luminosity) obtained:

$$\Gamma_H = 3.3^{+2.4}_{-2.7} \text{ MeV}. \quad (1.129)$$

1.7.4 Experimental Overview

Decay channels

The characteristics of the most important Higgs decay channels are the following (probed production modes and sensitivities to them can be seen at Fig. 1.10.):

- $b\bar{b}$ (Fig. 1.8a). This channel has the biggest branching ratio (almost half of the Higgs bosons decay through it), but due to the QCD background and performance of the $b-tagging$, analysis of this decay is challenging. Significance of the observation is 6.7σ [37]. The channel is particularly sensitive to high-p_T^H bins and to the VH production modes.

- WW^* (Fig. 1.8b). Despite a big branching ratio (21.4%), experimental sensitivity to this channel is low due to the identification of the charged vector bosons: in the lepton channels there is a neutrino carrying out energy and in the decay to quarks, one has difficulties with light flavour identification. As a final discriminant variable, transverse mass is used.

- $\tau^+\tau^-$ channel (Fig. 1.9a) is less frequent than bb, but also has a lower background. Significance of the observation is around 8σ [37]. This channel has good sensitivity to the VBF production mode and ggH (at high p_T^H).

- $ZZ^* \to 4\ell$ (Fig. 1.8b). Also known as a golden channel due to a pronounced peak over low background.

- $\gamma\gamma$ (Fig. 1.8a). This channel is characterised by a small narrow peak over a smooth background and, despite a small branching ratio (0.227%), is one of the most precise channel for the STXS measurements. Particularly, to ggH and ttH (tH) production modes, where $\gamma\gamma$ channels provides ones of the most precise measurements.

- $\mu^+\mu^-$ (Fig. 1.9c) is very rare but clean. Significance of the observation is around 2σ [37] (3σ [38]) at ATLAS (CMS).

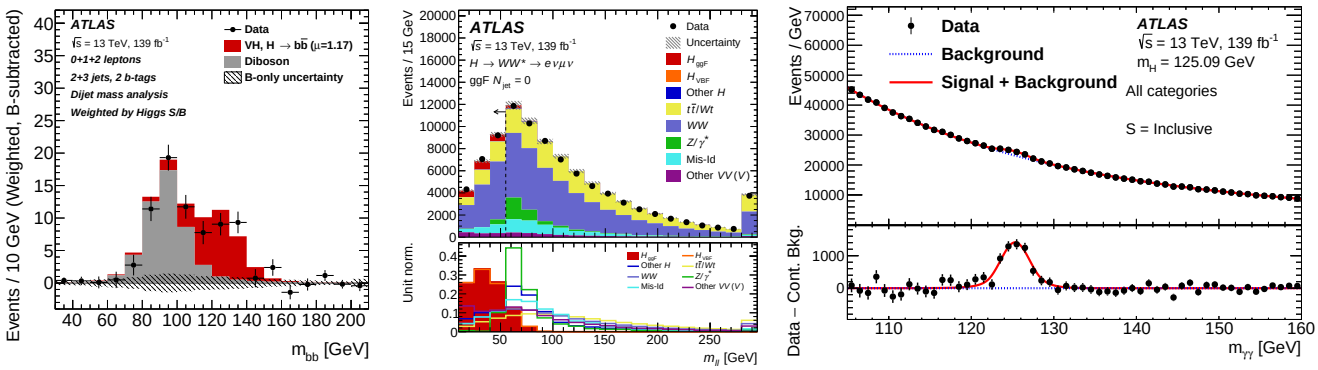

(a) $H \to \bar{b}b$ (b) $H \to WW^*$ (c) $H \to \gamma\gamma$

Figure 1.8: Invariant mass distributions for the (a) bb, (b) WW^* and (c) $\gamma\gamma$ channels. Source: [39, 40, 37].

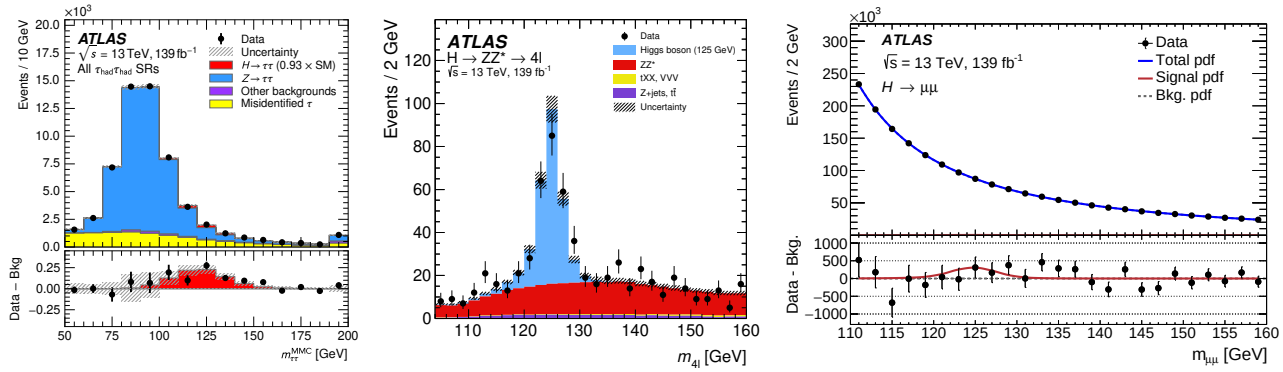

(a) $H \to \tau^+\tau^-$ (b) $H \to 4\ell$ (c) $H \to \mu^+\mu^-$

Figure 1.9: Invariant mass distributions for the (a) $\tau\tau$, (b) 4ℓ and (c) $\mu\mu$ channels. Source: [41, 42, 37].

Results of the most recent measurement of the signal strengths of the production modes per decay channel are shown in Fig. 1.10, and the combined measurement is illustrated in Fig. 1.12. The predicted and observed values of the production mode cross-sections and branching ratios are shown in Fig. 1.11. The combined STXS measurement (Section 4.2) results can be found in Fig. 1.13.

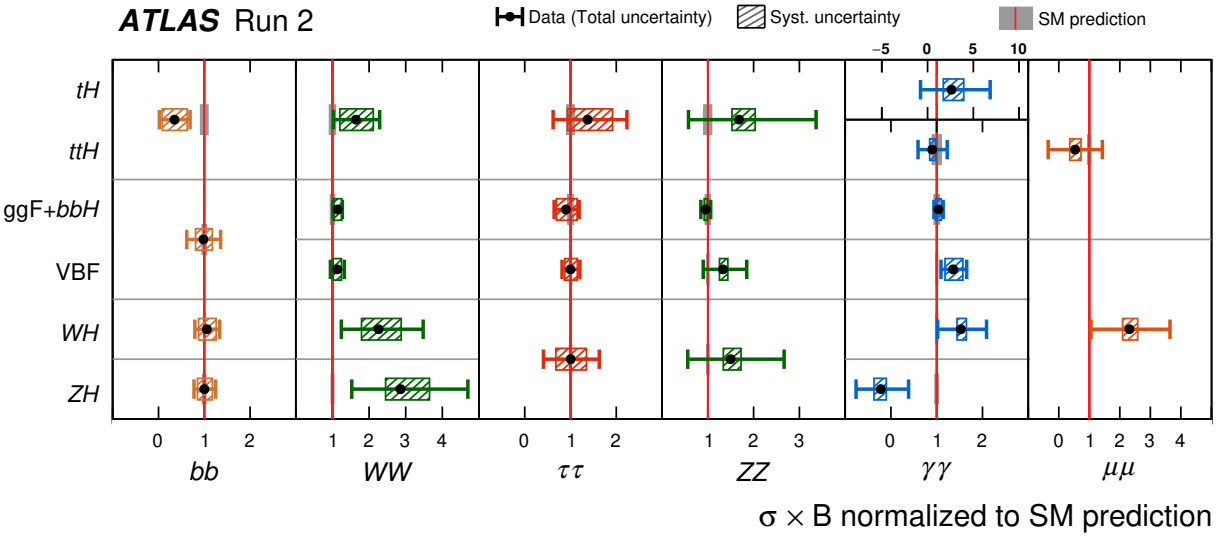

Figure 1.10: Signal strengths of production modes of various decay channels. Source: [26].

Global signal strength of the Higgs boson signal, measured by ATLAS [26], as a result of Run 2 is:

$$\begin{aligned}\mu =& 1.05 \pm 0.06 = 1.05 \pm 0.03\ (\text{stat}) \pm 0.05\ (\text{syst}) \\ =& 1.05 \pm 0.03\ (\text{stat}) \pm 0.03\ (\text{exp}) \pm 0.04\ (\text{sig.th}) \pm 0.02\ (\text{bkg.th})\end{aligned} \tag{1.130}$$

where "stat" is the statistical uncertainty, "exp" is the systematic experimental, "sigh.th" and "bkg.th" are theoretical uncertainties on the signal and background modelling, respectively.

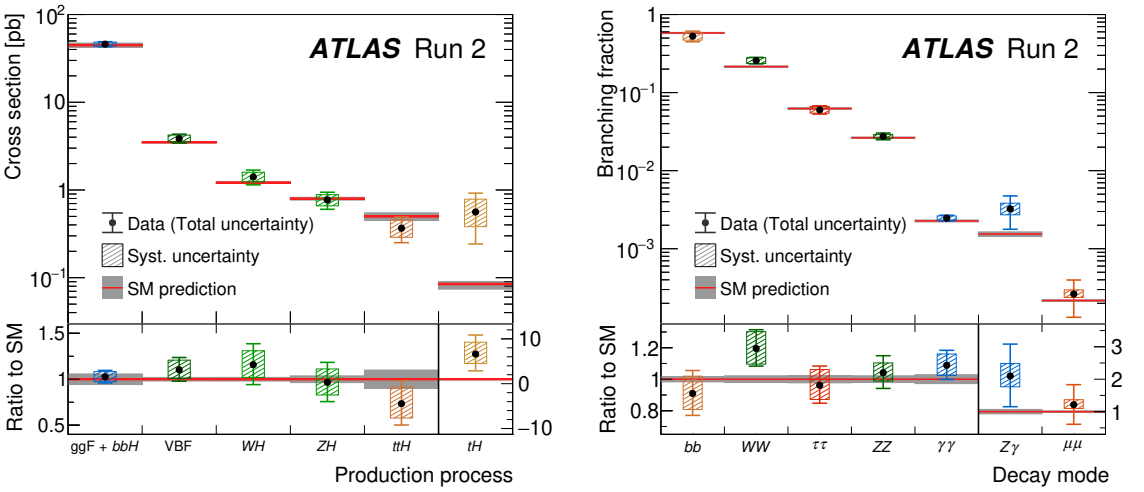

(a) (b)

Figure 1.11: Observed and predicted cross-section (a) and branching ratios (b) of various production modes and decay channels, respectively. Source: [26].

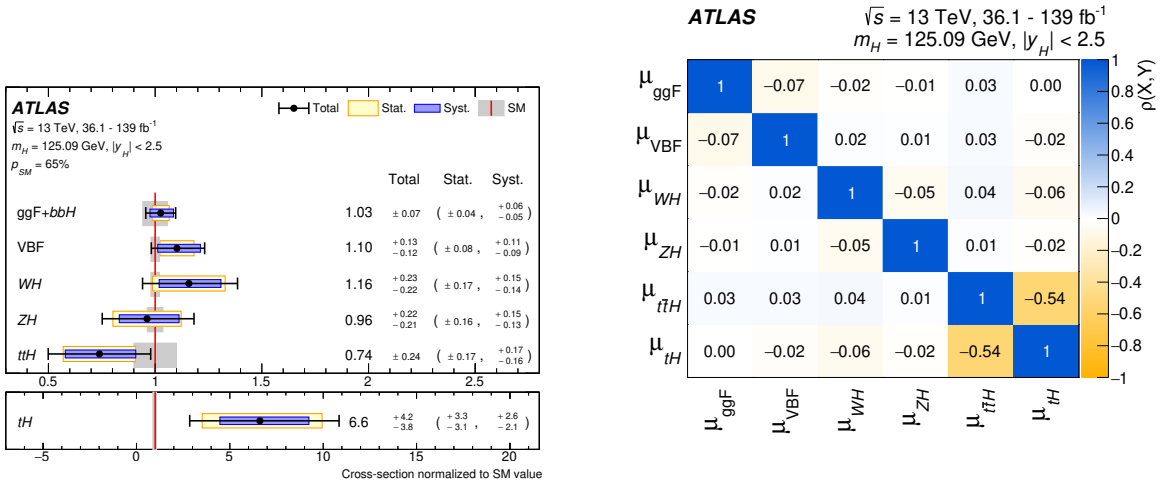

(a) (b)

Figure 1.12: Signal strengths of various production modes (a) and the observed correlation matrix of this measurement (b). Source: [26].

Higgs couplings

Couplings of the Higgs boson to elementary particles depends on their mass (Section 1.6.5). Values of these coupling have been tested at Run 2 (Fig. 1.14) and no deviations from the SM is found[29].

[29] Similar tests have been conducted at Run 1. No deviations from the SM is found neither.

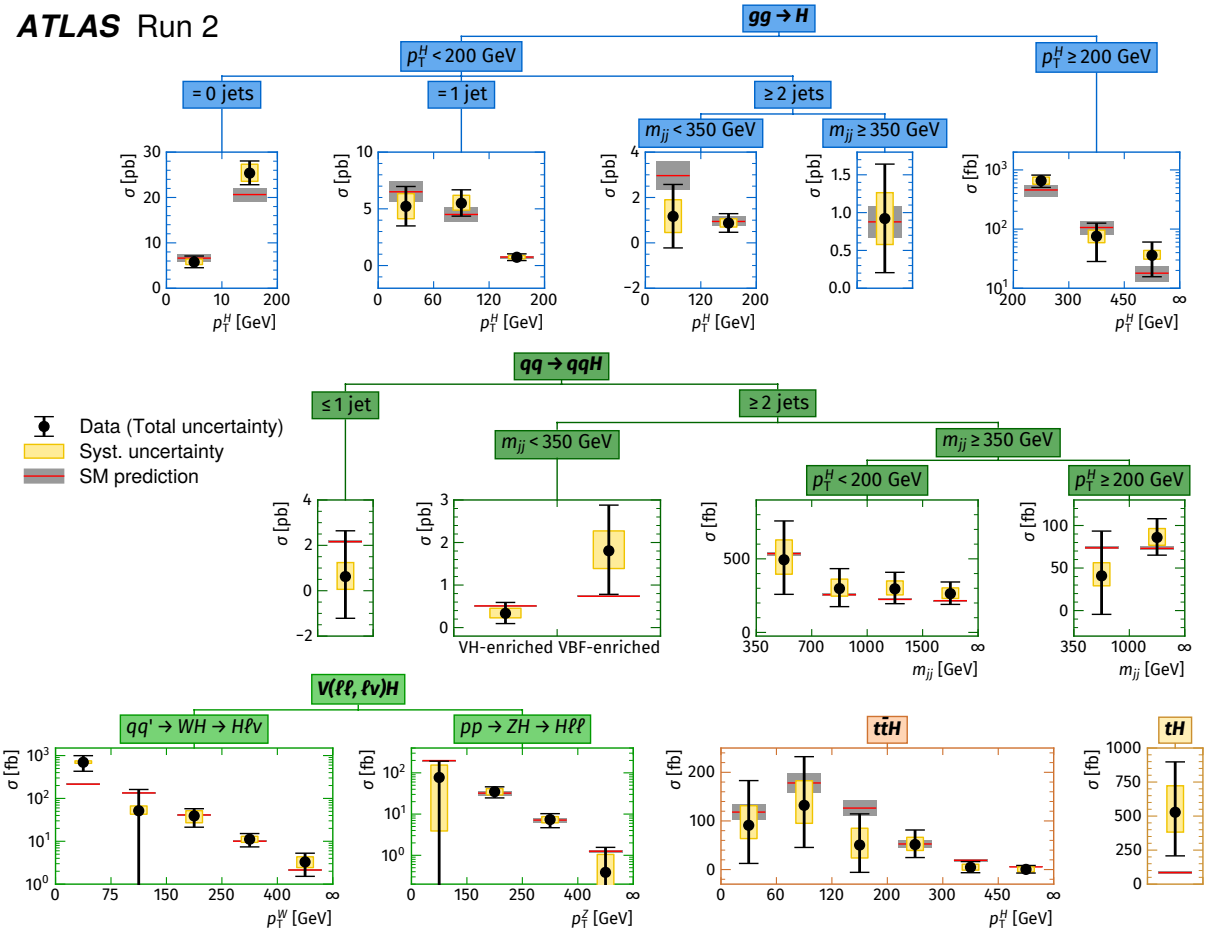

Figure 1.13: Combined measurement of the STXS cross-sections. Source: [26].

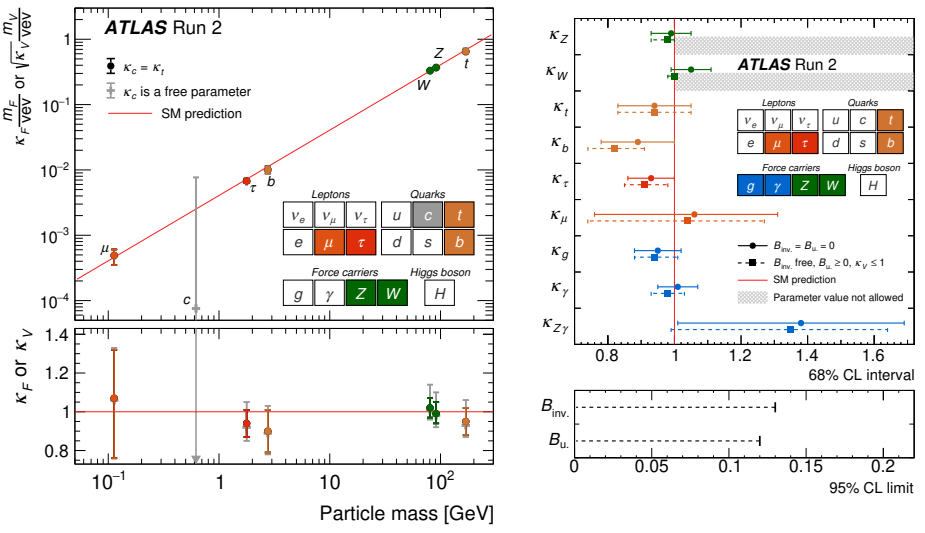

(a) (b)

Figure 1.14: Strength of the Yukawa couplings of the Higgs boson with elementary particles: as (a) function of their mass and (b) as ratio to the corresponding SM values. Source: [26].

CP-properties

Discovery of a new particle in 2012 with a mass of 125 GeV around did not answer question about its quantum numbers J^{CP}. Later analyses showed that this particle has zero spin and is compatible with a J^+ hypothesis, excluding the other probed ones [43]. However, the observed Higgs can still be a mixture of a few different CP states (in the SM, Higgs is J^+). For example, the CP-properties of the Higgs boson interaction with tau-leptons can be probed in the $H \to \tau\tau$ decay [44]. Given the interaction Lagrangian:

$$\mathcal{L}_{H\tau\tau} = -\frac{m_\tau}{v}\kappa_\tau \left(\cos\phi_\tau \bar{\tau}\tau + \sin\phi_\tau \bar{\tau} i\gamma^5 \tau\right) H, \tag{1.131}$$

with $v = 246$ GeV, κ_τ is the reduced Yukawa coupling strength, and ϕ_τ is the CP-mixing angle. In the SM, $\phi_\tau = 0$, hence the first term describes the SM term and the second one is the BSM coupling. Measurement of the mixing angle ϕ_τ are shown in Fig. 1.15.

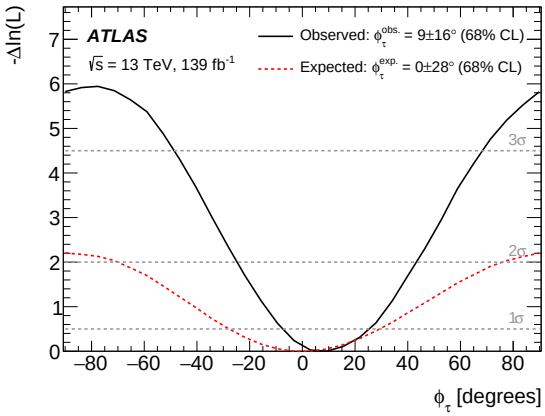

Figure 1.15: Measurement (expected and observed) of the CP mixing angle ϕ_τ. Source: [44].

1.8 Conclusion

In this chapter, the mathematical concepts, including symmetries, and the Standard Model of particle physics are described in details, to explain the observations of nature and the electroweak spontaneous symmetry breaking mechanism. The measurements on the Higgs boson discovered in 2012 are given.

2 - The ATLAS detector at the LHC

2.1 LHC

2.1.1 Introduction

The Large Hadron Collider (LHC) is a 27 km circular long proton-proton collider based at CERN on the border between France and Switzerland. It is designed to nominally operate at the centre-of-mass energy of $\sqrt{s} = 14$ TeV to supersede the previous largest hadron collider, Tevatron, which was running at 1.96 TeV until 2011. There are four main experiments at LHC: ATLAS (A Toroidal LHC Apparatus) and CMS (Compact Muon Solenoid) dedicated to general purpose physics, including the Higgs physics and search for supersymmetry, LHCb (Large Hadron Collider Beauty) focused on B-physics and CP-violation, and ALICE (A Large Ion Collider Experiment) dedicated to study quark-gluon plasma in heavy ion collisions.

The LHC machine (Fig. 2.1) is installed in the tunnel created for LEP (Large Electron–Positron Collider), and consists of [45] eight arcs (each 2.45 km long) with eight intersection zones called points. Each arc consists of 154 dipole bending magnets. The intersection zones comprise a straight 52 m long section and transition regions to bind the beam again inside the arcs.

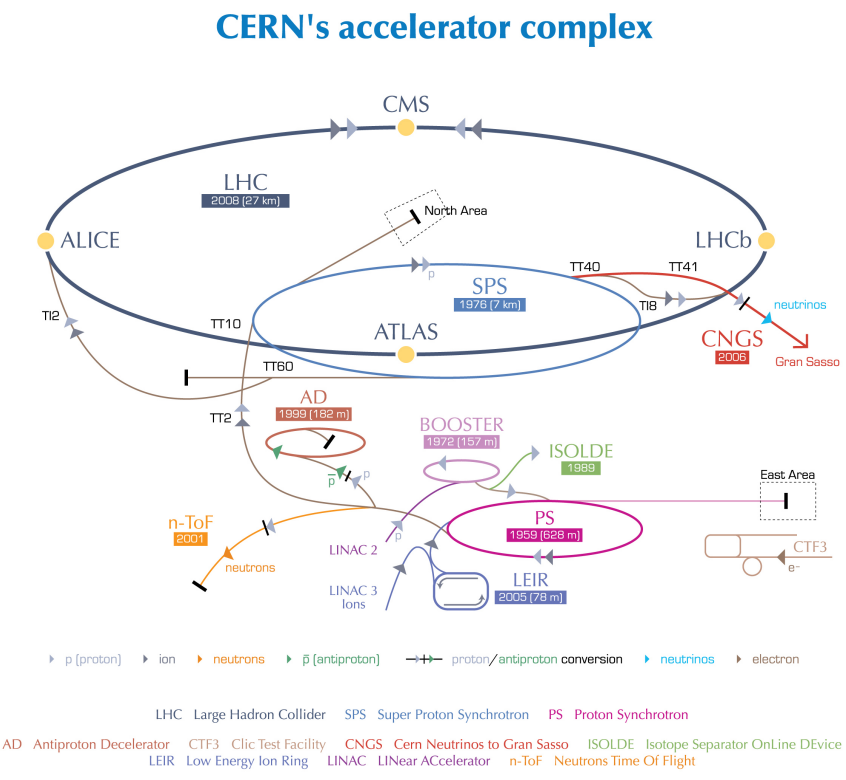

Figure 2.1: LHC layout with its four main experiments and the CERN accelerator complex. Source: [45].

The protons and heavy ions are produced in the ionisation process of hydrogen gas via electric field, which separates the nuclei (protons) from the electron clouds. The first step of acceleration takes place in the linear accelerators (linacs) 2 and 3 (see Fig. 2.1) and increases protons energy to 50 MeV. The protons are then transmitted to the PSB (proton super booster), where they get the energy of 1.4 GeV. At the next step, these protons are accelerated in the PS (proton synchrotron) to reach the energy of 25 GeV. The next acceleration occurs in the SPS (super proton synchrotron), increasing particles energy to 450 GeV. Finally, after SPS, the protons are sent to the LHC to obtain their target energy (6.5 TeV per beam at Run 2) using the TI2 and TI8 injection points. The heavy ions are accelerated in the Ion Rings instead of PSB.

Protons in the beam are composed to form bunches. Given the frequency of the LHC radio-frequency system (400 MHz), one can have at most 35640 possible bunches separated by 0.75 m distance (travelled by particles in approximately 2.5 ns). In the nominal conditions, the bunch spacing was fixed to 25 ns, limiting the maximum number of bunches to 3564. Due to the final time required by the SPS injection kicker to rise, the Run 2 was running with 2808 bunches. The structure of these bunches is called the bunch filling scheme. The period of time between the injection of new protons to the LHC, so-called fill, happens approximately every 10 hours.

2.1.2 Collisions

In particle physics, the measurements are usually done in the form of the probability of a given event to occur, expressed in the form of a cross-section σ (likelihood of a specific particle interaction or scattering process to occur) via the following relation:

$$N_{events} = \sigma \mathcal{L} \tag{2.1}$$

where N_{events} is the number of observed events, $\mathcal{L}$ is the integrated luminosity, which expresses total number of events occurring due to a particle flux on a given unit area. The luminosity L accumulated over a data-taking period T is given by:

$$\mathcal{L} = \int_T L(t)\,\mathrm{d}t. \tag{2.2}$$

The luminosity has unit of $\mathrm{cm}^{-2}\mathrm{s}^{-1}$ and is a pure characteristic of the machine. Knowing beam properties, one may derive luminosity using the following relation:

$$L = \frac{N_b^2 n_b f_{rev}}{4\pi\sigma_x^*\sigma_y^*}F = \frac{N_b^2 n_b f_{rev}\gamma_r}{4\pi\epsilon_n\beta^*}F, \tag{2.3}$$

where:

- N_b is the number of particles in a bunch
- n_b is the total number of bunches in a fill (2808)
- f_{rev} is the LHC revolution frequency (11.25 kHz)
- $\sigma^*_{x(y)}$ is the horizontal (vertical) beam spread size (16 mm)
- γ_r is the Lorentz factor
- ϵ_n is the normalised beam emittance (phase space volume of the beam, hence spread of momentum and coordinates)

- β^* is defined as: $\beta^* = \dfrac{\sigma^2 \gamma_r}{\epsilon_n}$
- F is the geometric luminosity reduction factor due to the crossing angle of the beams at the interaction point:

$$F = \left(1 + \left(\frac{\theta_c \sigma_z}{2\sigma^*}\right)^2\right)^{-1/2}, \tag{2.4}$$

with the beams crossing angle θ_c, the rms bunch length σ_z and the transverse rms beam size σ^*.

One of the main advantages of the LHC in comparison to the Tevatron [46] is the significantly increased statistics by a ten times factor due to enlarged instantaneous luminosity and centre-of-mass energy. The main Run 1 of the LHC took place from 2010 to 2013, with an integrated luminosity of $25\ \mathrm{fb}^{-1}$ collected altogether by ATLAS at centre-of-mass energy $\sqrt{s} = 7$ and 8 TeV. The Run 2 occurred from 2015 to 2018 at $\sqrt{s} = 13$ TeV consisting of $147\ \mathrm{fb}^{-1}$ integrated luminosity, recorded by ATLAS experiment, and $139\ \mathrm{fb}^{-1}$ can be used for physics analyses. The mean number of interaction per bunch-crossing (pile-up) varied between 13 and 36 during Run 2. This process complicates the reconstruction, contributes to the background noise and may lead to saturation of the various sub-detectors or triggers. Additionally, it complicates identification of the primary vortex. In Run 2, the LHC was running with instantaneous luminosity up to $10^{-34}\ cm^{-2}s^{-1}$, yielding an integrated luminosity (Fig. 2.2) of around 140 fb^{-1} for both ATLAS and CMS experiments. During Run 3, the centre-of-mass energy is 13.6 TeV and the planed integrated luminosity at ATLAS is around $300\ \mathrm{fb}^{-1}$.

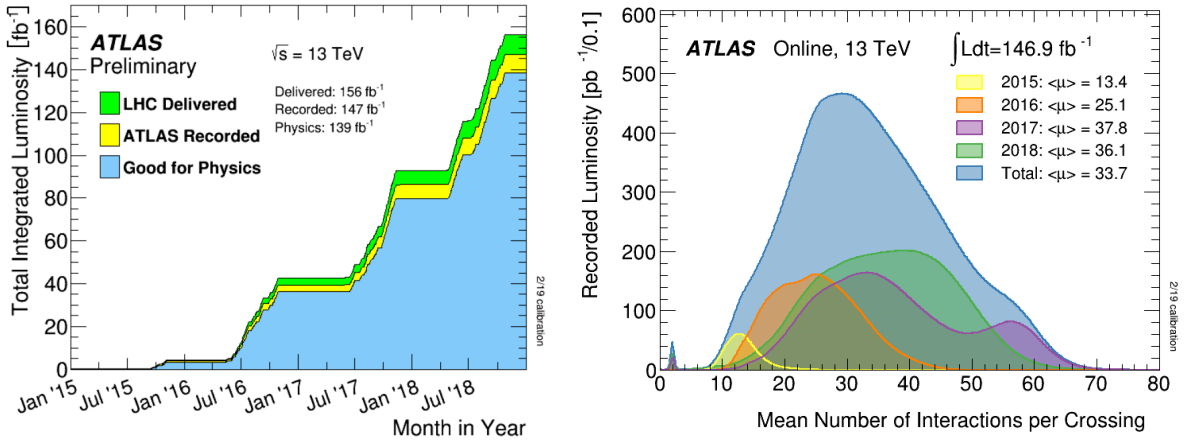

(a) (b)

Figure 2.2: (a) Luminosity delivered at Run 2 at the LHC (green), recorded by ATLAS (yellow) and available for physics analyses at ATLAS (blue). (b) Mean number of interactions per bunch-crossing for Run 2 at ATLAS. Source: [47].

2.2 ATLAS

The main properties of particles, such as electric charge, momentum and energy, are determined by combining information from the various sub-detectors (see Fig. 2.3). More details can be found in [48].

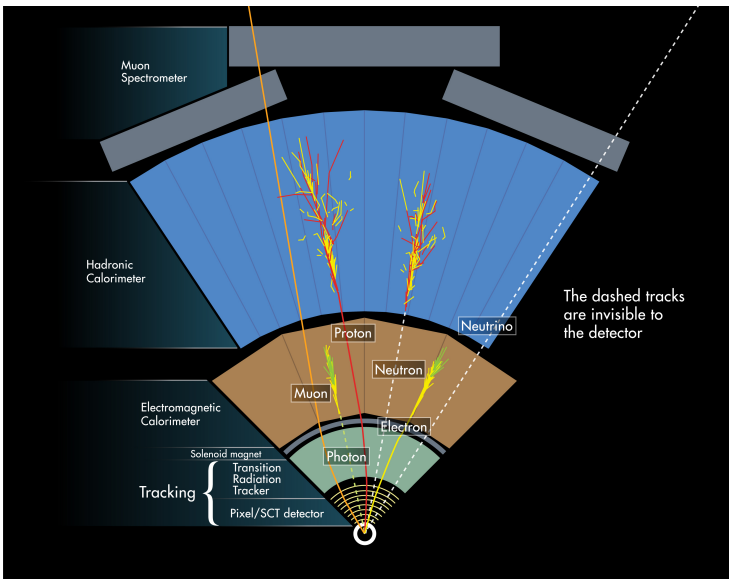

Figure 2.3: Illustration of passage of various particles through the detector layers: tracker, EM calorimeter, hadronic calorimeter and muon tracker. Source: [49].

The ATLAS (A Toroidal LHC Apparatus) [50] detector (Fig. 2.4) has a general cylindrical geometry with a height of 25 meters and length of 44 meters.

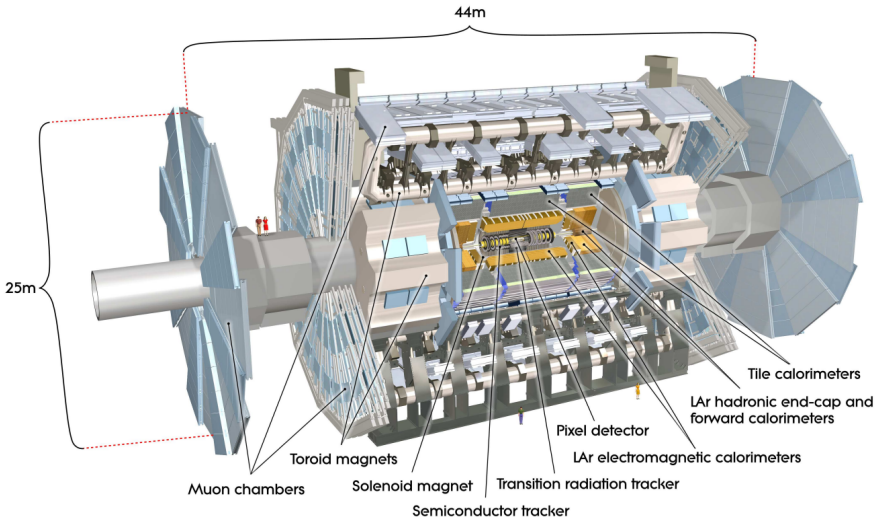

Figure 2.4: Overview of the ATLAS detector. Source: [50].

The detector consists of several sub-detectors, each playing a specific role: inner detector (tracking), electromagnetic calorimeter (photons and leptons), hadronic calorimeter (hadrons), muon spectrometer (tracks of muons) and magnetic systems for the ID and the muon spectrometer.

2.2.1 Coordinate system

The following right-handed coordinate system is chosen:

- Origin: centre of the detector;
- x-axis: from the IP to the direction inside the LHC ring;
- y-axis: upwards;
- z-axis: defined as $\vec{x} \times \vec{y}$ and is along the beam line.
- r, ϕ in the transverse plane: r is the transverse distance to the plane and ϕ is the azimuthal angle around the z-axis.
- η (pseudorapidity) defined as[1] $\eta = -\ln \tan\left(\frac{\theta}{2}\right)$

Distance between objects is given by the angular distance $\Delta R = \sqrt{(\Delta\eta)^2 + (\Delta\phi)^2}$.

2.2.2 Inner Detector (ID)

The tracking of particles is performed via the Inner detector (Fig. 2.5). It consists of the

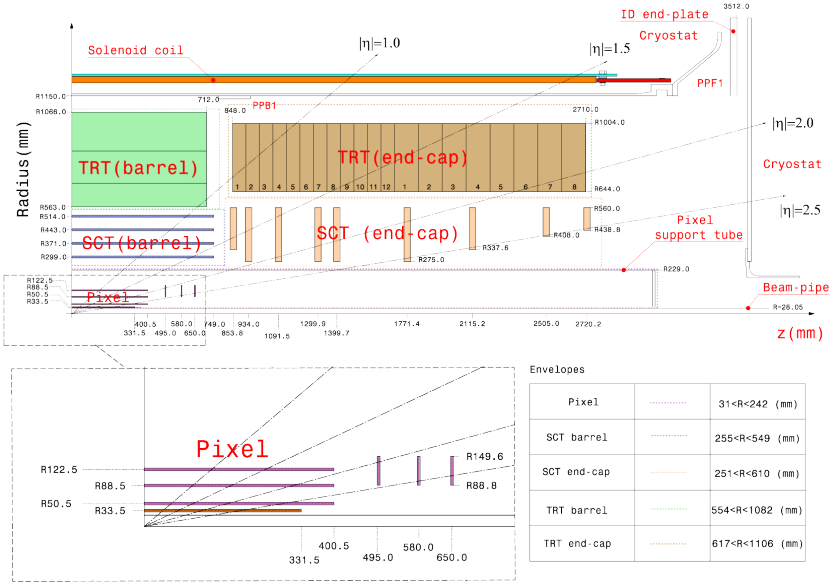

Figure 2.5: View in the $r - z$ plane of the ID used at Run 2. Source: [51].

following sub-detectors:

- Pixel detector, spanning regions from the radius of 33.25 mm to 122.5 mm, covering the range $|\eta| < 2.5$. This detector is made of three concentric cylindrical silicon-pixel layers in the barrel and of three silicon-pixel disks in the endcap. Three layers are needed to ensure the presence of at leaset three track points in order to reconstruct the trajectory of particles. The layers are segmented in $r - \phi$ and z-direction in 1744 sensors with a size of $2 \times 6\ cm$, each made of 47322 pixels of $50 \times 400\ \mu m^2$ size. Such design allows having a resolution of $\sigma_{r\phi} = 10\ \mu m,\ \sigma_z = 115\ \mu m$.

[1] In the limit of negligible particle mass, the pseudo-rapidity equals to rapidity: $y = \frac{1}{2}\ln\frac{E + p_z}{E - p_z}$

- IBL (insertable B-layer, which is a part of the inner detector), is the closest to the pipe detector material and covers the range $|\eta| < 3.0$. It was installed in 2014 for the Run 2 in order to deal with the increased instantaneous luminosity causing higher radiation damage. Besides that, an additional level allows adding of an additional interaction point of a particle in the ID to increase the tracking performance. The IBL is composed of 14 carbon fibre staves with a size of 2 cm for the width and 64 cm for the length. The radiation thickness of IBL is around 1.88%.

- SCT (Silicon microstrip tracker) has the same angular coverage $|\eta| < 2.5$ as the pixel detector. In the barrel, the detector consists of four concentric cylindrical silicon microstrip double-layers: one layer is axial (parallel to the beam line), and the other one is a stereo angle of $40\ \mu rad$ (around $2°$). In the endcap region, SCT consists of nine disks with a set of radial and stereo strips. SCT contain 2112 modules in the barrel and 1976 modules in the endcap, giving 4088 modules in total (with 6.2 million readout channels). Pitch size of a strip is $80\ \mu m$, allowing the intrinsic space resolution of $17\ \mu m$ in the $r - \phi$ plane. Typically, around eight particle hits happen within SCT.

- TRT (transition radiation tracker) covers a narrow region only up to $|\eta| = 2.0$. It consists of 4 mm diameter straw tubes filled with a $Xe/CO_2/O_2$ gas mixture (in the $70 : 27 : 3$ proportion, respectively). In the barrel region, there are 73 straw layers which are parallel to the beam axis. In the endcap, 768 straws fill 160 planes arranged radially in wheels. Lengths of the tubes varies from 144 cm in the barrel up to $37\ cm$ in the endcap. Despite being less precise than the previous layers (TRT has a spatial resolution of $130\ \mu m$ with around 351 000 readout channels), it plays an important role in the overall tracking performance due to a large number of hits (usually around 30). This detector also contributes to particle identification by measuring the transition radiation.

The main characteristics of the ID subdetectors are summarized in Table 2.1.

Subdetector	Element size	Intrinsic resolution [µm]	Barrel layer radii [mm]	Disk layer |z| [mm]
IBL	$50\,\mu\text{m} \times 250\,\mu\text{m}$	10×60	33.25	
Pixel	$50\,\mu\text{m} \times 400\,\mu\text{m}$	10×115	50.5, 88.5, 122.5	495, 580, 650
SCT	$80\,\mu\text{m}$	17	299, 371, 443, 514	from 839 to 2735
TRT	$4\,\text{mm}$	130	from 554 to 1082	from 848 to 2710

Table 2.1: Summary of the main characteristics of the ID sub-detectors. The intrinsic resolution of the IBL and the Pixel sensors is shown along r–ϕ and z. For SCT and TRT, only the resolution along r–ϕ is given [52, 53]. For SCT and TRT, the element size refers to the spacing of the read-out strips and the diameter of the straw tube, respectively. Source: [54].

Distribution of the material thickness at the end of ID in units of radiation length is given at Fig. 2.6 as a function of $|\eta|$.

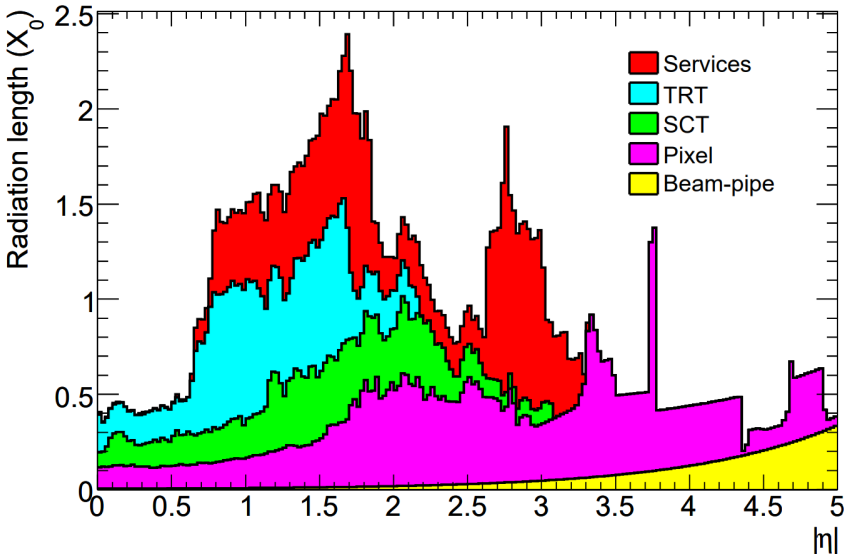

Figure 2.6: Distribution of the material thickness up to the end of ID as a function of $|\eta|$. Source: [55].

A $2\,\mathrm{T}$ magnetic field is created for the ID by a thin solenoid surrounding it, parallel to the beam axis. It has a radiative thickness of approximately $0.6\ X_0$ and allows for to bend charged particles to measure their momentum.

2.2.3 The calorimeter system

ATLAS calorimeter system (Fig. 2.7) consists of a few components. The main task of the electromagnetic calorimeter (ECal) is to measure the energies of photons and electrons by stopping them in the detector and measuring the energy of the electromagnetic cascade left from a particle. Given that the cleanest channels for the Higgs boson mass measurements ($H \to \gamma\gamma$ and $H \to 4l$) rely on photons and electrons, it is crucial to have as good energy and spatial resolution as possible.

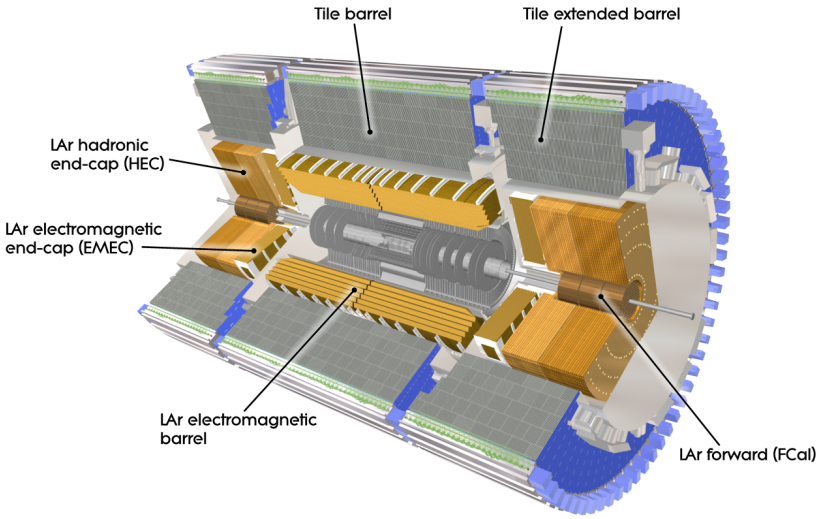

Figure 2.7: Overview of the ATLAS electromagnetic calorimeter. Source: [55].

The design of the electromagnetic calorimeter follows an original idea of Daniel Fournier [56] (D. Fournier, p. 356-359): an accordion design shown in Fig. 2.8, allowing for a crossing particle to interact with multiple inclined layers, regardless of the particle impact angle and to avoid dead regions of the detector. Also, such scheme permits to identify the crossing position of a particle with a greater spatial resolution than a usual structure with parallel layers.

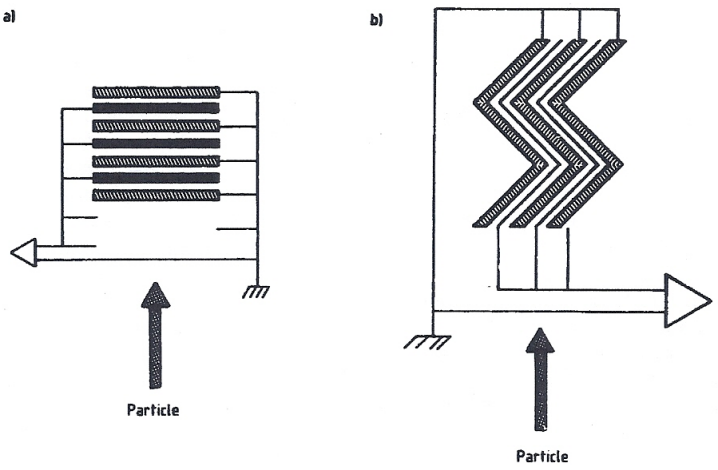

Figure 2.8: Concept of the (a) usual parallel scheme and the (b) accordion scheme of the electrodes. Source: [55].

The detector uses lead as the absorber material and liquid Argon as the active medium. Primary electrons and photons interact with the absorber material, creating electromagnetic shower in the active media. The EM calorimeter is divided into the following main sections:

- *barrel* ($|\eta| < 1.475$). It consists of the two symmetric parts separated by a $4\,\mathrm{mm}$ gap for cables at $z = 0$. Each half is composed of 16 modules with an angular size of $\Delta\phi = 22.5°$, having 1024 accordion-shaped lead absorbers. Drift gaps for electrodes have a size of $2.1\ mm$, leading to a total drift time of $450ns$ for an operating voltage of $2\ kV$. The total radiative thickness of the barrel varies from 22 to 30 X_0 (radiative length) in the region $|\eta| \in (0; 0.8)$ and from 24 to 33 X_0 in the region $|\eta| \in (0.8; 1.3)$. In order to prevent significant thickness variations with a change of η, the modules are segmented as illustrated in Fig. 2.9. Total number of the readout channels reaches 101 760.

- two *endcap* components ($1.375 < |\eta| < 3.2$) made of an outer wheel ($1.375 < |\eta| < 2.5$) and an inner wheel ($2.5 < |\eta| < 3.2$). The wheels are divided into eight wedge shaped modules with 768 (256) absorbers in the outer (inner) wheel with a thickness of $1.7\ mm$ ($2.5\ mm$). The radiative thickness of the endcap material varies from 24 to 38 X_0 in the region of $1.475 < |\eta| < 2.5$ and from 26 to 36 X_0 for $2.5 < |\eta| < 3.2$. Signal transfer happens via 62208 readout channels.

In order to improve shower shape (Section 4.4.1) identification and to allow tracking of the particles in the electromagnetic calorimeter (and rejection of jets mimicking electromagnetic showers), the detector is composed of the three main distinct layers (Fig. 2.10) and an additional thin one in front:

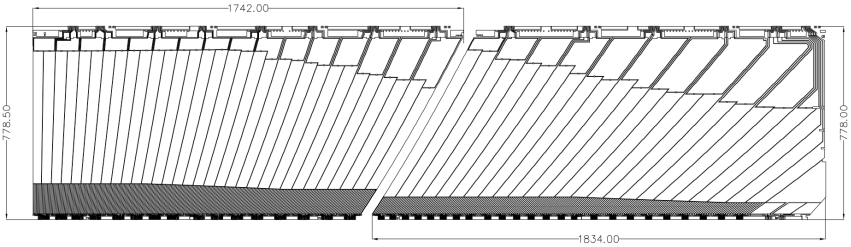

Figure 2.9: Segmentation of the electrode layers in the barrel. The units are in millimetres. Source: [55].

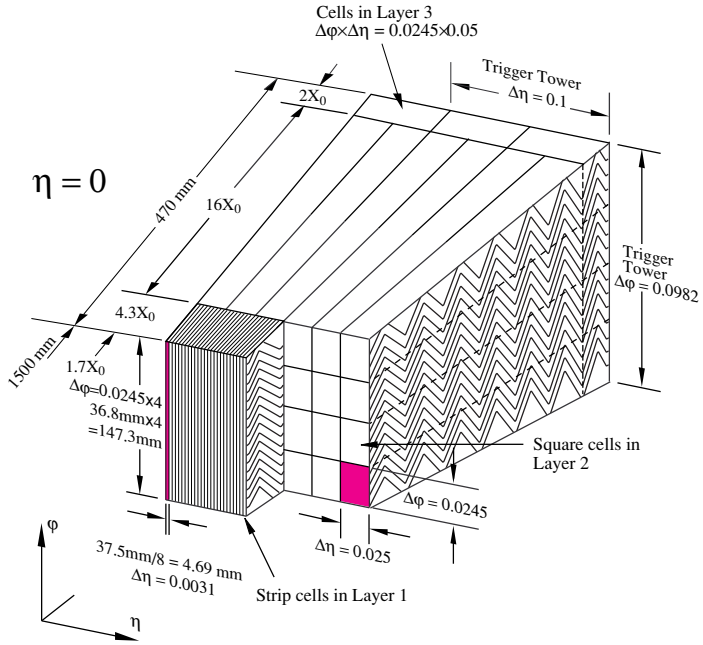

Figure 2.10: Longitudial composition of the barrel. Source: [55].

- L_0 *presampler* ($|\eta| < 1.8$ only) is an additional detector to correct for the energy losses in the upstream material (ID, magnets, cables, cryostats and others).
- L_1 and L_2 are the main calorimeter layers, where most of the particles energy is deposited. Having two layers allows extract more information on the shape of the shower (to distinguish electromagnetic one from the hadronic one). They are designed to ensure coverage of the most part of a shower.
- L_3 is an additional layer dedicated to cover the edge of the showers.

The overall performance of the electromagnetic calorimeter [57, 58] reaches the level of:

$$\frac{\sigma(E)}{E} = \frac{10\%}{\sqrt{E}} \oplus 0.7\% \tag{2.5}$$

for the energy resolution and for the polar angle: $\sigma(\theta) = \frac{60 \text{ mrad}}{\sqrt{E}}$ (E is in the units of GeV).

2.2.4 Hadronic calorimeter (HCal)

Energies of jets are mainly measured in the Hadronic calorimeter with energy resolution of: $\frac{\sigma(E)}{E} \sim \frac{50\%}{\sqrt{E}} \oplus 3\%$. The spatial resolution for a jet is $\Delta\eta \times \Delta\phi = 0.1 \times 0.1$ in $|\eta| < 2.5$ and $\Delta\eta \times \Delta\phi = 0.2 \times 0.2$ beyond $|\eta| = 2.5$.

This detector is a sampler calorimeter made of a large barrel ($|\eta| < 1.0$), two extended regions ($0.8 < |\eta| < 1.7$) and the endcap zones ($1.5 < |\eta| < 3.2$). The technologies for the central region and the endcaps are different:

- Barrel: steel (absorber) and scintillating tiles (active material). The tiles are azimuthally divided into 64 modules and longitudinally into three layers.
- Endcaps: copper plates (with varying from $50\,\mathrm{mm}$ for the closest to the interaction point to $25\,\mathrm{mm}$ to the furthest ones), interleaved with $8.5\,\mathrm{mm}$ LAr gaps as active medium. Each end-cap is composed of 32 wedge-shaped modules, longitudinally divided into two sections, resulting in 4 layers per each end-cap.

2.2.5 Forward calorimeter (FCAl)

To ensure almost 4π coverage of the detector, which is important for measuring missing energy E_T and forward objects (jets, leptons), the ATLAS calorimeter system is equipped with an additional detector called Forward calorimeter (FCal), covering region up to $|\eta| < 4.9$. This sub-detector uses the LAr technology and is also segmented into three layers in depth. The first layer use copper as an absorber material, and the other two use tungsten. FCal has a radiative thickness of approximately $10\ X_0$.

2.2.6 Muon Spectrometer

Since typical muons at the LHC have too high energies to be fully absorbed in a material of any of the detectors due to a weak interaction with the detector, it is only possible to measure their momentum by identifying the curvature of their trajectories outside of the previous sub-detectors. Illustration of the ATLAS muon spectrometer is given at Fig. 2.11.

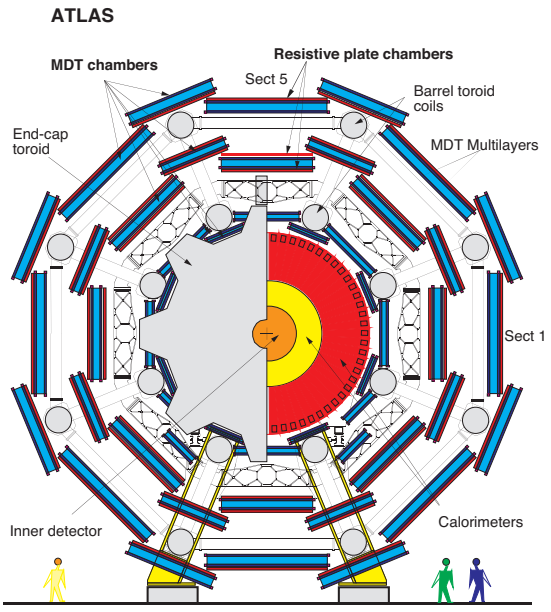

Figure 2.11: Cross-section of the ATLAS Muon Spectrometer. Source: [59].

The muon detector is triggered within tens of nanoseconds by events in the range $|\eta| < 2.7$ and performs measurements in the region $|\eta| < 2.7$ with momentum resolution $\sigma(p_T)$ varying from 4% at 50 GeV to 11% at 1 TeV, driving a sagitta of $500\,\mu\mathrm{m}$ to be measured with a precision of $50\,\mu\mathrm{m}$. Muons bending is achieved by three magnets: one in the barrel $|\eta| < 1.4$ and two in the endcap region $1.6 < |\eta| < 2.7$. In the transition region, both magnets contribute to the deflection.

The spectrometer is made of two different kinds of detectors, azimuthally arranged in eight parts, each divided in two sectors overlapping in ϕ[2]. The types of detectors (called *chambers*) are:

- *MDT* (Monitored drift chamber) covering the region $|\eta| < 2.7$ (except the innermost endcap zone, where only the $|\eta| < 2.0$ region is covered). Having three to eight tube layers, they provide a spatial resolution $\sigma(z) = 35\,\mu\mathrm{m}$. There are 1150 chambers in total, which provide 354'000 readout channels.
- *CSC* (Cathode-strip chambers) used in the innermost region of the endcap zones ($2.0 < |\eta| < 2.7$). They allow for a spatial resolution of $\sigma(R) \times \sigma(\phi) = 40\,\mu\mathrm{m} \times 5\,\mathrm{mm}$ with 30'700 readout channels.

For the purpose of triggering, two other types of detectors are used:

- *RPC* (Resistive plate chambers), covering $|\eta| < 1.05$ with a response time of $1.5\,\mathrm{ns}$ and spatial resolution $\sigma(z) \times \sigma(\phi) = 10\,\mathrm{mm} \times 10\,\mathrm{mm}$.
- *TGC* (Thin gap chamber), used to cover the remaining area $1.05 < |\eta| < 2.4$. Their response time is slightly slower and reaches $4\,\mathrm{ns}$. Spatial resolution $\sigma(R) \times \sigma(\phi) = 2\,\mathrm{mm} \times 3\,\mathrm{mm}$.

The magnetic field of the muon spectrometer is produced by three air-core toroids (one in the barrel and a pair for the endcaps). They are placed concentrically around the hadron calorimeter and produce magnetic field of $0.5\,\mathrm{T}$ in the barrel and $1\,\mathrm{T}$ in the end-cap.

2.2.7 Triggers

To reduce the event rate to the one that can be handled by electronics and to store only potentially meaningful events[3], a two level trigger system [60] is used at Run 2. It reduces event rate from $40\ MHz$ to $1\ kHz$ which are stored on the hardware.

2.2.8 Performance

The expected performance of the ATLAS detector is shown in Table 2.2.

[2]The overlap allows to reduce gaps in the detector coverage and to enable an alignment
[3]Events with high-energy events, which can substitute to an analysis

Detector component	**Required resolution**	η **coverage**	
		Measurement	Trigger
Tracking	$\sigma_{p_T}/p_T = 0.05\%\ p_T \oplus 1\%$	± 2.5	
EM calorimetry	$\sigma_E/E = 10\%/\sqrt{E} \oplus 0.7\%$	± 3.2	± 2.5
Hadronic calorimetry (jets)			
barrel and endcap	$\sigma_E/E = 50\%/\sqrt{E} \oplus 3\%$	± 3.2	± 3.2
forward	$\sigma_E/E = 100\%/\sqrt{E} \oplus 10\%$	$3.1 < \lvert\eta\rvert < 4.9$	$3.1 < \lvert\eta\rvert < 4.9$
Muon spectrometer	σ_{p_T}/p_T=10% at p_T = 1 TeV	± 2.7	± 2.4

Table 2.2: Expected performances of ATLAS detector. E and p_T are expressed in units of GeV. Source: [52].

2.3 Conclusion

The general-purpose ATLAS detector at the LHC allows to reconstruct various particles, using dedicated sub-detectors. Its organisation and performance are given. The inner detector serves to reconstruct tracks and identification of particle momentum. The electromagnetic calorimeter plays a key role in the $H \to \gamma\gamma$ analysis (Chapter 4), as provides the main information for the photon and electron identification, and in the combined Higgs EFT interpretation (Chapter 5) due to the leading constraining powers of the $H \to ZZ^* \to 4\ell$, $H \to \gamma\gamma$ measurements, primarily relying on the electromagnetic calorimeter. The hadronic calorimeter is mainly used for the jet energy measurements, such as $H \to b\bar{b}$ process or top-mass measurements. The muon wheels are used for the muon identification and their energy measurements and are essential for some processes, such as $H \to \mu\mu$.

3 - Calibration of the electromagnetic calorimeter with the E_T/p_T method

3.1 Introduction

Many analyses within the ATLAS experiment rely on the signature of a final state with the presence of photons or electrons. Their reconstruction commonly uses information from the electromagnetic calorimeter. Therefore, precise measurement of their energy is important. An energy calibration is required in order to correct for discrepancy between the reconstructed energy from the data and MC. It consists of reducing bias in the form of a shift (between the real energy of a particle and the reconstructed one) and resolution effects (manifesting in a difference between the energy spectrum spread). It plays an important role and might be a limitation for precise measurements. For example, the dominant systematic uncertainties (Tab. 3.1 for the $H \to \gamma\gamma$ and $H \to ZZ^*$ combination and 3.2 for $H \to \gamma\gamma$ only) on the Higgs boson mass measurement come from a calibration quantity (non-linearity). More generally, since most of the Higgs boson measurements are now dominated by systematics, any calibration improvement would improve the precision of the measurements and allow to probe possible BSM effects.

Source	Systematic uncertainty in m_H [MeV]
EM calorimeter response linearity	60
Non-ID material	55
EM calorimeter layer intercalibration	55
$Z \to ee$ calibration	45
ID material	45
Lateral shower shape	40
Muon momentum scale	20
Conversion reconstruction	20
$H \to \gamma\gamma$ background modelling	20
$H \to \gamma\gamma$ vertex reconstruction	15
e/γ energy resolution	15
All other systematic uncertainties	10

Table 3.1: Main components of the systematic uncertainties on the Higgs boson mass from the Run 1-Run 2 combination of $\gamma\gamma$ and $4l$ final states. Source: [61].

Source	Systematic uncertainty in $m_H^{\gamma\gamma}$ [MeV]
EM calorimeter cell non-linearity	± 180
EM calorimeter cell layer calibration	± 170
Non-ID material	± 120
ID material	± 110
Lateral shower shape	± 110
$Z \to e^+e^-$ calibration	± 80
Conversion reconstruction	± 50
Background model	± 50
Selection of the diphoton production vertex	± 40
Resolution	± 20
Signal Model	± 20

Table 3.2: Main components of the systematic uncertainties on the Higgs boson mass from the $H \to \gamma\gamma$ channel with Run 1-Run 2 combination. Source: [61].

As a baseline for the energy measurement [62], the LAr cluster energy is used, which is affected by the upstream energy losses and leakage outside of the cluster. To account for them, an MVA (Multivariate regression) is used, which is trained on MC. To ensure the same energy response as in data, additional calibrations are required. These calibrations are performed with a set of sequential corrections aiming to reduce as much as possible their remaining discrepancy. The electron and photon responses in data are calibrated such that they agree as much as possible with those expected from simulation using a large sample of $Z \to e^+e^-$ events. Hence, additional systematic uncertainties are required to cover the residual differences between these two types of particles. The e/γ calibration chain (Fig. 3.1) consists of several steps.

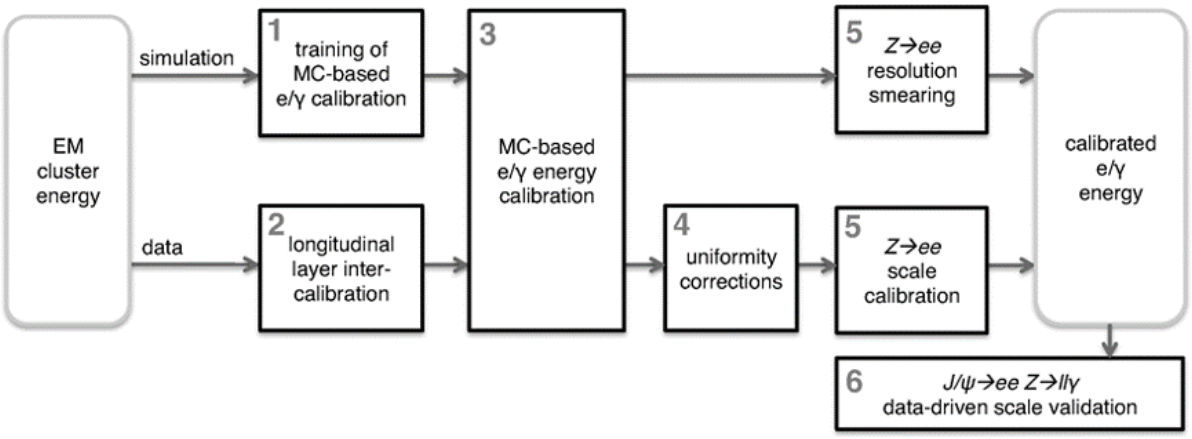

Figure 3.1: Overview of the $e\gamma$ calibration chain in ATLAS. Source: [63].

The calibration in Run 1 is described in [63]. The fist Run 2 calibration paper is [64]. Until then, the calorimeter cluster algorithm has been using a fixed sized cluster. After, the reconstruction algorithm is making use of a cluster of energy deposits measured in topologically connected calorimeter cells. These clusters are denoted as *topo-clusters* [65]. The preliminary calibration is described in [66] and the final calibration paper [62].

During the first step, a calibration for electrons and photons (converted and unconverted) is performed using a multivariate-based regression based on the variables[1] describing the EM clusters. The longitudinal inter-calibration equalises the energy deposit in the two main layers of the EM calorimeter between data and MC. The MC-based e/γ calibration is applied on the e/γ response as the next step to ensure matching the detected energy to the actual one of the particle. A set of so-called uniformity corrections is introduced to account for the non-modelling of some geometrical features of the detector and the mis-modelling of the LAr electronics response. After applying these corrections, some residual discrepancies between data and MC remain. Final calibration on the EM response of the electromagnetic calorimeter is done using a large sample of $Z \to e^+e^-$ events (more than 20 million events in the total Run 2 dataset after full selection). For this residual, also called in-situ, $Z \to e^+e^-$ calibration, the spectrum information of this standard candle process (in particular, mass and width), measured precisely by the LEP experiment [67] is used in the nominal approach, so-called template method, which is becoming particularly interesting as a measure of constraints coming from the linearity measurement. This method is designed to make the invariant mass of the e^+e^- system observed in data, and the one predicted by the MC agree as much as possible regarding

[1] For the converted photons, information describing the conversion status is also used.

the central position and the spread. For this, the data distribution is shifted, and the MC is smeared to have the exact energy resolution (distribution spread) as the actual data. Validation of the calibration electron energy scales at low energies is done via studying electron candidates from $J/\psi \to ee$ and $Z \to ll\gamma$ in data.

The in-situ corrections are deduced in 2 sequential steps:

- a global correction $\alpha(\eta)$ [68, 69, 70], depending only on the angular position (η) in the detector:

$$E_{data} = E_{MC}\big(1 + \alpha(\eta)\big) \tag{3.1}$$

- a linearity correction (variation of calibration factor with the electron's momentum) $\alpha(|\eta|, E_T)$[2], residual to the global one, *linearity*, eq. (3.2):

$$E'_{data} = E_{MC}\underbrace{\big(1 + \alpha(\eta)\big)}_{\text{global}} \times \underbrace{\big(1 + \alpha(E_T, \eta)\big)}_{\text{linearity}} \tag{3.2}$$

The linearity has been previously probed [71] (Fig. 3.2), because it is important for several analyses, like the Higgs mass measurements.

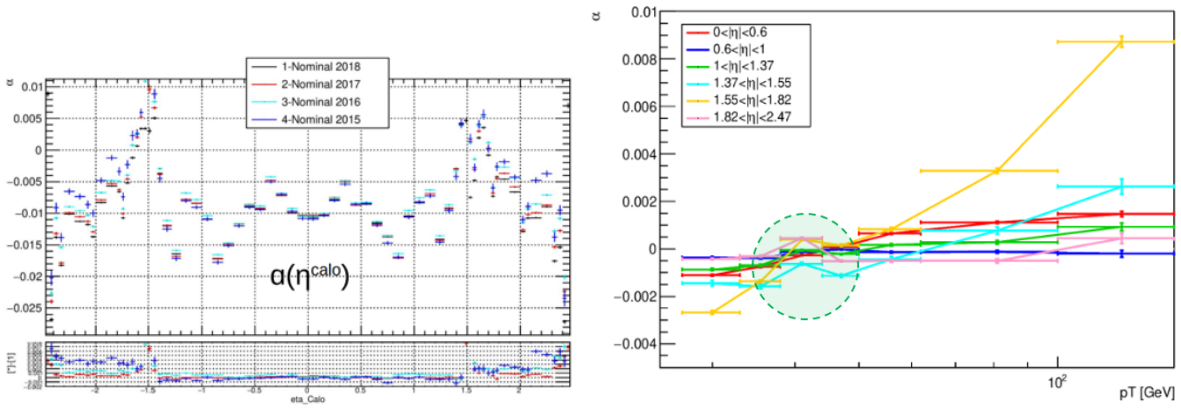

(a) (b)

Figure 3.2: Corrections $\alpha(\eta)$: (a) inclusive in p_T, (b) as a function of p_T. Source: [71].

Some excess around 45 GeV is found with the template method, which is the half-mass of Z-boson. This excess is probably due to a mismodelling of the Z-boson momentum in the MC simulations due to higher order QCD corrections [70]. It is essential to provide a cross-check with an alternative method, particularly the linearity dependence. An alternative method has been examined: the E_T/p_T method (where E_T is the transverse energy of the electron or positron measured by the calorimeter, and p_T is its transverse momentum measured by the tracker), exploiting both the EM calorimeter and the ID, combining information into a single variable, using the electrons from the $Z \to e^+e^-$ topology. A property of the E_T/p_T variable is that it has a more-peaking distribution than either E_T or p_T separately. This variable is not

[2]In the m_{ee} study, by p_T one usually means the calorimeter-measured energy. In the E_T/p_T study, p_T is measured in the tracker. In the linearity dependence ($\alpha(|\eta|, E_T)$, the energy is taken from the calorimeter in the both methods.

measured to be exactly unity[3] due to the resolution effects of the tracker and the calorimeter, and due to energy losses, particularly related to bremsstrahlung. The scale factor in this study is defined as the following quantity:

$$\alpha \equiv \frac{\langle E_T/p_T \rangle|_{Data}}{\langle E_T/p_T \rangle|_{MC}} - 1, \tag{3.3}$$

The angular brackets mean averaging in a broad sense, which could be a mean of the histogram or the central value of a fit function. Unlike the m_{ee} method, which has to deal with the kinematic correlations between the leading and sub-leading electrons and take care of the m_{ee} distribution when looking at a energy-dependent measurement, the E_T/p_T method only needs to study single electron an is therefore independent of a mismodelling of the transverse momentum of the Z-boson and has smaller systematics of this sort.

3.2 Datasets

The study uses 2018 data ($58.45\ fb^{-1}$) and its corresponding mc16e version of MC simulation. The $Z \to ee$ events are simulated [71] at NLO QCD in POWHEGBOX interfaced to PYTHIA8 parton shower model. MC samples are normalized to have the same luminosity as data. To account for the pileup mismodelling, a scale factor weights MC events to match the distribution of the number of interactions per bunch crossing (pileup) in data additionally scaled by $1/1.03$. For the campaigns of 2015 and 2016, an average pileup was recorded due to limited statistics. In contrast, the actual, not averaged pileup is used for data from 2017 and 2018, allowing more precise modelling of the pileup distribution in the MC [47]. For the simulation, only the $Z \to e^+e^-$ process is considered. The background processes which may also result in the same final state (e^+e^-, so-called irreducible background), such as $tt^-, Z \to \tau\tau$ and the di-boson VV production and mimicking this final states(fakes, also called reducible background), are estimated to have less than 1% contribution (Fig. 3.3) in comparison to $Z \to e^+e^-$ events after the full selection (Section 3.3) is applied. The fraction of background increases if the Z mass peak window is extended from [80, 100] GeV to [70, 110] GeV.

[3] Given electron mass 0.510^{-3} GeV and typical energies of 50 GeV, this ratio is non-distinguishable from unity.

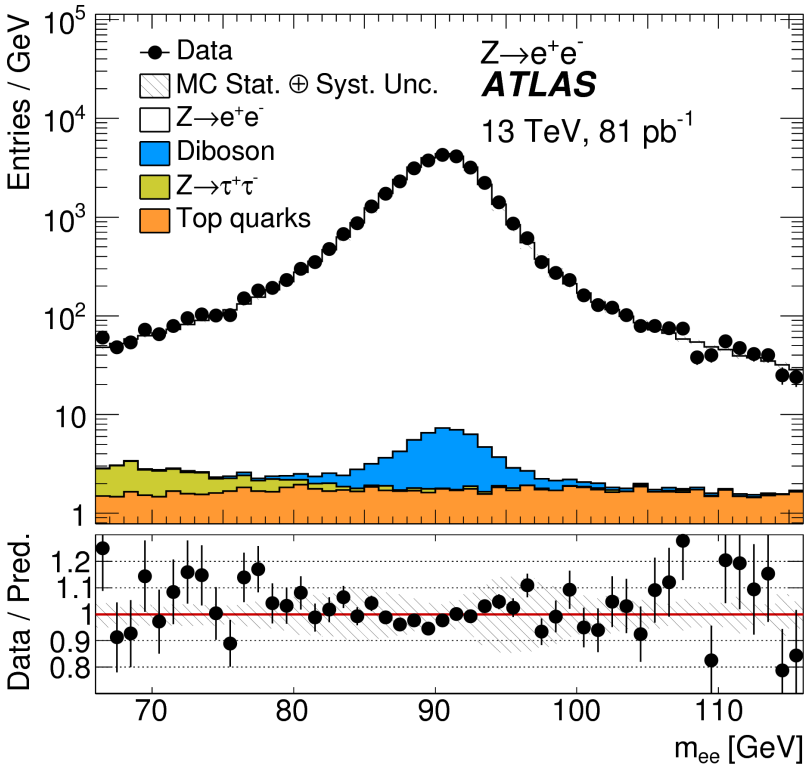

Figure 3.3: Example of the dilepton mass distribution after a $Z \to e^+e^-$ selection obtained with low pile-up 2015 data. The expected contributions from all background components are estimated with Monte Carlo simulations. Source: [72].

Increasing the statistics by including the decays of the charged vector bosons ($W^{\pm} \to e^{\pm}\nu$) is not done, although its cross-section is one magnitude higher. Neglecting them is explained by the problems with missing energy brought out by the neutrinos: one-electron spectrum would be polluted with background electrons (including fake ones), while an electron-positron pair, produced in the Z-boson decay, are more suitable for precise measurements.

3.3 Selection

The $Z \to e^+e^-$ selection procedure is the same as in the template method. Events are required to have a primary vertex with longitudinal position z_{vertex} smaller than 150 mm, to cut the non-collisional background (cosmic rays, halo beams, beam-gas interactions, pile-up, etc.). This background is further suppressed by a cut on the significance of the transverse impact parameter d_0 (distance from the track to the primary vertex (PV)): $|d_0/\sigma(d_0)| < 5$ and a cut on the longitudinal impact parameter with respect to the PV: $|z_0 \sin(\theta)| < 0.5\ mm$. The selection seeks for two opposite-charge electrons with highest p_T ($p_T > 27$ GeV) good quality clusters ("GoodOQ") in the acceptance of the central region of the electromagnetic calorimeter ($|\eta| < 2.47$). They are required to pass the medium-quality identification criterium (*medium likelihood ID*) and loose isolation (*FCLoose isolation*) [73, 74, 75] (more details in Section 4.4.2 dedicated to the reconstruction of electrons used in the $H \to \gamma\gamma$ analysis).

Scale factors are applied to correct the residual differences between data and MC for the trigger, identification and isolation efficiency. The invariant mass of the di-electron system is required to belong to the Z-boson peak region: $[80, 100]\ GeV$.

3.4 Construction of E_T/p_T variable

E_T/p_T variable combines information from two reconstructed quantities: E_T (from the calorimeter) and p_T (from the tracker). Each of them might be reconstructed in different ways. Hence, one needs to find appropriate ones.

3.4.1 Energy (from the calorimeter)

The distributions of total energy and its transverse part are illustrated in Fig. 3.4a and 3.4b, where one can see the pre-selection for energy (electrons with $E < 27$ GeV are cut off). As expected, the leading electron energy distribution is shifted to higher energies. The transverse energy spectrum (combined for both electrons) has a peak close to half-mass of the Z-boson, which is the most probable transverse energy in the reaction.

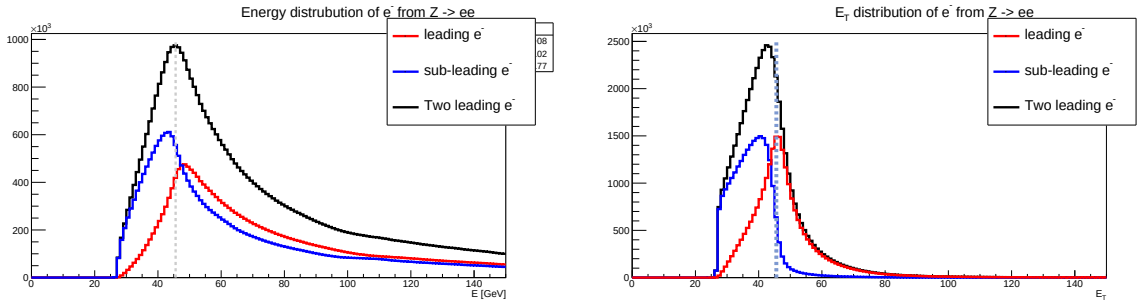

(a) (b)

Figure 3.4: Distributions of energy (a) and its transverse part (b) with 2018 data for the leading electron (red), sub-leading electron(blue) and the sum of the two (black). The black vertical dashed line stands to the half-mass of the Z boson. Source: [76].

3.4.2 Tracker Momentum

Within the ATLAS experiment, three following versions of p_T [74] are considered:

- *GSF* - Gaussian-sum filter, designed to account for the energy loss of a charged particle, assuming that the losses are gaussian-like distributed.
- *GSF_end* (momentum at the end of the tracker), which is computed as GSF, but with compensation of all possible momentum losses by bremsstrahlung in the tracker: $GSF_{end} = GSF \cdot (1 - f_{brem})$, where f_{brem} is the fraction of the momentum lost in the irradiation process defined as:

$$f_{brem} \equiv 1 - \frac{(q/p)^{IP}}{(q/p)^{ID}}, \tag{3.4}$$

  where IP is the interaction point (before any irradiation), and ID is at the end of the inner detector. In order to prevent over-compensating of momentum, a cut on $fBrem$ variable is introduced. Figure 3.5 illustrated the importance of this cut.
- $\pi - like$ - Fit of the track without considering an energy-loss term (assuming a π-like behaviour of the electron). This hypothesis reconstructs the electron with smaller energy than the truth one due to the loss by bremsstrahlung, which is not corrected for.

Technically, the fit, in this case, is done under the constant curvature assumption. Hence, the constant-curvature fit will accommodate the decreasing radius, preferring a smaller value to the truth.

The distributions of the various p_T types are illustrated in Fig. 3.5. The corresponding E_T/p_T distributions are shown in Fig. 3.6a (with a zoom on Fig. 3.6b). The GSF_{end} distribution is the broadest, since it undergoes a bremsstrahlung correction. The $\pi - like$ distribution vanishes faster at higher energies than GSF (because sometimes the GSF filter, designed to correct for the bremsstrahlung losses, over corrects energy), but has more tails at low energies, a direct consequence of the fact that the low transverse momentum tails, characteristic of bremsstrahlung, are corrected by the GSF.

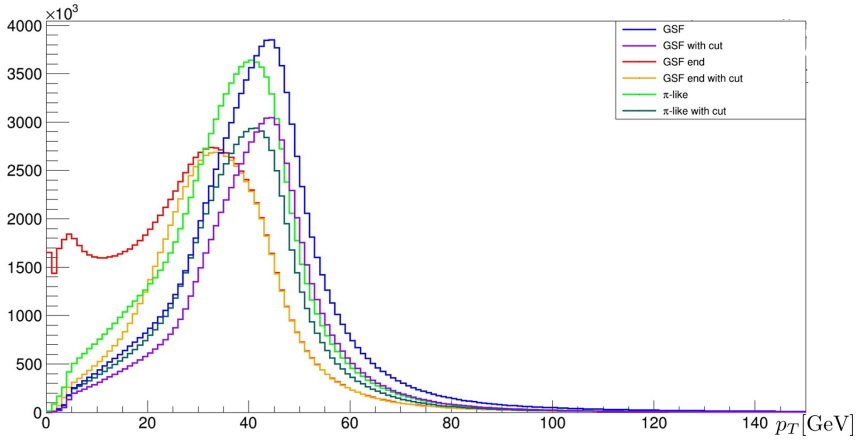

Figure 3.5: Distribution of various electron p_T types for MC with and without cut on $f_{brem} < 0.5$. The cut of the bremsstrahlung variable is crucial to prevent an over-correction. The red curve, representing the results without this cut, shows unphysical behaviour at low energy. After the cut (orange curve), the distribution shows no anomaly at low energy. Source: [76].

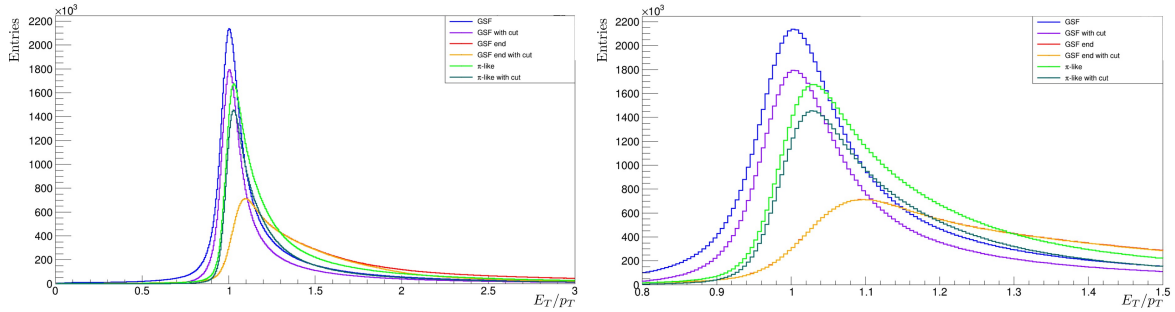

(a) (b)

Figure 3.6: E_T/p_T distributions for various electron p_T types with and without cut on $f_{brem} < 0.5$. The (b) plot is zoomed in E_T/p_T. Source: [76].

Distribution of the ratio MC to data between E_T for the three types of p_T is shown in Fig. 3.7a.

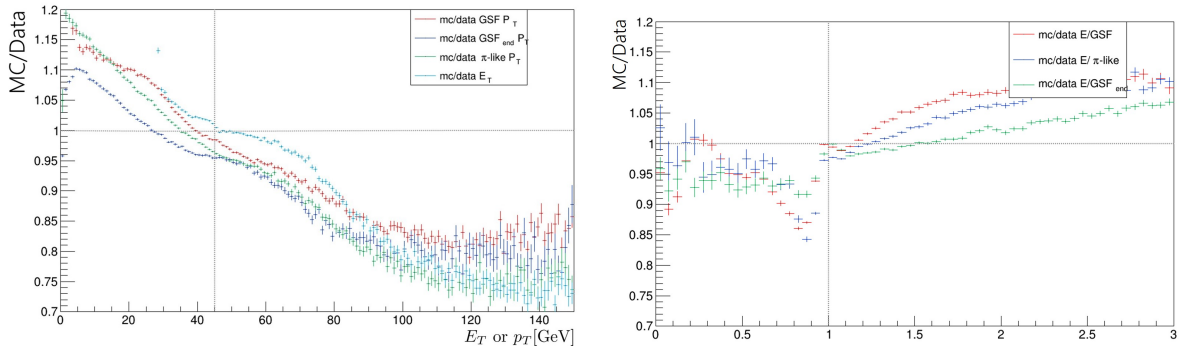

(a) (b)

Figure 3.7: Ratios MC/data of p_T and E_T (a) and E_T/p_T (b) for various p_T types: GSF (red), π-like (blue) and GSF_{end} (green). Source: [76].

It shows that the GSF p_T is better calibrated than the other p_T- types near the energy level of half mass of the Z-boson (characteristic energy of the $Z \to e^+e^-$ process).

Also, for all distributions, the mis-modelling of MC has the same trend with E_T. Thus the E_T/p_T ratio can compensate for this difference. From Fig. 3.7b, depicting E_T/p_T ratio between MC and data for the three various types of p_T, it is seen that GSF_{end} shows the best global agreement between data and MC. However, the GSF_{end} distribution is wider than the other types of momentum. For the present results, the GSF p_T momentum has shown the best results in terms of stability of the method with respect to any change in the configuration (E_T/p_T binning, range for the fit and others). The most peaking distribution for E_T/p_T originates from the GSF p_T, even though it has more tails to the left compared to $\pi - like\ p_T$.

3.4.3 Degradation of momentum with η and E_T

Variation of E_T/p_T distribution with η and E_T is shown in Fig. 3.8 and Fig. 3.9. The shape of E_T/p_T distribution is more sensitive to the change of the detector region (η) than the change in E_T. This difference mainly appears because the tracker resolution is highly sensitive to η. Tracker momentum is non-uniformly biased outside of the barrel due to the evolution of the amount of the material in the inner detector (Fig. 2.6). The fast degradation of momentum resolution is illustrated in Table 2.2.

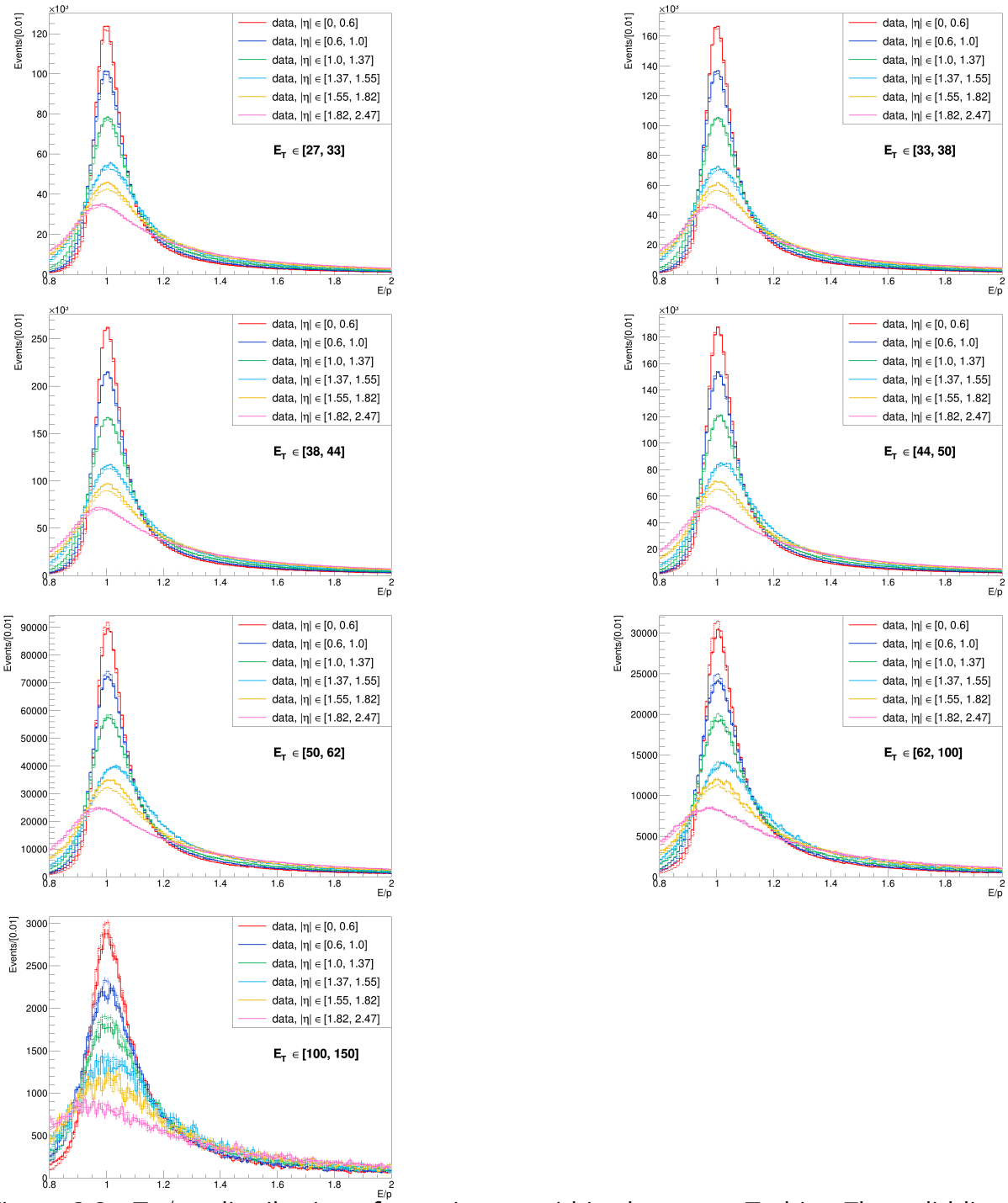

Figure 3.8: E_T/p_T distributions for various η within the same E_T bin. The solid line stands for data, and the dashed for MC. GSF p_T is used. Source: [76].

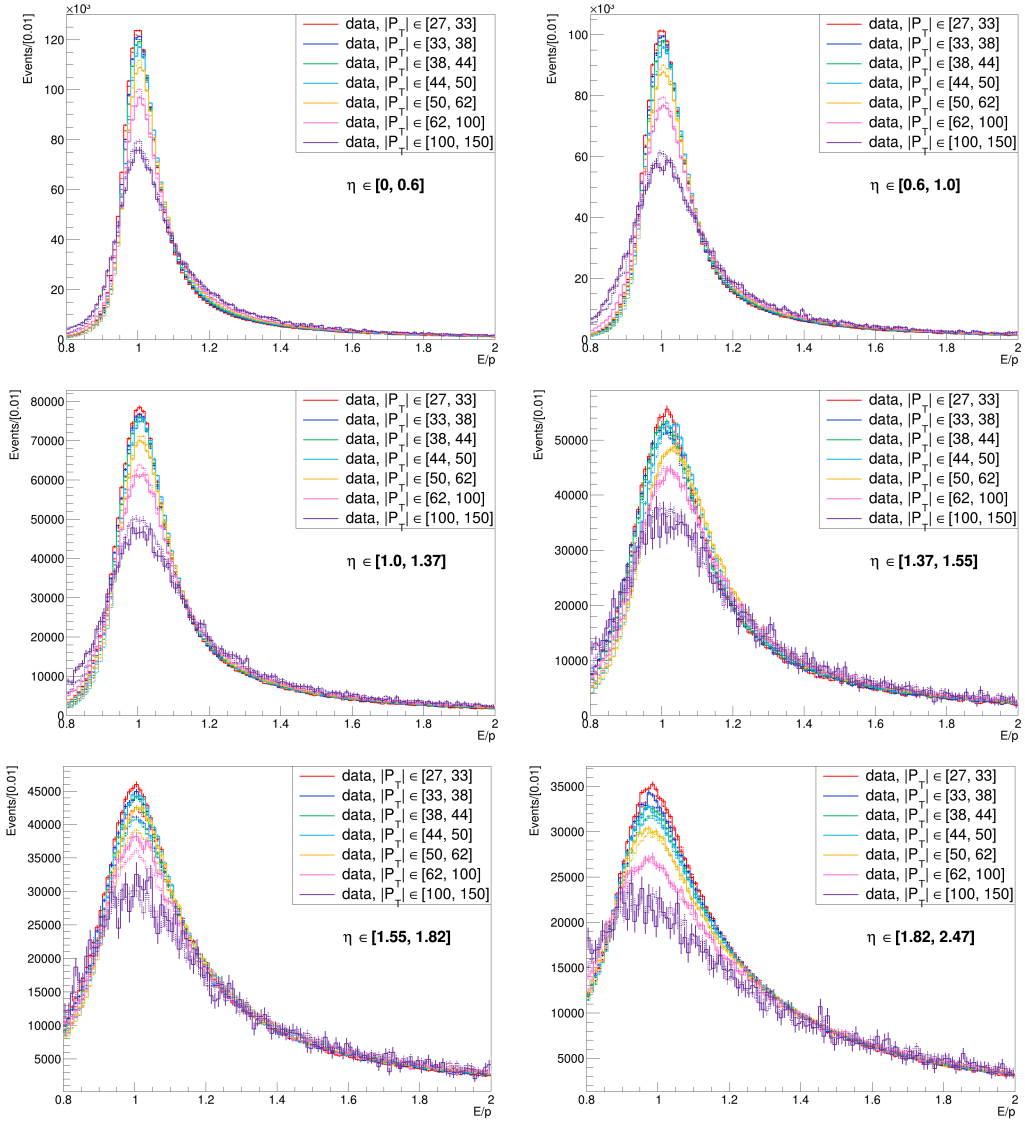

Figure 3.9: E_T/p_T distributions for various E_T with the same η. The solid line stands for data, and the dashed for MC. GSF p_T is used. Source: [76].

3.4.4 $p_T^Z - y^Z$ reweighting

A mismodelling of the Z-boson kinematic distributions (p_T^Z and y^Z, being the transverse momentum and rapidity) is observed at the big-value tails (Fig. 3.10). It may be caused by the residual missing higher-order QCD corrections to the NNLO modelling of the Z-boson production. Correcting for this mismodelling may improve the calibration performance, equalising initial properties of electrons for data and MC in terms of their initial kinematic distribution.

Correction of this effect (by reweighting the rapidity and p_T distributions) is done by discretising the 2D phase space ($y^Z \times p_T^Z$) into 800 0.5 GeV bins for p_T^Z $[0, 400]$ GeV and 12 bins in y (Fig. 3.11), following the binning used for the linearity measurements (see section 3.4.5). The fraction of events above the 400 GeV threshold is negligible.

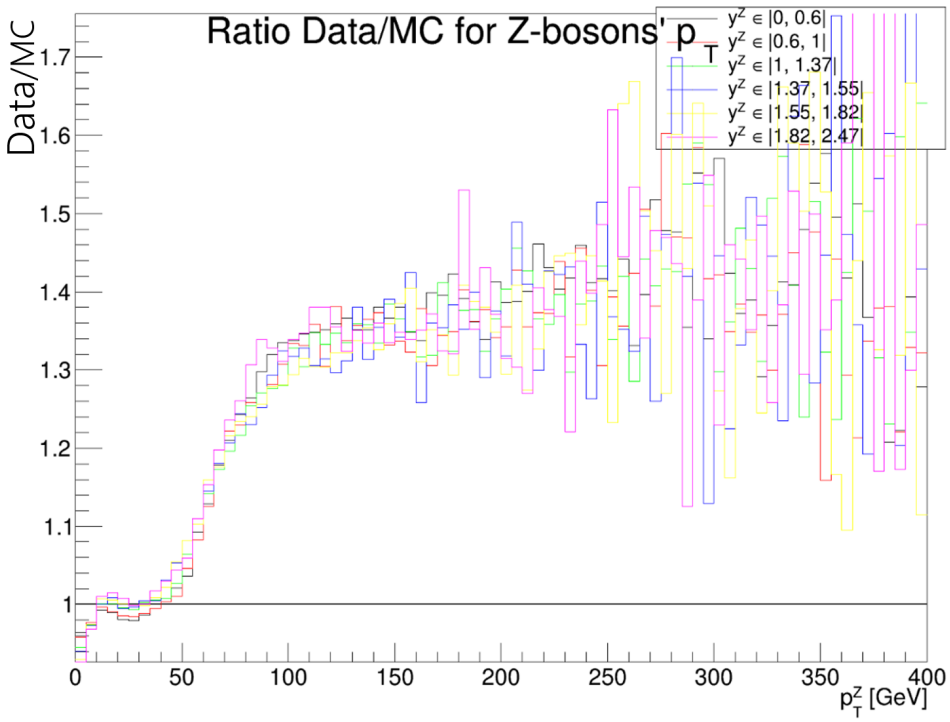

Figure 3.10: Ratio data/mc of p_T^Z distributions for various rapidity regions. These discrete 2D distributions are used as a $p_T^Z - y^Z$ weight applied to MC.

The resulting correction for the MC is implemented as an additional weight $w^{p_T^Z - y^Z}$ applied to each event. For each 2D bin, the weight is computed as the ratio between the total weight for data and MC.

Applying $p_T^Z - y^Z$ reweighting improves the agreement between data and MC for momentum, as shown in Fig 3.12, where the blue histogram goes closer to unity in the sub-plot (showing the MC/data ratio). The impact on E_T/p_T is small.

Weak sensitivity of E_T/p_T to $p_T^Z - y^Z$ reweighting, in comparison to the nominal method [71], can be explained by the fact that the E_T/p_T method treats both electrons from Z-boson decay independently, so that for each independent region in η and p_T, the correction applied to p_T is nearly the same for all events. Therefore, the correction itself leads to a nearly constant multiplicative factor to MC within a given phase-space region, effectively modifying the overall normalisation factor of the distribution.

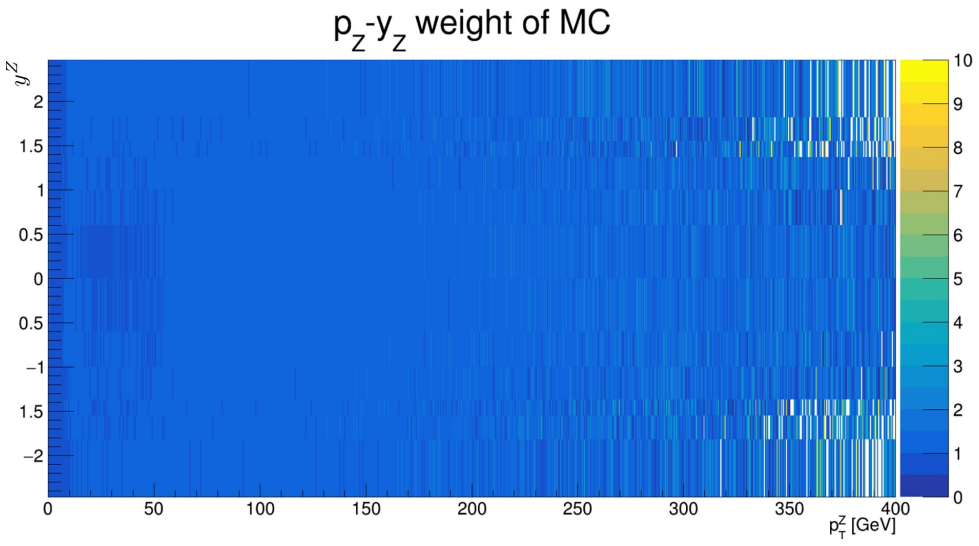

Figure 3.11: 2D ratio data/MC of $p_T^Z - y^Z$ distributions. Source: [76].

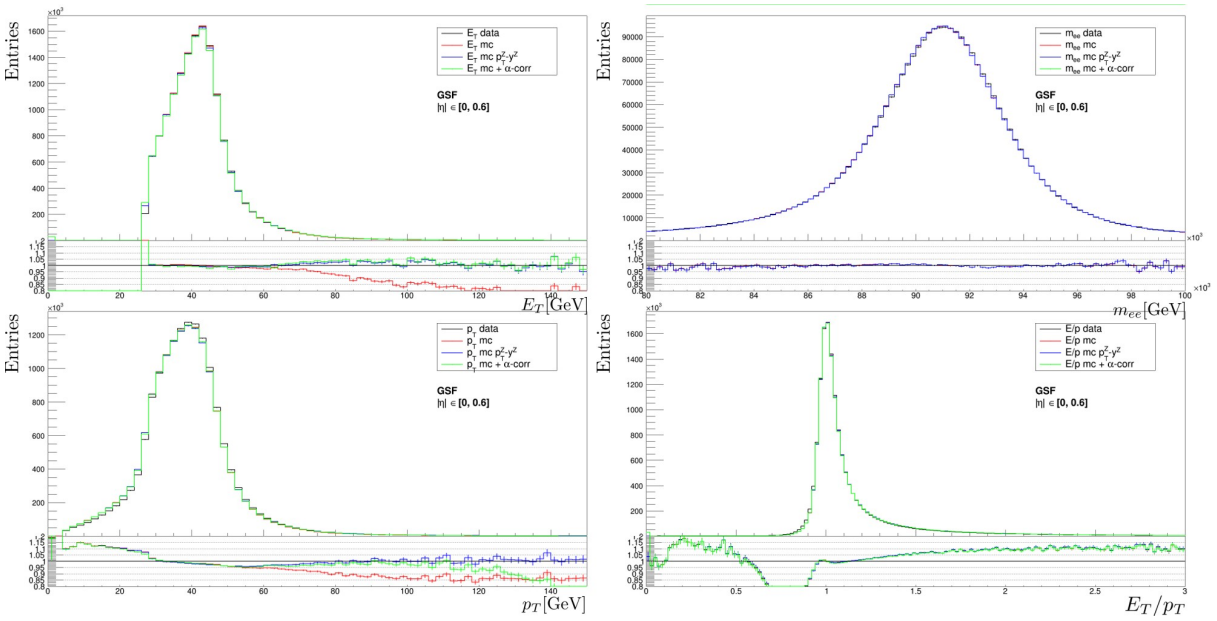

Figure 3.12: Distributions of: E_T (top left), GSF p_T (bottom left), m_{ee} (top right) and E_T/p_T (bottom right) for data (black) and three types of mc: nominal (red), with $p_T^Z - y^Z$ reweighting (blue) and with self-closure (after applying deduced α corrections $\alpha_{E/p}$. For the m_{ee} distribution, this correction is not applied on the plot) (green). Leading and sub-leading electrons. $|\eta| \in [0, 0.6]$. Sub-plots show the ratio MC/data. Source: [76].

3.4.5 Binning in η and E_T

Following the linearity measurements with the template method, [71], the same 2D binning in $|\eta|$ and E_T is chosen:

- 6 $|\eta|$ bins: [0, 0.6], [0.6, 1.0], [1.0, 1.37], [1.37, 1.55], [1.55, 1.82], [1.82, 2.47].
- 7 E_T bins: [27, 33], [33, 38], [38, 44], [44, 50], [50, 62], [62, 100], [100, 150] GeV.

giving 42 bins in total. The binning in η is conditioned by the material distribution in the ATLAS calorimeter system (Fig 2.6).

An independent study of the forward-backwards difference has been performed and is described in Sec. 3.6.2. It consisted of independent measurements of the linearity for the two parts of the detector: with $\eta < 0$ and $\eta > 0$.

3.5 E_T/p_T implementation

The estimation of the average value of the $\langle E_T/p_T \rangle$ quantity is obtained by a fit applied to the E_T/p_T distribution. This is done independently for 6 x 7 regions in $|\eta|$ and p_T, separately for data and MC. After examining the shape of E_T/p_T distributions, a few functional forms have been tested: Gaussian and Crystal Ball (CB, defined by eq. (4.15)) functions. All of the parameters are kept free in the fit.

Optimisation of the window

In order for the fit of E_T/p_T distribution to be less sensitive to possible lack of statistics and spread effects in some kinematic regions of phase space ($|\eta|$, E_T), it is made in a dynamic window. A two-step procedure (Fig 3.13, described in the next paragraph) allows getting more stable results with respect to variation of E_T/p_T binning and fit range.

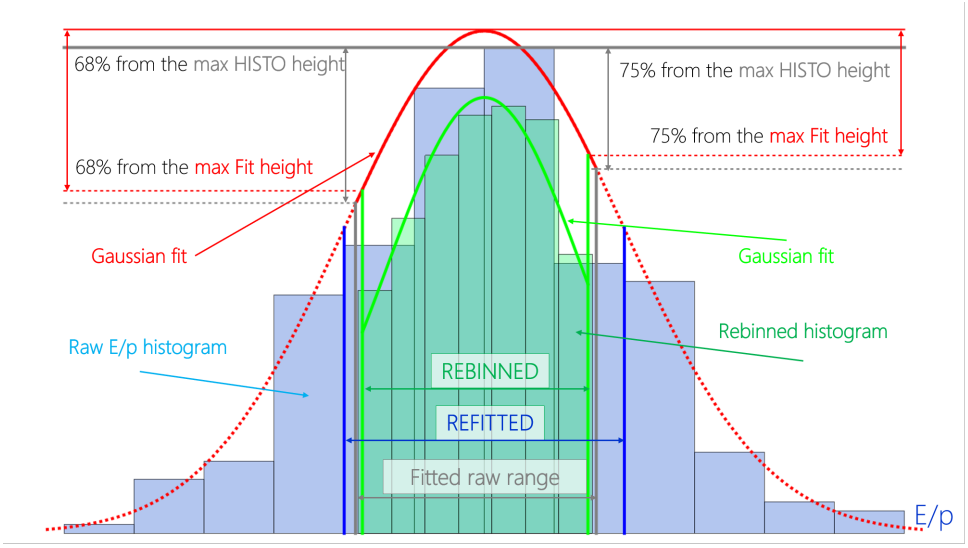

Figure 3.13: Illustration of the various ranges definition used. Source: [76].

During the first step, the E_T/p_T initial histograms (Fig. 3.13 in blue) are defined and filled independently for each kinematic region (E_T, $|\eta|$) both for data and MC in a preliminary wide range [0, 10] with 1000 bins (bin width of 0.01). This range is chosen wide enough to cover most events so that the normalisation of MC to data could be done. Another reason for the extension to $E/p < 10$ is that this cut is introduced in the selection of electrons (see Section 4.4.2 on the electron reconstruction). In order to eliminate a dependence of the fit results on the fit configuration (binning, statistical fluctuations, choice of the window and

others) a few step procedure has been developed. At each step a new range is defined, based on the results from the previous step results.

First range - *initial* Having only a raw E_T/p_T histogram, a range is defined based on the maximal height of the histogram (the grey horizontal line on top of the blue histogram). Then define the first encountered bins to the left and right from the peak, which have a content below 68% and 75% (respectively 15%) of the maximal height in order to perform a first Gaussian (respectively CB) fit. In Fig. 3.13 these levels are depicted with grey dashed horizontal lines. The resulting range spans between the grey solid vertical lines and is marked as fitted raw range. The first fit in this range is shown by a red curve. The range for fitting this histogram is chosen as a compromise between narrow enough to ensure a fit with a simple function and wide enough to increase statistics, thus reducing fit-uncertainties.

Second range - *re-fitted* From the fit curve, a new fit range, no more dependent on the initial binning, is deduced. For the new range, one defines again a level of 68% and 75% (respectively 15%) from the "maximal height" (red solid horizontal line) of the Gaussian (CB) fit curve from the previous step. This new range is illustrated by the green solid vertical lines. At this next step, one obtains and fills the new E_T/p_T histograms (shown in green) in the previously defined range to be used for fit. They are shown in green. For the final result, one needs to fit these new histograms in the range in which they are defined with a Gaussian (respectively CB) function. The fit curve is illustrated in green over the green histogram.

Fit function choice

E_T/p_T linearity measurements rely on the precise determination of E_T/p_T, extracted as the fit function's central value. Examination of E_T/p_T distributions has shown that they were well modelled with a Gaussian function or with Crystal Ball (including right tail with $E_T/p_T > 1$). With both functions, all their parameters are fit in the study. Uncertainty on the function parameters reduces with increasing statistics. However, in the regions where E_T/p_T is far from unity, the ratio data/MC is also far from unity due to mismodelling of radiative and detector processes. Therefore, capturing an additional tail of the E_T/p_T distribution by CB function does not significantly improve the uncertainties on the linearity values, even though making them more precise for the low-stat region (high η and E_T). E_T/p_T distribution fit with Gaussian and CB functions are shown on the Fig. 3.14 and Fig. 3.15.

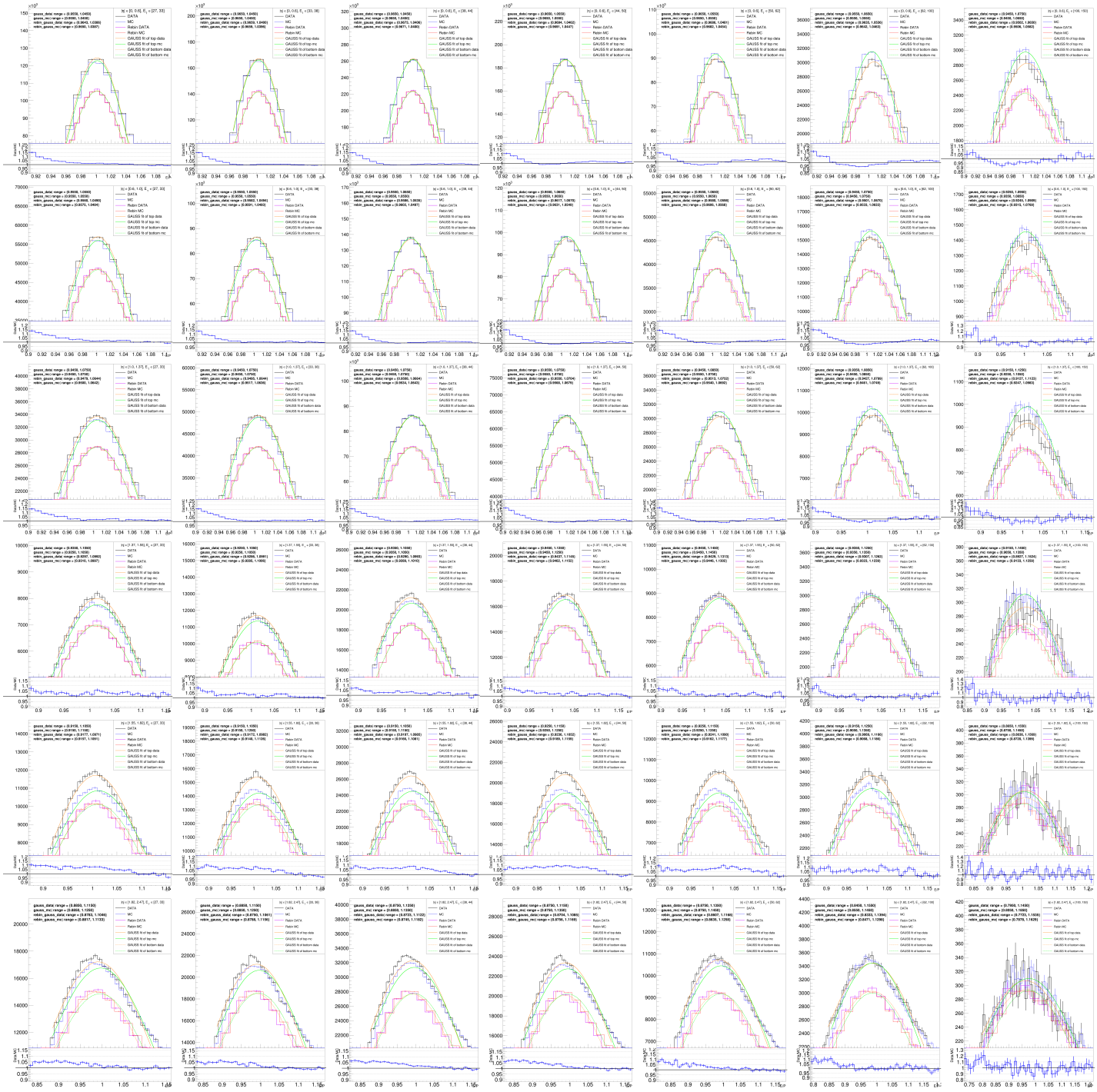

Figure 3.14: Illustration of E_T/p_T distributions fit with **Gaussian** function for all regions in η and E_T. $|\eta|$ increases along the column from top to bottom and E_T increases from left to right. Four histograms are shown: black (data initial), blue (MC initial), violet (data secondary) and red (MC secondary). Corresponding Gaussian fit curves are in orange and green, respectively. Sub-plots show data/MC ratio for the initial histogram. Source: [76].

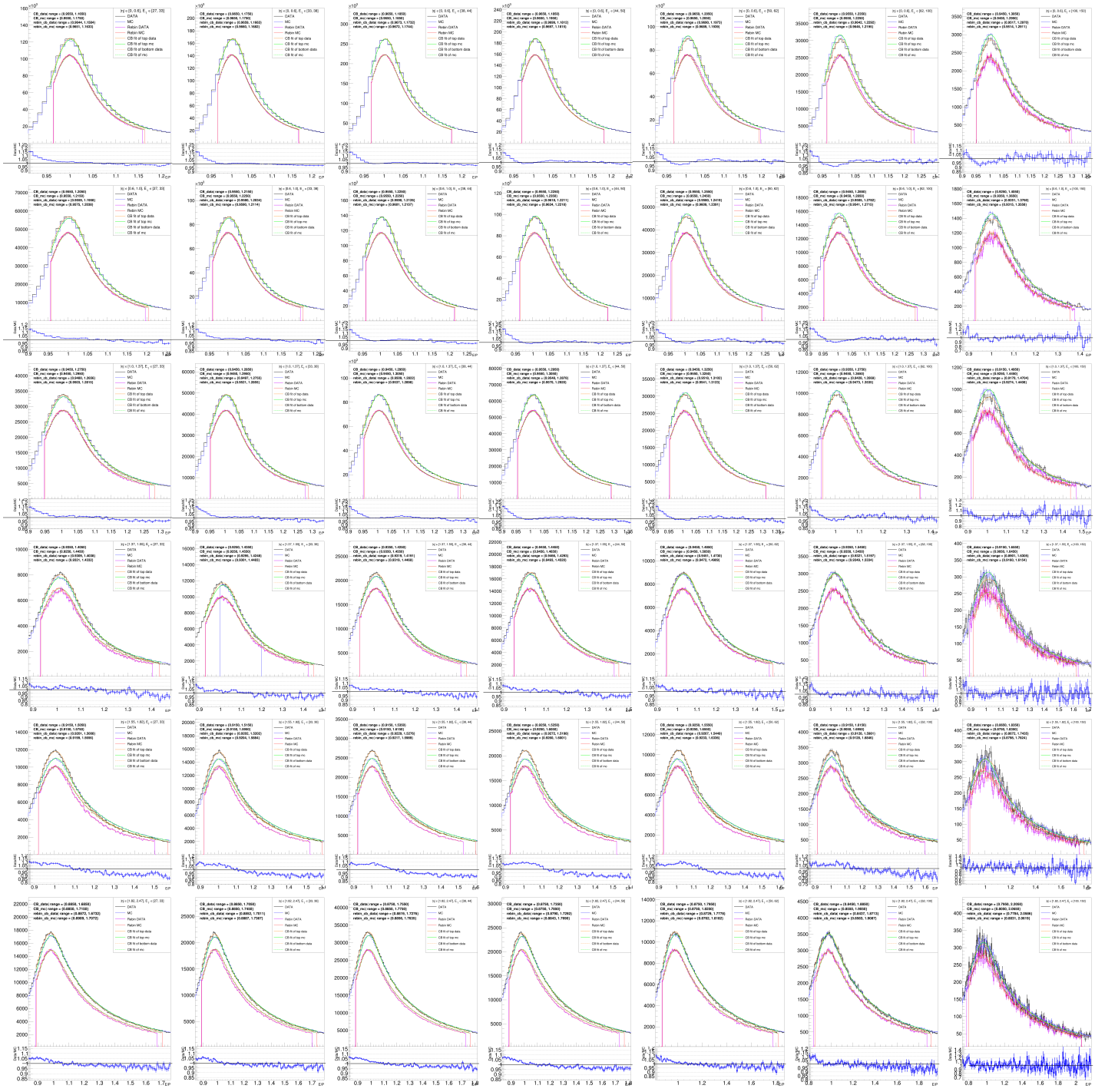

Figure 3.15: Illustration of E_T/p_T distributions fit with **Crystal Ball** function for all regions in η and E_T. $|\eta|$ increases along the column from top to bottom and E_T increases from left to right. Four histograms are shown: black (data initial), blue (MC initial), violet (data secondary) and red (MC secondary). Corresponding CB fit curves are in orange and green, respectively. Sub-plots show Data/MC ratio for the initial histogram. Source: [76].

3.6 Bias from the tracker

Since the E_T/p_T method also uses information on the momentum from the tracker, it may be affected by bias on p_T arising from any miscalibration of the inner detector (ID).

They might be reduced by applying a set of dedicated corrections. Biases are classified into 2 classes ([77]) (Fig. 3.16, another interesting paper is the recent one [78]):

- sagitta bias, resulting from a global rotation of the detector layers (error in the true angular coordinates of the detector layer), when reconstructed tracks appear to be rotated with respect to the true ones;
- length scale bias: a global bias on the detector layer radius, when reconstructed tracks appear to have a different curvature than the original ones. It might happen due to an incorrect determination of the true radius at which a given layer is located.

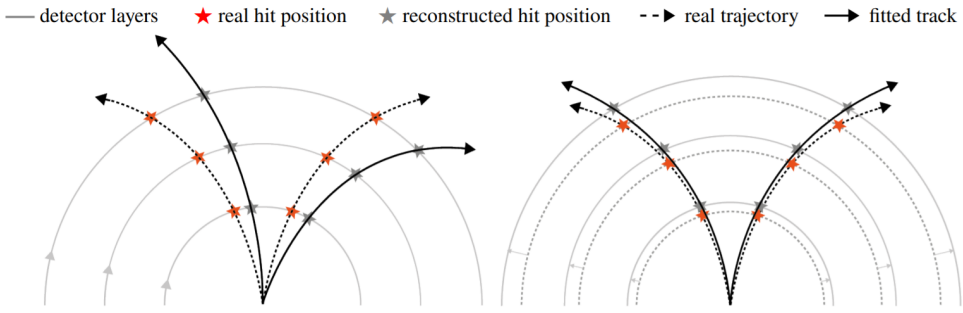

Figure 3.16: Illustration of two typical sources of bias from the tracker with a possible effect on the E_T/p_T quantity: sagitta bias (a) and length scale bias (b). Source: [77].

3.6.1 Sagitta bias

When electrons and positrons undergo the Lorentz force from the magnetic field in the inner detector, which determines their momentum, they rotate in opposite directions in the transverse plane due to their opposite electric charges. Therefore, due to the bias ϕ_{bias} on the angular position induced by sagitta bias, instead of the truth angle ϕ, one measures angle $\phi + \phi_{bias}$ of the crossed detector layer by the track. The effect has an opposite sign on a particle and an anti-particle. If an electron passes through a given detector layer with an actual angle ϕ in a given frame, then a positron with the same momentum has a true angle $-\phi$ in this frame. If the sagitta bias induces an angular shift $+\phi_{bias}$ when determining the truth layer angular position, it is the same for electrons and positrons with the same momentum. In that case, the electron is measured with angle $\phi + \phi_{bias}$, while the positron is determined with $-\phi + \phi_{bias} = -(\phi - \phi_{bias})$ angle in a given detector layer.

This bias has a consequence on the measured momentum of a given particle via its curvature in the magnetic field. Indeed, due to the sagitta bias, one can expect over-estimation of energy for particles with a given charge and under-estimation for their opposite charge counterparts: the curvature is increased for one particle and decreased for the other particle (Fig. 3.16a). Hence, the measured momentum of electrons and positrons is biased in the opposite direction

from the actual value. Given that, by independently measuring the difference between E_T/p_T linearity for electrons and positrons, one can probe the sagitta bias $\delta_{sagitta}$, assuming that E_T, measured in the calorimeter does not depend on the charge. Further on, it is assumed that the mass-shape m_{ee} linearity [71] is the benchmark and the only reason why E_T/p_T method for electrons and positrons gives different to its results is the sagitta bias.

According to the definitions from [77] of the influence of sagitta bias on the reconstructed momentum:

$$p^{rec} = p^{true}(1 + qp_T^{true}\delta_{sagitta})^{-1}, \tag{3.5}$$

where q is the particles charge and $\delta_{sagitta}$ - sagitta bias scale, the latest can be found as:

$$\delta_{sagitta} = \frac{\langle E/p^{rec}\rangle^+ - \langle E/p^{rec}\rangle^-}{2\langle E_T\rangle} \tag{3.6}$$

taking into account the relation:

$$p^- - p^+ = 2p^{true}p_T^{true}\delta_{sagitta}, \tag{3.7}$$

where $p^\pm$ denotes the measured momentum of positrons (electrons) respectively.

Let $\alpha^\pm$ be the linearity measured only over positrons (electrons), and p^{true} be a not-biased momentum, which is the same for them (since it is not biased), then

$$\alpha^+ - \alpha^- \propto \frac{E}{p^+} - \frac{E}{p^-} \propto \frac{E}{p_{true}^2}\Big(p^- - p^+\Big) = \frac{E}{p_{true}^2}(2p^{true}p_T^{true}\delta_{sagitta}) \tag{3.8}$$

$$= 2E_T\delta_{sagitta}$$

Therefore, the difference between linearities for electrons and positrons (at the first order) grows linearly with E_T. This is a simple consequence of the bias magnitude being small; thus, its effect on momentum is observed only in the first-order expansion.

Therefore, the sagitta bias magnitude can be estimated as:

$$\delta_{sagitta} \propto \delta\alpha\frac{1}{2E_T} \tag{3.9}$$

A deviation between the linearity dependencies for electrons and positrons (Fig. 3.17) appears, as expected, in the opposite direction from the reference values with the nominal historical method [71]. Hence, it allows us to estimate the sagitta bias using eq. (3.9).

Fig. 3.18(a) shows the dependency of $(\alpha^+ - \alpha^-)$ on E_T, and it behaves linearly with E_T, as predicted by eq. (3.9). Estimation of the sagitta bias itself $\delta_{sagitta}$ is shown in Fig. 3.18b, from which it is seen that for the central region of the calorimeter ($|\eta| < 1.0$) estimated value of the sagitta bias $\delta_{sagitta}^{E/p} \approx 0.05\ 10^{-3}\ GeV^{-1} = 0.05\ TeV^{-1}$. This value is in good agreement with the value of sagitta bias from the official study [77], shown in the Fig. 3.19b, where $\delta_{sagitta}^{official}$ for the barrel is found to be $\approx 0.05\ TeV^{-1}$.

Therefore, for the central region of the detector, the E_T/p_T method confirms the value of the sagitta bias found in the dedicated study.

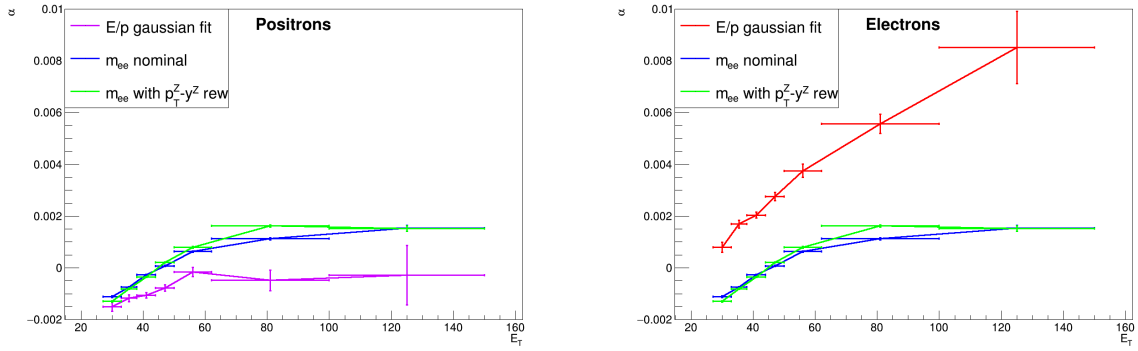

(a) (b)

Figure 3.17: Linearity measurements for positrons (a) and electrons (b) (green and violet curves, standing for different methods: the green is with $p_T^Z - y^Z$ reweighting and the violet is the nominal $\langle E_T/p_T \rangle$ result) with respect to the reference values (blue) of the m_{ee} method [71]. Source: [76].

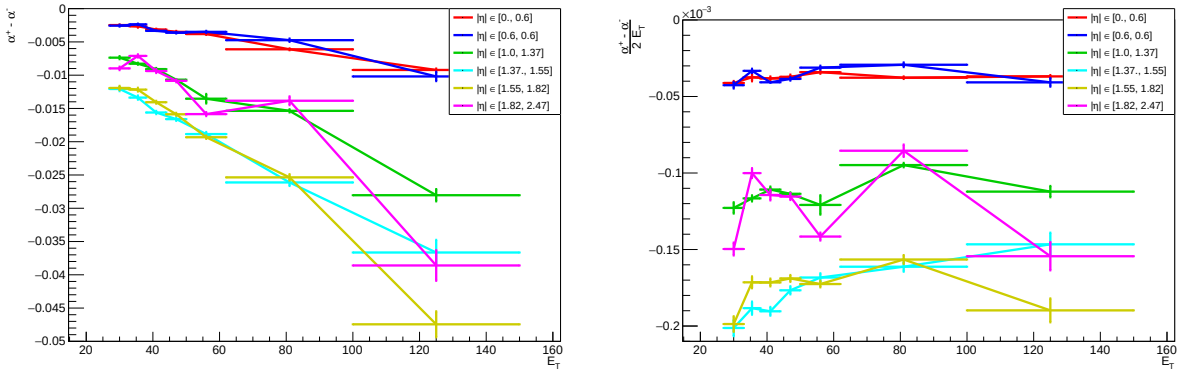

(a) (b)

Figure 3.18: The difference between linearities for positrons and electrons without (a) and with normalisation (right) on $2E_T$. This ratio $\left(\frac{\alpha^+ - \alpha^-}{2E_T}\right)$ is expected to be an estimate of the sagitta bias (formula (3.9)). Various colours represent different angular zones in the detector (red, blue, green, cyan, yellow, pink). The estimated sagitta bias is nearly flat with E_T in the barrel ($|\eta < 1.0|$) and oscillates around a constant outside. Source: [76].

3.6.2 Scale bias

Length-scale bias arising from misknowledge of the transverse scale in the inner detector can be probed by comparing the E_T/p_T linearity measurements with the nominal m_{ee} linearity (which is much less sensitive to any miscalibration of the tracker) under the assumption that the only reason for their difference comes from the tracker miscalibration.

An estimation of the scale bias has been performed using a muon analysis, and its results were provided in private [79]. The values found are shown in Fig. 3.20.

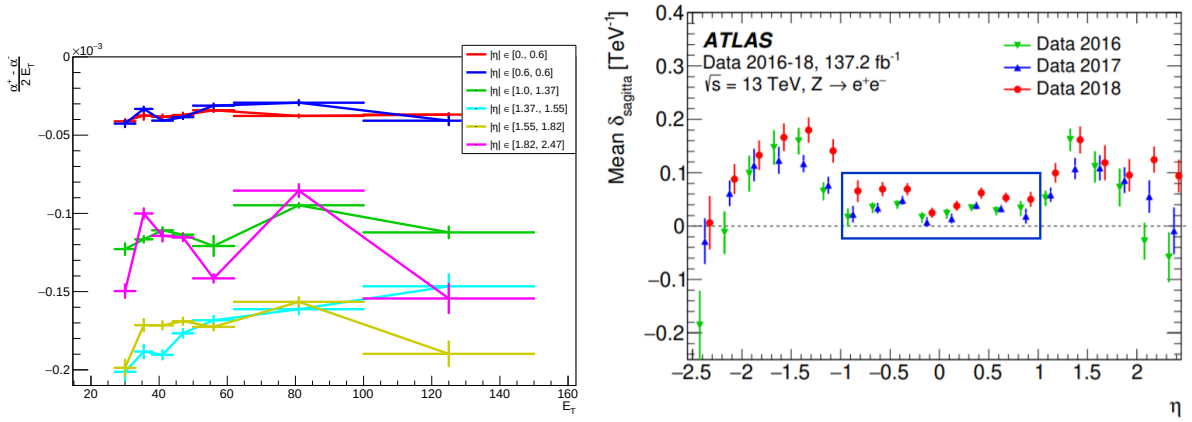

(a) (b)

Figure 3.19: Comparison of the official sagitta bias measurement (b) to (a) the estimation with E_T/p_T method in this study (same as Fig. 3.18). One sees that for the central region of the detector $|\eta| < 1.0$ the official value $\delta^{official}_{sagitta} \approx 0.05\,TeV^{-1}$ which is in a good agreement with the value from E_T/p_T study $\delta^{E/p}_{sagitta} \approx 0.045\,TeV^{-1}$. Source: [76].

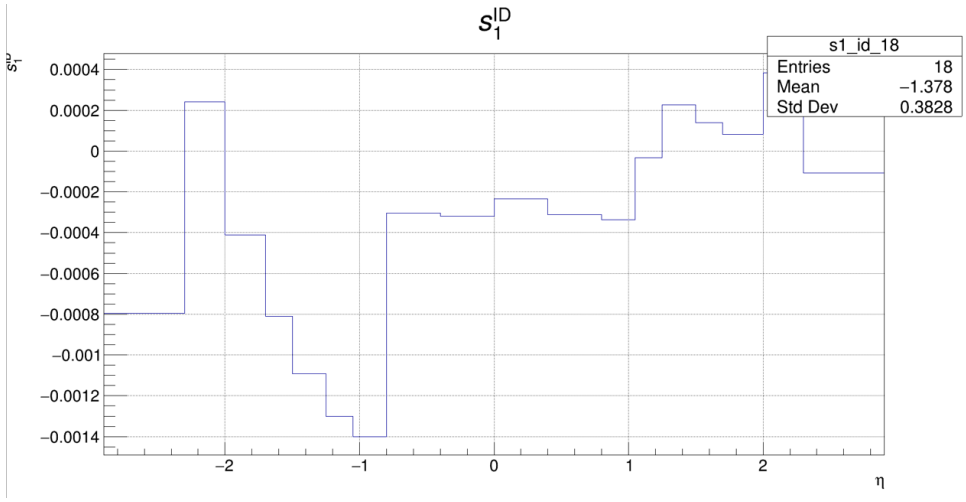

Figure 3.20: Scale bias from muon analysis ($Z \to \mu^+\mu^-$) as a function of η. Source: [79].

These corrections are evaluated [80] as follows:

$$p_T^{cor} = \frac{p_T^{MC} + \overbrace{s_0(\eta,\phi) + s_1(\eta,\phi)p_T^{MC}}^{shift\ correction}}{\underbrace{1 + \sum_{m=0}^{2} \Delta r_m(\eta,\phi)\left(p_T^{MC}\right)^{m-1} g_m}_{smearing}} \tag{3.10}$$

$$\propto \Big(p_{MC}(1+s_1) + s_0\Big)/(\text{spread correction})$$

Therefore, this estimation is equivalent to the following momentum shift:

$$p_{MC} \to p_{MC}(1 + s_1) \tag{3.11}$$

Here the s_0 correction is neglected, being a constant factor, with no dependence on the momentum.

The linearity measurements aim to correct data; therefore, eq. (3.11) can be transformed to the following correction of data:

$$p_{data} \to p_{data}/(1 + s_1) \tag{3.12}$$

The scale bias can be probed using the E_T/p_T method assuming that the only difference between m_{ee} and E_T/p_T linearities comes from this bias. Thus, using definitions of m_{ee} and E_T/p_T linearities ($\alpha_{m_{ee}}$ and $\alpha_{E/p}$, respectively), it comes:

$$\begin{aligned} 1 + \alpha_{m_{ee}} &= \frac{\langle E \rangle|_{data}}{\langle E \rangle|_{MC}} \\ 1 + \alpha_{E/p} &= \frac{\langle E_T/p_T \rangle|_{data}}{\langle E_T/p_T \rangle|_{MC}} \end{aligned} \tag{3.13}$$

and taking into account the requirement that corrected momentum for data equals the MC momentum, this makes:

$$\langle p_{mc} \rangle = \langle p_{data}^{cor} \rangle \equiv p_{data}^{uncor}/(1 + s_1), \tag{3.14}$$

One can estimate:

$$\begin{aligned} 1 + \alpha_{E/p} = \frac{\langle E_T/p_T \rangle|_{data}}{\langle E_T/p_T \rangle|_{MC}} \propto \overbrace{\frac{\langle E \rangle|_{data}}{\langle E \rangle|_{MC}}}^{1+\alpha_{m_{ee}}} \overbrace{\frac{\langle P \rangle|_{MC}}{\langle P \rangle|_{data}}}^{\frac{1}{1+s_1}} \Rightarrow \\ 1 + \alpha_{E/p} = \frac{1 + \alpha_{m_{ee}}}{1 + s_1} \Rightarrow s_1 = \frac{\alpha_{m_{ee}} - \alpha_{E/p}}{1 + \alpha_{E/p}} \end{aligned} \tag{3.15}$$

As the scale bias from muon analysis (Fig. 3.20) is asymmetric in η, the E_T/p_T linearities separately for $\eta > 0$ and $\eta < 0$ differ among themselves and differ from the inclusive in η linearity (Fig. 3.21).

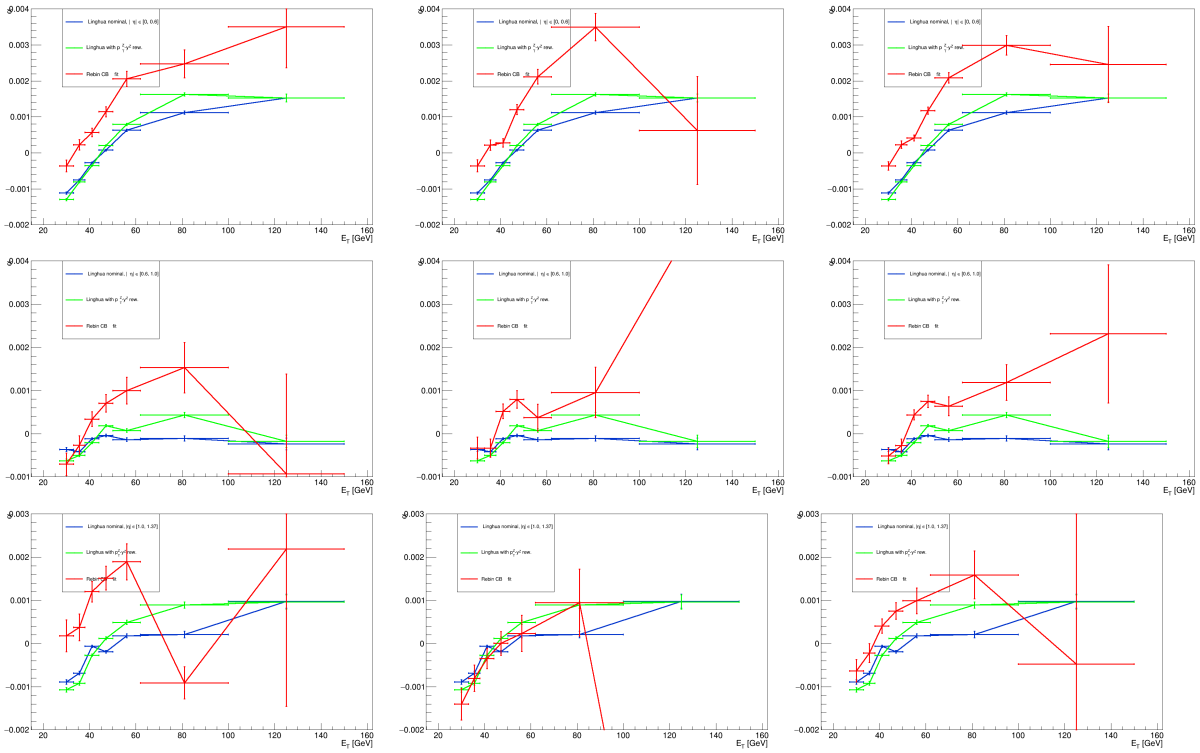

Figure 3.21: Linearity measurements for various $|\eta|$ regions for $\eta < 0$ (left), $\eta > 0$ (right) and inclusive in η. Red values stand to the ones found in this study with CB fit, green and blue represent m_{ee} linearity found in [71] with and without $p_T^Z - y^Z$ reweighting, respectively. The rows stand for various η regions: [0, 0.6], [0.6, 1.0] and [1.0, 1.37], respectively. Source: [76].

Estimation of s_1 dependency on η is based on $(\alpha_{m_{ee}} - \alpha_{E/p})$ and its official value are shown in Fig. 3.22. In the barrel, a good agreement between E_T/p_T estimation and the official values of s_1 is present. In the region $|\eta| < 1.5$, the E_T/p_T method can provide a reliable estimation of the bias, but neither for negative eta nor for the end-cap $|\eta| > 1.5$.

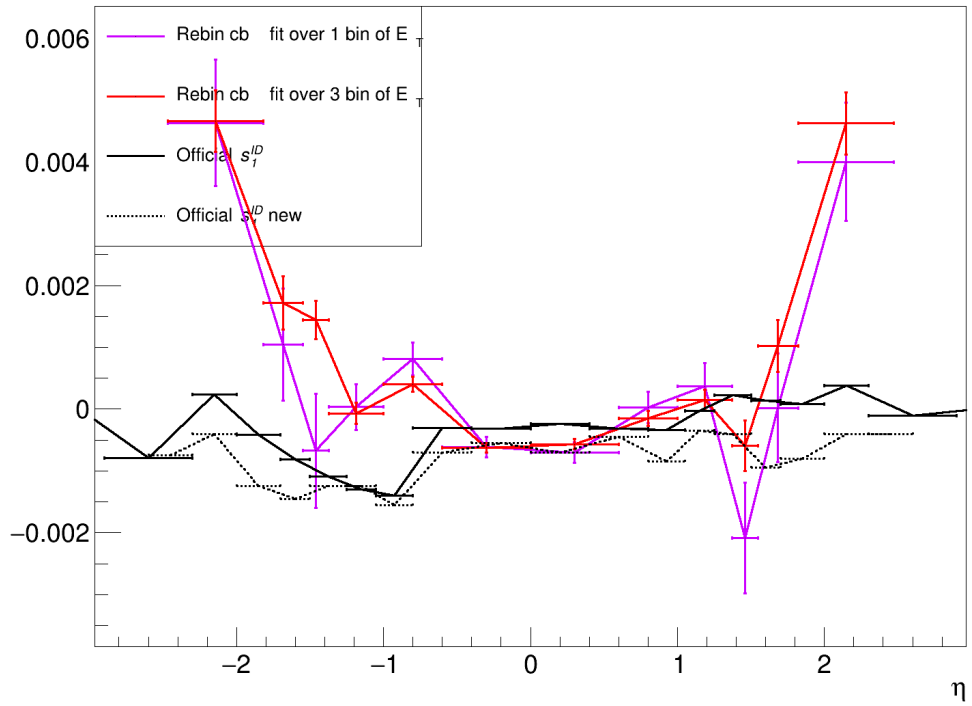

Figure 3.22: Estimation of the length-scale bias (s_1^{ID}) from eq. (3.15) as a difference between $\alpha_{m_{ee}}$ and $\alpha_{E/p}$ linearities. The official values of s_1^{ID} are shown in black solid and dashed lines (depending on the version of the results). In the central region, the $\langle E_T/p_T \rangle$-based method agrees with the official predictions. Source: [76].

3.6.3 Tracker resolution

Estimation of tracker resolution degradation with respect to the angular region in the detector η is illustrated by comparing of m_{ee} shapes for data and MC from the tracker[4] Fig. 3.23. At the same time, the resolution of the calorimeter degrades less (Fig. 3.24). The ratio between m_{ee} for data and MC is present in Fig. 3.25, showing a flatter behaviour for the calorimeter m_{ee} measurements. Quick degradation of the energy (momentum) resolution of the tracker gives a hint that a potential spread of the E_T/p_T distribution degrades with η, decreasing precision on measurements.

[4] m_{ee} from the tracker is computed using measurements of the momentum of electrons and their relative angle.

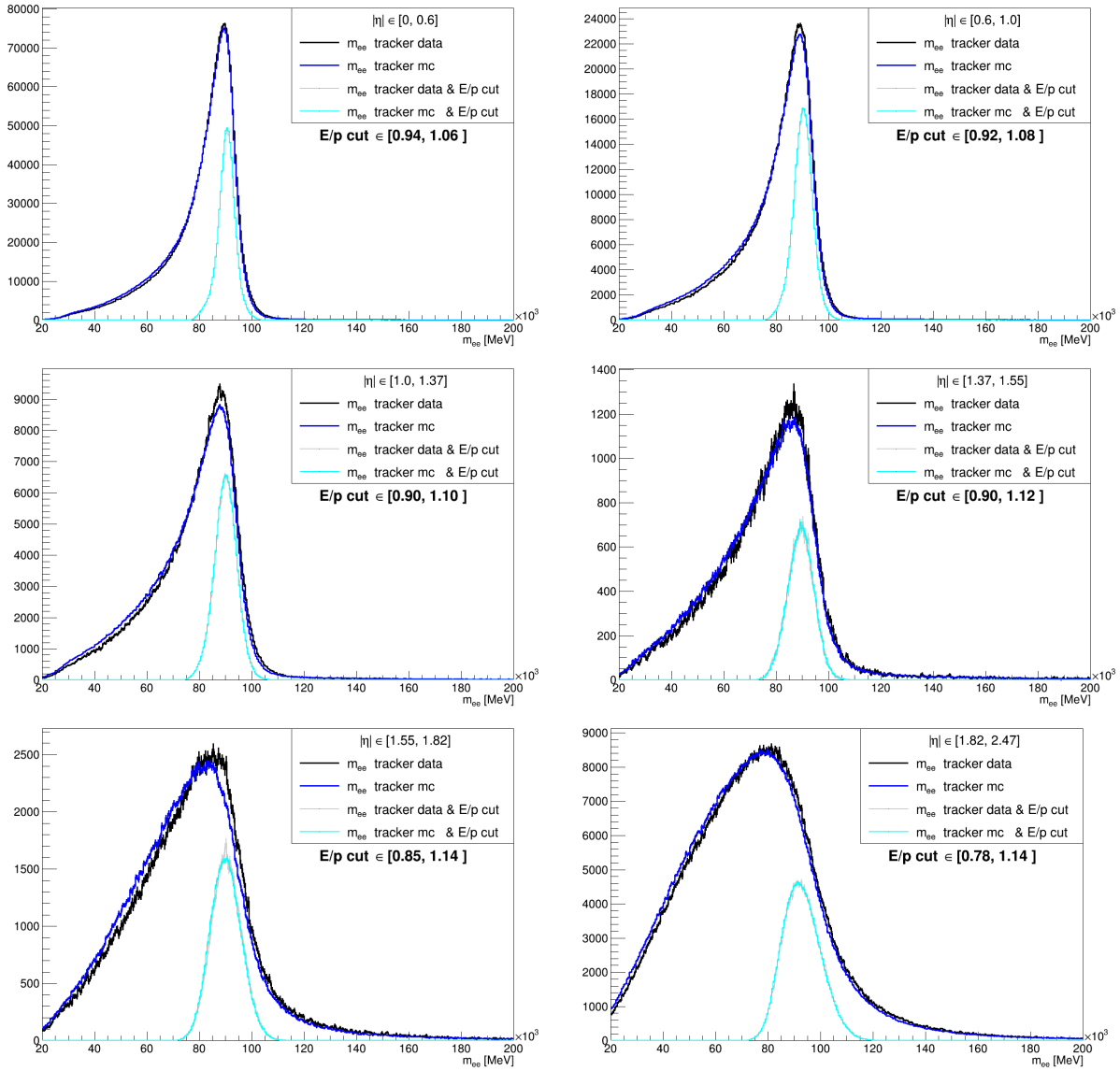

Figure 3.23: m_{ee} distributions from the tracker with and without cut on the leading electrons E_T/p_T. Source: [76].

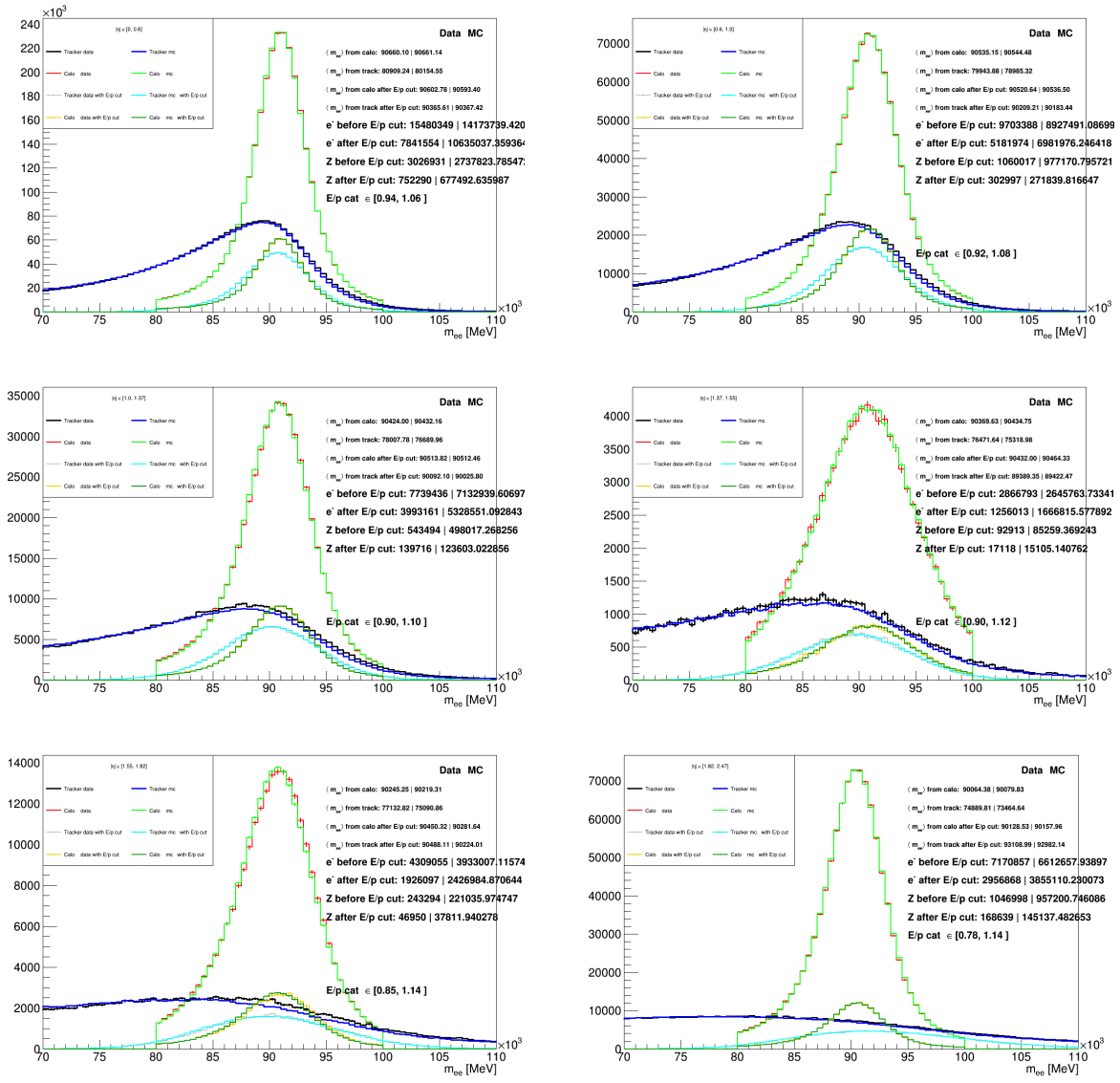

Figure 3.24: m_{ee} distributions from the calorimeter and tracker before and after cut on the leading electron E_T/p_T. Source: [76].

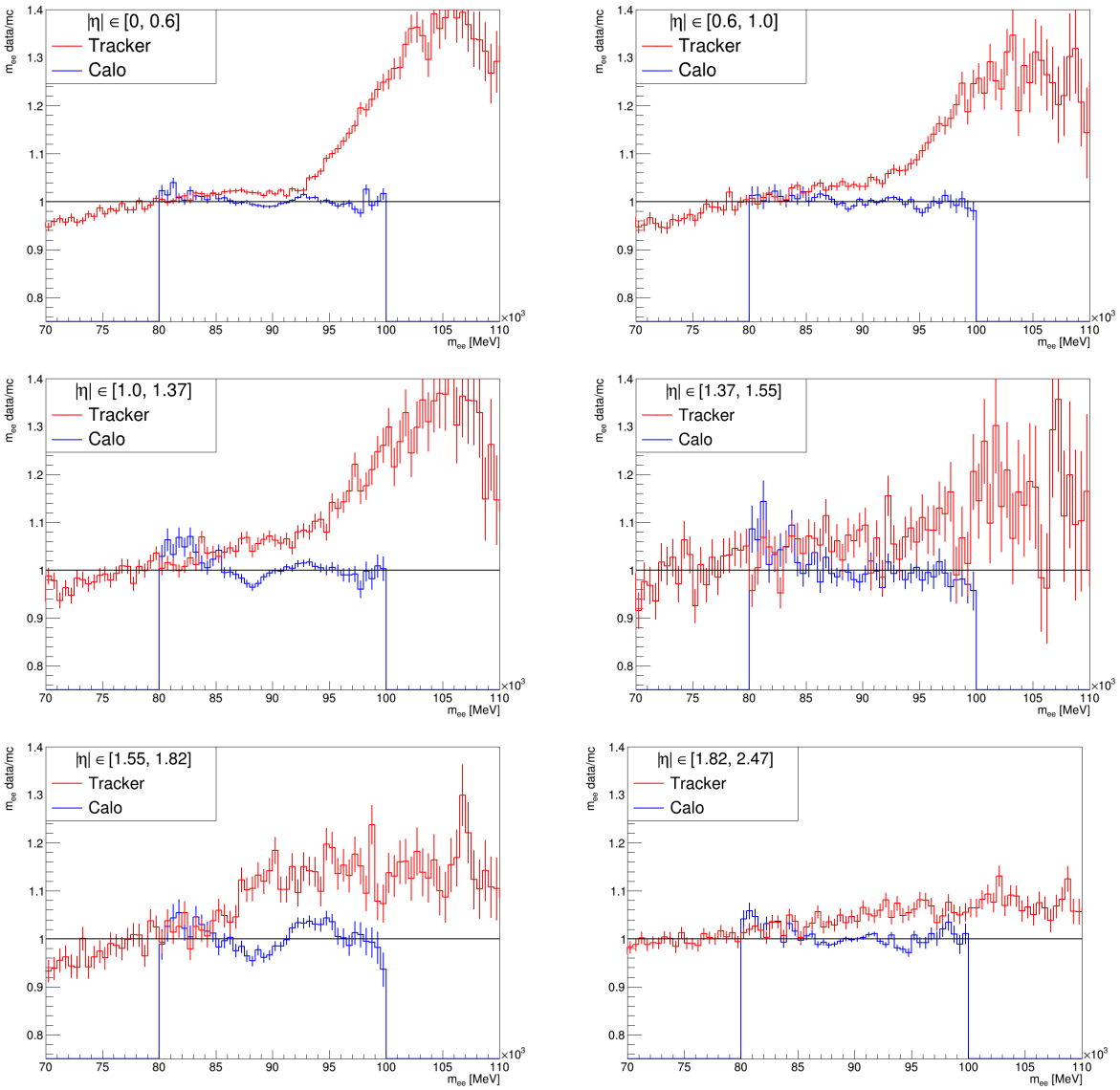

Figure 3.25: Ratios of m_{ee} distributions between data and MC obtained with calorimeter (blue) and tracker (red). The calorimeter distribution is cut on the Z-mass window. Source: [76].

3.6.4 Correlation between electrons

To check impact of treating the two electrons from Z-decay independently, the E_T/p_T shape for the sub-leading electron is compared between the two following configurations:

- Nominal (no additional cuts or selection);
- Sub-leading electron is kept only if the E_T/p_T ratio for the leading electron belongs to a certain range.

The similarity between the shapes (see Fig. 3.26) supports the hypothesis of no impact of treating the two electrons independently. Otherwise, it would not be possible to treat the electrons independently.

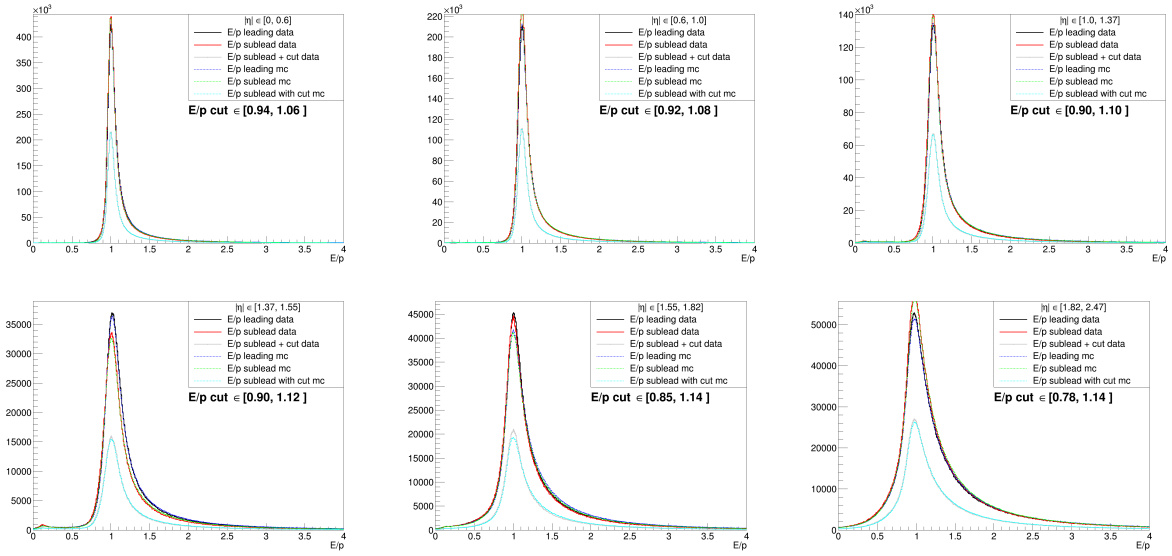

Figure 3.26: E_T/p_T distributions independently for leading (black for data and blue for MC) and sub-leading electrons: red for data and green for MC in a case of no cut. Grey and Cyan represent E_T/p_T distributions obtained for the sub-leading electron, when the leading one has E_T/p_T in a certain narrow range. Source: [76].

3.7 Results

The linearity measurements with the E_T/p_T method are shown in Fig. 3.27.

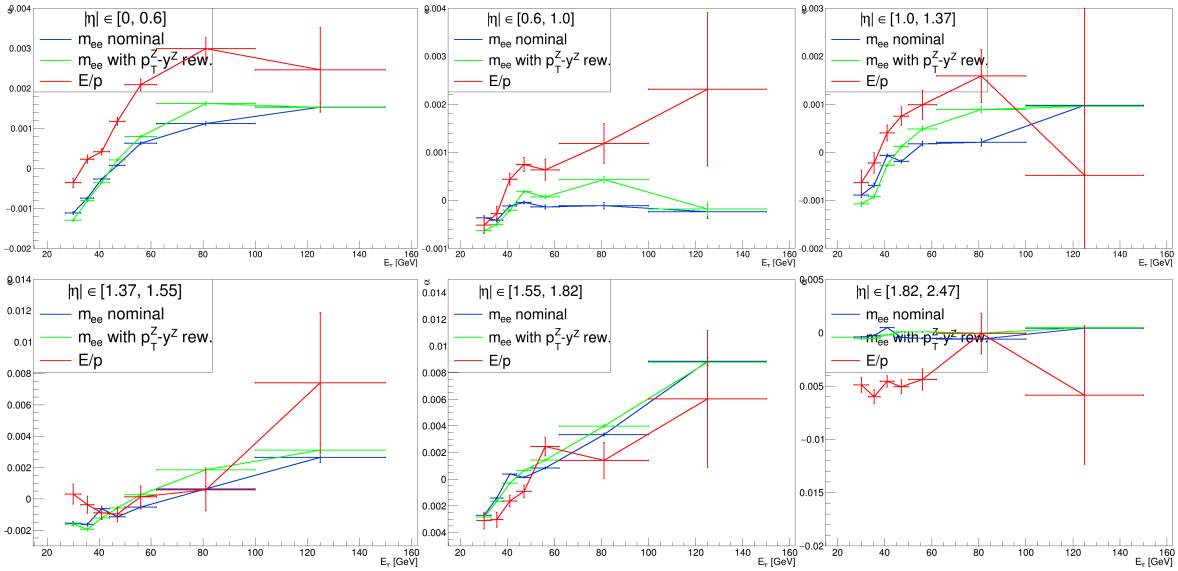

Figure 3.27: Linearity measurements results from E_T/p_T method (red) and nominal m_{ee} template method (blue and green, without and with $p_T^Z - y^Z$ reweighting, respectively). Source: [76].

There is a general agreement in trends between the linearities from the E_T/p_T and m_{ee} measurements. The methods get closer once the $p_T^Z - y^Z$ reweighting is applied (green curve). A global offset appears between the E_T/p_T and m_{ee} linearities, which might come from the tracker effect, to which the m_{ee} method is insensitive.

Alternative results with the Gaussian function are shown in Fig. 3.28, showing an excellent agreement with the nominal results obtained using the Crystal Ball function.

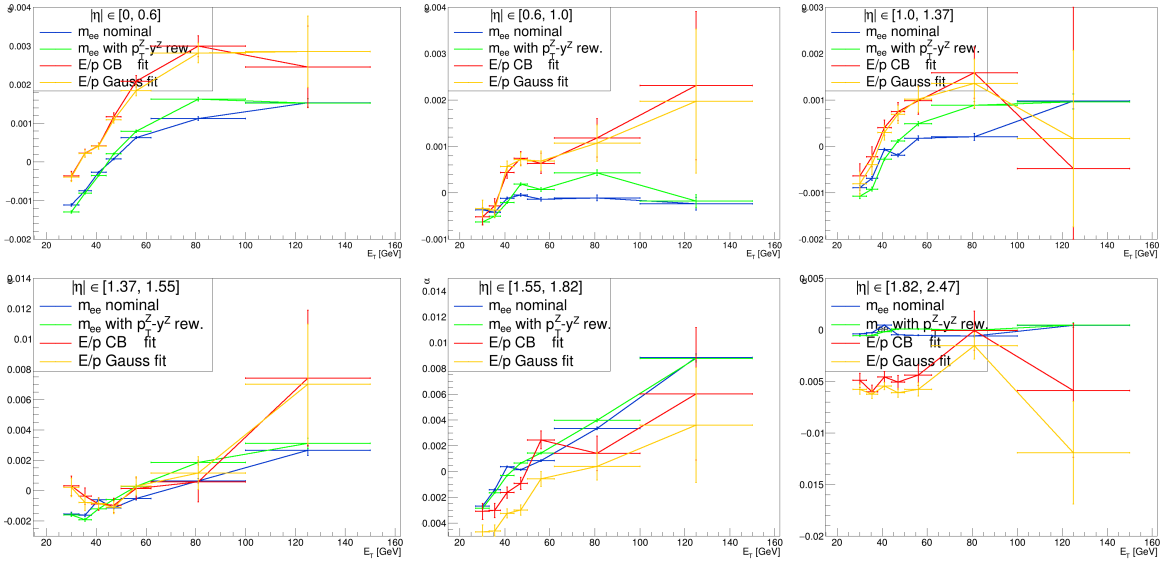

Figure 3.28: Linearity measurements from E_T/p_T method with CB fit (red), and Gaussian fit (orange) and nominal m_{ee} template method (blue and green - without and with $p_T^Z - y^Z$ reweighting, respectively). Source: [76].

3.7.1 Momentum correction

Since momentum from the tracker is biased, it is possible to correct it using dedicated corrections derived by the tracker working group. There are a few possible values for the scale correction to be applied:

- from the muon analyses ([80]):
  - A global 0.0007 bias;
  - η-dependent values, shown in Table. 3.3;
- from the ID (inner detector) alignment [77]:
  - A global 0.00087 bias (Fig. 3.29a);
  - η-dependent corrections, shown in Fig. 3.29b.

Region	$\Delta r_1^{\mathrm{ID}}(\times 10^{-3})$	Δr_2^{ID} [TeV^{-1}]	$s_1^{\mathrm{ID}}(\times 10^{-3})$
$\lvert\eta\rvert < 1.05$	$4.1^{+0.6}_{-0.9}$	$0.17^{+0.04}_{-0.03}$	$-0.6^{+0.1}_{-0.2}$
$1.05 \leq \lvert\eta\rvert < 2.0$	$5.5^{+2.5}_{-0.8}$	$0.34^{+0.07}_{-0.09}$	$-0.5^{+0.2}_{-0.5}$
$\lvert\eta\rvert \geqslant 2.0$	9^{+9}_{-2}	0.05 ± 0.01	$1.0^{+3.5}_{-1.6}$

Table 3.3: Parameters describing the scale bias derived from a muon analysis. The last column shows the η-dependent scale bias, which is a proxy for the correction we are interested in [80].

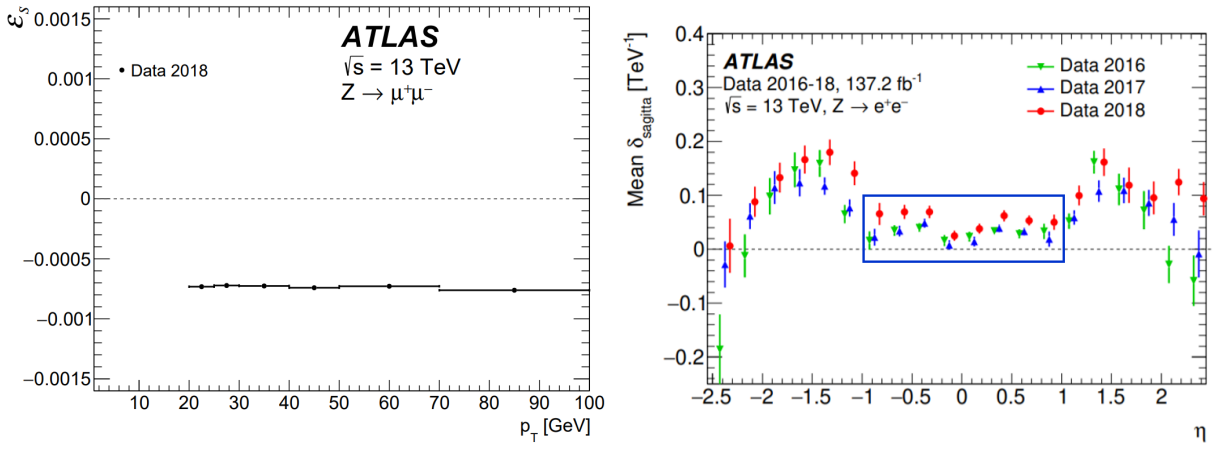

(a) (b)

Figure 3.29: Official length-scale bias estimations with E_T/p_T method for muons [77] as a function of p_T (a) and $|\eta|$ (b). Source: [76].

After applying the corresponding global correction, the resulting linearity dependencies are shown in Fig. 3.30.

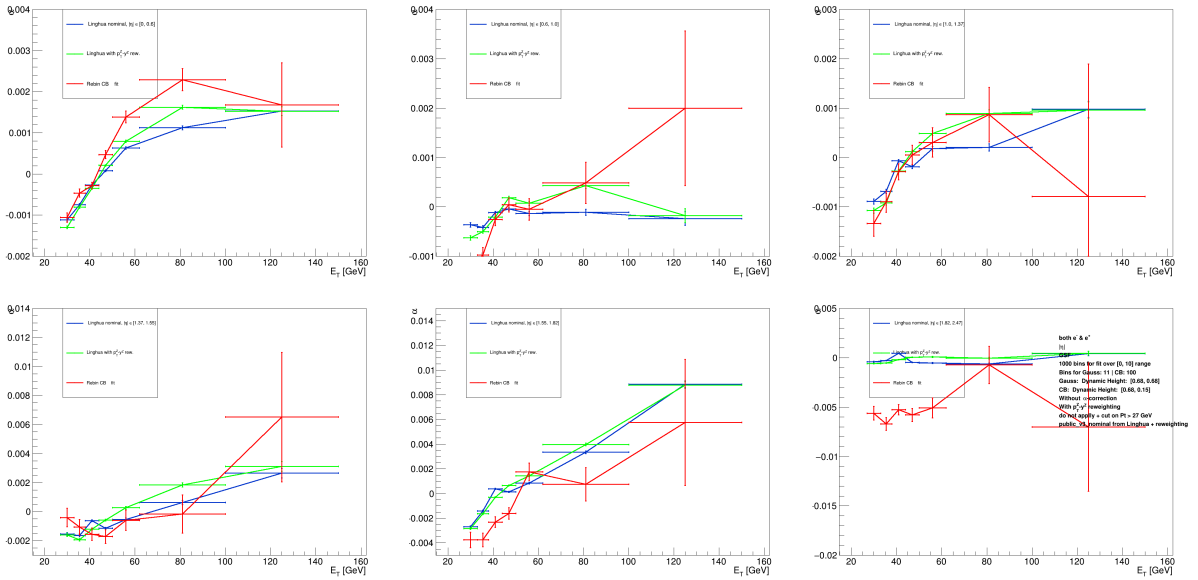

Figure 3.30: E_T/p_T linearity measurements after applying a global 0.0007 momentum correction. Source: [76].

3.7.2 Variation of the parameters

Consistency of the method has been investigated by varying various parameters both defining method properties, such as window choice, E_T/p_T binning, and applying or not applying some cuts:

- fBrem cut (not nominally applied) - cut on fBrem < 0.5
- Z-mass cut (is nominally applied) - cut on $m_{ee} \in [80, 100]$ GeV

No significant deviations in the E_T/p_T linearities have been observed after applying all such variations.

3.7.3 Validation of the method

In order to check the validity of the method and its reliability, a closure test has been conducted: the study was repeated over E_T/p_T distributions corrected with the values of linearity ($\alpha = f(E_T)$) found with raw distributions. In the ideal case, zero values of linearity would be found. Any deviation of the results from zero may serve as an estimate of the method uncertainty.

The linearity values before and after the closure test are shown in Fig. 3.31 and 3.32. The resulting linearities after performing the closure test for all of the detector regions, but the very forward, show almost zero values, confirming the method's stability and robustness. Only for the very forward region ($|\eta| \in [1.82, 2.47]$), linearities for high energy significantly differ from zero due to the instability of the method (for very low-stat regions) and miscalibration of the tracker.

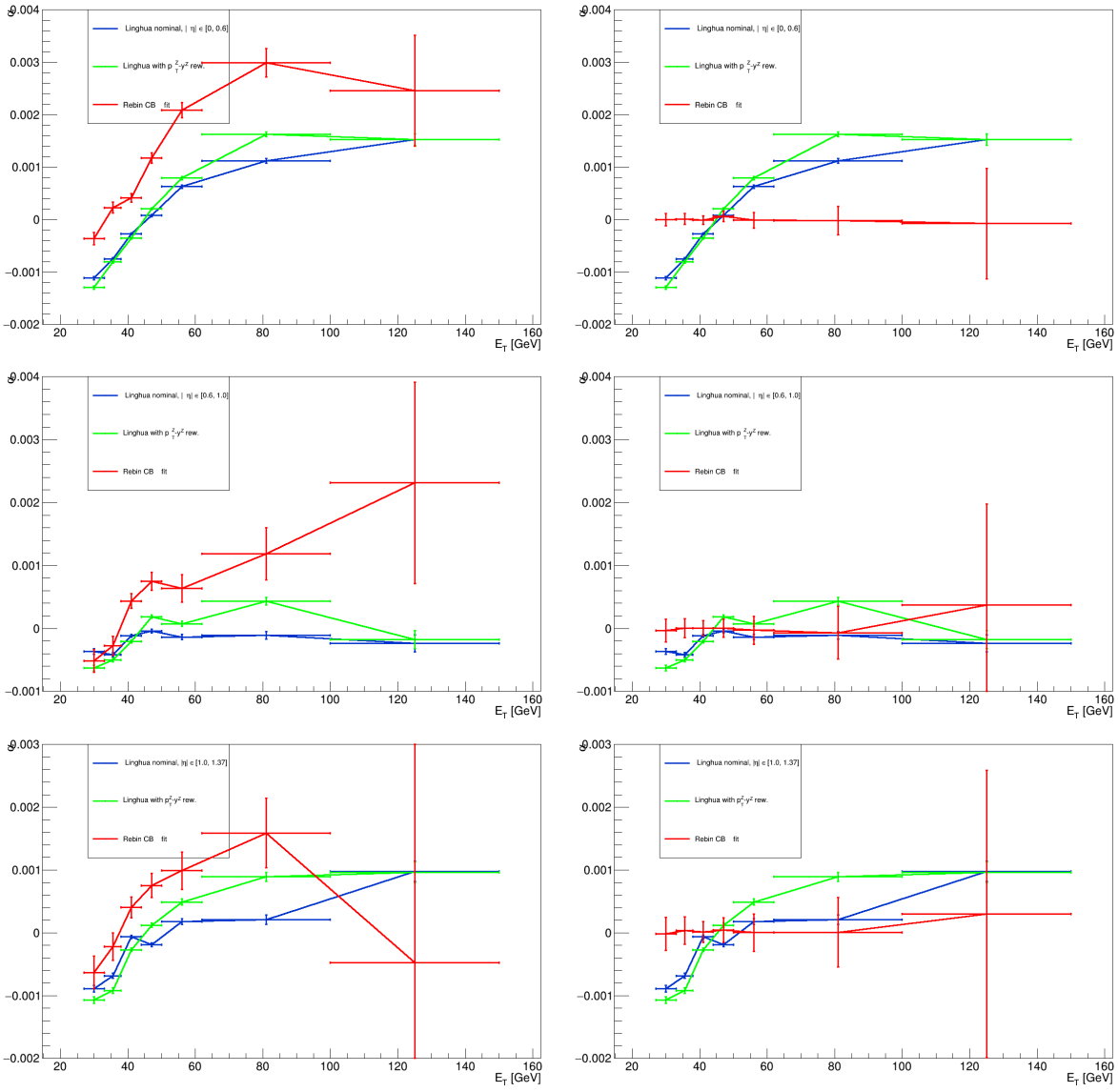

Figure 3.31: Linearity measurements for various $|\eta|$ regions before (left) and after applying the closure corrections (right). Red values stand to the ones found in this study with CB fit, green and blue represent m_{ee} linearity found in [71] with and without $p_T^Z - y^Z$ reweighting, respectively. The rows stand for various η regions: [0, 0.6], [0.6, 1.0] and [1.0, 1.37]. Source: [76].

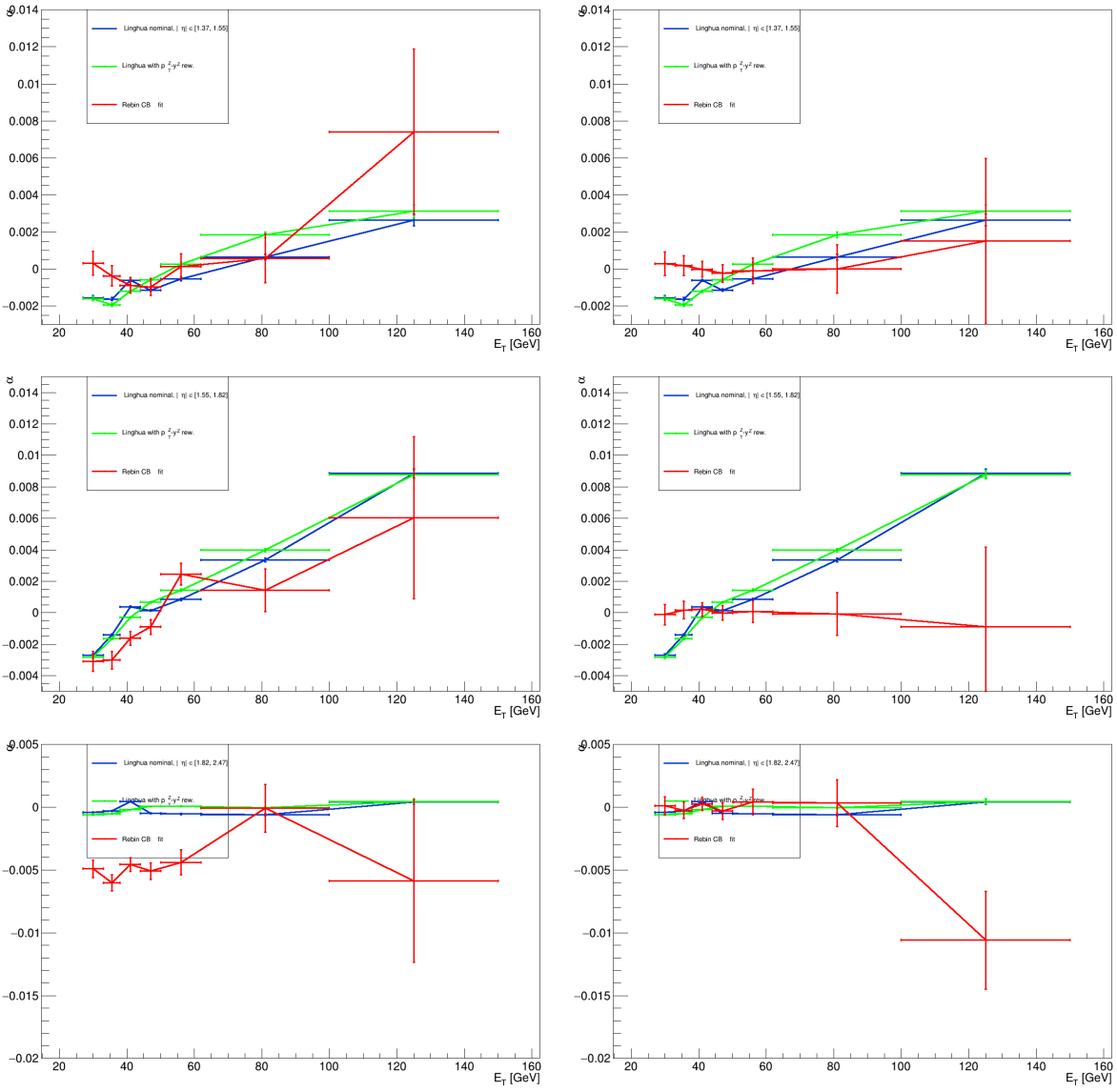

Figure 3.32: Linearity measurements for various $|\eta|$ regions before (left) and after applying the closure corrections (right). Red values stand to the ones found in this study with CB fit, green and blue represent m_{ee} linearity found in [71] with and without $p_T^Z - y^Z$ reweighting, respectively. The rows stand for various η regions: [1.37, 1.55], [1.55, 1.82] and [1.82, 2.47]. Source: [76].

3.8 Conclusion

The E_T/p_T method has been explored as an alternative to the classical template m_{ee} in-situ calibration method, relying not only on information from the calorimeter but also on the tracker to determine particles' momentum. The linearity results of the E_T/p_T method show the same tendency as the nominal ones, but often with an offset, which might be explained in the barrel by the tracker miscalibration (length-scale bias). Applying the $p_T^Z - y^Z$reweighting, allows getting closer results to the classical template method, that may be a hint for the usage of this reweighting. To compare performance of m_{ee} and E_T/p_T methods, a toy MC dataset was created with an injected value of α and both methods were used to estimate the bias. This is not documented in the thesis. Furthermore, with more statistics and a better-determined tracker calibration and bias, such a method could serve as a verification and cross-check of the m_{ee} template method, nominally used in Run 2 $e\gamma$ calibration.

4 - The $H \to \gamma\gamma$ coupling analysis with full Run 2 data

4.1 Introduction

The experimental signature of the $H \to \gamma\gamma$ signal is a narrow Gaussian-like peak with an approximate width of[1] 2 GeV emerging over a smoothly falling continuum background (Fig. 4.1), made of irreducible $\gamma\gamma$ and reducible γj and jj processes, where one or two jets are misidentified as photons. Impact of the signal-background interference is negligible in the coupling analysis.

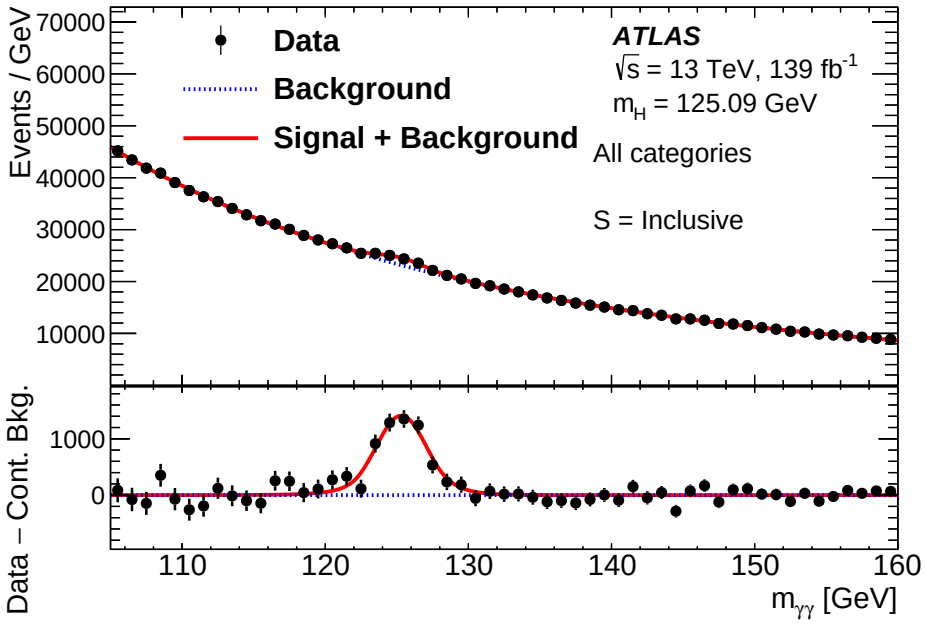

Figure 4.1: Diphoton invariant mass spectrum, inclusive over all the categories. Source: [39].

The full Run 2 $H \to \gamma\gamma$ coupling analysis at $\sqrt{s} = 13$ TeV exploits 139.0 fb^{-1} of pp collision data recorded by the ATLAS detector at the LHC. It supersedes the previous analyses made at the same energy [81] with 36 fb^{-1} (campaigns of 2015 + 2016) followed by the one with 80 fb^{-1} (2015-2017) [82], and the full Run 1 analysis at $\sqrt{s} = 7$ TeV and 8 TeV [83].

The objective of the analysis is to measure the Higgs boson couplings with various levels of granularity: starting from the inclusive measurement and separation of the dominant production modes, up to having fine granularity both in the production modes and detailed kinematic regions, defined by the multiplicity of jets, p_T of the Higgs, invariant masses of various combinations of final state particles, etc. This last scenario, so-called STXS (Section 4.2), presents the finest granularity of the phase space with the version STXS stage 1.2. Besides that,

[1] The intrinsic width of 4.07 MeV is negligible with respect to the resolution of the EM calorimeter.

the results are interpreted in the κ-framework and in the SMEFT (Standard-Model-Effective-Field-Theory) approach probing the Wilson coefficients. To prevent a consecutive description of the EFT interpretation (with the $H \to \gamma\gamma$ only and with the Higgs combination), this method and results are given only for the combined Higgs measurement and are described with more details.

The Higgs mass is fixed to 125.09 ± 0.24 GeV, corresponding to the results of the ATLAS and CMS combination of Run 1 data [84].

4.2 Simplified Template Cross-Sections (*STXS*)

The STXS framework measures production cross-sections in the fiducial regions of the phase space (Fig. 4.2, 4.3, 4.4) at the particle level (so-called *truth bins*) based on kinematic criteria as multiplicity of jets, invariant masses of di-jet or Higgs-and-jet systems and their transverse momentum. The final state of the Higgs boson decay is not considered for the classification of the STXS. All the production modes are treated independently, with different splits of the phase-space. Such an approach allows to establish a compromise between fiducial cross-sections with a dedicated decay channel, thus not combinable, and a measurement relative to a reference SM cross-section (signal strength), thus, with a higher theoretical systematic uncertainty. Also, the STXS separates out regions which are hard to predict (as for example, number of jets, N_{jets}).

The STXS is weakly dependent on the underlying model because they are restricted to the acceptance region of the detector, therefore requiring no extrapolation correction to the full phase space, which would rely on a specific theoretical model, in particular on the kinematic of the Higgs boson. Moreover, the STXS has been designed to allow model-independent interpretation of the results and simplify combinations between various analyses, targetting different final states with the same intermediate state. Results of STXS measurements can be used for constraining various BSM models and more generally be re-interpreted in an EFT theory.

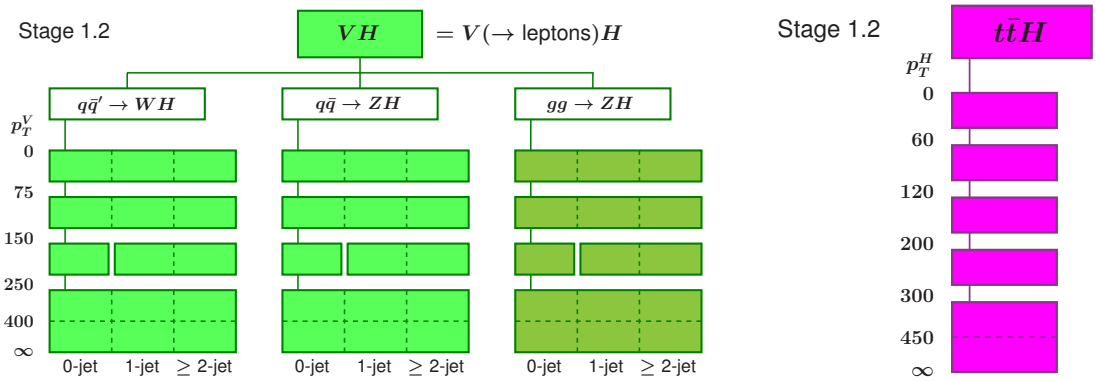

Figure 4.4: Discretisation of the phase-space in the stage 1.2 granularity of the STXS framework for the VH and $t\bar{t}H$ production modes. Source: [39].

Following the STXS 1.2 prescription, only the events with the Higgs boson rapidity $|y| < 2.5$ are considered. This restriction comes from the acceptance of the precision region of ATLAS and CMS detectors. With respect to the original optimistic granularity, for definition of stage 1.2

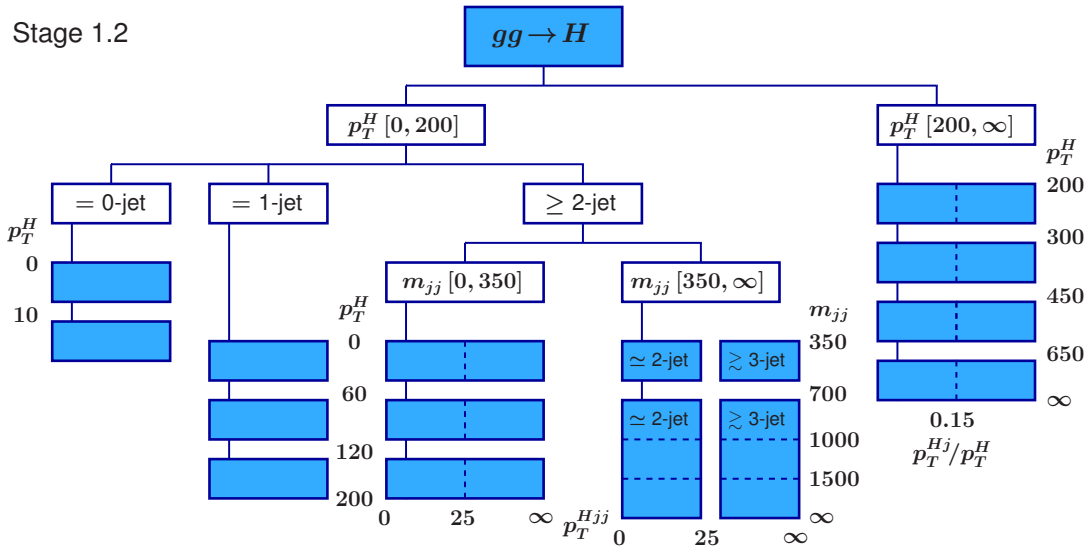

Figure 4.2: Discretisation of the phase-space in the stage 1.2 granularity of the STXS framework for the ggH production mode. Source: [39].

truth bins, a few modifications have been adopted due to the limited sensitivity of the analysis for some kinematic variables:

- the ggH and $qq \to Hqq$ processes are not split by p_T^{Hjj} due to the lack of sensitivity of the analysis. An additional split on m_{jj} variable is introduced.
- The $p_T^H > 200$ GeV region of the electroweak $qq \to Hqq$ process is split into three regions in m_{jj}: $[350, 700]$, $[700, 1000]$ and $[1000, \infty]$ GeV. As compared to the original STXS phase space, the edge of 1500 GeV is removed. Measurements for these regions are not done due to limited analysis sensitivity of the $H \to \gamma\gamma$ channel, but the splitting is included in combination with other channels.
- the VH leptonic is not split by the number of jets.

The analysis targets 28 truth-bins (Fig. 4.5), simultaneously measured in 101 reconstructed categories.

WH-ZH ambiguity

The WH and ZH production modes can easily be misidentified during the reconstruction: if one of the leptons from the Z-boson decay is missed, then the corresponding event is classified as coming from the WH production mode. This ambiguity leads to a strong anti-correlation between the WH and ZH signal strength (see Fig. 4.30).

All events are categorised into a set of orthogonal categories defined to target specific STXS truth bin to increase the measurement sensitivity[2] (Section 4.6). A simultaneous signal plus background fit over all categories is then performed to extract the STXS cross-sections.

[2]Measurement sensitivity can be viewed as signal over background ratio, S/B.

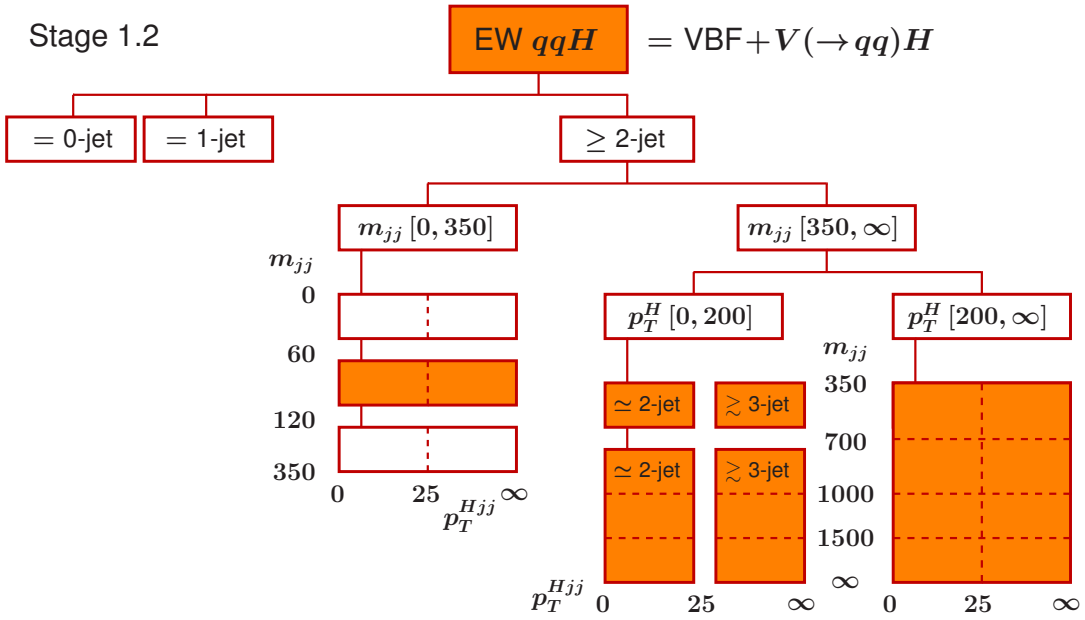

Figure 4.3: Discretisation of the phase-space in the stage 1.2 granularity of the STXS framework for the VBF production mode. Source: [39].

4.3 Datasets

The full Run 2 dataset after all the quality requirements [85], ensuring that the detector sub-components were working in good conditions, corresponds to the integrated luminosity of $139.0 \pm 2.4 fb^{-1}$ [47, 86]. The mean number of interactions per bunch crossing is $\langle \mu \rangle = 33.7$.

Table 4.1 presents an overview of generators for various signal and background processes. The signal Higgs samples are generated under assumption of Higgs boson mass 125 GeV and are shifted in the analysis to have a mass of 125.09 GeV. The intrinsic width in the simulation is set to 4.07 MeV [87]. Most of these signal processes are generated with Powheg Box v2 [88, 89, 90, 91]. The $tHqb$ and tHW processes are generated with MadGraph5_aMC@NLO 2.6 [92] in the 4-(5-) flavour scheme. The parton showering, hadronisation and effect of underlying event are modelled with Pythia8.2 [93, 94]. For the decays of the bottom and charm quarks, EvtGen 1.6.0 [95] is used. The PDF4LHC [96] parton distribution functions are used. The $\gamma\gamma$ and $V\gamma\gamma$ background samples are produced with Sherpa 2.2.4 [97]. The production of $t\bar{t}\gamma\gamma$ events is done with MadGraph5_aMC@NLO 2.3.3 using the NNPDF2.3LO PDF [98].

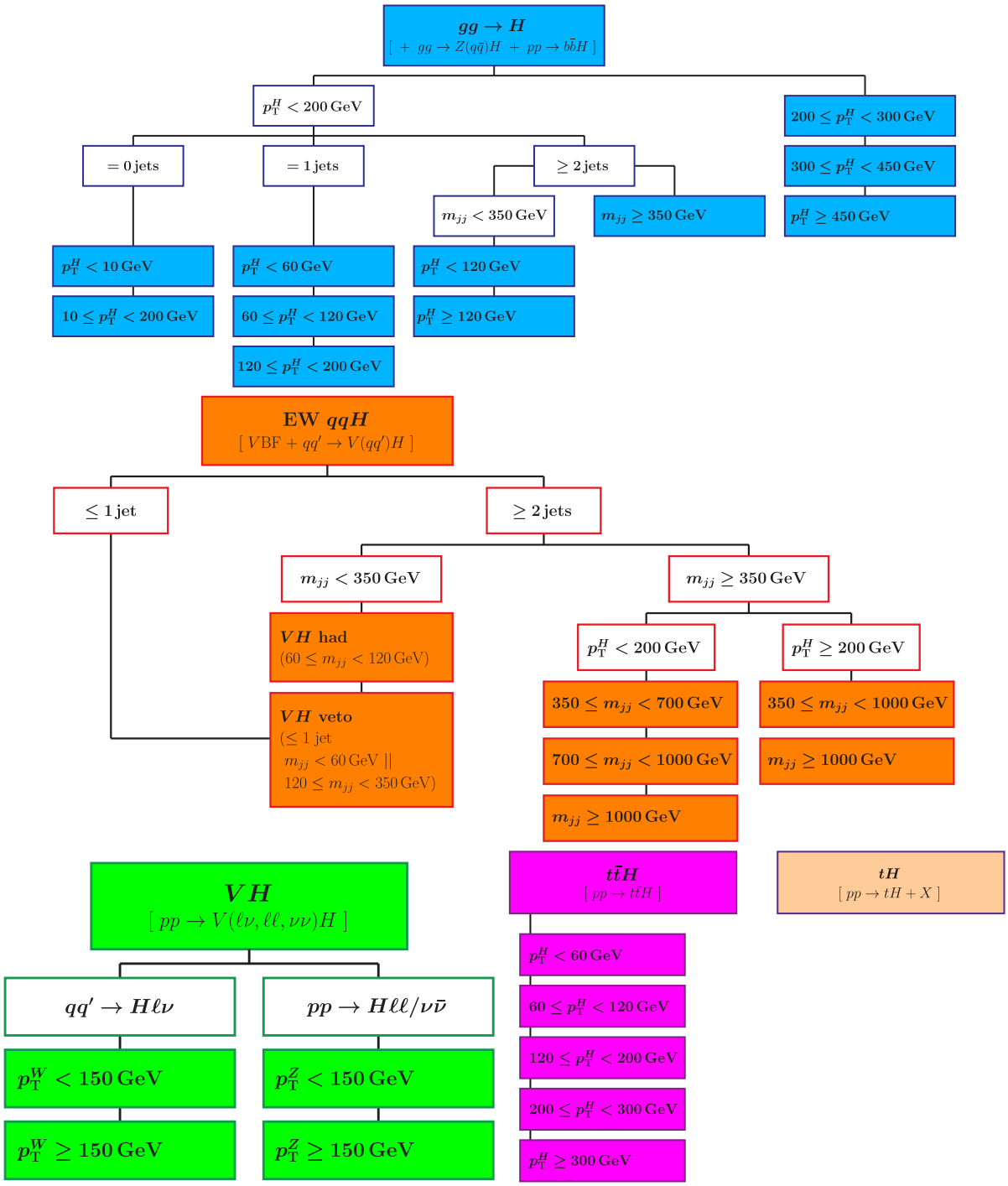

Figure 4.5: Definition of the 28 truth-bins used in the analysis. Source: [39].

The composition in the truth-bins of the simulated signal production modes is given in Fig. 4.6.

Process	Generator	Showering	PDF set	σ [pb] $\sqrt{s} = 13$ TeV	Order of σ calculation
ggF	NNLOPS	Pythia 8.2	PDF4LHC[15]	48.5	N^{3}LO(QCD)+NLO(EW)
VBF	Powheg Box	Pythia 8.2	PDF4LHC[15]	3.78	approximate-NNLO(QCD)+NLO(EW)
WH	Powheg Box	Pythia 8.2	PDF4LHC[15]	1.37	NNLO(QCD)+NLO(EW)
$q\bar{q} \to ZH$	Powheg Box	Pythia 8.2	PDF4LHC[15]	0.76	NNLO(QCD)+NLO(EW)
$gg \to ZH$	Powheg Box	Pythia 8.2	PDF4LHC[15]	0.12	NLO(QCD)
$t\bar{t}H$	Powheg Box	Pythia 8.2	PDF4LHC[15]	0.51	NLO(QCD)+NLO(EW)
$b\bar{b}H$	Powheg Box	Pythia 8.2	PDF4LHC[15]	0.49	NNLO(QCD)
$tHqb$	MadGraph5_aMC@NLO	Pythia 8.2	NNPDF3.0NNLO	0.074	NLO(QCD)
tHW	MadGraph5_aMC@NLO	Pythia 8.2	NNPDF3.0NNLO	0.015	NLO(QCD)
$\gamma\gamma$	Sherpa	Sherpa	NNPDF3.0NNLO		
$V\gamma\gamma$	Sherpa	Sherpa	NNPDF3.0NNLO		
$t\bar{t}\gamma\gamma$	MadGraph5_aMC@NLO	Pythia 8	NNPDF2.3nlo		

Table 4.1: Summary of configurations used for event generation of various Higgs production modes processes. The Higgs boson mass used is 125 GeV. The cross-sections for the background processes are omitted, since their normalisation is directly obtained from a fit to data. Source: [99].

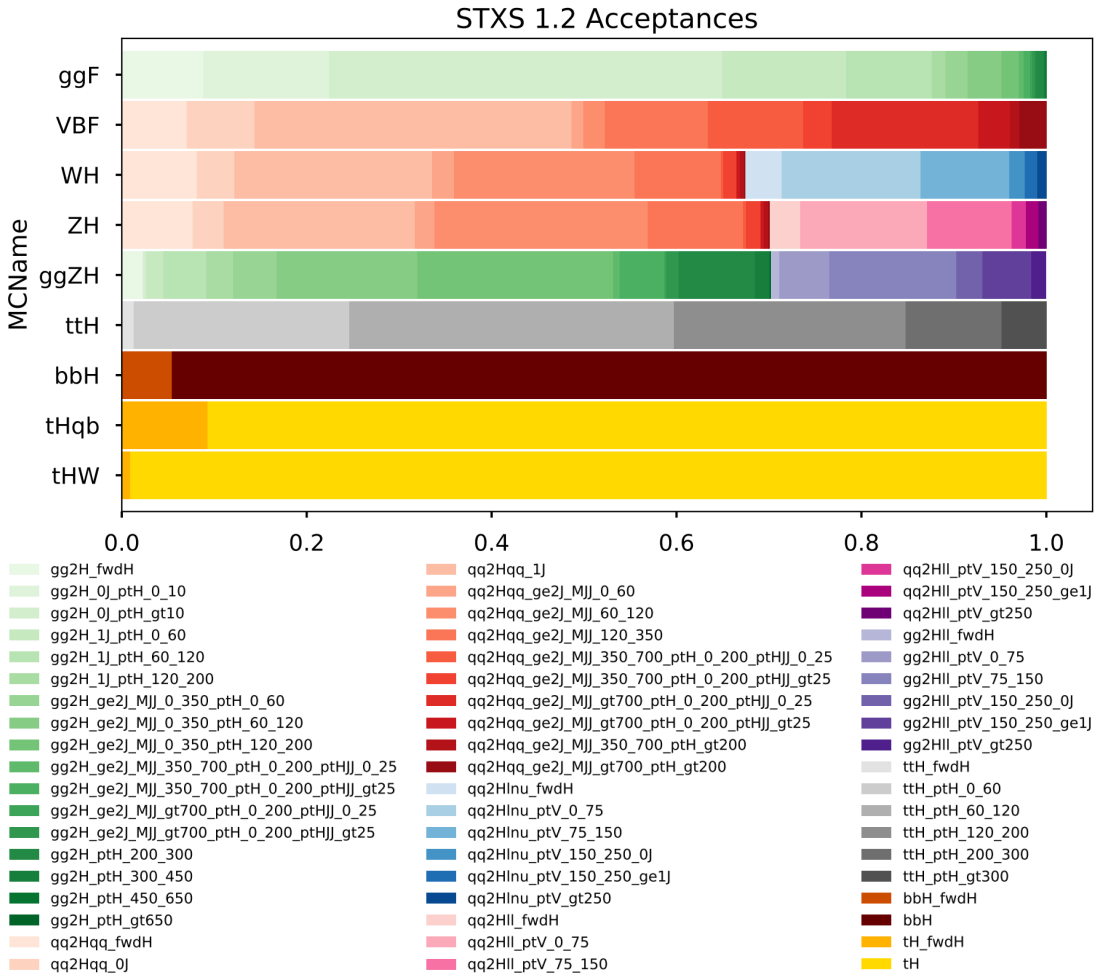

Figure 4.6: Composition of various MC production modes by the STXS stage 1.2 truth bins. Source: [99].

4.4 Selection

Most particles of the Standard Model are used in the selection, in order to select the primary objects (photons) of the $H \to \gamma\gamma$ channel and struggle against the irreducible and reducible background, as well as to select the secondary objects (electrons, muons, jets, MET) that appear in various topologies of the production modes. A categorisation (Section 4.6) is developed in order to optimise the sensitivity to the various truth bins.

4.4.1 Photons

Photons are reconstructed using a dynamic cluster in the EM calorimeter [100]. Each photon candidate is classified either as converted or unconverted. The converted status is positive if a photon has converted into an electron-positron pair by interacting with the material of the detector. Such a situation corresponds to the presence of two tracks forming a conversion vertex or of an electron signature with no hits in the ID. Otherwise, the photon candidate is labelled as unconverted. In the case of the presence of conversion vertices, the clusters should be associated with the tracks reconstructed in the ID. The so-called bad-quality photon candidates, affected by either dead or masked cells in the calorimeter are not considered in the analysis. An identification of the photon is made from shower shape variables (Table 4.2, Fig. 4.7, Fig. 4.8) in order to struggle against fake photons (mainly π^0).

Description of the shower shape variables is given in Table 4.2.

Category	Description	Variable	loose	tight
Acceptance	$\lvert\eta\rvert < 1.37 \cup 1.52 < \lvert\eta\rvert < 2.37$		+	+
Hadronic leakage	* Ratio of E_{T} in the first layer of the hadronic calorimeter to E_{T} of the EM cluster (used over the range $\lvert\eta\rvert < 0.8$ and $\lvert\eta\rvert > 1.37$)	$R_{\text{had l}}$	+	+
	* Ratio of E_{T} in the hadronic calorimeter to E_{T} of the EM cluster (used over the range $0.8 < \lvert\eta\rvert < 1.37$)	R_{had}	+	+
EM Middle layer	* Ratio of $3 \times 7\eta \times \phi$ to 7×7 cell energies	R_{η}	+	+
	* Lateral width of the shower	$w_{\eta 2}$	+	+
	* Ratio of $3 \times 3\eta \times \phi$ to 7×7 cell energies	R_{ϕ}	+	+
EM Strip layer	* Lateral shower width calculated from three strips around the strip with highest energy deposit	w_{s3}		+
	* Total lateral shower width	$w_{\text{tot } s_1}$		
	* Energy outside the core of 3 central strips but within 7 strips divided by energy within 3 central strips	F_{side}		+
	* Difference between the energy associated with the second maximum in the strip layer and the energy energy reconstructed in the strip with minimum value found between the first and second maxima	ΔE		+
	* Ratio of energy difference associated with the largest and second largest energy deposits to the sum of these energies	E_{ratio}		+

Table 4.2: Shower shape variables used for photon identification. Symbol: "*" marks whether a variable is used for the loose and selection. Source: [101].

Identification efficiency ranges from around 84% to 94% (85% to 98%) for the unconverted (converted) photon. A relaxed so-called loose identification is used first in order to preselect the photons. The candidates are required to pass kinematic cuts: $p_T > 25$ GeV (pre-selection

for a loose photon) and $|\eta| < 2.37$, excluding the transition region (also called crack region): $|\eta| \in [1.37, 1.52]$, where the excluded η region allows to focus to good quality photons in a finely-segmented region of the EM calorimeter.

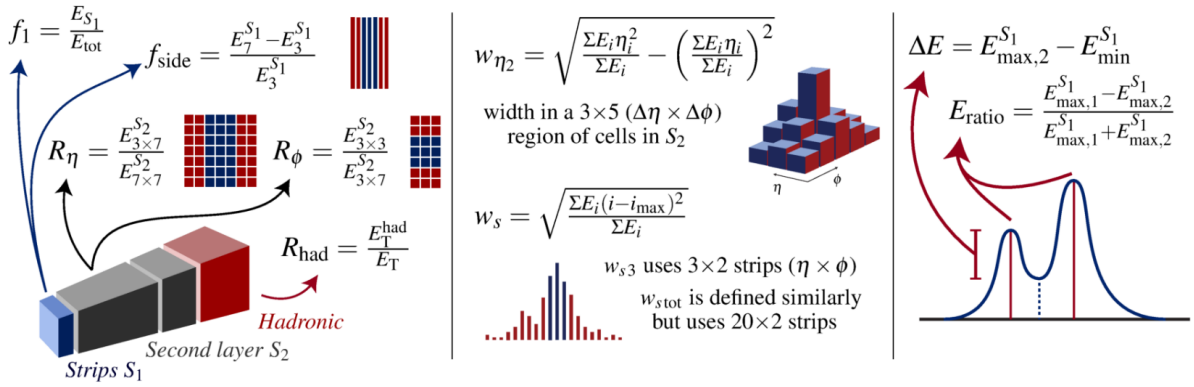

Figure 4.7: Illustration of the shower shape variables definition and their meaning. Source: [101].

.

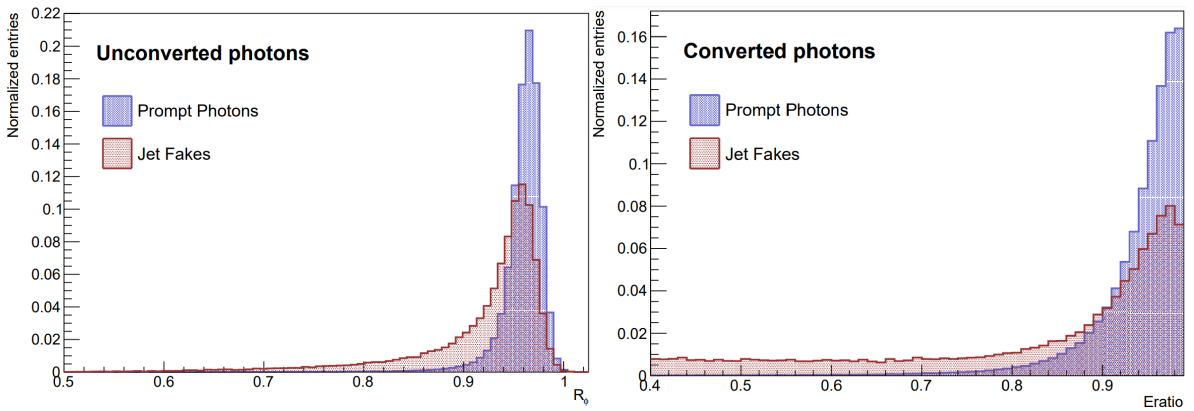

(a) R_ϕ (b) E_{ratio}

Figure 4.8: Example of the shower shape variables (a) R_ϕ for unconverted photons and (b) E_{ratio} for converted photons. Source: [101].

Even though the photon identification has reduced the contamination from misidentified particles (neutral mesons, dominantly π^0 in jets, that subsequently decay to photons), a further reduction is made by requiring an isolation of the photons. Two types of isolation are made: one exploiting the calorimeter and one exploiting the track.

The calorimeter isolation (Fig. 4.9) represents the amount of energy deposit of the shower induced by a photon (can also be used for electrons, etc.) in the cluster outside of the main window where the photon (this is true also for electron selection) deposits most of his energy.

A cut on this allows to suppress further the fake photons which have a wider shower extension, thus leaving some energy outside the window. The window is built around the

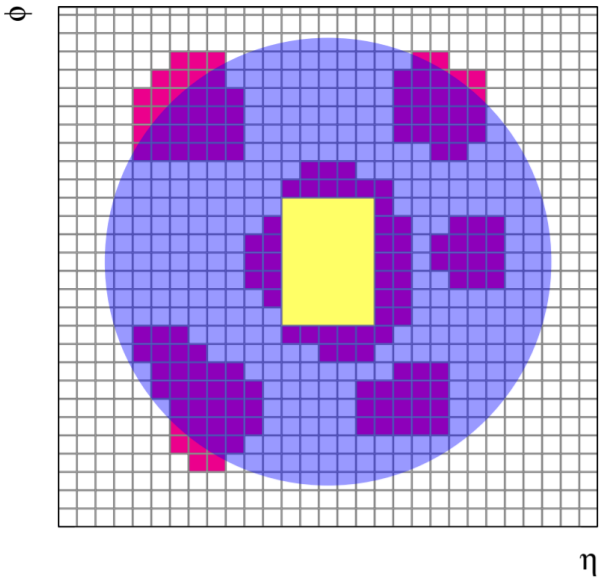

Figure 4.9: Schematic of the calorimeter isolation. The grid represents the cells of the second layer of the calorimeter in $\eta \times \phi$ directions. The prompt photon candidate mostly deposits energy in the centre of the rectangle window (yellow). The blue cone represents the isolation cone. All topological clusters (red), for which the barycentres fall within the isolation cone are included in the computation of the isolation variable. The energy deposited in the $\Delta\eta \times \Delta\phi = 0.125 \times 0.175$ window of the 5 × 7 cells (yellow) is substracted in the computation. Source: [74].

barycentre of the electron energy cluster and has a size of $\Delta\eta \times \Delta\phi = 5 \times 7$ cells in the second layer of the EM calorimeter. The calorimeter isolation variable is obtained by summing the transverse energy deposit in a cone of angular dimension $R = \sqrt{\Delta(\eta)^2 + \Delta(\phi)^2} = 0.2$, neglecting the window surrounding the photon. The cut on the calorimeter isolation variable is $E_T^{iso} < 0.065 \times E_T$.

A track isolation variable, p_T^{iso}, defined as a scalar sum of all momentum of tracks with $p_T > 1$ GeV not associated with a photon conversion in a cone of $\Delta R < 0.2$ surrounding the photon cluster, is computed. Photons are required to satisfy: $p_T^{iso} < 0.05 \times E_T$.

4.4.2 Electrons

Since electrons and photons have similar energy deposit signature in the calorimeter, their shower shape variables are rather similar. In the central region of the detector, the e/γ misidentification is at the level of 2%, increasing up to 7 % in the end-cap and decreasing with energy.

Electrons are also reconstructed with dynamic, variable-size energy clusters in the EM calorimeter [74, 75] and are not taken into account, if they are affected by dead or masked cells in the calorimeter or if they have $p_T < 10$ GeV. Also, the transition region of $|\eta| \in [1.37, 1.52]$ is vetoed. An illustration of electron pass through the detector system is given in Fig. 4.10.

Electrons are identified with a likelihood based identification [74], using information both from the tracker and calorimeter. Medium working point is chosen for electron candidates [73],

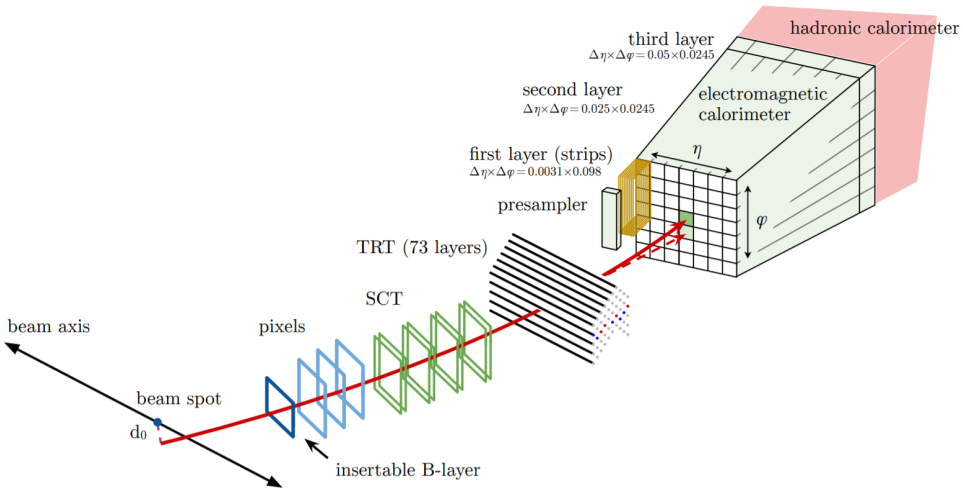

Figure 4.10: Illustration of the path of an electron through the various sub-detectors. The red trajectory shows the hypothetical path of an electron. The dashed one indicates the path of a photon produced by the interaction of the electron with the material in the tracking system. Source: [74].

which has around 88% efficiency for identifying a prompt electron with $E_T = 40\ GeV$.

Electrons are required to have $p_T > 10$ GeV. Moreover, an electrons's track must be related to the vertex association, by the following set of conditions: $|d_0/\sigma(d_0)| < 5$ (transverse impact parameter) and $|z_0 \sin(\theta)| < 0.5\ mm$ (longitudinal impact parameter). Analysis selection further requires electrons to satisfy a condition on the isolation variables:

$$\begin{aligned} E_T^{iso}|_{\Delta R<0.2} &< 0.2 \cdot p_T \\ p_T^{iso}|_{\Delta R<0.2} &< 0.15 \cdot p_T \end{aligned} \tag{4.1}$$

4.4.3 Muons

Muon candidates are reconstructed using tracks from the ID and the muon spectrometer [102] (Section 2.2.6). Kinematic cut requires muons to obey the following criteria: $p_T > 10$ GeV, $|\eta| < 2.7$. The impact parameters are required to be: $|d_0/\sigma(d_0)| < 3$ and $|z_0 \sin(\theta)| < 0.5\ mm$ for the transverse and longitudinal, respectively. Further selections are applied to eliminate muon candidates coming either from kaons and pions or charged hadrons, responsible for the most significant contamination. The latest ones are characterised by the presence of a distinct kink in the radiation of muons, therefore declining muons trajectory in the MS from the original one in the ID. A few quantities are computed, characterising the difference between trajectories in these two detectors, therefore identifying a muon candidate:

- q/p significance: charge-to-momentum ratio, divided by its error.
- ρ': the absolute difference between momenta normalised on the value obtained from the combined track.
- normalised χ^2 of a combined track fit.

After passing the medium working point selection, a muon candidate undergoes a set of dedicated corrections, including the sagitta-bias correction. Finally, muons are required to fulfil

calorimeter- and track-based isolation requirements, which are 95-97% efficient for muons with $p_T \in [10, 60]\ GeV$ and are 99% efficient for higher p_T.

4.4.4 Jets and b-tagging

Jets are reconstructed using the anti-kt [103] algorithm with $R = 0.4$ parameter. It consists of a recursive grouping of the energy deposits of protojets[3] with other ones, according to the definition of a distance that promotes high p_T deposits:

$$d_{ij} = \min(\frac{1}{p_{T,i}^2}, \frac{1}{p_{T,j}^2}) \times \frac{\Delta_{ij}^2}{R^2} \tag{4.2}$$

where p_{Ti} and p_{Tj} are the transverse momentum deposits of the protojets, $\Delta_{ij}^2 = (y_i - y_j)^2 + (\phi_i - \phi_j)^2$ is geometrical distance information. The algorithm is the following:

- For each protojet i, compute $d_i \equiv p_T^{-2}$
- For each pair of protojets i and j, compute d_{ij} defined by the eq. (4.2).
- Among all d_i and d_{ij} find the smallest: d_{min}:
  - if d_{min} is a d_i, then this object can no more be merged. This object is labelled as jet and is removed from the list of remnant protojets.
  - otherwise, if d_{min} is a d_{ij}, then the protojets i and j are merged together to form a new single protojet (and their 4-momentums are summed).

Preselected jets must satisfy the following criterium: $p_T^{jet} > 25\ GeV$ and $|y^{jet}| < 4.4$. Candidates overlapping with photons (electrons) with $\Delta R = 0.4\ (0.2)$ are removed.

B-mesons have a unique signature in the detector system due to their long life-time ($\approx 1.5\ ps$), corresponding to $\approx 450 \times \gamma\ \mu m$ displaced vertex, thus having large impact parameters. Reconstruction of the corresponding b-quarks (b-tagging) is done via a procedure, involving use of Recurrent Neural Network (RNN) [104] as one of the variables. This RNN combines information from trajectories of particles, identified in the ID. Identification efficiency is increased by enhancing presence of muons in the semi-leptonic decays of b-hadrons.

4.4.5 Tau-leptons

The dominant part of the tau-leptons decays hadronically (65% branching ratio) and their reconstruction [105] follows the one of jets: tau-candidates are seeded by jets. Minimal selection requires $p_T > 5$ GeV and $|\eta| < 2.5$. Tracks are associated with the tau-candidates if they are in a cone of $\Delta R < 0.25$ around the direction and have $p_T > 1$ GeV. Furthermore, the track is required to satisfy the following geometrical conditions: $|d_0| < 1.0$ mm longitudinally and $|z_0 \sin\theta| < 1.5$ mm. For the leptonic channels, the corresponding lepton reconstruction is used.

4.4.6 Top reconstruction

Reconstruction of the top quarks is a challenging task due to the complex experimental signature of its decay. Moreover, being unstable, it decays before hadronisation. The main

[3] Protojet is an object at a given step. At the beginning, it is a topocluster.

decays are:

$$\begin{aligned} t &\to b^+W^- \to bq\bar{q} \\ \bar{t} &\to b^-W^+ \to \bar{b}q\bar{q} \\ t &\to b^+W^- \to b\ell\bar{\nu}_\ell \\ \bar{t} &\to b^-W^+ \to \bar{b}\bar{\ell}\nu_\ell, \end{aligned} \tag{4.3}$$

leading to the creation of up to six jets in $t\bar{t}$ production (in the hadronic final states of $W^\pm$, which have the branching fraction of 67% [48]). A reasonable assumption is that each quark produces only one jet in the final state. Therefore, the individual hadronic top-quark can be reconstructed from the three leading jets. In this way, the selection requires the presence of at least three jets, with one being b-tagged. For the leptonic decays, the presence of at least one b-jet and at least one lepton are required. Due to missing energy, the 4-momentum of the W-boson is derived using the constrain:

$$m_W^2 = \left[E_\ell + \sqrt{p_{\nu,x}^2 + p_{\nu,y}^2 + p_{\nu,z}^2}\right]^2 - \left[\vec{p}_l + \{p_{\nu,x}, p_{\nu,y}, p_{\nu,z}\}\right]^2 \tag{4.4}$$

Among the two solutions of this equation, the one giving the smallest absolute value for $p_{\nu,z}$ is chosen. If none of the solutions is real, then the $m_T = m_W$ constraint is applied, where the m_T is the total transverse mass, defined as: $m_T = E^2 - p_Z^2$.

4.4.7 E_T^{miss}

The missing transverse energy E_T^{miss} [106] is defined as a negative sum of transverse momentum, p_T, over all selected particles in the reaction (photons, electrons, muons and jets) and over all low-p_T particles, which tracks are associated to the initial diphoton vertex, but not assigned to any of the previously selected objects:

$$\vec{E}_T^{miss} = -\sum_{\text{obj}} \vec{p}_T \mid \text{obj} \in \mu, e, \gamma, \text{ hadronic } \tau, \text{ jets, soft-term} \tag{4.5}$$

where the soft-term is reconstructed from detector signals not associated with any hard object passing the selection cuts[107].

Often, one also uses a hard-object equivalent H_T, which is defined in a similar way, but only from the reconstructed hard-objects:

$$\vec{H}_T = -\sum_{\text{obj}} \vec{p}_T \mid \text{obj} \in \mu, e, \gamma, \tau, \text{ jets} \tag{4.6}$$

Another quantity is the E_T^{miss} significance:

$$E_T^{miss} \text{ significance } = \frac{E_T^{miss}}{\sqrt{H_T}} \tag{4.7}$$

4.4.8 Inclusive selection for the diphoton system

The selection requires presence of at least one vertex with at least two tracks. The primary vertex is chosen by a neural network, exploiting multiple variables (sum of p_T^2, etc.). The Higgs boson candidate is reconstructed from the two highest p_T tight and isolated photons.

To increase precision on the reconstructed vertex position (thus, resolution), two independent NNs (Neural Networks) are used: for unconverted $\gamma\gamma$ pair and for the one with at least one converted photon. The NNs combine information both from the calorimeter (longitudinal direction of the photons deduced by combining information from the two front layers of the calorimeter) and from the tracker, which is the primary source of information: $\Delta\phi$ between the diphoton system and the tracks being under consideration, the scalar sum of p_T and p_T^2 of the tracks. The simulations showed that the algorithm was able to reconstruct the truth vertex not further than 0.3 mm from the truth one in 76% of the time (using ggH signal events). A slight decrease in the vertex reconstruction efficiency is present for the $t\bar{t}H$ events since the NNs have been trained over the ggH samples. However, retraining over the entire dataset does not lead to a valuable improvement in performance. Finally, the leading and sub-leading photons have to satisfy $p_T/m_{\gamma\gamma} > 0.35$ and 0.25, respectively. The predicted SM Higgs boson efficiency is 39%. In addition, events passing the $b\bar{b}\gamma\gamma$ selection[4] are removed to allow combination between analyses. The removal has a negligible effect on the $H \to \gamma\gamma$ analysis and mainly affects $t\bar{t}H$ events.

Events failing the tight identification or the isolation criterium are used as control sample (*CS*) for background estimation with ABCD method [108].

4.5 Parameters of Interest

The analysis targets a few various parameters-of-interests (POI) in different granularities. The following schemes are considered:

- 1-POI, inclusive $\mu \equiv \sigma^{\gamma\gamma}_{\text{obs}}/\sigma^{\gamma\gamma}_{\text{SM}}$, targetting the overall Higgs boson production signal strength.
- 6-POI scheme, $\{\mu_i\}$, with i being a production mode: ggF, VBF, WH, ZH, ttH and tH. In this scheme, signal strengths of the production modes are measured simultaneously.
- 28-POI scheme, $\{\mu_t\}$, with t running over all the STXS truth-bins.

4.6 Categorisation

The events passing the diphoton selection criterium are divided in a set of 101 orthogonal categories[5], designed to enhance sensitivity to the STXS signals (truth bins), maximising the signal purity (S/B ratio). The categorisation procedure consists of two steps:

- Initial Multiclass BDT categorisation (45 classes), aiming on providing the smallest error and correlation on the measured STXS.
- Secondary Binary BDT (101 independent), further boosting analysis sensitivity (estimated as the inverse determinant $|C|^{-1}$ of the covariance matrix. See Section 4.6.2 for more details), by improving background rejection.

For the training, the dataset has been split into a few parts: 50% for training and 25% both for validation and testing.

[4] Events originating from the $HH \to b\bar{b}\gamma\gamma$ decay. They are removed, in order not to use the same events in a combination of $H \to \gamma\gamma$ and $HH \to b\bar{b}\gamma\gamma$ channels.

[5] The number of the categories is much larger than the one of the truth-bins because there are up to three categories targetting a truth-bin.

4.6.1 Multiclass BDT

The multiclass BDT is trained on the signal MC only in order to separate the various truth-bins as classes. As a result, for each event a set of scores (equal to the number of classes) is assigned: one score for each truth bin, equivalently for each class. The scores can be treated as bayesian probabilities to the event to belong to a given class. In the training, all STXS bins were treated with equal prior probabilities to prevent any bias in the classification. Variables used for the BDT are given in the Table 4.3.

η_{γ_1}, η_{γ_2}, $p_{\mathrm{T}}^{\gamma\gamma}$, $y_{\gamma\gamma}$,
$p_{\mathrm{T},jj}^{\dagger}$, m_{jj}, and Δy, $\Delta\phi$, $\Delta\eta$ between j_1 and j_2,
$p_{\mathrm{T},\gamma\gamma j_1}$, $m_{\gamma\gamma j_1}$, $p_{\mathrm{T},\gamma\gamma jj}\dagger$, $m_{\gamma\gamma jj}$
Δy, $\Delta\phi$ between the $\gamma\gamma$ and jj systems,
minimum ΔR between jets and photons,
invariant mass of the system comprising all jets in the event,
dilepton p_T, di-e or di-μ invariant mass (leptons are required to be oppositely charged),
$E_{\mathrm{T}}^{\mathrm{miss}}$, p_T and transverse mass of the lepton + $E_{\mathrm{T}}^{\mathrm{miss}}$system,
p_T, η, ϕ of top-quark candidates, $m_{t_1t_2}$
Number of jets†, of central jets ($\lvert\eta\rvert < 2.5$)†, of b-jets† and of leptons,
p_T of the highest-p_T jet, scalar sum of the p_T of all jets,
scalar sum of the transverse energies of all particles ($\sum E_{\mathrm{T}}$), $E_{\mathrm{T}}^{\mathrm{miss}}$ significance,
$\left\lvert E_{\mathrm{T}}^{\mathrm{miss}} - E_{\mathrm{T}}^{\mathrm{miss}}(\text{primary vertex with the highest } \sum p_{\mathrm{T,track}}^2)\right\rvert > 30\,\mathrm{GeV}$
Top reconstruction BDT of the top-quark candidates,
$\Delta R(W,b)$ of t_2,
η_{j_F}, $m_{\gamma\gamma j_F}$
Average number of interactions per bunch crossing.

Table 4.3: Training variables used as input to the multiclass BDT. The dagger symbol † denotes variables that have two versions with different jet p_T requirements. The most forward jet is denoted as j_F. $\Delta R(W,b)$ is the ΔR between the W and b components of a top-quark candidate. Source: [39].

The BDT has been trained by minimising a multiclass cross-entropy loss. In a case of m classes and N observations, it is given by the following formulae:

$$\mathcal{L} = -\sum_{i}^{N} y_i \, \ln\left(\hat{y}_i\right), \tag{4.8}$$

where y_i is an m-dimensional vector, having all zero components, apart from one in a given position, representing the real class to which a given event belong. $\hat{y}_i$ is a softmax prediction of the BDT (with $z = BDT(x)$):

$$\hat{y}_i = softmax(z_i) = \frac{\exp^{z_i}}{\sum\limits_{j} \exp^{z_j}} \tag{4.9}$$

A few examples of Multiclass BDT's outputs are shown in Fig 4.11. It has been found that reweighting events from different classes to have the same yields, could improve the classification performance.

To accommodate for different cross-sections of the real measurements, the outputs from the multiclass BDT are multiplied on a weight designed to give the best stat-only precision on the STXS measurements. Otherwise, the classifier would tend to ignore classes with low cross-section. These weights have been defined using the D-optimality procedure (Section 4.6.2).

4.6.2 D-optimality criteria

Any machine learning problem requires a scalar value to be optimised (loss-function). Given the presence of both statistical errors on the measurement and their correlation, one may consider using a variable based on the correlation matrix.

It can be shown [109] that in order to provide an optimal background rejection (considering different cross-sections for each truth bin) and to make use of the output scores (from the multiclass BDT), one may parametrise gain in information obtained from an experiment as:

$$\mathcal{I} = \frac{1}{2}\ln\frac{|\Sigma_{exp} + \Sigma_{theo}|}{|\Sigma_{exp}|}, \tag{4.10}$$

where $|\cdot|$ is the matrix determinant, Σ_{exp} is the expected covariance matrix and Σ_{theo} is the covariance matrix of the SM uncertainties.

In this case, for two categorisations, yielding covariance matrices: Σ^1_{exp} and Σ^2_{exp}, the ratio between information gains described by eq (4.10), shows the following:

$$|\Sigma^1_{exp} + \Sigma_{theo}| \cdot \Sigma_{exp} + |\Sigma^2_{exp}| > |\Sigma^2_{exp} + \Sigma_{theo}| \cdot \Sigma_{exp} + |\Sigma^1_{exp}|, \tag{4.11}$$

which can be rewritten into:

$$|\Sigma^{-1}_{theo}\Sigma^1_{exp} + 1| \cdot \Sigma_{exp} + |\Sigma^2_{exp}| > |\Sigma^{-1}_{theo}\Sigma^2_{exp} + 1| \cdot \Sigma_{exp} + |\Sigma^1_{exp}| \tag{4.12}$$

In the case there statistical uncertainties dominate a measurement (which is the case for the STXS measurement), the elements of the $\Sigma^{-1}_{theo}\Sigma^i_{exp}$ matrix are small (compare to a unity matrix), hence can be neglected in the $|\Sigma^{-1}_{theo}\Sigma^2_{exp} + 1|$ term. Therefore, expression becomes:

$$|\Sigma^2_{exp}| > |\Sigma^1_{exp}|. \tag{4.13}$$

Evaluation of the expected covariance matrix Σ_{exp} is done using via analysing an Asimov dataset build over a simple counting likelihood, containing no information on the signal shape. For this, the signal yields for various categories c are expressed as:

$$N^c = B^c_{S_{90}} + \sum_t \mu_t \cdot L \cdot \sigma^{\gamma\gamma}_t \cdot \epsilon^{ct}_{S_{90}}, \tag{4.14}$$

where S_{90} is the region in $m_{\gamma\gamma}$ space covering 90% of the signal (independently in each category). $\epsilon^{ct}_{S_{90}}$ is the signal efficiency of the truth bin t in the category c in the S_{90} window. $B^c_{S_{90}}$ is the background yield in the same region. Background yield is extracted using an exponential form of the second order if a category contains more than 400 events and of the first order otherwise. μ_t is the signal strength of the truth bin t.

To further optimize the classification procedure in terms of maximising the inverse determinant $|C|^{-1}$ of the covariance matrix, a set of weights w_i for each class is computed. In this way, events are assigned to the STXS class i corresponding to the maximal value of $w_i z_i$. Weights are computed from minimising the following determinant: $S \times \vec{w}$, where S in the $N \times M$ score matrix for N events and M training classes (truth bins). $\vec{w}$ is the weight vector to be optimised. The $s_{ij} \cdot w_j$ represents the weighted output score for the i-th event in the j-th truth-bin. Initially, all the weights are set to unity and then iteratively updated so as to maximise $|C|^{-1}$, computed from a simulated dataset for each analysis region by mixing events from each signal sample (proportions are chosen to match their SM cross-sections), along with a simulated continuum background spectrum (normalised to data in the control region of $95 \leq m_{\gamma\gamma} < 105$. Such range is chosen to not overlap with the data side-bands of $[105 - 120]$ GeV and $[130 - 160]$ GeV used for the background studies).

4.6.3 Binary BDT

To further improve the categorisation performance, an independent binary BDT (Fig. 4.12) for each class has been trained in order to separate signal from the continuous and resonant backgrounds.

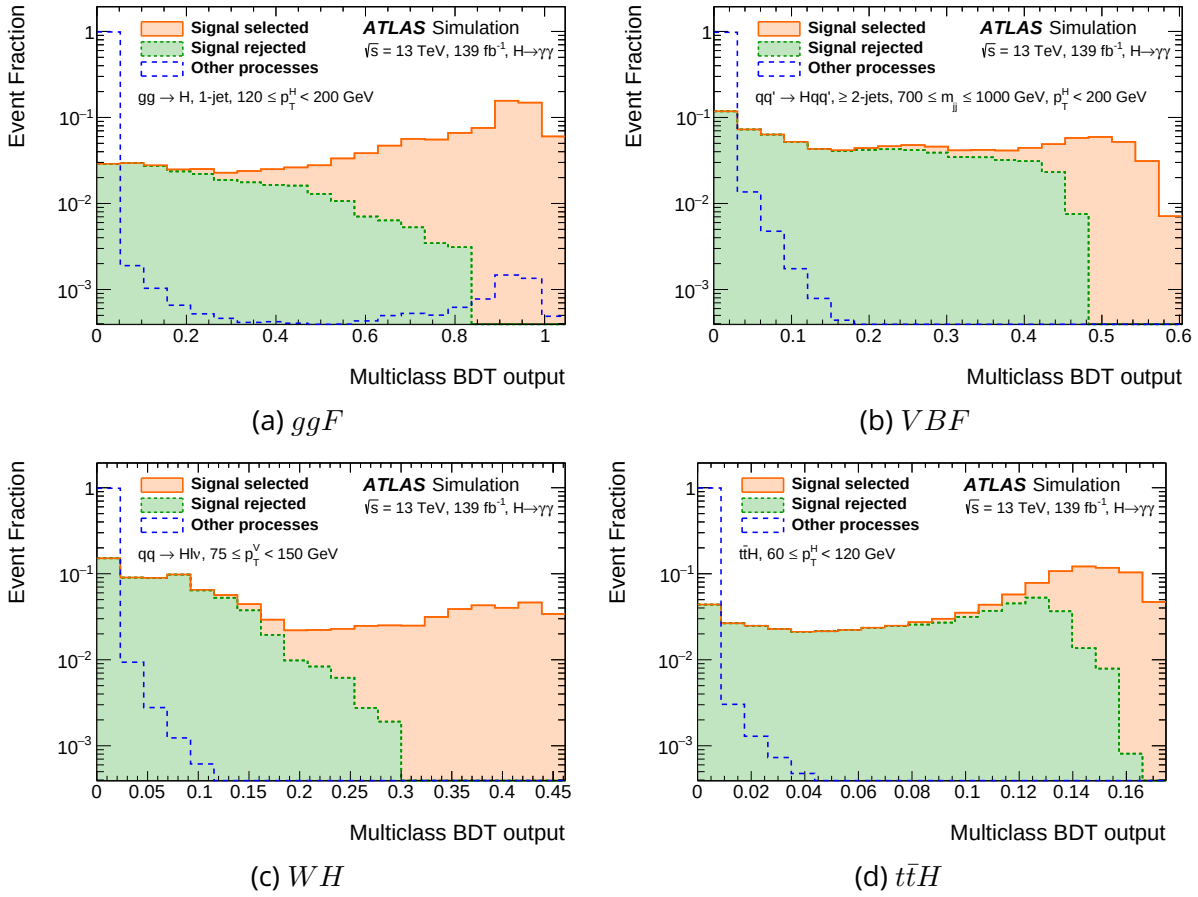

(a) ggF (b) VBF

(c) WH (d) $t\bar{t}H$

Figure 4.11: Examples of Multiclass BDT outputs for a given truth-bin. Source: [39].

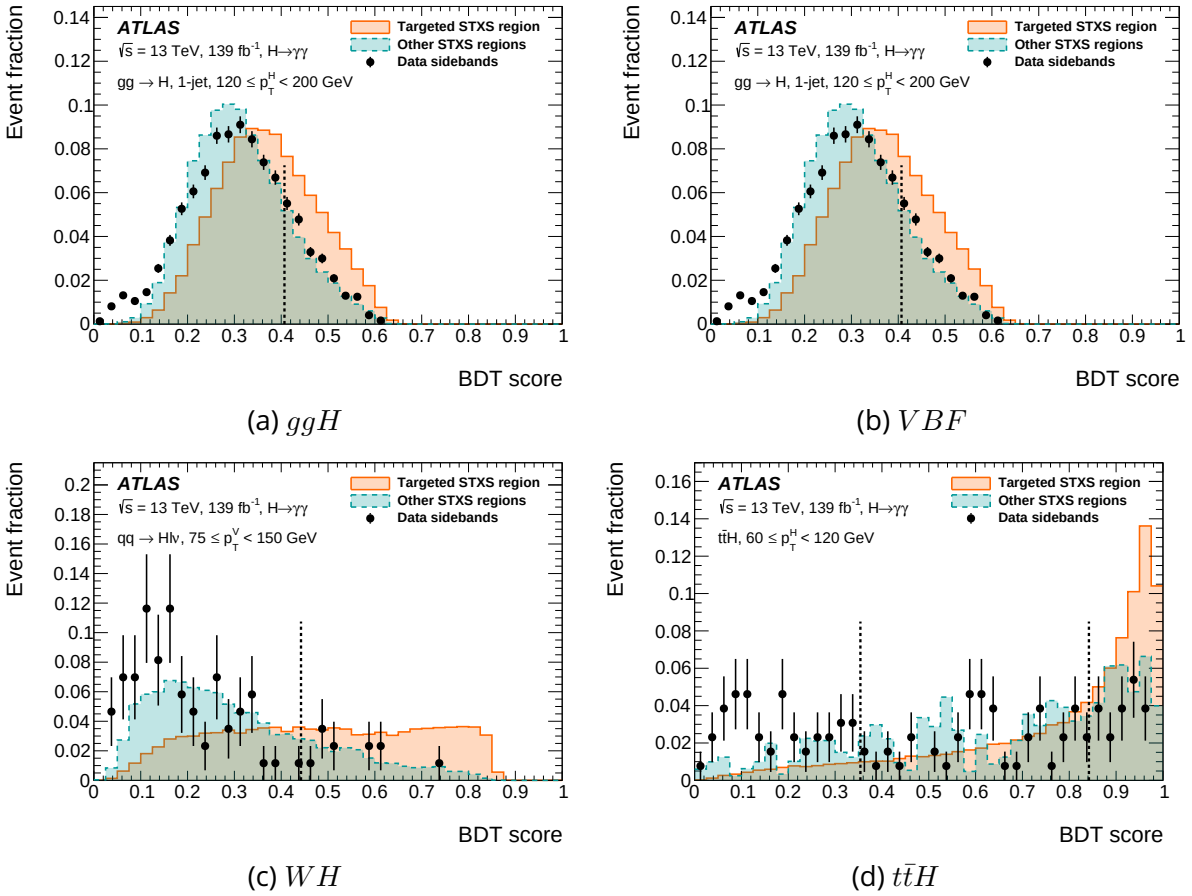

(a) ggH (b) VBF

(c) WH (d) $t\bar{t}H$

Figure 4.12: Examples of binary BDT outputs for a few representative classes: (a) ggH, (b) VBF, (c) WH and (d) $t\bar{t}H$. Side-bands is defined as $m_{\gamma\gamma} \in [105, 120]$ and $m_{\gamma\gamma} \in [130, 160]$. Vertical dashed lines show edges of the BDT scores used for categorisation. Source: [39].

Strategies for training are essentially different between the main production modes: for (ggH, VBF and VH) and for ($t\bar{t}H$, tHW). The difference is caused by a specific treatment for the top-quark related production modes, forced by the reconstruction techniques. Variables used for the training are listed in Table 4.4.

ggF, VBF and VH

For each truth bin, originating from these production modes, a BDT has been trained to provide a separation between the signal and background. Signal is formed by all events from the targetted STXS. Background consists of two types: continuum (events with no Higgs boson in the final state[6] and resonant. The continuum one is obtained from the MC TI samples. The resonant one is composed of the remaining contributions from the other STXS regions, but not the current targetted one.

For a training, all three components (STXS signal, continuum background and resonant background) have been reweighted to have the same yield. In this way, the BDT training is not biased toward a component with the largest yield (resonant background).

[6] $\gamma\gamma$, γj and jj components. See Section 4.9.1

STXS classes	Variables
Individual STXS classes from $gg \to H$ $qq' \to Hqq'$ $qq \to H\ell\nu$ $pp \to H\ell\ell$ $pp \to H\nu\bar{\nu}$	All multiclass BDT variables, $\vec{p}_{\mathrm{T}}^{\,\gamma\gamma}$ projected to the thrust axis of the $\gamma\gamma$ system ($p_{\mathrm{Tt}}^{\gamma\gamma}$), $\Delta\eta_{\gamma\gamma}$, $\eta^{\mathrm{Zepp}} = \frac{\eta_{\gamma\gamma}-\eta_{jj}}{2}$, $\phi^*_{\gamma\gamma} = \tan\left(\frac{\pi-\lvert\Delta\phi_{\gamma\gamma}\rvert}{2}\right)\sqrt{1-\tanh^2\left(\frac{\Delta\eta_{\gamma\gamma}}{2}\right)}$, $\cos\theta^*_{\gamma\gamma} = \left\lvert\frac{(E^{\gamma_1}+p_z^{\gamma_1})\cdot(E^{\gamma_2}-p_z^{\gamma_2})-(E^{\gamma_1}-p_z^{\gamma_1})\cdot(E^{\gamma_2}+p_z^{\gamma_2})}{m_{\gamma\gamma}\sqrt{m_{\gamma\gamma}^2+(p_{\mathrm{T}}^{\gamma\gamma})^2}}\right\rvert$ Number of electrons and muons.
all $t\bar{t}H$ and tHW STXS classes combined	p_T, η, ϕ of γ_1 and γ_2, p_T, η, ϕ and b-tagging scores of the six highest-p_T jets, $E_{\mathrm{T}}^{\mathrm{miss}}$, $E_{\mathrm{T}}^{\mathrm{miss}}$ significance, $E_{\mathrm{T}}^{\mathrm{miss}}$ azimuthal angle, Top reconstruction BDT scores of the top-quark candidates, p_T, η, ϕ of the two highest-p_T leptons.
$tHqb$	$p_{\mathrm{T}}^{\gamma\gamma}/m_{\gamma\gamma}$, $\eta_{\gamma\gamma}$, p_T, invariant mass, BDT score and $\Delta R(W,b)$ of t_1, p_T, η of t_2, p_T, η of j_F, Angular variables: $\Delta\eta_{\gamma\gamma t_1}$, $\Delta\theta_{\gamma\gamma t_2}$, $\Delta\theta_{t_1 j_F}$, $\Delta\theta_{t_2 j_F}$, $\Delta\theta_{\gamma\gamma j_F}$ Invariant mass variables: $m_{\gamma\gamma j_F}$, $m_{t_1 j_F}$, $m_{t_2 j_F}$, $m_{\gamma\gamma t_1}$ Number of jets with $p_T > 25$ GeV, Number of b-jets with $p_T > 25$ GeV*; Number of leptons*, $E_{\mathrm{T}}^{\mathrm{miss}}$significance*

Table 4.4: Training variables used for the binary classifiers. The asterisk symbol * denotes tH training variables that are only used for the classifiers suppressing the continuum background. Other tH training variables are used in all three tH classifiers. The most forward jet is denoted as j_F. The differences in η and ϕ between γ_1 and γ_2 are denoted respectively as $\Delta\phi_{\gamma\gamma}$ and $\Delta\eta_{\gamma\gamma}$. $\Delta R(W,b)$ is the ΔR between the W and b components of a top-quark candidate. Source: [39].

Training variables (features) at this stage consist of the same as for the multi class BDT training and some additional ones, related to the $\gamma\gamma$ and jj systems:

- $\gamma\gamma$: $\Delta y_{\gamma\gamma}$ (defined as difference between the two photons rapidities), $p_T^{\gamma\gamma}$ and $\phi^*_{\gamma\gamma}$
- counters: N_{e}, N_{μ}
- others:
  - $Zepp = (\eta_{\gamma\gamma} - (\eta_{j1} + \eta_{j2}))/2$
  - $|\cos\theta^*| = \frac{|\sinh(\Delta\eta^{\gamma\gamma})|}{\sqrt{1+\left(p_{\mathrm{T}}^{\gamma\gamma}/m_{\gamma\gamma}\right)^2}} \frac{2p_{\mathrm{T}}^{\gamma 1} p_{\mathrm{T}}^{\gamma 2}}{m_{\gamma\gamma}^2}$

During the training, a feature is removed if is correlated with $m_{\gamma\gamma}$ larger than 5% (either for signal or background). $p_T^{\gamma\gamma}$ is always considered.

top-related

For the $t\bar{t}H$ and tHW classes, independent BDT-classifiers are used to separate signal and the continuum background. For the $tHqb$ class, a specialisation is introduced to enhance sensitivity to the top-Yukawa coupling modifier κ_t. Firstly, the class is split into two-subclasses to separate production with $\kappa_t = 1$ from $\kappa_t = -1$ via a neural network binary classifier. In each of these sub-classes, events are divided into categories to separate the signal from the continuous background using a neural network binary classifier. For all these top-related classes, binary classifiers for suppressing continuous background are trained on the control regions of data.

4.6.4 Optimisation of the subsplitting of classes

Each of the classes may be split into up to three subclasses. A decision on the splitting is made by a comparison of the significance with the sub-splitting in up to 3 subclasses. For each scenario, a scan over all the possible cut values on the BDT score is made. For the significance computation (eq. A.46), the signal and background yields are computed in a window containing 90% of all signal events. Background yield is obtained as a sum of the one from the MC TI template (non-resonant) and the resonant one (from other STXS regions). A decision to split is accepted if the gain in total significance is above 5% and if the obtained subclass has at least 10 events.

4.7 Signal Modelling

The modelling (also called parametrisation) of the final discriminant signal shape ($m_{\gamma\gamma}$) is obtained for each reconstructed category by fitting the simulated $m_{\gamma\gamma}$ spectrum with a double-sided Crystal Ball (DSCB) function, illustrated on Fig. 4.13.

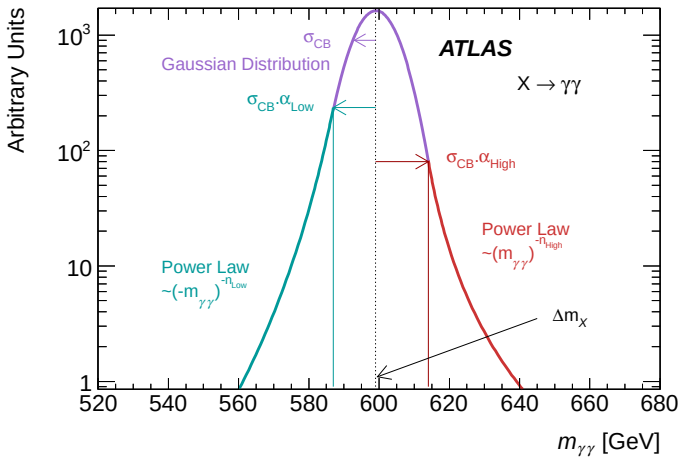

Figure 4.13: Illustration of the Double-Sided Crystal Ball (DSCB) function, shown on an arbitrary example of BSM signal at high mass. Source: [110].

The analytical expression for a Crystal Ball is:

$$f(x;\alpha,n,\bar{x},\sigma) = N \cdot \begin{cases} \exp(-\frac{(x-\bar{x})^2}{2\sigma^2}), & ;\text{for } \frac{x-\bar{x}}{\sigma} > -\alpha \\ A \cdot (B - \frac{x-\bar{x}}{\sigma})^{-n}, & ;\text{for } \frac{x-\bar{x}}{\sigma} \leqslant -\alpha \end{cases} \tag{4.15}$$

with

$$\begin{aligned} A &= \left(\tfrac{n}{|\alpha|}\right)^n \cdot \exp\left(-\tfrac{|\alpha|^2}{2}\right) & B &= \tfrac{n}{|\alpha|} - |\alpha| & N &= \tfrac{1}{\sigma(C+D)} \\ C &= \tfrac{n}{|\alpha|} \cdot \tfrac{1}{n-1} \cdot \exp\left(-\tfrac{|\alpha|^2}{2}\right) & D &= \sqrt{\tfrac{\pi}{2}}\left(1 + \operatorname{erf}\left(\tfrac{|\alpha|}{\sqrt{2}}\right)\right), \end{aligned} \tag{4.16}$$

where $\bar{x}$ is the mean of the Gaussian core, σ its spread, α the effective distance from the mean, expressed in units of gaussian variance, where the Gaussian core is glued with the

polynomial tails, n is the power of this polynomial. Similarly, the double-sided Crystal Ball function has two asymmetric tails. All the parameters are fitted. The advantage of the DSCB is a good separation of the core and tails, simplifying applying various relative systematic variations: μ_{CB} and σ_{CB}. An illustration of this function is given on Fig. 4.13.

Several studies have shown relatively small bias on the fitted signal yield in injection test over Asimov dataset[7] with signal and background MC.

Higgs boson mass, has been measured in the combination of ATLAS and CMS Run 1 data, with a good precision. Therefore, MC samples can be generated with a central value of the Higgs boson mass of $125\ GeV$ and might be re-interpreted to any close value by shifting the μ_{CB} parameter: $\mu_{CB} = m_H + \mu_{CB}^{125\ \text{GeV}} - 125$ GeV.

Nominally, fit is done in the mass range 110 to 140 GeV over the unbinned dataset by minimising the likelihood. In a case of fit failure, a binned 1 GeV χ^2 fit is used instead. In this case, the range might be more narrow to ensure absence of empty bins.

A variation of the signal range has been tested: narrowing the range to [113, 138] GeV, but it showed to be less stable for low-stat categories. It is explained that a smaller fit range is more sensitive for statistical fluctuation appearing in the tails, hence might shift the peak position.

Various categories, targetting the same truth bin, but with different purity, as well as categories targetting different p_T^H, differ in the signal spread (Fig. 4.14).

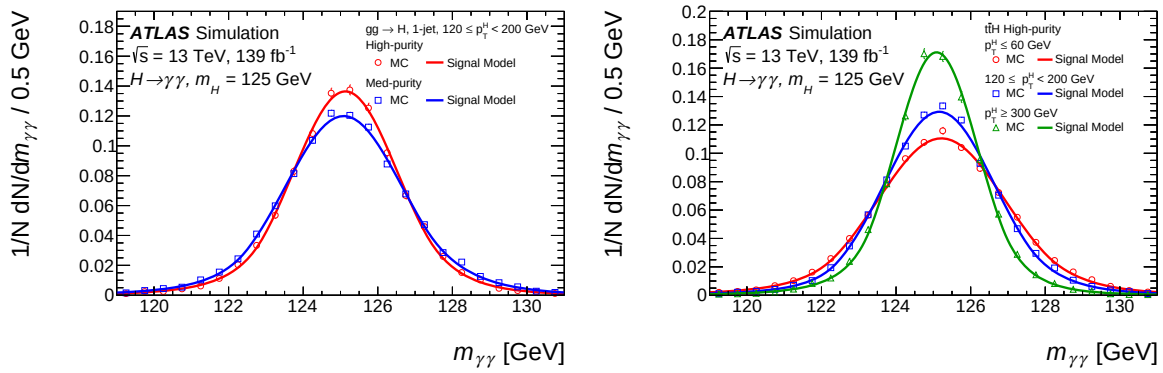

(a) (b)

Figure 4.14: Illustrations of signal modelling shape. (a) shows evolution of the spectrum with purity in signal. (b) shows evolution with p_T^H. Source: [39].

The signal resolution for the various categories, in a smallest window containing $90\ \%$ of the events, is reported in Figure 4.15.

[7] Section A.7.1.

Category	S	B	σ [GeV]	f [%]	Z
$gg \to H$					
0-jet, $p_T^H < 10$ GeV	695	26 000	3.43	2.6	4.3
0-jet, $p_T^H \geq 10$ GeV	1440	47 000	3.41	3.0	6.6
1-jet, $p_T^H < 60$ GeV, High-purity	168	4250	3.20	3.8	2.6
1-jet, $p_T^H < 60$ GeV, Med-purity	197	11 500	3.38	1.7	1.8
1-jet, $60 \leq p_T^H < 120$ GeV, High-purity	186	3310	3.10	5.3	3.2
1-jet, $60 \leq p_T^H < 120$ GeV, Med-purity	180	7780	3.37	2.3	2.0
1-jet, $120 \leq p_T^H < 200$ GeV, High-purity	23.0	182	2.61	11	1.7
1-jet, $120 \leq p_T^H < 200$ GeV, Med-purity	40.7	717	3.00	5.4	1.5
$\geq$ 2-jets, $m_{jj} < 350$ GeV, $p_T^H < 60$ GeV, High-purity	23.5	1050	3.08	2.2	0.72
$\geq$ 2-jets, $m_{jj} < 350$ GeV, $p_T^H < 60$ GeV, Med-purity	43.1	4360	3.39	0.98	0.65
$\geq$ 2-jets, $m_{jj} < 350$ GeV, $p_T^H < 60$ GeV, Low-purity	47.5	16 800	3.51	0.28	0.37
$\geq$ 2-jets, $m_{jj} < 350$ GeV, $60 \leq p_T^H < 120$ GeV, High-purity	49.1	901	3.03	5.2	1.6
$\geq$ 2-jets, $m_{jj} < 350$ GeV, $60 \leq p_T^H < 120$ GeV, Med-purity	93.9	6440	3.30	1.4	1.2
$\geq$ 2-jets, $m_{jj} < 350$ GeV, $120 \leq p_T^H < 200$ GeV, High-purity	15.5	74.8	2.64	17	1.7
$\geq$ 2-jets, $m_{jj} < 350$ GeV, $120 \leq p_T^H < 200$ GeV, Med-purity	22.7	343	2.97	6.2	1.2
$\geq$ 2-jets, $350 \leq m_{jj} < 700$ GeV, $p_T^H < 200$ GeV, High-purity	4.31	47.5	2.72	8.3	0.62
$\geq$ 2-jets, $350 \leq m_{jj} < 700$ GeV, $p_T^H < 200$ GeV, Med-purity	15.4	380	3.02	3.9	0.78
$\geq$ 2-jets, $350 \leq m_{jj} < 700$ GeV, $p_T^H < 200$ GeV, Low-purity	10.5	1080	3.31	0.97	0.32
$\geq$ 2-jets, $700 \leq m_{jj} < 1000$ GeV, $p_T^H < 200$ GeV, High-purity	2.34	33.3	2.84	6.6	0.40
$\geq$ 2-jets, $700 \leq m_{jj} < 1000$ GeV, $p_T^H < 200$ GeV, Med-purity	4.23	136	3.07	3.0	0.36
$\geq$ 2-jets, $700 \leq m_{jj} < 1000$ GeV, $p_T^H < 200$ GeV, Low-purity	3.34	429	3.26	0.77	0.16
$\geq$ 2-jets, $m_{jj} \geq 1000$ GeV, $p_T^H < 200$ GeV, High-purity	1.14	14.5	2.97	7.3	0.30
$\geq$ 2-jets, $m_{jj} \geq 1000$ GeV, $p_T^H < 200$ GeV, Med-purity	2.52	47.5	3.10	5.0	0.36
$\geq$ 2-jets, $m_{jj} \geq 1000$ GeV, $p_T^H < 200$ GeV, Low-purity	2.49	142	3.37	1.7	0.21
$200 \leq p_T^H < 300$ GeV, High-purity	15.3	38.0	2.28	29	2.3
$200 \leq p_T^H < 300$ GeV, Med-purity	29.4	236	2.64	11	1.9
$300 \leq p_T^H < 450$ GeV, High-purity	1.52	2.13	2.02	42	0.95
$300 \leq p_T^H < 450$ GeV, Med-purity	6.75	17.7	2.16	28	1.5
$300 \leq p_T^H < 450$ GeV, Low-purity	4.66	43.1	2.46	9.8	0.70
$450 \leq p_T^H < 650$ GeV, High-purity	1.00	1.25	1.85	45	0.81
$450 \leq p_T^H < 650$ GeV, Med-purity	0.800	2.00	1.98	29	0.53
$450 \leq p_T^H < 650$ GeV, Low-purity	0.830	10.7	2.19	7.2	0.25
$p_T^H \geq 650$ GeV	0.220	1.08	1.73	17	0.20
$qq' \to Hqq'$					
0-jet, High-purity	0.330	25.0	3.33	1.3	0.07
0-jet, Med-purity	1.27	471	3.35	0.27	0.06
0-jet, Low-purity	10.7	18 800	3.48	0.06	0.08
1-jet, High-purity	1.08	2.78	2.99	28	0.61
1-jet, Med-purity	3.50	26.1	3.11	12	0.67
1-jet, Low-purity	2.88	145	3.24	2.0	0.24
$\geq$ 2-jets, $m_{jj} < 60$ GeV, High-purity	0.350	2.10	2.71	14	0.24
$\geq$ 2-jets, $m_{jj} < 60$ GeV, Med-purity	0.670	19.0	2.79	3.4	0.15
$\geq$ 2-jets, $m_{jj} < 60$ GeV, Low-purity	1.92	243	2.93	0.78	0.12
$\geq$ 2-jets, $60 \leq m_{jj} < 120$ GeV, High-purity	3.45	6.34	2.65	35	1.3
$\geq$ 2-jets, $60 \leq m_{jj} < 120$ GeV, Med-purity	4.99	43.0	2.85	10	0.75
$\geq$ 2-jets, $60 \leq m_{jj} < 120$ GeV, Low-purity	2.99	87.3	3.01	3.3	0.32
$\geq$ 2-jets, $120 \leq m_{jj} < 350$ GeV, High-purity	2.98	24.4	2.93	11	0.59
$\geq$ 2-jets, $120 \leq m_{jj} < 350$ GeV, Med-purity	6.73	204	2.94	3.2	0.47
$\geq$ 2-jets, $120 \leq m_{jj} < 350$ GeV, Low-purity	8.78	1360	2.99	0.64	0.24
$\geq$ 2-jets, $350 \leq m_{jj} < 700$ GeV, $p_T^H < 200$ GeV, High-purity	2.52	2.75	2.96	48	1.4
$\geq$ 2-jets, $350 \leq m_{jj} < 700$ GeV, $p_T^H < 200$ GeV, Med-purity	9.15	34.7	3.06	21	1.5
$\geq$ 2-jets, $350 \leq m_{jj} < 700$ GeV, $p_T^H < 200$ GeV, Low-purity	5.97	106	3.27	5.3	0.57
$\geq$ 2-jets, $700 \leq m_{jj} < 1000$ GeV, $p_T^H < 200$ GeV, High-purity	2.91	3.00	2.90	49	1.5
$\geq$ 2-jets, $700 \leq m_{jj} < 1000$ GeV, $p_T^H < 200$ GeV, Med-purity	5.60	22.7	3.11	20	1.1
$\geq$ 2-jets, $m_{jj} \geq 1000$ GeV, $p_T^H < 200$ GeV, High-purity	10.8	3.89	3.01	74	4.2
$\geq$ 2-jets, $m_{jj} \geq 1000$ GeV, $p_T^H < 200$ GeV, Med-purity	10.7	19.0	3.23	36	2.3

Category	S	B	σ [GeV]	f [%]	Z
$\geq$ 2-jets, $350 \leq m_{jj} < 700$ GeV, $p_T^H \geq 200$ GeV, High-purity	1.31	2.19	2.48	37	0.81
$\geq$ 2-jets, $350 \leq m_{jj} < 700$ GeV, $p_T^H \geq 200$ GeV, Med-purity	1.40	9.22	2.49	13	0.45
$\geq$ 2-jets, $350 \leq m_{jj} < 700$ GeV, $p_T^H \geq 200$ GeV, Low-purity	1.16	65.5	2.54	1.7	0.14
$\geq$ 2-jets, $700 \leq m_{jj} < 1000$ GeV, $p_T^H \geq 200$ GeV, High-purity	2.51	3.02	2.43	45	1.3
$\geq$ 2-jets, $700 \leq m_{jj} < 1000$ GeV, $p_T^H \geq 200$ GeV, Med-purity	1.49	47.4	2.54	3.0	0.22
$\geq$ 2-jets, $m_{jj} \geq 1000$ GeV, $p_T^H \geq 200$ GeV, High-purity	5.65	1.57	2.39	78	3.3
$\geq$ 2-jets, $m_{jj} \geq 1000$ GeV, $p_T^H \geq 200$ GeV, Med-purity	2.96	6.31	2.55	32	1.1
$qq \to H\ell\nu$					
$p_T^V < 75$ GeV, High-purity	1.91	4.91	3.17	28	0.81
$p_T^V < 75$ GeV, Med-purity	2.59	20.2	3.28	11	0.57
$75 \leq p_T^V < 150$ GeV, High-purity	2.62	2.05	3.02	56	1.6
$75 \leq p_T^V < 150$ GeV, Med-purity	2.08	12.4	3.23	14	0.58
$150 \leq p_T^V < 250$ GeV, High-purity	1.74	2.06	2.78	46	1.1
$150 \leq p_T^V < 250$ GeV, Med-purity	0.16	2.90	3.17	5.2	0.09
$p_T^V \geq 250$ GeV, High-purity	1.36	1.79	2.41	43	0.91
$p_T^V \geq 250$ GeV, Med-purity	0.02	3.12	3.15	0.78	0.01
$pp \to H\ell\ell$					
$p_T^V < 75$ GeV, High-purity	1.14	1.82	3.25	39	0.78
$p_T^V < 75$ GeV, Med-purity	1.06	215	3.29	0.49	0.07
$75 \leq p_T^V < 150$ GeV, High-purity	1.07	1.58	3.08	40	0.77
$75 \leq p_T^V < 150$ GeV, Med-purity	0.02	1.81	3.06	1.2	0.02
$150 \leq p_T^V < 250$ GeV, High-purity	0.71	1.79	2.78	28	0.50
$150 \leq p_T^V < 250$ GeV, Med-purity	0.10	16.5	2.88	0.62	0.03
$p_T^V \geq 250$ GeV	0.27	2.06	2.48	12	0.18
$pp \to H\nu\bar{\nu}$					
$p_T^V < 75$ GeV, High-purity	0.60	170	3.50	0.35	0.05
$p_T^V < 75$ GeV, Med-purity	1.15	1020	3.57	0.11	0.04
$p_T^V < 75$ GeV, Low-purity	0.87	2630	3.67	0.03	0.02
$75 \leq p_T^V < 150$ GeV, High-purity	0.58	2.30	2.97	20	0.37
$75 \leq p_T^V < 150$ GeV, Med-purity	1.83	17.8	3.26	9.3	0.43
$75 \leq p_T^V < 150$ GeV, Low-purity	2.18	288	3.44	0.75	0.13
$150 \leq p_T^V < 250$ GeV, High-purity	0.92	2.00	2.75	32	0.61
$150 \leq p_T^V < 250$ GeV, Med-purity	0.75	2.54	2.94	23	0.45
$150 \leq p_T^V < 250$ GeV, Low-purity	0.26	11.7	3.28	2.2	0.08
$p_T^V \geq 250$ GeV, High-purity	0.67	1.55	2.46	30	0.50
$p_T^V \geq 250$ GeV, Med-purity	0.05	1.97	3.05	2.6	0.04
$t\bar{t}H$					
$p_T^H < 60$ GeV, High-purity	3.04	4.01	3.18	43	1.4
$p_T^H < 60$ GeV, Med-purity	2.78	13.3	3.37	17	0.74
$60 \leq p_T^H < 120$ GeV, High-purity	4.30	4.09	3.06	51	1.9
$60 \leq p_T^H < 120$ GeV, Med-purity	2.99	8.61	3.31	26	0.97
$120 \leq p_T^H < 200$ GeV, High-purity	4.65	3.52	2.73	57	2.1
$120 \leq p_T^H < 200$ GeV, Med-purity	1.66	4.16	2.93	29	0.77
$200 \leq p_T^H < 300$ GeV	3.39	2.26	2.46	60	1.9
$p_T^H \geq 300$ GeV	2.73	1.66	2.12	62	1.8
tH					
$tHqb$, High-purity	0.55	2.16	3.04	20	0.36
$tHqb$, Med-purity	0.14	2.78	3.45	4.9	0.09
$tHqb$, BSM ($\kappa_t = -1$)	0.12	1.86	3.25	6.0	0.09
tHW	0.16	6.91	2.74	2.3	0.06
Low-purity top	5.18	65.8	3.32	7.3	0.63

Figure 4.15: Expected signal (S) and background (B) yields in the smallest window containing 90% of the events, the half-width of which is given by σ. The signal purity ($f = S/(S+B)$) and expected significance ($Z = \sqrt{(2((S+B)\ln(1+S/B) - S))}$) are given. For the signal yield computation, only the signal processes corresponding to the targeted STXS bin is considered. Source: [39].

4.8 Purities

STXS purity plot (Fig. 4.16) illustrates the fraction of events belonging to a given truth-bin, reconstructed in a category targetting it. For the visualisation, the STXS categories with the same kinematic criterium, but different quality criteria are merged together.

Diagonal structure of the plot gives a hint on the quality of the categorisation and the reconstruction performance.

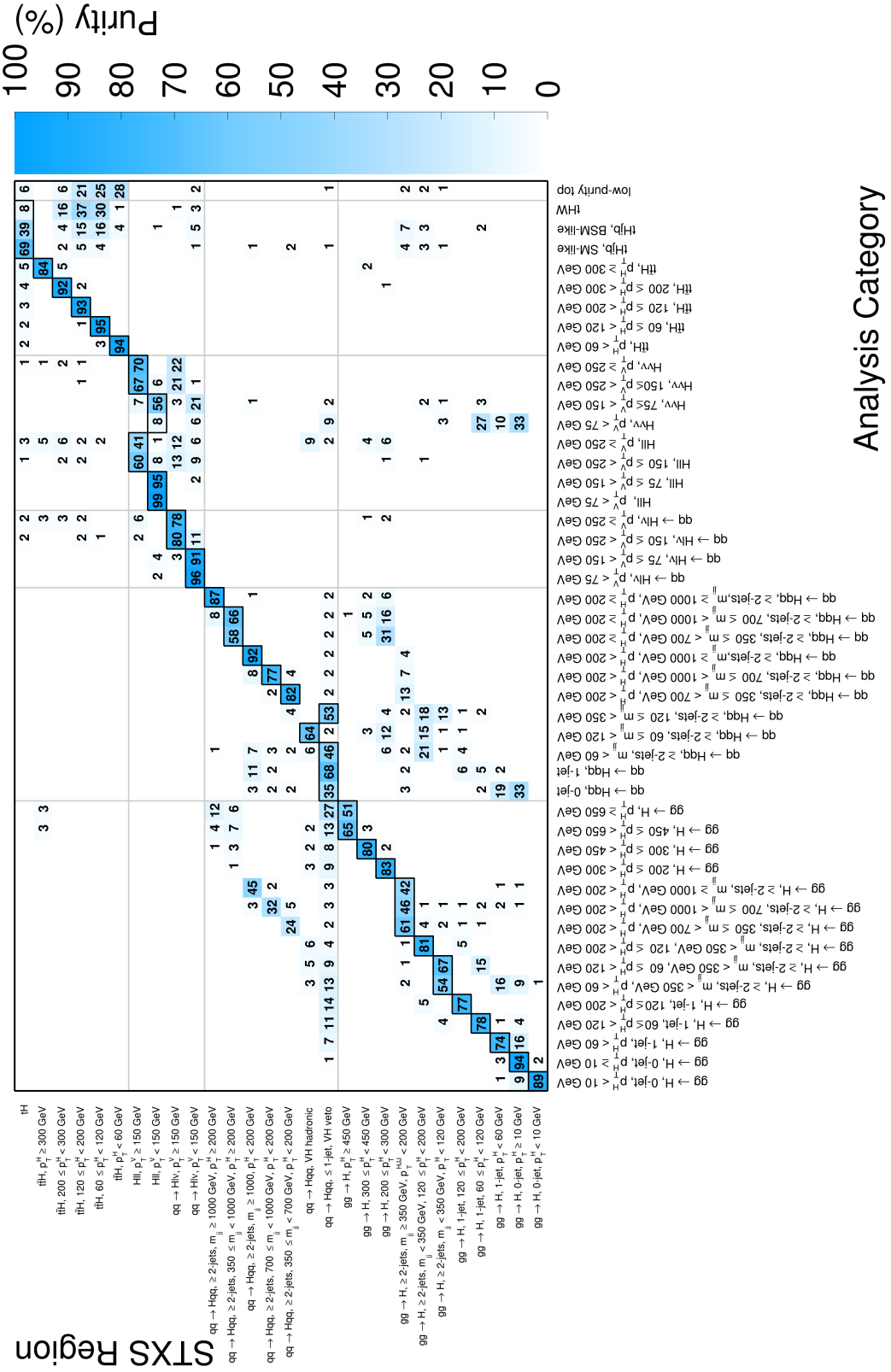

Figure 4.16: STXS purity for each merged reconstructed category (horizontal axis) and truth-bins (vertical axis). Source: [39].

4.9 Background Modelling

Due to the low signal to background ratio, it is crucial to model well the background and be able to extract its components (Fig. 4.17) for the diagnostic purpose.

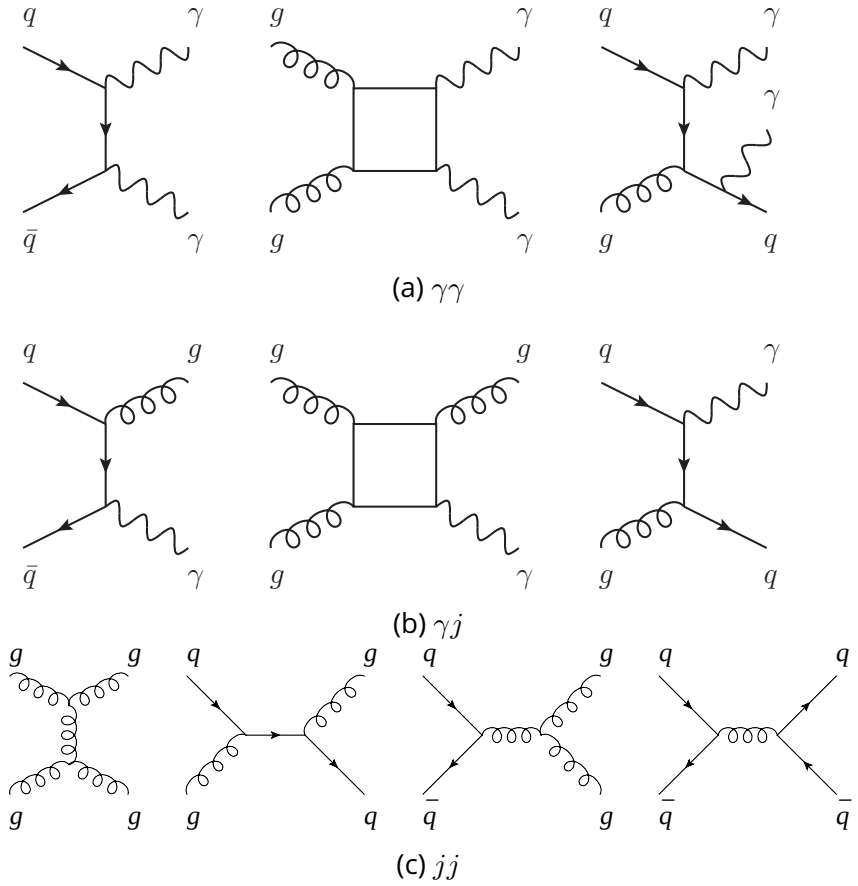

Figure 4.17: Leading Feynman diagrams for the background in the $H \to \gamma\gamma$ channel: $\gamma\gamma$, γj and jj, respectively. Source: [111].

The dominant background after identification originates from the continuum SM diphoton production. In addition, many photons are produced inside jets through neutral mesons (mainly π^0) decaying into pairs of photons (this is a reducible background, which is suppressed via selection on the photon id and isolation). Therefore, a non-negligible fraction of the background comes from γj and jj pairs, where one or two jets are misidentified as photons. The background composition (fractions of $\gamma\gamma$, γj and jj) for each reconstructed category is evaluated using a data-driven technique. $\gamma\gamma$ spectrum is directly modelled in MC simulations, while computational expenses of precise modelling of γj and jj distributions force to obtain their spectrum by renormalising the $\gamma\gamma$ one, as it is described in Section 4.9.2. Background decomposition as a function of μ (the mean number of interactions per bunch crossing) is shown on Fig. 4.18.

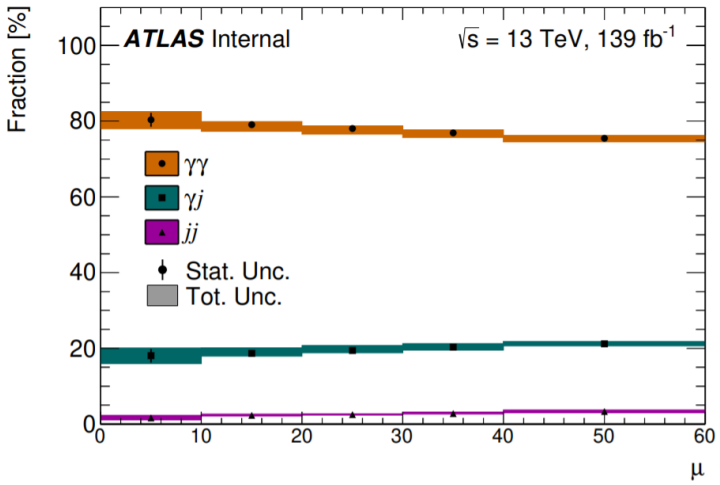

Figure 4.18: Background composition ($\gamma\gamma$, γj and jj) as a function of mean number of interactions per bunch crossing. Source: [99].

4.9.1 Background Templates

Background events are generated using SHERPA for the $\gamma\gamma$ process. Due to the computational complexity and low precision of the processes involving multiple jets, the γj and jj background components are obtained using the reweighting procedure (Section 4.9.2). Fractions of $\gamma\gamma$, γj and jj are directly obtained from the side-bands of data for each category, using 2x2 ABCD method [108].

Due to the low statistics and significant contributions of other background types for the VH and $t\bar{t}H$ processes, background templates for such processes (categories) are constructed using a dedicated procedure:

- VH: SHERPA $\gamma\gamma$ samples are mixed with the $V\gamma\gamma$ ones.
- $t\bar{t}H$: only $t\bar{t}\gamma\gamma$ sample is used.

The obtained samples are in a good agreement with the data side-bands ($[105 - 120]$ GeV and $[130 - 160]$ GeV), passing the nominal selection, including the photon tight identification and isolation cuts.

For low-statistics categories (less than 20 effective entries per 0.25 GeV bin of the MC background template), a dedicated treatment was used: only exponential functional forms are considered and the choice on the order is made via the Wald test (Section 4.9.5).

To further improve the background modelling and minimize the effect of limited MC statistics, a smoothing procedure (Section 4.9.3), based on the Gaussian Process Regression (GPR) is used.

4.9.2 Background reweighting

To emulate the γj and jj components, the $\gamma\gamma$ background spectrum is reweighted in order to match the one observed in data for γj and jj respectively. This γj (jj) rescaling is done by obtaining a linear function, representing the ratio between jj (γj) and $\gamma\gamma$ distributions in

the real data. This function is further used to re-normalise MC $\gamma\gamma$ distribution to obtain the γj (jj) spectrum. All three components are further summed up with the coefficients being their purities, found via ABCD method, using the equation 4.17, where $a_{\gamma(j)j}$ and $b_{\gamma(j)j}$ are the parameters of the linear function, obtained by reweighting γj (jj) to $\gamma\gamma$ (Fig. 4.20), $f_{\gamma j(\gamma)}$ is the fraction of γj (jj) events, computed with ABCD method.

$$f(m_{\gamma\gamma}) = \Big[a_{\gamma j}\big(\frac{m_{\gamma\gamma}-132.5}{160-105}+b_{\gamma j}\big)\Big] f_{\gamma j}\Big(\frac{N_{orig}}{N_{rw}^{\gamma j}}\Big) + \Big[a_{jj}\big(\frac{m_{\gamma\gamma}-132.5}{160-105}+b_{jj}\big)\Big] f_{jj}\Big(\frac{N_{orig}}{N_{rw}^{jj}}\Big) + f_{\gamma\gamma} \tag{4.17}$$

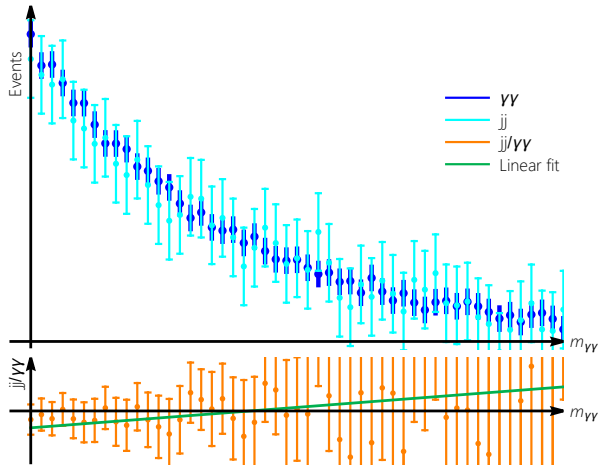

Figure 4.19: Illustration of obtaining linear function for the background reweigthing for $\gamma\gamma$ (blue) and jj (cyan) components from data. The $jj/\gamma\gamma$ ratio plot (orange) is fitted with a linear function (green) and this function weights $\gamma\gamma$ MC to emulate the jj component.

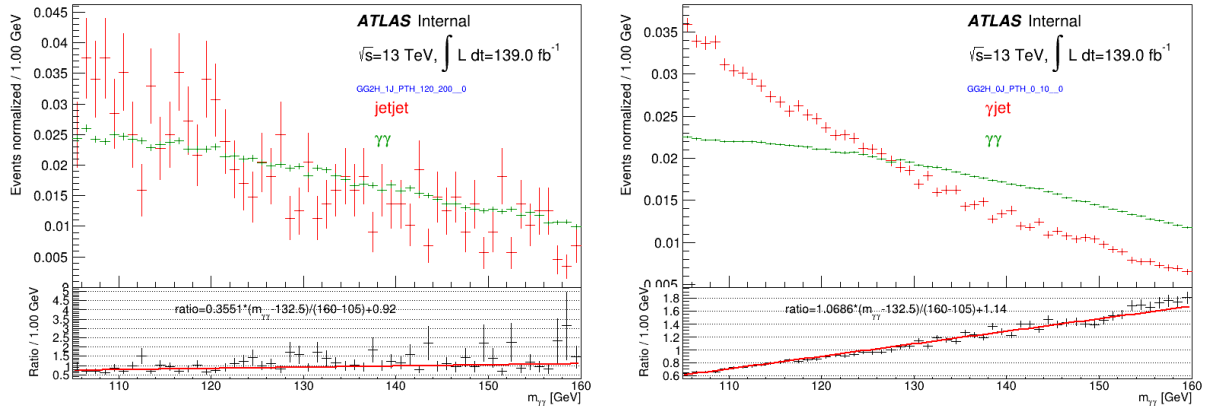

(a) (b)

Figure 4.20: Examples of the γj and jj components for one category for the ggH category with 1 jet, $120 \leq p_T^H \leq 200$ GeV and High purity for γj (a) and jj (b) components, respectively.

4.9.3 Background Smoothing

Potential bias on the background modelling (Spurious Signal, Section 4.9.4) is estimated from a series of signal plus background fits over the background template for each category.

Therefore, it may suffer from statistical fluctuations, causing fake signal-like bumps in a pure background template. A way to address this issue is to use the so-called Gaussian Process Regression (GPR) [112] defined as a set of random processes, where all finite subsets of these processes have a multivariate normal distribution. To parametrise it, two quantities must be defined from a dataset: mean and correlation matrix, where the latest is often simplified and represented via a kernel. The kernel analytically determines the level of correlation $l(x)$ between two distinct points, which may also depend on the points. For smoothly-falling functions, a usual choice is the Gibbs kernel:

$$K(x, x') = \frac{\sqrt{2l(x)l(x')}}{l(x)^2 + l(x')} \cdot \exp\left(-\frac{(x - x')^2)}{l(x)^2 + l(x')^2}\right) \tag{4.18}$$

This procedure is used for all categories, having at least 20 effective entries per a 0.25 GeV bin of the MC background template, as this threshold was found to be sufficient to not introduce much bias.

Examples of the smoothed templates are presented in Fig. 4.21.

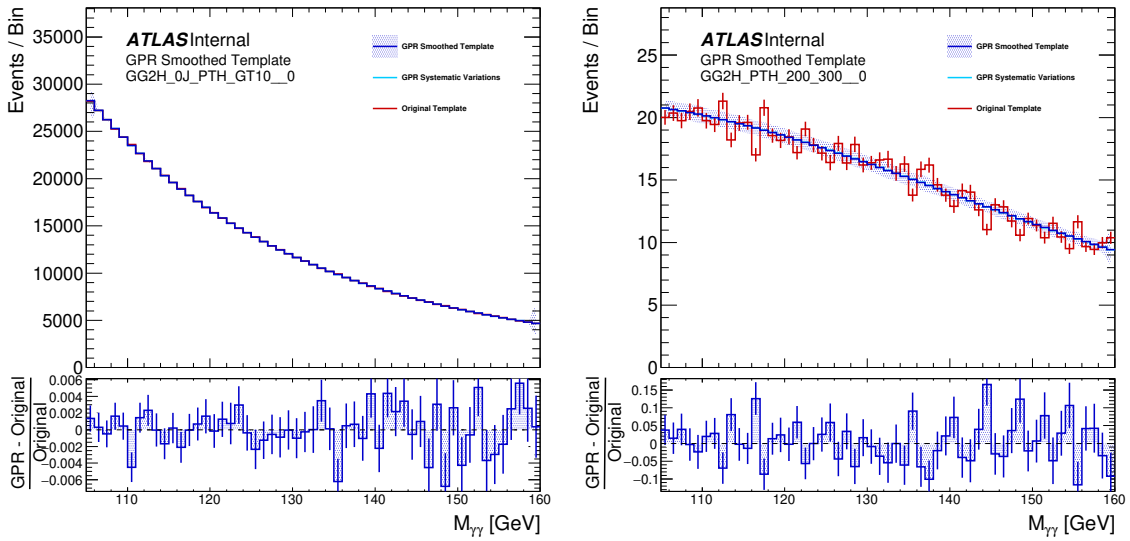

(a) High-stat category (b) Low-stat category

Figure 4.21: Examples of background templates before (red) and after (blue) GPR smoothing for a high-stat (a) and low-stat (b) categories. Source: [99].

4.9.4 Spurious signal test

Spurious signal refers to false signal that arise from mis-modelling of the background shape and serves as a measure of a bias related to the choice of the functional form to describe the background. Both the polynomial family and order need to be chosen. A few various functional forms have been tested:

- Polynomial: $P^n(x) = \sum_{i=1}^{n} a_i x_i^n$
- Exponential: $\exp\left(a_i x_i^n\right)$
- Bernstein: $B_N(x) = \sum_{i=0}^{N} c_i \cdot b_{i,N}$ with $b_{i,N} = \binom{N}{i} x^i (1-x)^{N-i}$

On one hand, increasing the polynomial order will improve the resemblance of the fit function to the MC spectrum. However, it will become more sensitive to local statistical fluctuations due to having too many degrees of freedom tending to accommodate the desired shape. On the other hand, a tiny amount of degrees of freedom might not be enough to interpolate a spectrum with some features, not easily represented by a simple exponent or a polynomial. Besides that, the spurious signal is used to estimate the possible bias from the choice of the functional form to represent the real invariant-mass spectrum. Such estimation is crucial, since the S/B ratio is tiny. The spurious signal is defined as the maximal value of signal-component found in a simultaneous signal + background fit of pure background component of the MC simulations under various functional form hypotheses describing the background spectrum's descending shape (Fig. 4.22).

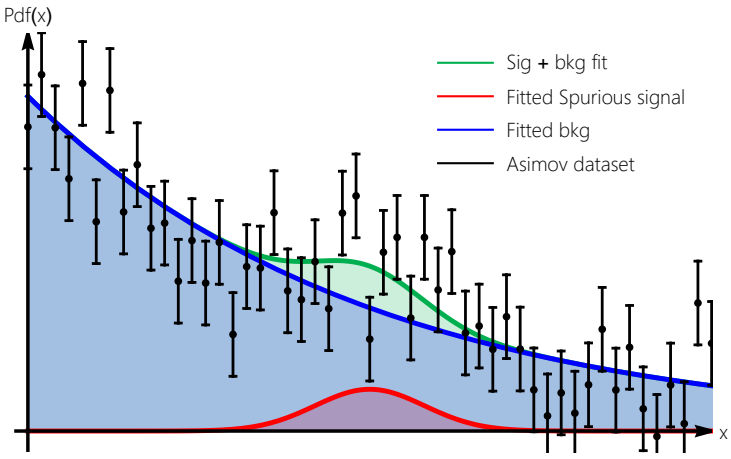

Figure 4.22: Illustration of a spurios signal (red), found in a signal + background fit (green) of pure background template (black).

A functional form, which is far away from the actual shape of the distribution, might give an unlimited amount of signal found. Therefore, a few requirements to the quality of the signal + background fit are required:

- χ^2-probability of the function to match the observed distribution is required to be greater than 1% (Section 4.9.6);
- $N_{sp} < 10\%\ N_{S,expected}$, where N_{sp} is the fitted spurious signal and $N_{S,expected}$ is the expected SM signal in a given category;
- $N_{sp} < 20\%\ \sigma_{S,expected}$, where $\sigma_{S,expected}$ is the statistical uncertainty on the fitted amount of the signal events for the Asimov dataset;

The fit is performed over the binned dataset with 0.25 GeV bins. A few studies have shown relatively small bias induced by the binning with respect to the unbinned dataset. For this test, the spurious signal value found with a given binning (0.25, 0.50, 1.00, 2.50 GeV) was compared to the one obtained over the unbinned dataset. Examples of the study are shown on Fig. 4.23. The results of the background modelling, along with the values of the spurious signal are shown in Fig. 4.24.

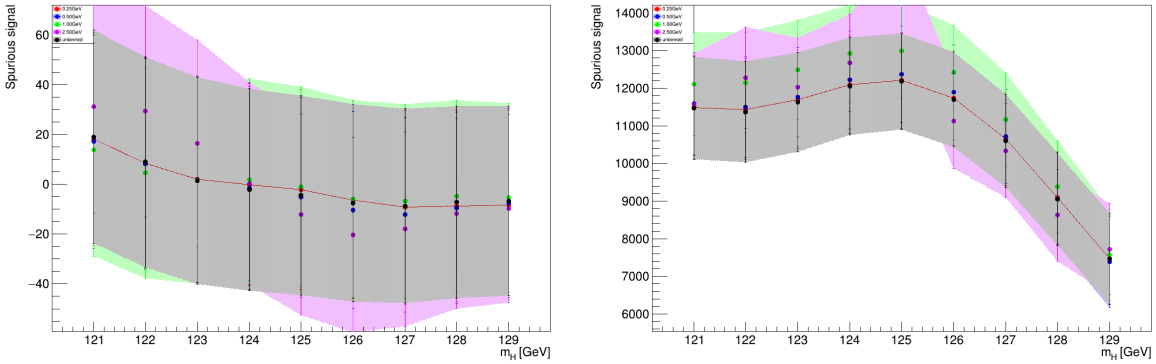

(a) 10k generated events (b) 10M generated events

Figure 4.23: Example of spurious signal study on the bin size for a given number of generated events. A set of events following ExpPoly2 distribution has been generated and fit using the same functional form. The unbinned fit (black) and the tiniest among studied once (0.5 GeV) has shown the smallest bias.

Category	Function	N_{data}	N_{spur}	Wald
$gg \to H$				
0-jet, $p_{\text{T}}^H < 10$ GeV	ExpPoly2	191623	64.8	
0-jet, $p_{\text{T}}^H \geq 10$ GeV	ExpPoly2	349266	50.4	
1-jet, $p_{\text{T}}^H < 60$ GeV, High-purity	ExpPoly2	32644	20.7	
1-jet, $p_{\text{T}}^H < 60$ GeV, Med-purity	ExpPoly2	85229	24.9	
1-jet, $60 \leq p_{\text{T}}^H < 120$ GeV, High-purity	Exp	26236	23.7	
1-jet, $60 \leq p_{\text{T}}^H < 120$ GeV, Med-purity	ExpPoly2	56669	21.3	
1-jet, $120 \leq p_{\text{T}}^H < 200$ GeV, High-purity	ExpPoly2	1570	1.48	
1-jet, $120 \leq p_{\text{T}}^H < 200$ GeV, Med-purity	ExpPoly2	6163	5.33	
$\geq$ 2-jets, $m_{jj} < 350$ GeV, $p_{\text{T}}^H < 60$ GeV, High-purity	ExpPoly2	8513	1.51	
$\geq$ 2-jets, $m_{jj} < 350$ GeV, $p_{\text{T}}^H < 60$ GeV, Med-purity	ExpPoly2	31163	13.6	
$\geq$ 2-jets, $m_{jj} < 350$ GeV, $p_{\text{T}}^H < 60$ GeV, Low-purity	ExpPoly2	120357	15.7	
$\geq$ 2-jets, $m_{jj} < 350$ GeV, $60 \leq p_{\text{T}}^H < 120$ GeV, High-purity	ExpPoly2	7582	2.26	
$\geq$ 2-jets, $m_{jj} < 350$ GeV, $60 \leq p_{\text{T}}^H < 120$ GeV, Med-purity	ExpPoly2	48362	6.21	
$\geq$ 2-jets, $m_{jj} < 350$ GeV, $120 \leq p_{\text{T}}^H < 200$ GeV, High-purity	ExpPoly2	728	0.004	
$\geq$ 2-jets, $m_{jj} < 350$ GeV, $120 \leq p_{\text{T}}^H < 200$ GeV, Med-purity	PowerLaw	3007	0.983	
$\geq$ 2-jets, $350 \leq m_{jj} < 700$ GeV, $p_{\text{T}}^H < 200$ GeV, High-purity	Exp	432	0.487	
$\geq$ 2-jets, $350 \leq m_{jj} < 700$ GeV, $p_{\text{T}}^H < 200$ GeV, Med-purity	ExpPoly2	3084	1.33	
$\geq$ 2-jets, $350 \leq m_{jj} < 700$ GeV, $p_{\text{T}}^H < 200$ GeV, Low-purity	Exp	7999	5.78	
$\geq$ 2-jets, $700 \leq m_{jj} < 1000$ GeV, $p_{\text{T}}^H < 200$ GeV, High-purity	Exp	302	0.560	
$\geq$ 2-jets, $700 \leq m_{jj} < 1000$ GeV, $p_{\text{T}}^H < 200$ GeV, Med-purity	Exp	1033	1.44	
$\geq$ 2-jets, $700 \leq m_{jj} < 1000$ GeV, $p_{\text{T}}^H < 200$ GeV, Low-purity	Exp	3187	4.32	
$\geq$ 2-jets, $m_{jj} \geq 1000$ GeV, $p_{\text{T}}^H < 200$ GeV, High-purity	Exp	113	0.192	
$\geq$ 2-jets, $m_{jj} \geq 1000$ GeV, $p_{\text{T}}^H < 200$ GeV, Med-purity	Exp	332	0.804	
$\geq$ 2-jets, $m_{jj} \geq 1000$ GeV, $p_{\text{T}}^H < 200$ GeV, Low-purity	PowerLaw	1020	1.09	
$200 \leq p_{\text{T}}^H < 300$ GeV, High-purity	Exp	420	1.68	
$200 \leq p_{\text{T}}^H < 300$ GeV, Med-purity	Exp	2296	0.714	
$300 \leq p_{\text{T}}^H < 450$ GeV, High-purity	Exp	25	0.407	✓
$300 \leq p_{\text{T}}^H < 450$ GeV, Med-purity	Exp	186	0.259	
$300 \leq p_{\text{T}}^H < 450$ GeV, Low-purity	Exp	422	0.121	
$450 \leq p_{\text{T}}^H < 650$ GeV, High-purity	Exp	15	0.138	✓
$450 \leq p_{\text{T}}^H < 650$ GeV, Med-purity	Exp	25	0.391	✓
$450 \leq p_{\text{T}}^H < 650$ GeV, Low-purity	Exp	109	0.031	
$p_{\text{T}}^H \geq 650$ GeV	Exp	14	0.448	✓
$qq' \to Hqq'$				
0-jet, High-purity	Exp	176	0.180	
0-jet, Med-purity	ExpPoly2	3238	4.73	
0-jet, Low-purity	ExpPoly2	133314	49.7	
1-jet, High-purity	Exp	19	0.125	✓
1-jet, Med-purity	Exp	187	0.361	
1-jet, Low-purity	PowerLaw	1040	1.97	
$\geq$ 2-jets, $m_{jj} < 60$ GeV, High-purity	Exp	17	0.499	✓
$\geq$ 2-jets, $m_{jj} < 60$ GeV, Med-purity	Exp	157	0.489	
$\geq$ 2-jets, $m_{jj} < 60$ GeV, Low-purity	PowerLaw	1978	1.29	
$\geq$ 2-jets, $60 \leq m_{jj} < 120$ GeV, High-purity	Exp	53	0.165	✓
$\geq$ 2-jets, $60 \leq m_{jj} < 120$ GeV, Med-purity	Exp	329	0.520	
$\geq$ 2-jets, $60 \leq m_{jj} < 120$ GeV, Low-purity	PowerLaw	709	1.15	
$\geq$ 2-jets, $120 \leq m_{jj} < 350$ GeV, High-purity	Exp	214	1.08	
$\geq$ 2-jets, $120 \leq m_{jj} < 350$ GeV, Med-purity	ExpPoly2	1671	1.07	
$\geq$ 2-jets, $120 \leq m_{jj} < 350$ GeV, Low-purity	PowerLaw	11195	6.34	
$\geq$ 2-jets, $350 \leq m_{jj} < 700$ GeV, $p_{\text{T}}^H < 200$ GeV, High-purity	Exp	25	0.162	✓
$\geq$ 2-jets, $350 \leq m_{jj} < 700$ GeV, $p_{\text{T}}^H < 200$ GeV, Med-purity	Exp	260	0.443	
$\geq$ 2-jets, $350 \leq m_{jj} < 700$ GeV, $p_{\text{T}}^H < 200$ GeV, Low-purity	Exp	753	1.17	
$\geq$ 2-jets, $700 \leq m_{jj} < 1000$ GeV, $p_{\text{T}}^H < 200$ GeV, High-purity	Exp	25	0.670	✓
$\geq$ 2-jets, $700 \leq m_{jj} < 1000$ GeV, $p_{\text{T}}^H < 200$ GeV, Med-purity	Exp	166	0.713	
$\geq$ 2-jets, $m_{jj} \geq 1000$ GeV, $p_{\text{T}}^H < 200$ GeV, High-purity	Exp	48	1.47	✓
$\geq$ 2-jets, $m_{jj} \geq 1000$ GeV, $p_{\text{T}}^H < 200$ GeV, Med-purity	Exp	142	0.270	
$\geq$ 2-jets, $350 \leq m_{jj} < 700$ GeV, $p_{\text{T}}^H \geq 200$ GeV, High-purity	Exp	18	0.189	✓
$\geq$ 2-jets, $350 \leq m_{jj} < 700$ GeV, $p_{\text{T}}^H \geq 200$ GeV, Med-purity	Exp	84	0.513	✓
$\geq$ 2-jets, $350 \leq m_{jj} < 700$ GeV, $p_{\text{T}}^H \geq 200$ GeV, Low-purity	Exp	595	0.721	
$\geq$ 2-jets, $700 \leq m_{jj} < 1000$ GeV, $p_{\text{T}}^H \geq 200$ GeV, High-purity	Exp	19	0.110	✓
$\geq$ 2-jets, $700 \leq m_{jj} < 1000$ GeV, $p_{\text{T}}^H \geq 200$ GeV, Med-purity	Exp	411	0.193	
$\geq$ 2-jets, $m_{jj} \geq 1000$ GeV, $p_{\text{T}}^H \geq 200$ GeV, High-purity	Exp	23	1.30	✓
$\geq$ 2-jets, $m_{jj} \geq 1000$ GeV, $p_{\text{T}}^H \geq 200$ GeV, Med-purity	Exp	56	0.329	✓
$qq \to H\ell\nu$				
$0 \leq p_{\text{T}}^V < 75$ GeV, High-purity	Exp	40	0.277	
$0 \leq p_{\text{T}}^V < 75$ GeV, Med-purity	Exp	158	0.609	
$75 \leq p_{\text{T}}^V < 150$ GeV, High-purity	Exp	15	0.069	
$75 \leq p_{\text{T}}^V < 150$ GeV, Med-purity	Exp	104	0.255	
$150 \leq p_{\text{T}}^V < 250$ GeV, High-purity	Exp	17	0.128	✓
$150 \leq p_{\text{T}}^V < 250$ GeV, Med-purity	Exp	21	0.150	
$p_{\text{T}}^V \geq 250$ GeV, High-purity	Exp	16	0.237	✓
$p_{\text{T}}^V \geq 250$ GeV, Med-purity	Exp	27	0.054	✓
$pp \to H\ell\ell$				
$0 \leq p_{\text{T}}^V < 75$ GeV, High-purity	Exp	12	0.027	
$0 \leq p_{\text{T}}^V < 75$ GeV, Med-purity	PowerLaw	1620	2.28	
$75 \leq p_{\text{T}}^V < 150$ GeV, High-purity	Exp	13	0.015	
$75 \leq p_{\text{T}}^V < 150$ GeV, Med-purity	Exp	18	0.016	
$150 \leq p_{\text{T}}^V < 250$ GeV, High-purity	Exp	14	0.059	✓
$150 \leq p_{\text{T}}^V < 250$ GeV, Med-purity	Exp	136	0.194	
$p_{\text{T}}^V \geq 250$ GeV	Exp	14	0.311	✓
$pp \to H\nu\bar{\nu}$				
$0 \leq p_{\text{T}}^V < 75$ GeV, High-purity	Exp	1174	12.3	✓
$0 \leq p_{\text{T}}^V < 75$ GeV, Med-purity	Exp	6897	4.13	
$0 \leq p_{\text{T}}^V < 75$ GeV, Low-purity	ExpPoly3	18084	9.95	
$75 \leq p_{\text{T}}^V < 150$ GeV, High-purity	Exp	16	0.407	✓
$75 \leq p_{\text{T}}^V < 150$ GeV, Med-purity	Exp	124	1.30	✓
$75 \leq p_{\text{T}}^V < 150$ GeV, Low-purity	Exp	2019	1.96	
$150 \leq p_{\text{T}}^V < 250$ GeV, High-purity	Exp	16	0.121	✓
$150 \leq p_{\text{T}}^V < 250$ GeV, Med-purity	Exp	17	0.184	✓
$150 \leq p_{\text{T}}^V < 250$ GeV, Low-purity	Exp	87	0.644	✓
$p_{\text{T}}^V \geq 250$ GeV, High-purity	Exp	15	0.237	✓
$p_{\text{T}}^V \geq 250$ GeV, Med-purity	Exp	18	0.201	✓
$t\bar{t}H$				
$p_{\text{T}}^H < 60$ GeV, High-purity	Exp	35	0.040	
$p_{\text{T}}^H < 60$ GeV, Med-purity	Exp	96	0.192	
$60 \leq p_{\text{T}}^H < 120$ GeV, High-purity	Exp	34	0.038	
$60 \leq p_{\text{T}}^H < 120$ GeV, Med-purity	Exp	74	0.274	
$120 \leq p_{\text{T}}^H < 200$ GeV, High-purity	Exp	39	0.018	
$120 \leq p_{\text{T}}^H < 200$ GeV, Med-purity	Exp	37	0.057	
$200 \leq p_{\text{T}}^H < 300$ GeV	Exp	23	0.261	
$p_{\text{T}}^H \geq 300$ GeV	Exp	19	0.180	✓
tH				
$tHqb$, High-purity	Exp	17	0.371	✓
$tHqb$, Med-purity	Exp	19	0.320	✓
$tHqb$, BSM ($\kappa_t = -1$)	Exp	14	0.496	✓
tHW	Exp	38	0.070	
Low-purity top	Exp	500	0.870	

Figure 4.24: Summary of the background modelling, showing selected functional form, number of the observed events in data and the estimation of the spurious signal uncertainty for each analyses category. The last column indicates whether the Wald test is used for determination of the functional form. Source: [39].

4.9.5 Wald test

For the low-statistics categories, having less than 4400 effective entries per a template, large statistical fluctuations cannot be addressed via the GPR smoothing, otherwise it may introduce bias. To accommodate for the statistical fluctuations, for this categories only the exponential family of function is tested.

A decision on increasing order of exponent from i to j is made by the Wald test, where the following statistics is computed:

$$\lambda_{ij} = -2 \ln \left(\frac{\mathcal{L}_i}{\mathcal{L}_j} \right) \tag{4.19}$$

where $\mathcal{L}_{i(j)}$ is the likelihood value of the fit of the data side-bands with exponential of the order $i(j)$. A higher-order exponent is chosen if the $p-value$ of λ_{ij} is greater than 5%. Illustrations of the Wald test for low-statistics categories is given in Fig. 4.25.

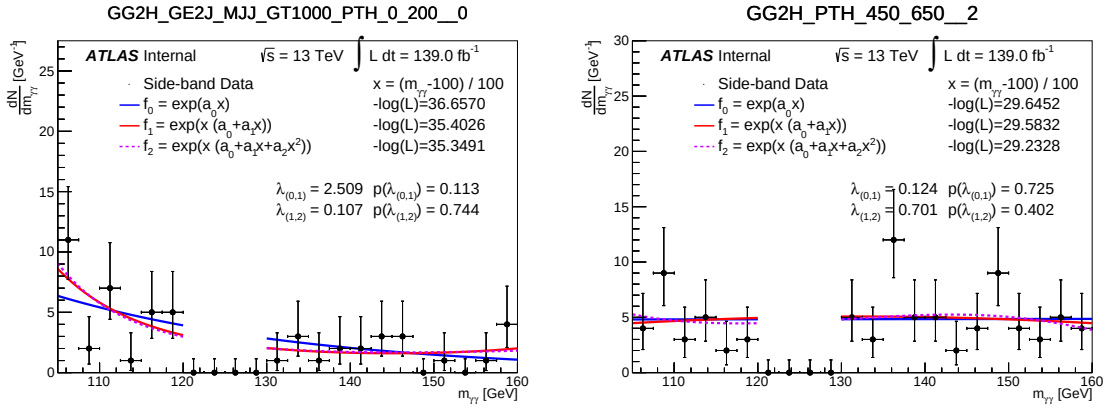

(a) (b)

Figure 4.25: Examples of Wald test on the real data for two categories. The exponential of the first order is in blue, of the second order is in red and the third-order is in violet dashed line. The signal region is blinded. Source: [99].

4.9.6 χ^2-probability of background fit

To evaluate the fit quality of the background template with a given function, the χ^2-probability is computed. Since the χ^2 method is sensitive to the number of entries (one has to rely on the gaussian behaviour of the number of entries in each bin), it is desirable to have around 30 entries in each bin. To ensure this situation for the low-statistics categories, the following procedure has been adapted: starting from the initial binning of 0.25 GeV, find a minimal number of bins to merge, so that each bin has more than 30 effective entries. For example, one checks the 0.50 GeV binning of the entire background template, then 0.75 GeV and so on. The maximal allowed bin size is 5.0 GeV, which corresponds to the scanned range in the spurious signal study.

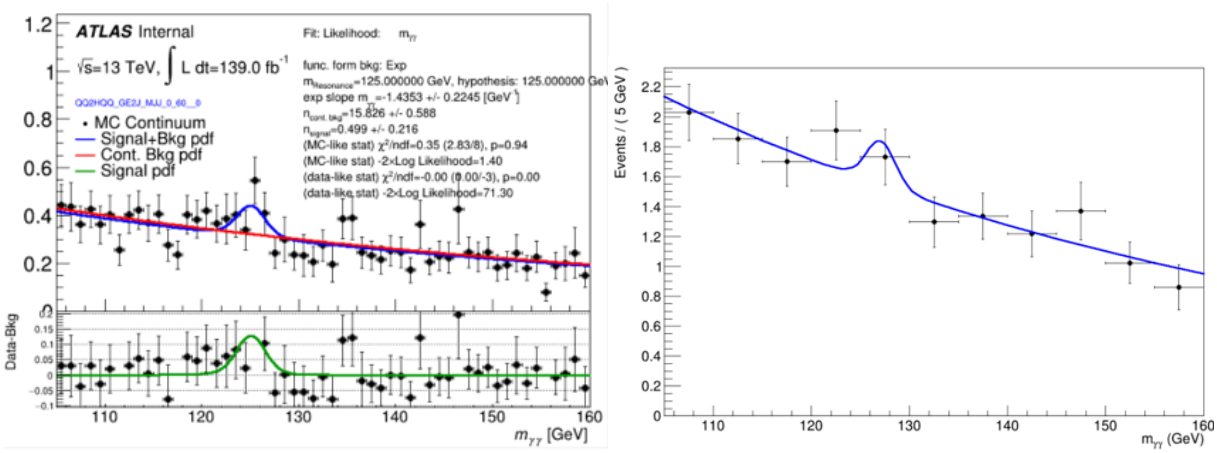

(a) (b)

Figure 4.26: Illustration of the binning used to compute spurious signal (a) and the binning obtained to compute the χ^2-probability for one category.

4.10 Systematic uncertainties

Breakdown of uncertainties on the inclusive signal strength ($\mu \equiv \sigma^{\gamma\gamma}_{\text{obs}}/\sigma^{\gamma\gamma}_{\text{SM}}$) is shown on Table 4.5 and Table 4.6 shows impact of various groups of systematic uncertainties on each of the production mode separately. In this scenario, the 6 production modes: ggF (+bbH), VBF, WH, ZH, ttH and tH are probed simultaneously

Impact of systematic uncertainty on the inclusive signal strength measurement	
Uncertainty source	$\Delta\mu$ [%]
Branching Ratio	± 3.0
Underlying Event and Parton Shower (UEPS)	± 2.4
Modelling of Heavy Flavour Jets in non-$t\bar{t}H$ Processes	$< \pm 1$
Higher-Order QCD Terms (QCD)	± 3.6
Parton Distribution Function and α_S Scale (PDF+α_S)	± 2.1
Matrix Element	± 1.1
Photon Energy Resolution (PER)	± 2.8
Photon Energy Scale (PES)	$< \pm 1$
Jet/E_T^{miss}	$< \pm 1$
Photon Efficiency	± 2.5
Background Modelling	± 1.2
Flavour Tagging	$< \pm 1$
Leptons	$< \pm 1$
Pileup	± 1.5
Luminosity	± 1.8
Higgs Boson Mass	$< \pm 1$

Table 4.5: The impact of the systematic uncertainty for the signal strength measurement. Source: [99].

	ggH + bbH	VBF	WH	ZH	$t\bar{t}H$	tH
Uncertainty source	$\Delta\sigma$[%]	$\Delta\sigma$[%]	$\Delta\sigma$[%]	$\Delta\sigma$[%]	$\Delta\sigma$[%]	$\Delta\sigma$[%]
Underlying Event and Parton Shower (UEPS)	± 3	± 15	± 2.5	± 4.2	± 3.6	± 48
Modeling of Heavy Flavor Jets in non-$t\bar{t}H$ Processes	$< \pm 1$	$< \pm 1$	$< \pm 1$	$< \pm 1$	$< \pm 1$	± 13
Higher-Order QCD Terms (QCD)	± 1.8	± 3.5	± 4.2	± 12	± 2.8	± 16
Parton Distribution Function and α_S Scale (PDF+α_S)	$< \pm 1$	± 1.8	± 1.7	± 3	$< \pm 1$	± 6.7
Matrix Element	$< \pm 1$	± 2.8	$< \pm 1$	± 1.2	± 2.4	± 7.7
Photon Energy Resolution (PER)	± 3	± 2.6	± 3.4	± 4.4	± 2.7	± 8.9
Photon Energy Scale (PES)	$< \pm 1$	$< \pm 1$	± 1.1	± 1.9	$< \pm 1$	± 7.1
Jet/E_T^{miss}	± 1.4	± 5.9	$< \pm 1$	± 2.2	± 3.4	± 23
Photon Efficiency	± 2.7	± 2.6	± 3.3	± 3.5	± 2.9	± 9.2
Background Modeling	± 1.9	± 4.4	± 3.6	± 7.3	± 2.5	± 62
Flavor Tagging	$< \pm 1$	$< \pm 1$	$< \pm 1$	$< \pm 1$	± 1.5	± 3.8
Leptons	$< \pm 1$	$< \pm 1$	$< \pm 1$	$< \pm 1$	$< \pm 1$	± 1.6
Pileup	± 1.5	± 2.2	± 1.9	± 2	± 1.2	± 7.4
Luminosity	± 1.8	± 2	± 2.4	± 2.7	± 2.2	± 6.5
Higgs Boson Mass	$< \pm 1$	$< \pm 1$	$< \pm 1$	$< \pm 1$	$< \pm 1$	± 2.5

Table 4.6: Expected contribution of groups of systematic uncertainties to the total error on the observed cross section times branching ratio. $\Delta\sigma$ shows the impact of systematic variations on σ. Source: [99].

Pull of uncertainties the ggF production mode is shown on Fig. 4.27. To obtain this pull, the signal strength of all the other production modes were kept floating, hence emulating performance of a combined fit over the all 6 production modes considered. The VBF production mode is mainly dominated by the parton shower VBF uncertainty, while the VH modes are also limited by spurious signal, QCD scale and photon identification/isolation uncertainties.

Work of the dedicated groups aims on reducing all kind of uncertainties, limiting performance of the measurements: starting from reducing uncertainties of identification of individual objects (electrons, photons, muons, jets and others) to reducing theoretical uncertainties, contributing to the underlying event and parton shower modelling.

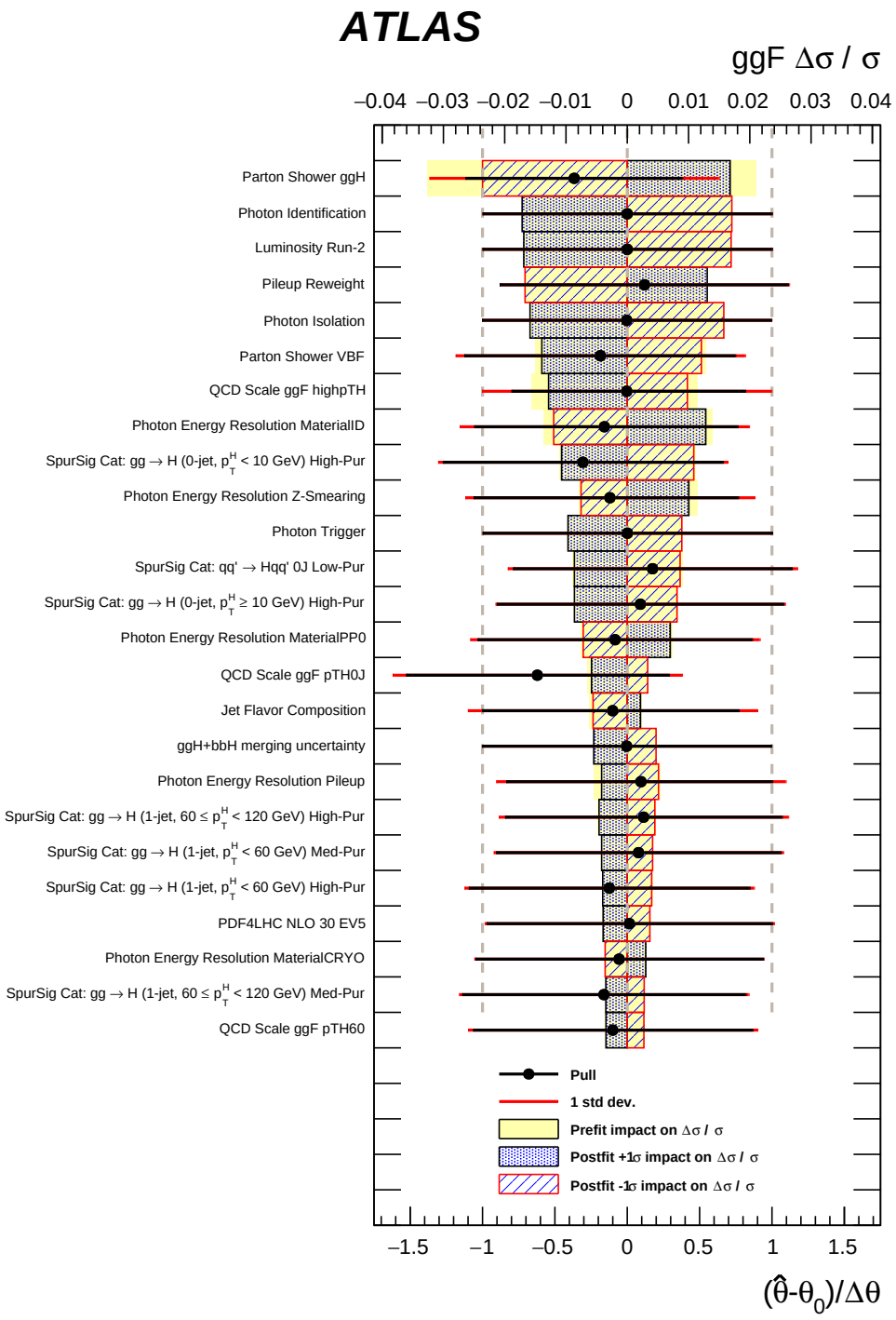

Figure 4.27: Pulls of uncertainties in the 6POI schemes for the ggH production mode. To obtain the pull, signal strength of the other five production modes (VBF, WH, ZH, ttH and tH) were kept floating, to match the condition of the combined fit of the production modes signal strength. Source: [39].

4.11 Results

Diphoton invariant mass distributions for each production mode are shown on Fig. 4.28.

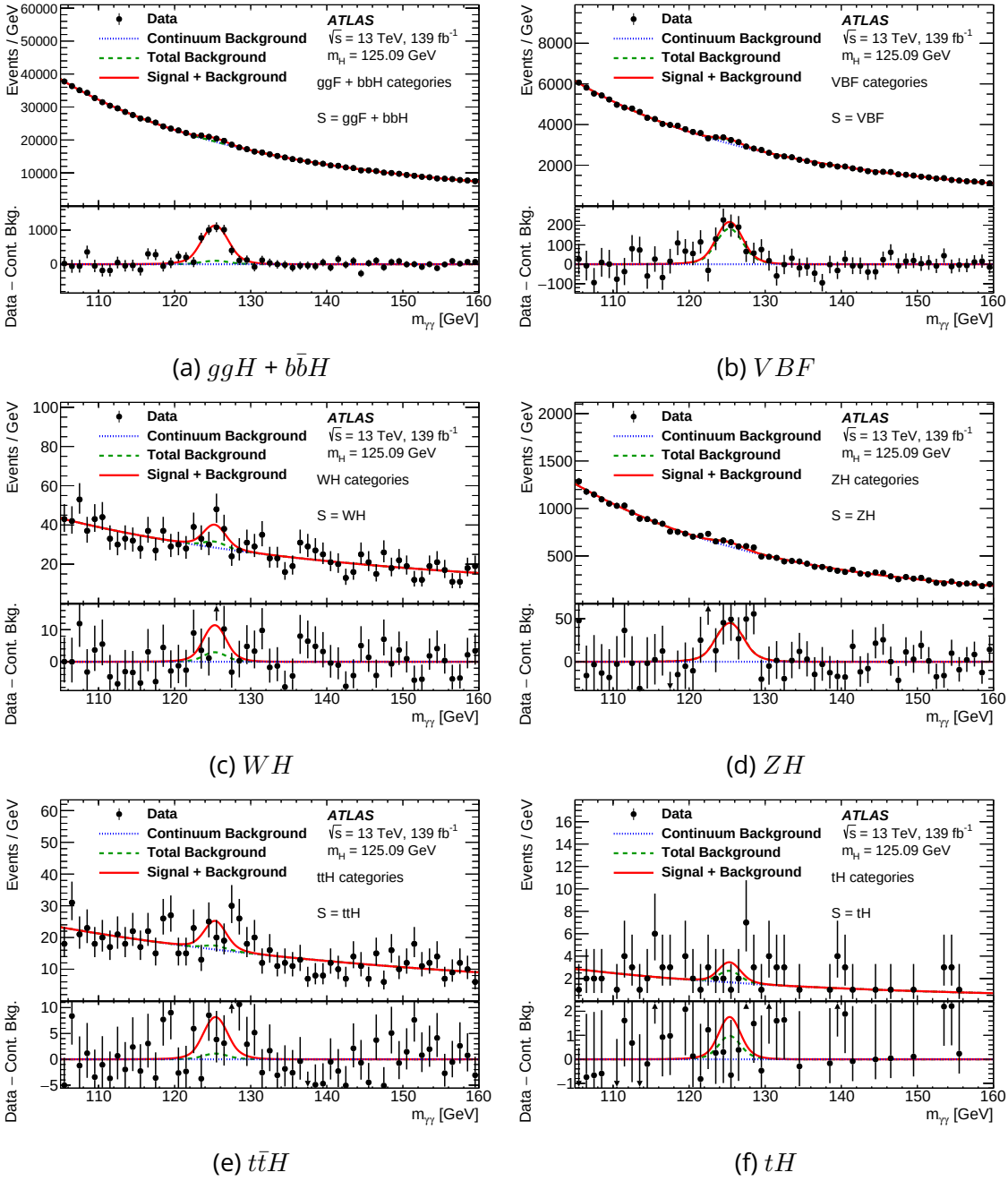

(a) $ggH + b\bar{b}H$ (b) VBF

(c) WH (d) ZH

(e) $t\bar{t}H$ (f) tH

Figure 4.28: Distributions of diphoton invariant mass for events categorised to belong to a given production process. Errors on the points show the statistical uncertainty. Source: [39].

The results are provided in a few forms, representing various granularities of the STXS bins, including the inclusive one, 6 POI and 28 POI schemes. The latest one is also used for the interpretations and for the couplings combination. The measurements are reported as the signal strengths, which is defined as the ratio of the experimentally found cross-section to the SM prediction.

4.11.1 Inclusive

The inclusive signal strengths of the Higgs boson production is measured as:

$$\mu = 1.045^{+0.10}_{-0.09} = 1.045\ ^{+0.08}_{-0.07}(stat.)\ ^{+0.05}_{-0.05}(\text{theory syst.})\ ^{+0.03}_{-0.04}(\text{exp. syst.}), \tag{4.20}$$

where the dominant contribution to the systematic uncertainties are the photon energy resolution and photon efficiency uncertainty (2.8 % and 2.5%, respectively) from the experiment and QCD scale and $H \to \gamma\gamma$ branching ratio (3.6% and 3.0%) from theory.

Corresponding cross-section of the Higgs boson production and consecutive decay into a di-photon pair is measured to be:

$$\left(\sigma \times \mathcal{B}_{\gamma\gamma}\right)_{obs} = 121^{+10}_{-9}\ fb = 121 \pm 7(stat.)\ ^{+7}_{-6}(syst.)\ fb, \tag{4.21}$$

while from the SM scenario it is expected:

$$\left(\sigma \times \mathcal{B}_{\gamma\gamma}\right)_{exp} = 116 \pm 6\ fb. \tag{4.22}$$

The cross-sections of each truth-bin σ_t are deduced from the unfolding procedure, using the formulae below, showing the dependency of number of events in an observed category c as a sum over all the truth-bins t, luminosity $\mathcal{L}$, and acceptance, efficiency matrices ϵ_{tc} and A_{tc}:

$$n_s^c = \sum_t \sigma_t \epsilon_{tc} A_{tc} \mathcal{L} \tag{4.23}$$

4.11.2 Production modes

The next level of the finer granularity is the measurements of production modes of the Higgs boson: ggH, VBF, WH, ZH, $t\bar{t}H$ and tH. The best-fit values along with their uncertainties are depicted on Fig. 4.29, with the covariance matrix shown on Fig. 4.30.

Numerical values of the cross-sections are reported in Table 4.7. This measurement corresponds to a p-value of 55%. Current precision for the ggH and VBF processes is no more limited by statistics but has similar contributions from the statistical and systematic uncertainties. Lack of statistics still dominates the electroweak (WH, ZH) and top ($t\bar{t}H$, þ) processes.

Process ($\lvert y_H\rvert < 2.5$)	Value [fb]	Uncertainty [fb] Total	Stat.	Syst.	SM pred. [fb]
ggH +$b\bar{b}H$	106	± 10	± 8	± 6	102 ± 6
VBF	9.5	$^{+2.2}_{-2.0}$	$^{+1.5}_{-1.4}$	$^{+1.7}_{-1.4}$	8.0 ± 0.2
WH	4.2	$^{+1.5}_{-1.4}$	$^{+1.5}_{-1.4}$	$^{+0.4}_{-0.2}$	2.8 ± 0.1
ZH	-0.4	$^{+1.1}_{-1.0}$	$^{+1.1}_{-0.9}$	$^{+0.2}_{-0.3}$	1.8 ± 0.1
$t\bar{t}H$	1.0	$^{+0.4}_{-0.3}$	$^{+0.4}_{-0.3}$	± 0.1	1.1 ± 0.1
tH	0.5	$^{+0.8}_{-0.6}$	$^{+0.8}_{-0.6}$	$^{+0.3}_{-0.2}$	$0.2^{+0.01}_{-0.02}$

Table 4.7: Best-fit values and breakdown of their uncertainties for the production cross sections of the Higgs boson times the $H \to \gamma\gamma$ branching ratio. SM predictions are obtained from the prediction of [113], multiplied by an acceptance factor for the region $|y_H| < 2.5$, computed using the Higgs boson simulation samples described in Section 4.3. Source: [39].

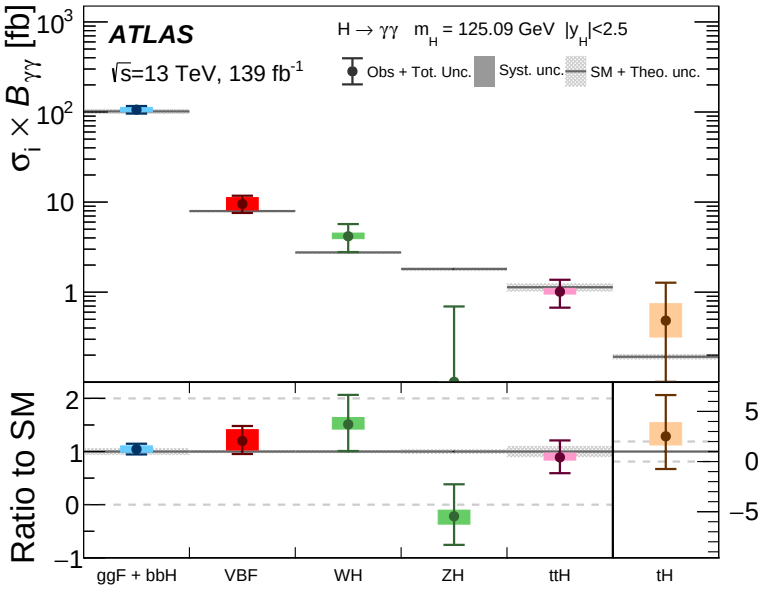

Figure 4.29: Best-fit values for the cross-sections ($|y_H| < 2.5$) in the 6 POI regime. Values are shown as the ratio to the SM prediction. Source: [39].

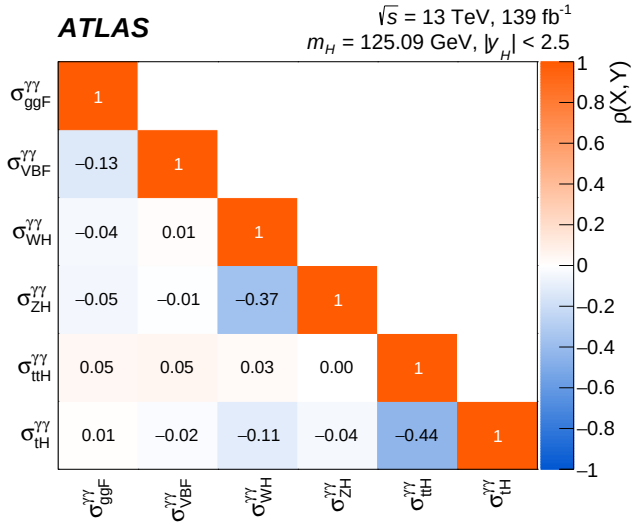

Figure 4.30: Observed covariance matrix of the measurement in the 6 POI scheme of production cross-section times $H \to \gamma\gamma$ branching ratio. The largest correlations are between the WH and ZH ($t\bar{t}H$ and þ) modes due to experimental difficulty to distinguish the double lepton decays of the Z-boson from semi-leptonic decays of W-boson (a possibility to miss one top-quark). Source: [39].

Sensitivities of the production modes signal strengths measurements

An additional cross-check on the best-fit value and its uncertainty for each POI can be done by examining the section of the likelihood curve for this variable. Ensuring a continuum surface with no anomalies around the global minimum, one can prevent possible issues in the fit.

Furthermore, the likelihood surface can be used to graphically deduce confidence intervals (Section A.6.2): 68% and 95%, which are mainly used.
To compute the NLL at a given value of POI θ^i $(\ln(\theta^i))$, one needs to fix $\theta \equiv \theta^i$, leaving other parameters floated (implying no constraints on their values) and to perform a fit. Result of 1D likelihood scans are shown on the Fig. 4.31.

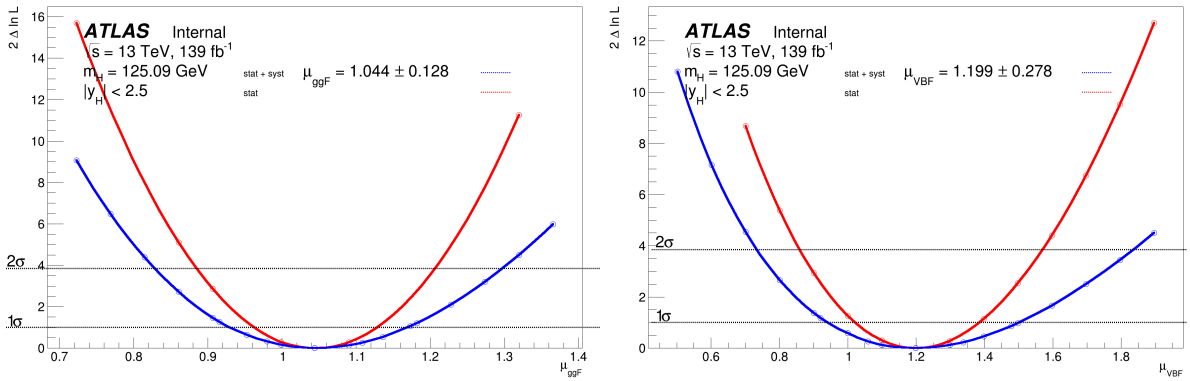

(a) ggH (b) VBF

Figure 4.31: Likelihood scans in the 6 POI scheme. The red curve shows the stat-only distribution of $2\Delta\ln\mathcal{L}$. (systematic uncertainties are neglected by fixing their central values to those observed in the real data). The blue curve represents the full likelihood, where no parameters are fixed.

The simultaneous 2D scans of the ggF (σ_{ggF}) and VBF (σ_{VBF}) cross-sections are given by Fig. 4.32.

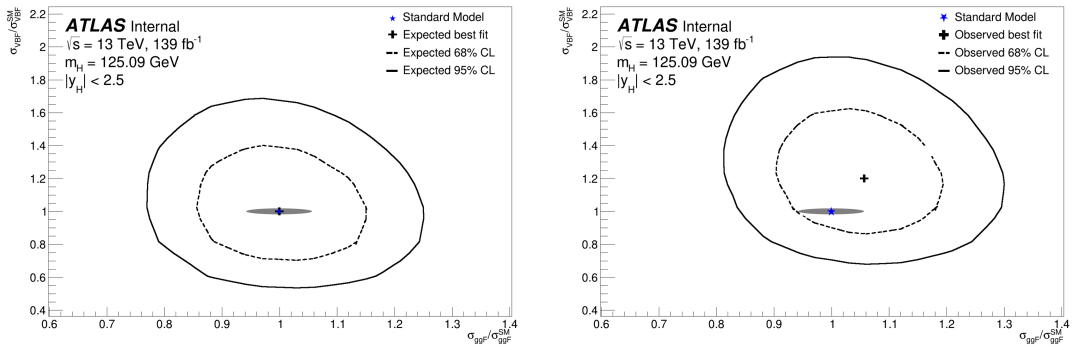

Figure 4.32: 2D likelihood contours span over $ggH \times VBF$ cross-sections. The left (right) figure shows the expected (observed) results. The black cross represents the best-fit value. The blue star stands to the SM value. The possible misknowledge on the SM cross-sections are indicated by the gray band. The two contours show the 68% and 95% Confidence Limits in black solid and dashed, respectively.

Significances

Significances of the observation of various production modes are computed in the units of sigma using the likelihood-based formula (Section A.6.6). Therefore, to compute the significance for

a given production mode, one needs to perform two fits: under the assumption of no signal (hence, $\mu = 0$) and with no assumption on the model (thus, the unconstrained likelihood). To check the validity of the analysis, both the observed (over the actual data sample) and the expected (over the Asimov dataset) significances (Table 4.8) are computed. No anomalies are found.

Process	Significance	
	Observed	Expected
ggH	11.7	12.0
VBF	6.8	6.5
WH	3.5	2.6
ZH	0	0
$t\bar{t}H$	3.1	3.7
tH	0.75	0.39

Table 4.8: Significances of production signal strength in the 6 POI scheme.

Limits

Following the prescription on the statistical limit (Section A.6.4), a dedicated study has been conducted to obtain limit on the signal strength of the tH production mode. The expected limit on the signal strength value is 5.89 and the observed one is $8.41\times$ SM.

4.11.3 STXS

Measurements of the 28 truth-bins are given in Fig 4.33 and Table 4.9. Their correlation is illustrated in Fig. 4.34.

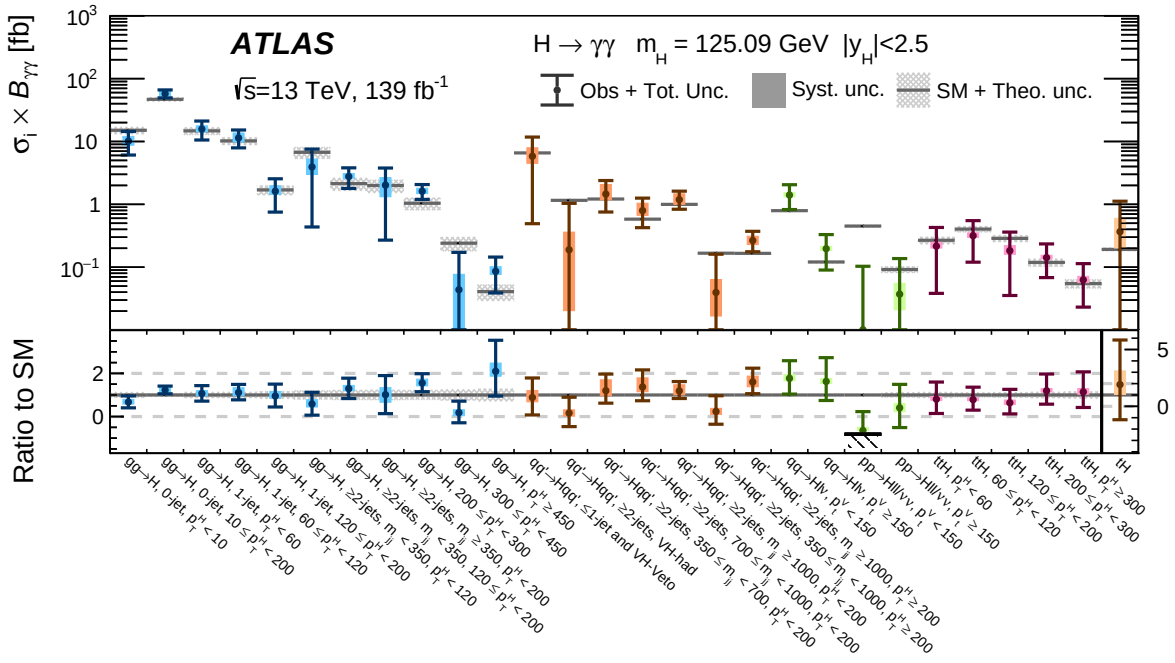

Figure 4.33: Observed cross-sections in units of their SM values for 28 POI scheme obtained in a simultaneous fit. Source: [39].

STXS region ($\sigma_i \times \mathcal{B}_{\gamma\gamma}$)	Value [fb]	Uncertainty [fb] Total	Stat.	Syst.	SM prediction [fb]
$gg \to H$ (0-jet, $p_{\mathrm{T}}^H < 10$ GeV)	10.2	$^{+4.3}_{-4.1}$	± 3.8	$^{+1.9}_{-1.4}$	$15.09^{+1.97}_{-1.96}$
$gg \to H$ (0-jet, $p_{\mathrm{T}}^H \geqslant 10$ GeV)	57.64	$^{+8.6}_{-8.1}$	± 7.0	$^{+4.93}_{+4.09}$	$46.92^{+3.44}_{-3.47}$
$gg \to H$ (1-jet, $0 \leq p_{\mathrm{T}}^H < 60$ GeV)	15.79	$^{+5.38}_{+5.22}$	$^{+4.99}_{+4.98}$	$^{+2.02}_{+1.59}$	$14.78^{+2.01}_{-2.01}$
$gg \to H$ (1-jet, $60 \leq p_{\mathrm{T}}^H < 120$ GeV)	11.40	$^{+3.84}_{+3.47}$	$^{+3.10}_{+3.09}$	$^{+2.28}_{+1.59}$	$10.24^{+1.41}_{-1.41}$
$gg \to H$ (1-jet, $120 \leq p_{\mathrm{T}}^H < 200$ GeV)	1.62	$^{+0.9}_{-0.9}$	$^{+0.86}_{+0.85}$	$^{+0.36}_{+0.19}$	$1.70^{+0.29}_{-0.29}$
$gg \to H$ ($\geqslant$ 2-jets, $m_{jj} < 350$ GeV , $p_{\mathrm{T}}^H < 120$ GeV)	3.93	$^{+3.64}_{+3.49}$	$^{+3.39}_{+3.36}$	$^{+1.33}_{+0.95}$	$6.74^{+1.41}_{-1.41}$
$gg \to H$ ($\geqslant$ 2-jets, $m_{jj} < 350$ GeV , $120 \leq p_{\mathrm{T}}^H < 200$ GeV)	2.78	$^{+1.04}_{+0.99}$	$^{+0.99}_{+0.96}$	$^{+0.32}_{+0.21}$	$2.14^{+0.49}_{-0.49}$
$gg \to H$ ($\geqslant$ 2-jets, $m_{jj} \geqslant 350$ GeV , $p_{\mathrm{T}}^H < 200$ GeV)	2.02	$^{+1.76}_{+1.75}$	$^{+1.64}_{+1.61}$	$^{+0.65}_{+0.70}$	$1.99^{+0.47}_{-0.47}$
$gg \to H$ ($200 \leq p_{\mathrm{T}}^H < 300$ GeV)	1.62	$^{+0.45}_{+0.42}$	$^{+0.41}_{+0.39}$	$^{+0.19}_{+0.14}$	$1.04^{+0.23}_{-0.23}$
$gg \to H$ ($300 \leq p_{\mathrm{T}}^H < 450$ GeV)	0.04	$^{+0.13}_{+0.11}$	$^{+0.12}_{+0.11}$	$^{+0.03}_{+0.03}$	$0.24^{+0.06}_{-0.06}$
$gg \to H$ ($p_{\mathrm{T}}^H \geqslant 450$ GeV)	0.09	$^{+0.06}_{+0.05}$	$^{+0.06}_{+0.05}$	$^{+0.02}_{+0.01}$	$0.04^{+0.01}_{-0.01}$
$qq' \to Hqq'$ VH-veto	5.83	$^{+5.94}_{+5.34}$	$^{+5.55}_{+5.17}$	$^{+2.12}_{+1.33}$	$6.59^{+0.14}_{-0.15}$
$qq' \to Hqq'$ VH-Had	0.19	$^{+0.85}_{+0.73}$	$^{+0.83}_{+0.71}$	$^{+0.17}_{+0.17}$	$1.16^{+0.04}_{-0.04}$
$qq' \to Hqq'$ ($\geqslant$ 2-jets, $350 \leq m_{jj} < 700$ GeV , $0 \leq p_{\mathrm{T}}^H < 200$ GeV)	1.46	$^{+0.94}_{+0.70}$	$^{+0.71}_{+0.64}$	$^{+0.61}_{+0.29}$	$1.22^{+0.03}_{-0.03}$
$qq' \to Hqq'$ ($\geqslant$ 2-jets, $700 \leq m_{jj} < 1000$ GeV , $0 \leq p_{\mathrm{T}}^H < 200$ GeV)	0.80	$^{+0.46}_{+0.37}$	$^{+0.39}_{+0.35}$	$^{+0.25}_{+0.13}$	$0.58^{+0.02}_{-0.02}$
$qq' \to Hqq'$ ($\geqslant$ 2-jets, $m_{jj} \geqslant 1000$ GeV , $0 \leq p_{\mathrm{T}}^H < 200$ GeV)	1.19	$^{+0.43}_{+0.35}$	$^{+0.33}_{+0.30}$	$^{+0.28}_{+0.19}$	$1.00^{+0.03}_{-0.03}$
$qq' \to Hqq'$ ($\geqslant$ 2-jets, $350 \leq m_{jj} < 1000$ GeV , $p_{\mathrm{T}}^H \geqslant 200$ GeV)	0.04	$^{+0.12}_{+0.10}$	$^{+0.12}_{+0.10}$	$^{+0.02}_{+0.02}$	$0.17^{+0.00}_{-0.00}$
$qq' \to Hqq'$ ($\geqslant$ 2-jets, $m_{jj} \geqslant 1000$ GeV , $p_{\mathrm{T}}^H \geqslant 200$ GeV)	0.27	$^{+0.11}_{+0.09}$	$^{+0.10}_{+0.08}$	$^{+0.05}_{+0.04}$	$0.17^{+0.00}_{-0.00}$
$qq \to H\ell\nu$ ($0 \leq p_{\mathrm{T}}^V < 150$ GeV)	1.41	$^{+0.65}_{+0.58}$	$^{+0.63}_{+0.57}$	$^{+0.14}_{+0.09}$	$0.79^{+0.02}_{-0.02}$
$qq \to H\ell\nu$ ($p_{\mathrm{T}}^V \geqslant 150$ GeV)	0.20	$^{+0.13}_{+0.11}$	$^{+0.13}_{+0.11}$	$^{+0.02}_{+0.01}$	$0.12^{+0.00}_{-0.00}$
$pp \to H\ell\ell$ ($0 \leq p_{\mathrm{T}}^V < 150$ GeV)	-0.29	$^{+0.40}_{+0.08}$	$^{+0.39}_{+0.08}$	$^{+0.07}_{+0.00}$	$0.45^{+0.02}_{-0.02}$
$pp \to H\ell\ell$ ($p_{\mathrm{T}}^V \geqslant 150$ GeV)	0.04	$^{+0.10}_{+0.08}$	$^{+0.10}_{+0.08}$	$^{+0.02}_{+0.02}$	$0.09^{+0.01}_{-0.01}$
$t\bar{t}H$ ($0 \leq p_{\mathrm{T}}^H < 60$ GeV)	0.22	$^{+0.21}_{+0.18}$	$^{+0.21}_{+0.18}$	$^{+0.03}_{+0.01}$	$0.27^{+0.04}_{-0.04}$
$t\bar{t}H$ ($60 \leq p_{\mathrm{T}}^H < 120$ GeV)	0.32	$^{+0.23}_{+0.20}$	$^{+0.23}_{+0.20}$	$^{+0.04}_{+0.02}$	$0.40^{+0.04}_{-0.04}$
$t\bar{t}H$ ($120 \leq p_{\mathrm{T}}^H < 200$ GeV)	0.18	$^{+0.18}_{+0.15}$	$^{+0.18}_{+0.15}$	$^{+0.04}_{+0.02}$	$0.29^{+0.04}_{-0.04}$
$t\bar{t}H$ ($200 \leq p_{\mathrm{T}}^H < 300$ GeV)	0.14	$^{+0.09}_{+0.07}$	$^{+0.09}_{+0.07}$	$^{+0.01}_{+0.01}$	$0.12^{+0.02}_{-0.02}$
$t\bar{t}H$ ($p_{\mathrm{T}}^H \geqslant 300$ GeV)	0.06	$^{+0.05}_{+0.04}$	$^{+0.05}_{+0.04}$	$^{+0.01}_{+0.01}$	$0.06^{+0.01}_{-0.01}$
tH	0.37	$^{+0.76}_{+0.60}$	$^{+0.72}_{+0.57}$	$^{+0.23}_{+0.17}$	$0.19^{+0.01}_{-0.02}$

Table 4.9: Best-fit values and uncertainties for the production cross-section times $H \to \gamma\gamma$ branching ratio ($\sigma_i \times \mathcal{B}_{\gamma\gamma}$) in each STXS region. The values for the ggH process also include the contributions from $b\bar{b}H$ production. Source: [39].

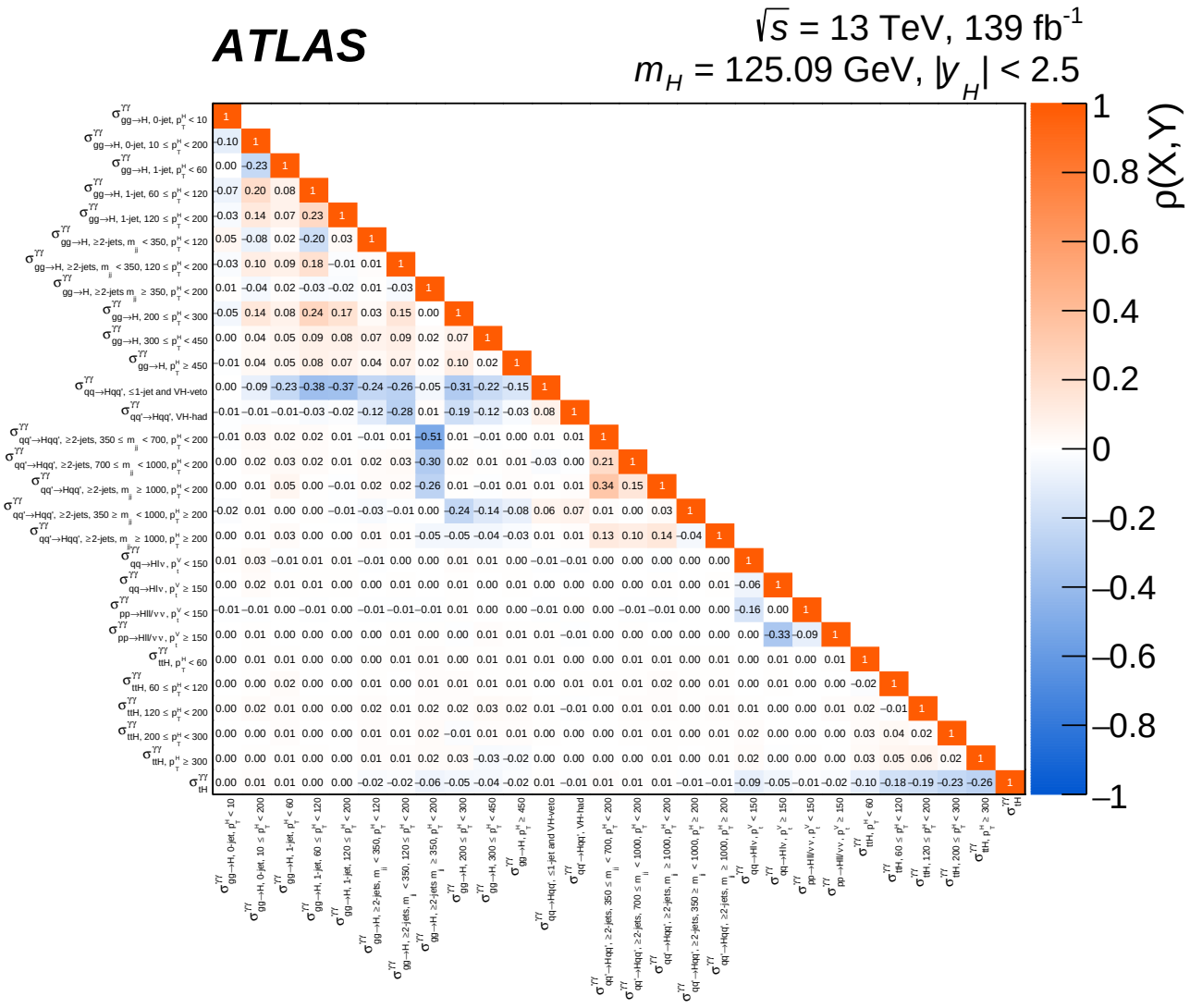

Figure 4.34: Observed correlation matrix between the STXS cross-sections in the 28 POI scheme. Source: [39].

4.12 κ-framework interpretation

Another way of probing the Higgs boson properties is to study its unique couplings, which are strictly defined in the SM by the masses of the particles, leaving no free parameter to fit. To overcome this [113], one can introduce to each vertex containing the Higgs boson a multiplicative coupling parameter, κ, being equal to unity in the SM and to probe this value.

At the leading order[8], for a given process $i \to H \to f$, the Higgs boson production cross-section can be expressed as:

$$\sigma_i \mathcal{B}_{\gamma\gamma} = \frac{\kappa_i^2 \sigma_i^{SM} \cdot \kappa_f^2 \Gamma_f^{SM}}{\kappa_H^2 \Gamma_H^{SM}} \tag{4.24}$$

[8]Even though, computations of the cross-sections are done at higher orders.

where σ_i is the production cross-section of the $i \to H$ process, $\mathcal{B}_{\gamma\gamma}$- branching ration of the $H \to \gamma\gamma$ decay and $\Gamma^{\gamma\gamma}$ is its width, and $\Gamma_H(\kappa)$ is the total width of the Higgs boson. All these values are parametrised as a function of κ. The SM predictions for the branching ratio ($\mathcal{B}_{\gamma\gamma}$) and the process cross-section (σ_i) are computed from the highest available order in the QCD and EW couplings [113].

The parametrisation used (based on LO diagram for each process) is shown in Table 4.10.

Production cross section	Main interference	Effective modifier	Resolved modifier
σ(ggF)	t–b	κ_g^2	$1.040\,\kappa_t^2 + 0.002\kappa_b^2 - 0.038\,\kappa_t\kappa_b - 0.005\,\kappa_t\kappa_c$
σ(VBF)	-	-	$0.733\,\kappa_W^2 + 0.267\,\kappa_Z^2$
$\sigma(q\bar{q} \to ZH)$	-	-	κ_Z^2
$\sigma(gg \to ZH)$	t–Z	-	$2.456\,\kappa_Z^2 + 0.456\,\kappa_t^2 - 1.903\,\kappa_Z\kappa_t$ $- 0.011\,\kappa_Z\kappa_b + 0.003\,\kappa_t\kappa_b$
$\sigma(WH)$	-	-	κ_W^2
$\sigma(t\bar{t}H)$	-	-	κ_t^2
$\sigma(tHW)$	t–W	-	$A\,\kappa_t^2 + B\,\kappa_W^2 + C\,\kappa_t\kappa_W$, category-dependent
$\sigma(tHq)$	t–W	-	$A\,\kappa_t^2 + B\,\kappa_W^2 + C\,\kappa_t\kappa_W$, category-dependent
$\sigma(b\bar{b}H)$	-	-	κ_b^2
Partial and total decay widths			
$\Gamma^{\gamma\gamma}$	t–W	κ_γ^2	$1.589\,\kappa_W^2 + 0.072\,\kappa_t^2 - 0.674\,\kappa_W\kappa_t + 0.009\,\kappa_W\kappa$ $+ 0.008\,\kappa_W\kappa_b - 0.002\,\kappa_t\kappa - 0.002\,\kappa_t\kappa_\tau$
Γ^{gg}	t–b	κ_g^2	$1.111\,\kappa_t^2 + 0.012\,\kappa_b^2 - 0.123\,\kappa_t\kappa_b$
Γ_H	-	κ_H^2	$0.581\,\kappa_b^2 + 0.215\,\kappa_W^2 + 0.063\,\kappa_\tau^2$ $+ 0.026\,\kappa_Z^2 + 0.029\,\kappa_c^2 + 0.0023\,\kappa_\gamma^2$ $+ 0.0004\,\kappa_s^2 + 0.00022\,\kappa_\mu^2$ $+ 0.082\,(\Gamma^{gg}/\Gamma^{gg}_{\text{SM}})$

Table 4.10: Parametrisation of Higgs boson production cross sections σ_i, partial decay width and total width Γ_H, as functions of the coupling-strength modifiers κ. Category-dependent means that such a parametrisation is done independently for each category, with their own values of A, B and C. For the other production modes, the parametrisation is the same for all the categories targetting the given production mode. Source: [99].

A few couplings of the Higgs boson are examined:

- EW-bosons: $\kappa_\mathcal{W}$ and $\kappa_\mathcal{Z}$ to W- and Z boson, respectively. They are usually probed together as κ_V.
- Heavy fermions (t, b, c and τ, μ), usually probed together as κ_F.

A few options for parametrising the Higgs boson production via ggH channel and di-photon decay, which occur via a loop, are used:

- unresolved (effective), which by introducing effective couplings of the Higgs boson to gluons and photons (κ_g and κ_γ, respectively). In a sense, they parametrise the production and the decay modes of the Higgs.
- resolved: loop corrections are directly expressed in terms of actual couplings to various SM particles circulating in these loops. Parametrisations of observables (cross-sections,

decay widths) as a function of coupling modifiers at LO are shown in Table 4.10. Such an assumption is valid under the assumption that BSM particles do not have a significant effect on the kinematics of the corresponding process.

The $ggZH$ loop-process is always considered as the resolved, because at LO it occurs through a box, loop diagram.

Studies are performed in a few approaches:

- κ_t. Only coupling to the top-quark is tested.
- κ_g-κ_γ plane, probing effective couplings to the ggH and $H \to \gamma\gamma$ loops.
- $\kappa_\mathcal{V}$-$\kappa_\mathcal{F}$ plane, where a few universal couplings are introduced: to the EW vector bosons ($\kappa_V = \kappa_\mathcal{W} = \kappa_\mathcal{Z}$) and to the heavy fermions ($\kappa_\mathcal{F} = \kappa_t = \kappa_b = \kappa_c = \kappa_\tau = \kappa_\mu$).
- Ratios of the coupling modifiers, defined by the Eq. (4.25).

$$\begin{aligned} \kappa_{g\gamma} &= \kappa_g\kappa_\gamma/\kappa_H. \\ \lambda_{Vg} &= \kappa_V/\kappa_g. \\ \lambda_{tg} &= \kappa_t/\kappa_g. \end{aligned} \tag{4.25}$$

The λ_{Vg} and λ_{tg} parameters are introduced, since they do not depend any more on κ_H.

In all these four models, couplings to other particles are not modified (considered to be as in the SM, strictly equal to unity).

Results of the scans are shown by Fig. 4.35.

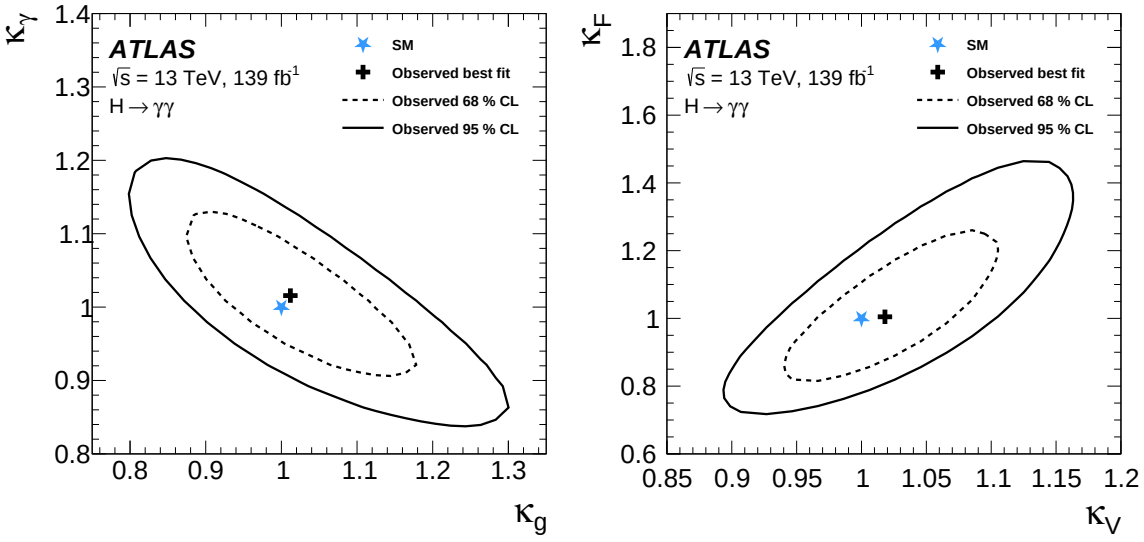

(a) (b)

Figure 4.35: Likelihood scans in the (a) gluon-photon and (b) vector bosons-fermions effective couplings. Source: [39].

4.13 Conclusion

The $H \to \gamma\gamma$ channel is one of the most precise channels for the Higgs boson measurements, given a good resolution of the electromagnetic calorimeter. The results are presented in various granularities, from the inclusive measurement to the STXS one. The latest ones are interpreted in the κ-framework and in an EFT approach. The results are in agreement with the Standard Model.

5 - SMEFT and BSM interpretations

5.1 Introduction

Various experimental results give a hint that the current Standard Model of particle physics may not be the ultimate theory. If new physics exists at high energies, not reachable at the LHC, one can still get access to it via the low-energy[1] (Fig. 5.1) deviations. More generally, it would be interesting to test the structure of the Lagrangian.

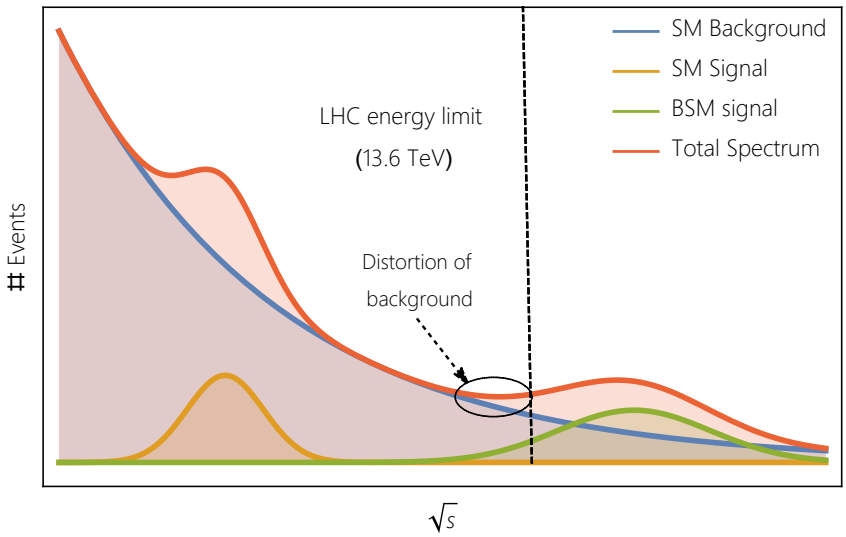

Figure 5.1: Illustration of a new hypothetical resonance (green), not reachable at the LHC. A deviation of the SM expected background shape may allow to access it.

The Standard Model Effective Field Theory (SMEFT) [114] provides a way to access hypothetical new physics (from an energy scale $\Lambda \gg q$) at the accessible energy scale. Therefore, a general effective SMEFT Lagrangian can be build up in terms of the SM operators, respecting its symmetries[2]:

$$\mathcal{L}_{SMEFT} = \mathcal{L}_{SM} + \sum_{d\geq 4} \sum_{k} \frac{\mathcal{C}_k^{(d)}}{\Lambda^{d-4}} \mathcal{O}_k^{(d)}, \tag{5.1}$$

where $\mathcal{L}_{SM}$ is the SM Lagrangian, $\mathcal{O}_k^{(d)}$ is a complete set of the basis operators[3] of dimension[4] d, usually chosen in the Warsaw basis [115] and $\mathcal{C}_k^{(d)}$ are Wilson coefficients[5] (WC for Wilson Coefficients), which describe strength of a given operator $\mathcal{O}_k^{(6)}$.

[1] compared to characteristic energies of BSM processes, which may be out of the LHC range.

[2] space-time translational invariance (energy-momentum conservation) and gauge-symmetries.

[3] Basis operators are the SM operators (matter and gauge fields) in all possible combinations, respecting the SM symmetries of the dimension d. Terms with higher-than-four dimension are scaled by the new physics scale Λ in a relevant power to obtain an energy dimension-4 expression.

[4] By dimension, the one of energy is assumed. All terms in a Lagrangian are dimension-4.

[5] Later on, index (d) will be omitted, since only the dimension-6 operators are considered.

The Taylor-expansion is general and can be used for matching to any given ultraviolet-complete BSM model (Section 5.8.3).

In this analysis, only the dimension-6 terms are considered. Terms suppressed by Λ (dimension-5)[6] and other odd powers are traditionally not considered, as they violate the baryon and lepton numbers and are not relevant to the Higgs physics. The higher even-order terms (dimension 8 or higher) are not considered, as expected to be minor with respect to the dimension-6 ones[7]. For the measurement, the energy scale Λ is set to 1 TeV and for any other arbitrary value Λ', the results on a given Wilson coefficient can be directly obtained from a scaling by the $(\Lambda'/\Lambda)^2$ factor.

Also, only CP-even operators with a potential impact on the STXS cross-sections above 0.1% (when $\mathcal{C}_i = 1$) are considered. Imaginary parts of the operators are not probed. For the differential cross-sections interpretation (Section 5.5), only c_{HG}, c_{tH} and c_{tG} are taken into account, since only these operators are found to be probed with a relatively good precision (Section 5.5).

The full Warsaw basis consists of more than 2000 operators, which cannot be constrained simultaneously. To reduce the amount of the parameters, some additional symmetry assumptions can be implied, given sensitivities to various parameters. Given that Higgs boson is much heavier than the light quarks, they are kinematically undistinguishable and the current analyses are not sensitive enough to them (for example, $H \to \bar{u}u$, $H \to \bar{d}d$ and $H \to \bar{s}s$ analyses have no sensitivity).

For this reason, the so-called top-scheme [116] makes use of these restrictions and treats in the same way: quarks of the first two generations $u = (u, c)$, $d = (d, s)$ Hence, one is left with 3 generations of leptons (e, μ, τ) and 4 types of quarks: u, d, t, b.

[6] There is only one dimension-5 term, Weinberg operator, $\left(\bar{\tilde{L}}H\right)\left(\tilde{H}^{\dagger}L\right)$, generating neutrino mass term and violating leptonic number.

[7] Potential impact of the dimension-8 terms is discussed in Section 5.7.2.

The corresponding operators with this symmetry are given in Table 5.1.

Wilson coefficient	Operator	Wilson coefficient	Operator
c_H	$(H^\dagger H)^3$	$c_{Qq}^{(1,1)}$	$(\bar{Q}\gamma_\mu Q)(\bar{q}\gamma^\mu q)$
$c_{H\Box}$	$(H^\dagger H)\Box(H^\dagger H)$	$c_{Qq}^{(1,8)}$	$(\bar{Q}T^a\gamma_\mu Q)(\bar{q}T^a\gamma^\mu q)$
c_G	$f^{abc}G_\mu^{a\nu}G_\nu^{b\rho}G_\rho^{c\mu}$	$c_{Qq}^{(3,1)}$	$(\bar{Q}\sigma^i\gamma_\mu Q)(\bar{q}\sigma^i\gamma^\mu q)$
c_W	$\epsilon^{IJK}W_\mu^{I\nu}W_\nu^{J\rho}W_\rho^{K\mu}$	$c_{Qq}^{(3,8)}$	$(\bar{Q}\sigma^iT^a\gamma_\mu Q)(\bar{q}\sigma^iT^a\gamma^\mu q)$
c_{HDD}	$\left(H^\dagger D^\mu H\right)^*\left(H^\dagger D_\mu H\right)$	$c_{qq}^{(3,1)}$	$(\bar{q}\sigma^i\gamma_\mu q)(\bar{q}\sigma^i\gamma^\mu q)$
c_{HG}	$H^\dagger H\, G_{\mu\nu}^A G^{A\mu\nu}$	$c_{tu}^{(1)}$	$(\bar{t}\gamma_\mu t)(\bar{u}\gamma^\mu u)$
c_{HB}	$H^\dagger H\, B_{\mu\nu}B^{\mu\nu}$	$c_{tu}^{(8)}$	$(\bar{t}T^a\gamma_\mu t)(\bar{u}T^a\gamma^\mu u)$
c_{HW}	$H^\dagger H\, W_{\mu\nu}^I W^{I\mu\nu}$	$c_{td}^{(1)}$	$(\bar{t}\gamma_\mu t)(\bar{d}\gamma^\mu d)$
c_{HWB}	$H^\dagger\tau^I H\, W_{\mu\nu}^I B^{\mu\nu}$	$c_{td}^{(8)}$	$(\bar{t}T^a\gamma_\mu t)(\bar{d}T^a\gamma^\mu d)$
$c_{Hl,11}^{(1)}$	$(H^\dagger i\overleftrightarrow{D}_\mu H)(\bar{l}_1\gamma^\mu l_1)$	$c_{Qu}^{(1)}$	$(\bar{Q}\gamma_\mu Q)(\bar{u}\gamma^\mu u)$
$c_{Hl,22}^{(1)}$	$(H^\dagger i\overleftrightarrow{D}_\mu H)(\bar{l}_2\gamma^\mu l_2)$	$c_{Qu}^{(8)}$	$(\bar{Q}T^a\gamma_\mu Q)(\bar{u}T^a\gamma^\mu u)$
$c_{Hl,33}^{(1)}$	$(H^\dagger i\overleftrightarrow{D}_\mu H)(\bar{l}_3\gamma^\mu l_3)$	$c_{Qd}^{(1)}$	$(\bar{Q}\gamma_\mu Q)(\bar{d}\gamma^\mu d)$
$c_{Hl,11}^{(3)}$	$(H^\dagger i\overleftrightarrow{D}_\mu^I H)(\bar{l}_1\tau^I\gamma^\mu l_1)$	$c_{Qd}^{(8)}$	$(\bar{Q}T^a\gamma_\mu Q)(\bar{d}T^a\gamma^\mu d)$
$c_{Hl,22}^{(3)}$	$(H^\dagger i\overleftrightarrow{D}_\mu^I H)(\bar{l}_2\tau^I\gamma^\mu l_2)$	$c_{tq}^{(1)}$	$(\bar{q}\gamma_\mu q)(\bar{t}\gamma^\mu t)$
$c_{Hl,33}^{(3)}$	$(H^\dagger i\overleftrightarrow{D}_\mu^I H)(\bar{l}_3\tau^I\gamma^\mu l_3)$	$c_{tq}^{(8)}$	$(\bar{q}T^a\gamma_\mu q)(\bar{t}T^a\gamma^\mu t)$
$c_{He,11}$	$(H^\dagger i\overleftrightarrow{D}_\mu H)(\bar{e}_1\gamma^\mu e_1)$	$c_{eH,22}$	$(H^\dagger H)(\bar{l}_2 e_2 H)$
$c_{He,22}$	$(H^\dagger i\overleftrightarrow{D}_\mu H)(\bar{e}_2\gamma^\mu e_2)$	$c_{eH,33}$	$(H^\dagger H)(\bar{l}_3 e_3 H)$
$c_{He,33}$	$(H^\dagger i\overleftrightarrow{D}_\mu H)(\bar{e}_3\gamma^\mu e_3)$	c_{uH}	$(H^\dagger H)(\bar{q}Y_u^\dagger u\widetilde{H})$
$c_{Hq}^{(1)}$	$(H^\dagger i\overleftrightarrow{D}_\mu H)(\bar{q}\gamma^\mu q)$	c_{tH}	$(H^\dagger H)(\bar{Q}\widetilde{H}t)$
$c_{Hq}^{(3)}$	$(H^\dagger i\overleftrightarrow{D}_\mu^I H)(\bar{q}\tau^I\gamma^\mu q)$	c_{bH}	$(H^\dagger H)(\bar{Q}Hb)$
c_{Hu}	$(H^\dagger i\overleftrightarrow{D}_\mu H)(\bar{u}_p\gamma^\mu u_r)$	c_{tG}	$(\bar{Q}\sigma^{\mu\nu}T^A t)\widetilde{H}\, G_{\mu\nu}^A$
c_{Hd}	$(H^\dagger i\overleftrightarrow{D}_\mu H)(\bar{d}_p\gamma^\mu d_r)$	c_{tW}	$(\bar{Q}\sigma^{\mu\nu}t)\tau^I\widetilde{H}\, W_{\mu\nu}^I$
$c_{HQ}^{(1)}$	$(H^\dagger i\overleftrightarrow{D}_\mu H)(\bar{Q}\gamma^\mu Q)$	c_{tB}	$(\bar{Q}\sigma^{\mu\nu}t)\widetilde{H}\, B_{\mu\nu}$
$c_{HQ}^{(3)}$	$(H^\dagger i\overleftrightarrow{D}_\mu^I H)(\bar{Q}\tau^I\gamma^\mu Q)$	$c_{ll,1221}$	$(\bar{l}_1\gamma_\mu l_2)(\bar{l}_2\gamma^\mu l_1)$
c_{Ht}	$(H^\dagger i\overleftrightarrow{D}_\mu H)(\bar{t}\gamma^\mu t)$		
c_{Hb}	$(H^\dagger i\overleftrightarrow{D}_\mu H)(\bar{b}\gamma^\mu b)$		

Table 5.1: Definition of the relevant EFT operators impacting the Higgs boson production and decay in top-scheme of the Warsaw basis. $G_{\mu\nu}^a$, $W_{\mu\nu}^I$ and $B_{\mu\nu}$ are the gauge field tensors of the strong and electroweak interactions, H is the Higgs field, T^a is the $SU(3)$ generator, and τ^I are the Pauli matrices. Source: [117].

5.2 Input channels

The SMEFT results are based on a combination of channels with Run 2 (Table 5.2). To compare the performance of the STXS interpretation with the corresponding differential cross-section (Section 5.5), the $H \to \gamma\gamma + H \to 4\ell$ combined datasets are used.

Analysis (production modes) Decay channel	Production mode	L [fb^{-1}]	Reference	Binning	SMEFT	2 HDM and (h) MSSM
$H \to \gamma\gamma$	(ggF,VBF,WH,ZH,$t\bar{t}H$,tH)	139	[39] [118]	STXS-1.2 differential	✓ ✓(subset)	✓
$H \to ZZ^*$	(ggF,VBF,WH + ZH,$t\bar{t}H$ + tH)	139	[119] [35]	STXS-1.2 differential	✓ ✓(subset)	✓
	($t\bar{t}H$ + $t\bar{t}H$- multilepton)	36.1	[120]	STXS-0		✓
$H \to \tau\tau$	(ggF,VBF,WH + ZH,$t\bar{t}H$ +tH)	139	[121]	STXS-1.2	✓	✓
	($t\bar{t}H$ + $t\bar{t}H$- multilepton)	36.1	[120]	STXS-0		✓
$H \to WW^*$	(ggF,VBF)	139	[42]	STXS-1.2	✓	✓
	(WH, ZH)	36.1	[122]	STXS-0		✓
	($t\bar{t}H$ + $t\bar{t}H$- multilepton)	36.1	[120]	STXS-0		✓
$H \to b\bar{b}$	(WH, ZH)	139	[123]	STXS-1.2	✓	✓
	(VBF)	126	[124]	STXS-1.2	✓	✓
	($t\bar{t}H$ + tH)	139	[125]	STXS-1.2	✓	✓
	(inclusive)	139	[126]	STXS-1.2	✓	
$H \to Z\gamma$	(inclusive)	139	[127]	STXS-0	✓	✓
$H \to \mu\mu$	(ggF + $t\bar{t}H$ + $t\bar{t}H$, VBF + WH + ZH)	139	[128]	STXS-0	✓	✓

Table 5.2: Summary of input analyses used for the EFT reinterpretation. All the channels used for the STXS SMEFT interpretation are also used for the mapping SMEFT to 2HDM (Section 5.8). Source: [117].

The STXS granularities along with their signal strengths best-fit-values and uncertainties are shown on Fig. C.1, C.2, C.3.

Independent SMEFT results are obtained using only the STXS combination of all the available channels (which are marked in Table 5.2). The BSM interpretation is performed only for the STXS combination.

The $36\ fb^{-1}$ VH $\to WW$ and $t\bar{t}H-$multilepton analyses are not included in the STXS SMEFT combination as they are not expected to give a contribution on the constraints. The VH $\to cc$ analysis is added to the SMEFT combination to directly probe the Yukawa SMEFT modifier[8], however it is excluded from the BSM interpretation as not expected to contribute to the constraint. The $H \to b\bar{b}$ inclusive analysis is included to the SMEFT combination to improve constraining of the high p_T^H tails, but is excluded from the BSM analysis as considered to have a negligible effect.

5.3 Simulation of the SMEFT impact

Simulation of the EFT effects is made only for signal processes (Section C.6), neglecting the modifications of the background processes for each of the input analyses, as it has been shown to be valid with the current precision.

[8]Recently, another treatment of the branching ratio parametrisation has been adopted (see Section 5.3 on the treatment of the denominator in the Taylor expansion of the signal strength parametrisation), which led to exclusion of the VH $\to cc$ dataset. However, for most of the results in this thesis, the old treatment (including VH $\to cc$) is used.

Calculations of the tree-level processes are performed with SMEFTsim [129] package with top-symmetry, following the recommendation of the LHC EFT working group [130]. The following EW inputs are used:

- $G_F = 1.1663787 \times 10^{-5}$ GeV^{-2} which is the Fermi constant [131];
- $m_Z = 91.1876$ GeV [131];
- $m_W = 80.387$ GeV [132];

Since the SM and BSM processes are independent, the total matrix element consists of two independent contributions from the SM and BSM terms:

$$\mathcal{M} = \mathcal{M}_{SM} + \mathcal{M}_{BSM} \tag{5.2}$$

From the Taylor expansion of the BSM part of the matrix element (eq. 5.1), one gets:

$$\mathcal{M}_{BSM} = \mathcal{M}^{(6)}_{BSM} + \mathcal{O}(\Lambda^{-4}) \tag{5.3}$$

This leads to the following expression for the squared matrix element (proportional to the cross-section or width):

$$\sigma \propto |\mathcal{M}|^2 = \underbrace{|\mathcal{M}_{SM}|^2}_{\text{SM}} + \underbrace{2\mathcal{R}\{\mathcal{M}_{SM}\mathcal{M}^*_{BSM}\}}_{\text{SM-BSM interference}} + \underbrace{|\mathcal{M}_{BSM}|^2}_{\text{BSM}}, \tag{5.4}$$

where $\mathcal{R}(\cdot)$ represents the real part. Taking into account the decomposition of the Lagrangian (eq. 5.1), and truncating to order 6, one finds:

$$|\mathcal{M}|^2 \approx \underbrace{|\mathcal{M}_{SM}|^2}_{\text{SM}} + \underbrace{2\mathcal{R}\left\{\sum_k \mathcal{M}_{SM}\frac{\mathcal{C}^{(6)}_k}{\Lambda^2}\mathcal{M}^*_k\right\}}_{\text{SM-D6 interference}} + \underbrace{\sum_k \left(\frac{\mathcal{C}^{(6)}_k}{\Lambda^2}\right)^2 |\mathcal{M}_k|^2}_{\text{BSM, diagonal term}} + \underbrace{\sum_{i<j}\left(\frac{\mathcal{C}^{(6)}_i\mathcal{C}^{(6)}_j}{\Lambda^4}\right)\mathcal{M}_i\mathcal{M}^*_j}_{\text{BSM, Interference between WC}} \tag{5.5}$$

Therefore, cross-section consists of three terms, with the following notation:

$$\sigma = \sigma_{SM} + \sigma_{int} + \sigma_{BSM}. \tag{5.6}$$

In order to perform measurements of a set of Wilson coefficients $\mathcal{C}_i$, given an STXS signal strength μ_{STXS} (or corresponding values in the bins of differential cross-sections), it is required to parametrise $\mu_{\text{STXS}} = \mu_{\text{STXS}}(\mathcal{C}_i)$. By definition, signal strength in an STXS truth-bin is the ratio of the observed cross-section to the one predicted by the SM:

$$\mu^{STXS} = \frac{\sigma^{STXS}}{\sigma^{STXS}_{SM}} \tag{5.7}$$

with the STXS cross-sections deduced as:

$$\sigma^{STXS}_{i\to f} = \frac{N_{events}}{\epsilon\mathcal{B}(H\to f)\mathcal{L}} \tag{5.8}$$

where N_{events} is the total number of events observed, ϵ is the reconstructed efficiency times acceptance, $\mathcal{B}(H \to f)$ is the branching ratio of the final state f and $\mathcal{L}$ is luminosity. Presence of a new physics may potentially affect all the terms from the equation above, apart from

luminosity (which is measured independently and is a common characteristic of a physical run) and the observed number of events, since they are taken from data[9].

Hence, parametrisation $\mu_{\text{STXS}}(\mathcal{C}_i)$ is conditioned by the dependence on new physics of the acceptance times efficiency (Section 5.4.2) and branching ratio.

To account for the state-of-art computation of the SM cross-sections and reduce the perturbative QCD uncertainty, the SMEFT impact on a cross-section σ is expressed as a relative correction to the SM prediction:

$$\sigma = \sigma_{SM}^{\text{best known order}} \left(1 + \frac{\sigma_{int}^{LO}}{\sigma_{SM}^{LO}} + \frac{\sigma_{BSM}^{LO}}{\sigma_{SM}^{LO}}\right), \tag{5.9}$$

where σ_{int}^{LO} is the interference and σ_{BSM}^{LO} is the pure BSM contributions[10].

Taking into account the tiny width of the Higgs and its scalar nature, it is legitimate to use the narrow width approximation, neglecting the propagator correction[11]. In this way, the cross-section of a truth bin t, observed in the decay channel with final state f, takes the form:

$$(\sigma \times \mathcal{B})^{tf} = \sigma^t \times \mathcal{B}^f = \sigma^t \frac{\Gamma^{H\to f}}{\Gamma^H} = \underbrace{(\sigma_{SM}^t + \sigma_{int}^t + \sigma_{BSM}^t)}_{\text{production xs}} \frac{\overbrace{(\Gamma_{SM}^{H\to f} + \Gamma_{int}^{H\to f} + \Gamma_{BSM}^{H\to f})}^{\text{Partial decay width}}}{\underbrace{(\Gamma_{SM}^{H} + \Gamma_{int}^{H} + \Gamma_{BSM}^{H})}_{\text{Total Higgs Width}}} \tag{5.10}$$

Factorising out the SM terms, one finds

$$\sigma^t \frac{\Gamma^{H\to f}}{\Gamma^H} = \sigma_{SM}^t \frac{\Gamma_{SM}^{H\to f}}{\Gamma_{SM}^H} \underbrace{\left(1 + \frac{\sigma_{int}^t}{\sigma_{SM}^t} + \frac{\sigma_{BSM}^t}{\sigma_{SM}^t}\right)}_{\text{Impact on the production xs}} \frac{\overbrace{\left(1 + \frac{\Gamma_{int}^{H\to f}}{\Gamma_{SM}^{H\to f}} + \frac{\Gamma_{BSM}^{H\to f}}{\Gamma_{SM}^{H\to f}}\right)}^{\text{Impact on the partial decay width}}}{\underbrace{\left(1 + \frac{\Gamma_{int}^{H}}{\Gamma_{SM}^{H}} + \frac{\Gamma_{BSM}^{H}}{\Gamma_{SM}^{H}}\right)}_{\text{Impact on the total Higgs width}}} \tag{5.11}$$

where the interference ratios $\left(\frac{\sigma_{int}^t}{\sigma_{SM}^t}, \frac{\Gamma_{int}^{H\to f}}{\Gamma_{SM}^{H\to f}} \text{ and } \frac{\Gamma_{int}^{H}}{\Gamma_{SM}^{H}}\right)$ are suppressed by Λ^2 and have linear dependencies on the SMEFT operators, since they originate from the SM-D6 interference term in $\mathcal{M}$, which is linear in $\mathcal{C}$. The quadratic ones $\left(\frac{\sigma_{BSM}^t}{\sigma_{SM}^t}, \frac{\Gamma_{BSM}^{H\to f}}{\Gamma_{SM}^{H\to f}} \text{ and } \frac{\Gamma_{BSM}^{H}}{\Gamma_{SM}^{H}}\right)$ are suppressed by Λ^4 and have quadratic dependencies on the Wilson coefficients. Thus, the relevant ratios can be expressed as:

[9] The efficiency also gets modified by WC (Section 5.4.2).
[10] An assumption that the LO EFT corrections are valid at higher computational orders is made.
[11] And given that all the used measurements are performed on-shell.

$$\begin{aligned}
\frac{\sigma^t_{int}}{\sigma^t_{SM}} &= \sum_k \mathcal{A}^t_k \mathcal{C}_k & \qquad \frac{\sigma^t_{BSM}}{\sigma^t_{SM}} &= \sum_{k,j} \mathcal{B}^t_{kj} \mathcal{C}_k \mathcal{C}_j \\
\frac{\Gamma^{H\to f}_{int}}{\Gamma^{H\to f}_{SM}} &= \sum_k \mathcal{A}^f_k \mathcal{C}_k & \qquad \frac{\Gamma^{H\to f}_{BSM}}{\Gamma^{H\to f}_{SM}} &= \sum_{k,j} \mathcal{B}^f_{kj} \mathcal{C}_k \mathcal{C}_j \\
\frac{\Gamma^{H}_{int}}{\Gamma^{H}_{SM}} &= \sum_k \mathcal{A}^H_k \mathcal{C}_k & \qquad \frac{\Gamma^{H}_{BSM}}{\Gamma^{H}_{SM}} &= \sum_{k,j} \mathcal{B}^H_{kj} \mathcal{C}_k \mathcal{C}_j
\end{aligned} \tag{5.12}$$

where $\mathcal{A}^t_k$ is a constant factor expressing the linear variation of the cross-section of the Higgs boson production in the truth-bin t, conditioned by a Wilson coefficient $\mathcal{C}_k$ by the $2\mathcal{R}\{\mathcal{M}_{SM}\mathcal{M}^*_{BSM}\}$ term in eq. 5.4. The $\mathcal{A}^{H\to f}_k$ and $\mathcal{A}^H_k$ terms show the impact on the Higgs decay to the final state f width and the total width, respectively. More details on these coefficients and how they are estimated are given in Section 5.4.1. The $\mathcal{B}$ coefficients are also constant and describe the impact caused by the quadratic terms (by a simultaneous plugging-in of two Wilson coefficients: $\mathcal{C}_k$, $\mathcal{C}_j$, which can coincide).

Linear Parametrisation

Neglecting the quadratic terms in eq. 5.11 and taking into account definitions from eq. 5.12, one finds the following parametrisation of signal strength of the truth-bin t observed in the final state f[12]:

$$\mu^{tf} = \frac{(1+\mathcal{A}^t_k\mathcal{C}_k)\left(1+\mathcal{A}^f_k\mathcal{C}_k\right)}{(1+\mathcal{A}^H_k\mathcal{C}_k)} \approx \frac{1+\left(\mathcal{A}^t_k+\mathcal{A}^f_k\right)\mathcal{C}_k}{(1+\mathcal{A}^H_k\mathcal{C}_k)} \tag{5.13}$$

where the numerator is Taylor-expanded up to the linear terms.

Historically, it was traditionally used a Taylor expansion for the denominator, leading to a simple linear parametrisation of the signal strength:

$$\mu^{tf} = 1 + \left[\mathcal{A}^t_k + \mathcal{A}^{H\to f}_k - \mathcal{A}^H_k\right]\mathcal{C}_k \tag{5.14}$$

which is a linear function in all Wilson coefficients.

Close to the finalisation of the analysis, the initial version with a not-expanded denominator started to be used in order to be more precise:

$$\mu^{tf} = \frac{1+\left(\mathcal{A}^t_k+\mathcal{A}^f_k\right)\mathcal{C}_k}{(1+\mathcal{A}^H_k\mathcal{C}_k)} \tag{5.15}$$

Impact of various operators in the linear only and the quadratic[13] parametrisations is shown on Fig. 5.2.

[12] The sum symbol over the Wilson coefficients is omitted for simplicity (using Einstein convention).

[13] Later on, by "quadratic", one should always understand linear + quadratic parametrisation, which accounts for all the terms.

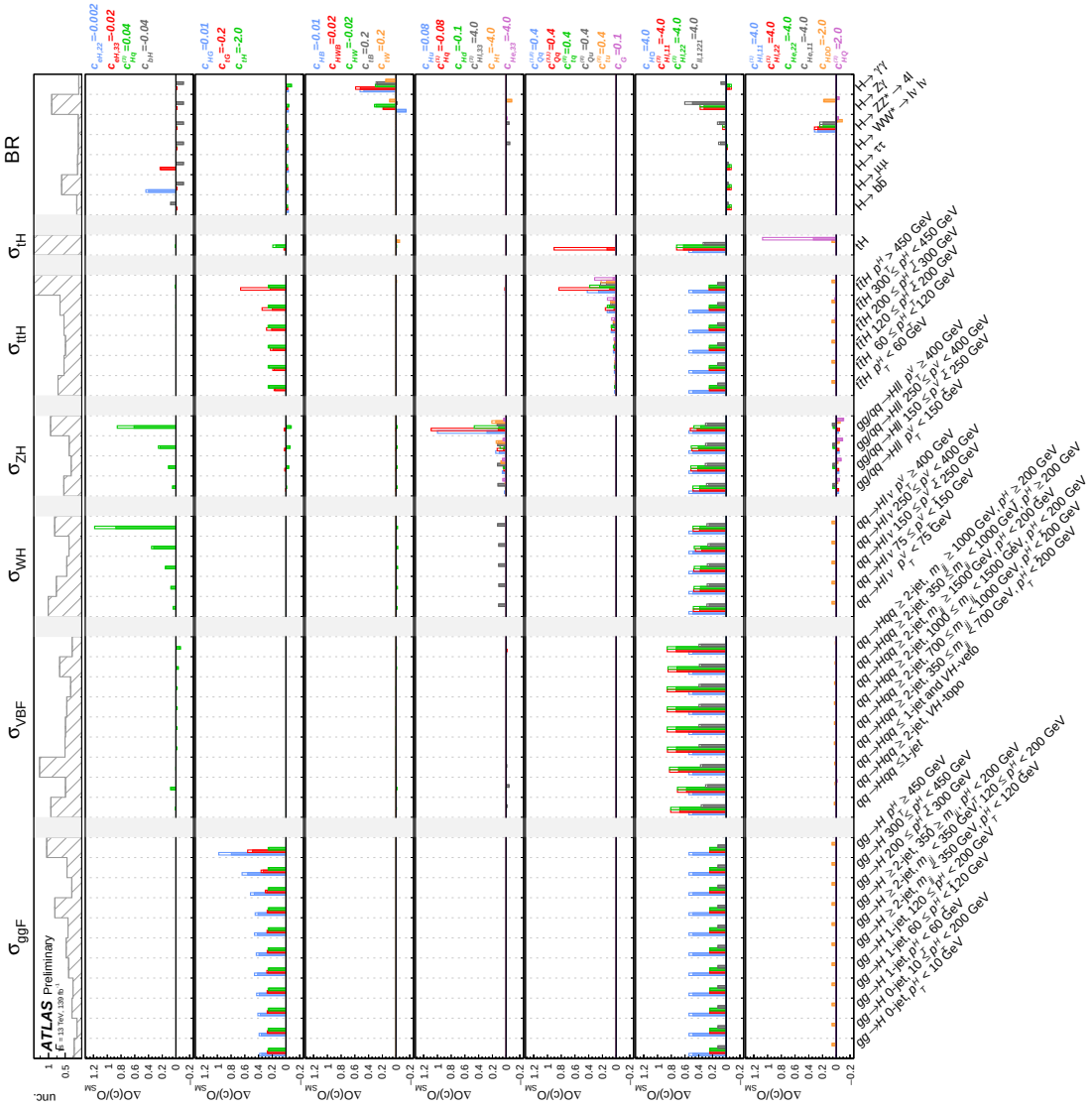

Figure 5.2: Impact of the most relevant operators on the STXS cross-sections and the branching ratios for the linearised (filled rectangles) and quadratic (transparent) SMEFT model. Vertical axis show ratios of the interference cross-sections to the SM ones, while a given Wilson coefficient takes value written on the right. Source: [117].

5.4 SMEFT STXS interpretation

5.4.1 Simulation of SMEFT effects

To obtain the $\mathcal{A}$ (linear) coefficients describing the STXS signal strength parametrisation, the following procedure is used:

- For each Wilson coefficient $\mathcal{C}_i$, generate 10^6 MC events with MadGraph for the squared matrix element containing only the interference term between the SM and BSM parts, setting value of $\mathcal{C}_i$ to unity[14].

[14]There are more precise approaches, when one generates three sets of events, setting the $\mathcal{C}_i$ to

- Compute the coefficients using eq. 5.12:

$$\mathcal{A}_i = \frac{\sigma_{int}|_{\mathcal{C}_i}}{\sigma_{SM}} \frac{1}{\mathcal{C}_i}, \tag{5.16}$$

  where $\sigma_{int}|_{\mathcal{C}_i}$ is the cross-section induced by the SM-D6 interference terms with the given value of the Wilson coefficient $\mathcal{C}_i$, σ_{SM} is the SM cross-section and $\mathcal{C}_i$ is the value of the Wilson coefficient used to generate these events (yielding to the cross-section $\sigma_{int}|_{\mathcal{C}_i}$);

- Compute parametrisation of the STXS signal strength of each truth-bin t for each channel f in terms of Wilson coefficients, using eq. 5.15.

5.4.2 Acceptance effects

Analyses use specific kinematic cuts to separate the signal region. Value of these cuts are optimised based on the MC simulation under the SM assumption. Therefore, presence of a new physics may alternate the acceptance and efficiency. Hence, one needs to account for their dependencies on the Wilson coefficients. It is found that analyses with more than two particles in the final state (mainly, $H \to ZZ^*$ and $H \to WW^*$) are significantly affected by the change in the acceptance caused by variation of the Wilson coefficients. Illustration of lepton kinematic distributions distortions are illustrated in Fig. 5.3.

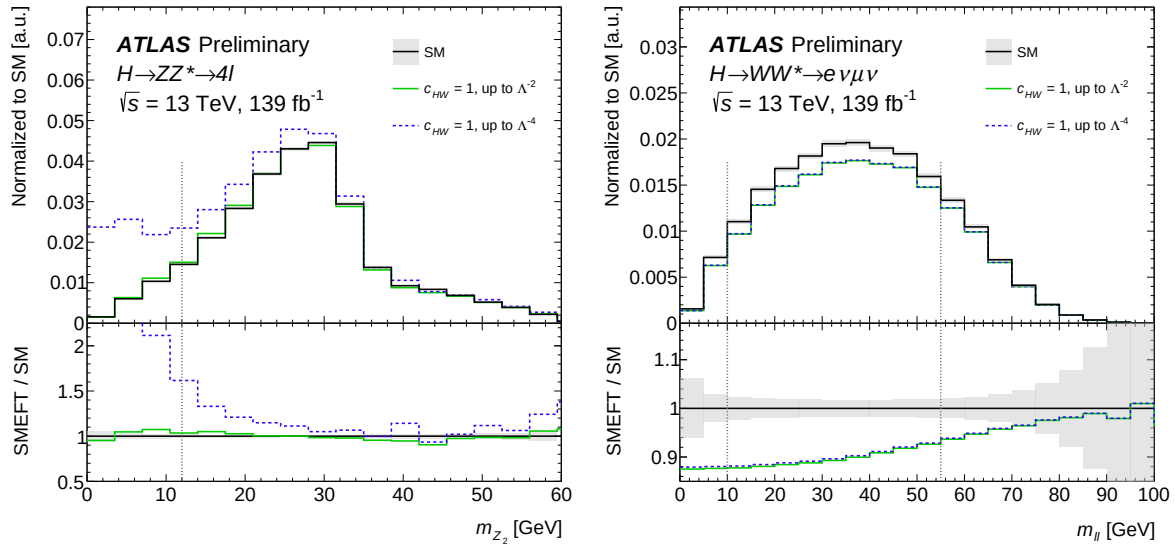

(a) $H \to ZZ^*$ (b) $H \to WW^*$

Figure 5.3: Distribution of $m_{\ell\ell}$ observable from (a) $H \to ZZ^*$ (for the sub-dominant Z) and (b) $H \to WW^*$ used in the analysis for the SM prediction and for different values of c_{HW}. Source: [117].

Following the original publication on the $H \to 4\ell$ EFT interpretation [133], the acceptance parametrisation is modelled by a multi-dimensional Lorentz function:

$$\frac{A^{EFT}(\mathcal{C}_i)}{A^{SM,LO}} = \alpha_0 + \frac{\alpha_1}{\beta_0 + \sum_i \left(\beta_i \cdot (\gamma_i + \mathcal{C}_i)^2\right)} \tag{5.17}$$

$\{-0.5, 0.1, 1.0\}$. Then, the value of the coefficient $\mathcal{A}$ is averaged over the three ones, standing for various values of $\mathcal{C}_i$.

where α_i, β_i and γ_i are numerical constants derived from the simulation. The sum is over all the Wilson coefficients considered.
To obtain the parametrisation of the acceptance from the equation (5.17), one needs to study the impact on the yields before and after the cuts:

$$A_i^{EFT,\ H\to X} = \frac{N_i^{EFT,\ H\to X,\ \text{after cuts}}}{N_i^{EFT,\ H\to X,\ \text{no cuts}}}, \tag{5.18}$$

with the yield $N_i^{EFT,H\to X}$ defined as[15]:

$$N_i = N_{\text{SM}} \cdot \left(1 + \frac{\sigma_{\text{int}}}{\sigma_{\text{SM}}} + \frac{\sigma_{\text{BSM}}}{\sigma_{\text{SM}}}\right) \cdot \frac{1 + \frac{\Gamma^{H\to X}_{\text{int}}}{\Gamma^{H\to X}_{\text{SM}}} + \frac{\Gamma^{H\to X}_{\text{BSM}}}{\Gamma^{H\to X}_{\text{SM}}}}{1 + \frac{\Gamma^{H}_{\text{int}}}{\Gamma^{H}_{\text{SM}}} + \frac{\Gamma^{H}_{\text{BSM}}}{\Gamma^{H}_{\text{SM}}}}. \tag{5.19}$$

Taking into account the definition of the cross-section and of ratios of width and performing a linear Taylor expansion, the following expression appears[16]:

$$\frac{A_i}{A_{SM}} = \frac{N_i^{\text{cuts}}}{N_i^{\text{no cuts}}} \cdot \frac{N_{SM}^{\text{no cuts}}}{N_{SM}^{\text{cuts}}} \tag{5.20}$$

Substituting expression for N_i, defined by eq. 5.19 and recalling definitions of the $\mathcal{A}$ coefficients[17], one finds:

$$\begin{aligned}\frac{A_i}{A_{SM}} &= \frac{N_{SM}^{\text{cuts}}\left(1 + \mathcal{A}_t^{\text{cuts}} + \mathcal{A}_f^{\text{cuts}} - \mathcal{A}_H^{\text{cuts}}\right)}{N_{SM}^{\text{cuts}}\left(1 + \mathcal{A}_t^{\text{no cuts}} + \mathcal{A}_f^{\text{no cuts}} - \mathcal{A}_H^{\text{no cuts}}\right)} \cdot \frac{N_{SM}^{\text{no cuts}}}{N_{SM}^{\text{cuts}}} \\ &\approx 1 + \mathcal{A}_t^{\text{cuts}} + \mathcal{A}_f^{\text{cuts}} - \mathcal{A}_H^{\text{cuts}} - \left(\mathcal{A}_t^{\text{no cuts}} + \mathcal{A}_f^{\text{no cuts}} - \mathcal{A}_H^{\text{no cuts}}\right)\end{aligned} \tag{5.21}$$

Then, the final expression for a number of events as a function of Wilson coefficients can be expressed as[18]:

$$\begin{aligned} N_i &= \sigma_i A_i \mathcal{L} \\ &= \underbrace{\sigma_{SM}\left(1 + \mathcal{A}_t + \mathcal{A}_f - \mathcal{A}_H\right)}_{\text{cross-section } \sigma_i} \\ &\cdot \underbrace{A_{SM}\left(1 + \mathcal{A}_t^{\text{cuts}} + \mathcal{A}_f^{\text{cuts}} - \mathcal{A}_H^{\text{cuts}} - \mathcal{A}_t^{\text{no cuts}} - \mathcal{A}_f^{\text{no cuts}} + \mathcal{A}_H^{\text{no cuts}}\right)}_{\text{Acceptance } A_i} \\ &\cdot \underbrace{\mathcal{L}}_{\text{Luminosity}} \\ &\propto \underbrace{\sigma_{SM} A_{SM} \mathcal{L}}_{\text{SM number of events}} \cdot (\text{corrections}) = N_{SM} \cdot (\text{corrections}) \end{aligned} \tag{5.22}$$

Expanding the dependence on $\mathcal{A}$:

[15] For simplicity, it will be denoted as N_i further on in the text.
[16] By A_i, one should understand A_i^{EFT} which is the acceptance caused by a Wilson Coefficient $\mathcal{C}_i$.
[17] Impact of the linear terms $\mathcal{A}$ should not be confused with the acceptance A.
[18] For simplicity, indexes of Wilson coefficients i and a sum over them is omitted.

$$
\begin{aligned}
N_i = N_{SM} \cdot \Big(1 + \Big[& \mathcal{A}_t + \mathcal{A}_f - \mathcal{A}_H \\
& + (\mathcal{A}_t^{\text{cuts}} - \mathcal{A}_t^{\text{no cuts}}) \\
& + \left(\mathcal{A}_f^{\text{cuts}} - \mathcal{A}_f^{\text{no cuts}}\right) \\
& - (\mathcal{A}_H^{\text{cuts}} - \mathcal{A}_H^{\text{no cuts}}) \\
\Big] \mathcal{C}_i \Big).
\end{aligned}
\tag{5.23}
$$

For the $H \to ZZ^*$ channel, impact of the acceptance effect on the production side is estimated to be small (less than 10%) for the STXS regions where the analysis has sensitivity, hence the $\mathcal{A}_t^{\text{cuts}}$ and $\mathcal{A}_t^{\text{no cuts}}$ terms have almost the same value and their difference can be safely neglected.

The $\mathcal{A}_H$ terms describe the dependence of the total Higgs width on the Wilson coefficients and come from the theoretical predictions, with no dependency on the analysis cuts. Therefore, the $(\mathcal{A}_H^{\text{cuts}} - \mathcal{A}_H^{\text{no cuts}})$ difference vanishes.

The remaining expression reduces to:

$$
N_{EFT} = N_{SM}\Big(1 + \left[\sum_i A_i^{\text{STXS}} + \sum_i \left[A_i^{H\to X} - A_i^{H}\right] + \sum_i \left[A_i^{H\to X,\text{ with cuts}} - A_i^{H\to X,\text{ no cuts}}\right]\right] c_i\Big). \tag{5.24}
$$

After all computations, for the $H \to ZZ^*$ channel for all STXS bins the same acceptance parametrisation is applied. For the $H \to WW^*$, there are two types of independent parametrisations: for the ggF and VBF production modes.

5.4.3 PCA sensitivity optimisation

With the available statistics, channels considered and the level of theoretical uncertainties[19], it is not possible to constrain reasonably well all Wilson coefficients. Nevertheless, it is possible to try to suppress the flat directions[20] in the EFT space, where there is no sensitivity. Furthermore, one may find the most sensitive directions. It can be done via a PCA[21] [134] (Principal component analysis) method (Fig. 5.4), which requires having a covariance matrix of the simultaneous fit of all Wilson coefficients.

[19] See ranking plots for the order of the dominant systematic uncertainties.

[20] Flat directions in the parameter space are those along which the likelihood variation is almost flat. Along them, uncertainty on the parameters is too high to make a reliable estimation.

[21] PCA is a statistical method, prescribing linear transformation of the input variables (rotation) to a new basis, which decorrelates the variables as much as possible.

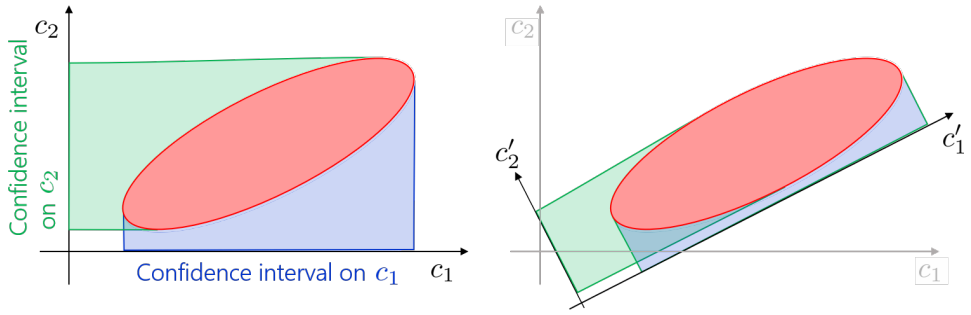

(a) (b)

Figure 5.4: Illustration of the PCA method. The data points are spread in the red region, leading to the constraint on the axes (a) showed by the blue and green shaded areas. Redefinition (b), here with a simple rotation, of the axes allows to identify the most informative directions, where the smallest part of the variance of the dataset is located.

Since this expected EFT covariance matrix cannot be directly evaluated due to the convergence problems, the sensitivity of the measurement can be estimated using the expected STXS covariance matrix (Fig. 5.5), translated to the EFT basis. It is possible because the STXS and the EFT bases are both orthogonal, hence the EFT covariance matrix can be obtained by propagating the parametrisation of the STXS cross-sections in terms of Wilson coefficients through the expected STXS covariance matrix as:

$$\mathcal{C}_{\text{EFT}}^{-1} = P^T \mathcal{C}_{\text{STXS}}^{-1} P, \tag{5.25}$$

where $\mathcal{C}_{\text{EFT}}^{-1}$ and $\mathcal{C}_{\text{STXS}}^{-1}$ are the inverses of covariances matrices of the Wilson coefficients measurement and the STXS fits. P is the transfer matrix from the STXS cross-sections to the EFT Wilson coefficient space.

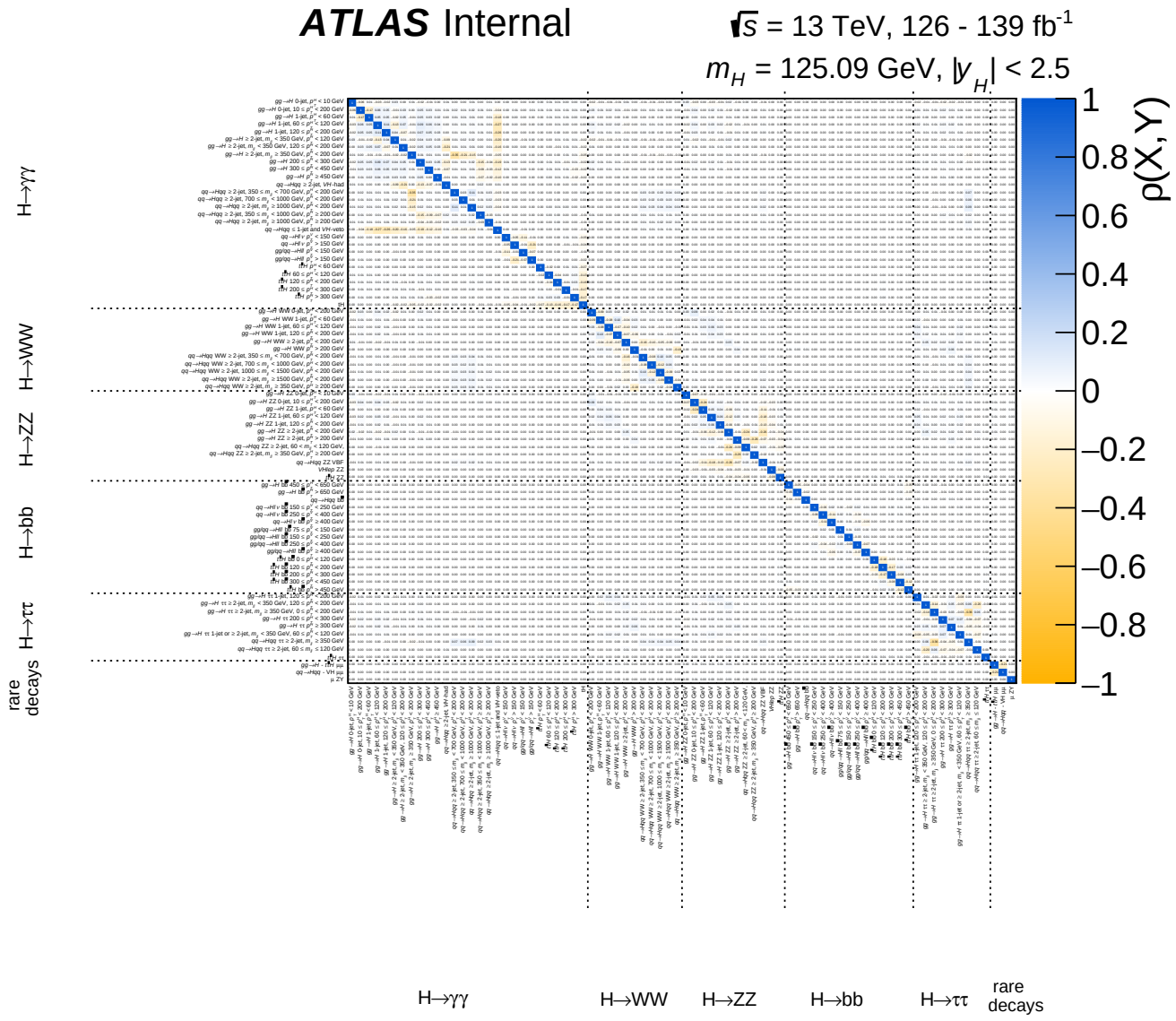

Figure 5.5: Expected covariance matrix of the combined STXS x BR measurement. Such split treats the categories from various final state independently. Source: [135].

To determine Wilson coefficients to which the fit is sensitive, the eigenvalues and eigenvectors of the inverse EFT covariance matrix (Fisher information) must be calculated. An eigenvalue e_i expresses uncertainty (variance) on the fit in the direction of the corresponding eigenvector e_i: $\sigma_{e_i} \propto \frac{1}{\sqrt{E_i}}$. Since the Wilson coefficients with uncertainties much larger that 1 cannot be measured, eigenvectors with eigenvalues $e_i < 0.1$ are omitted. Visualisation of the EV-decomposition of the Wilson coefficients used in the analysis is given on Fig. 5.6.

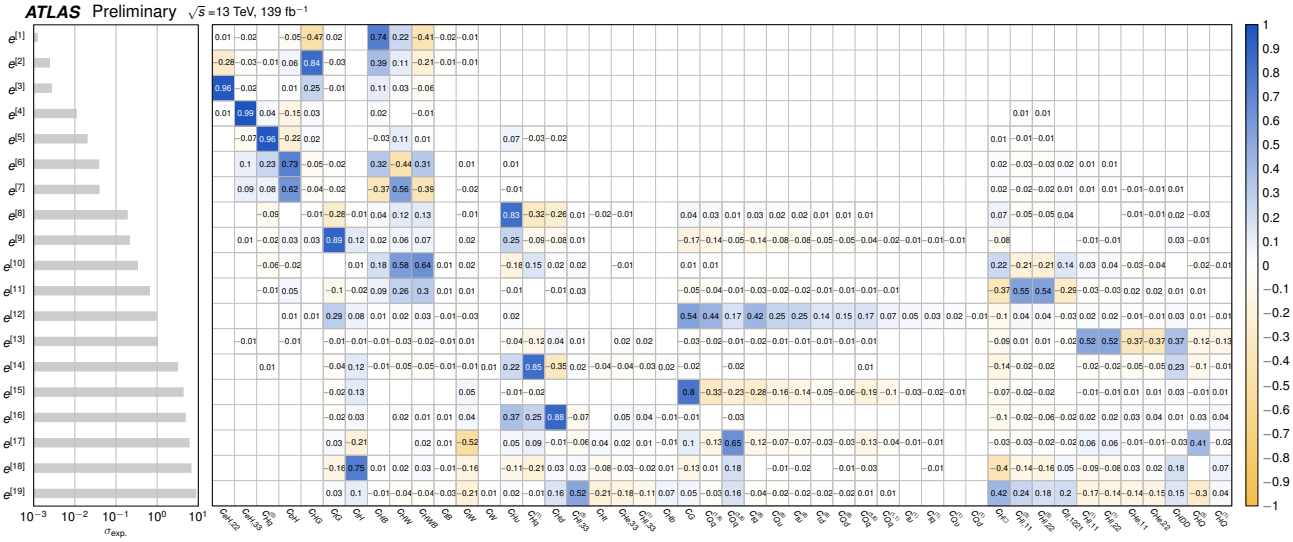

Figure 5.6: Transfer matrix from Warsaw basis to the eigen-vector basis. Left sub-plot illustrates expected uncertainty on eigenvectors. Source: [117].

Fit basis

In general, the PCA transformation mixes up all Wilson coefficients present in the analysis, hence it might be not easy for theorists to interpret the constraints on the eigenvectors. One way to preserve the physical interpretability, while still benefitting from the PCA increase of sensitivity, is to perform the PCA transformation only within groups of Wilson coefficients of the same physics thematic. The following groups are defined:

- $c_{eH,33}$, $c_{eH,22}$, c_{bH}[22] are the Yukawa coupling modifiers of the $H \to \tau\tau$, $H \to \mu\mu$, and $H \to b\bar{b}$ decays, respectively. They can be constrained separately from the respective Higgs channels that enter the combination. In the fit, there will still be residual correlations of these Wilson coefficients with other SMEFT ones, in particular for c_{bH} due to the large contribution to the total width modification.

- $c_{Hq^{(3)}}$, which affects both the WH and ZH production modes with an increasing impact over p_V^T, and is mostly constrained by the $VH(bb)$ analysis.

[22] Operators corresponding to the coefficients of the type $c_{eH,ii}$ (index i runs over flavours of leptons: 1 for electron, 2 for muon and 3 for tau) have the form: $\left(H^\dagger i\overleftrightarrow{D}_\mu H\right)(\bar{e}_i\gamma^\mu e_i)$. Due to the covariant derivative (containing B-fields, which after the EW-symmetry breaking become Z and W fields), it affects the coupling of the Higgs boson with leptons (electron, muon, tau) and weak bosons (and photons).

- e_{glob}: $c_{ll,221}$, $c_{Hl_{11}^{(3)}}$, $c_{Hl_{22}^{(3)}}$, $c_H\Box$ affect primarily the Fermi constant (as a shift) corresponding to an overall normalisation across different production modes. $c_{H\Box}$ is the Higgs propagator correction, affecting the overall normalization. These operators are grouped together to separate out the overall normalisation effects.

- e_{ggH}: c_{HG}, c_{tG} and c_{tH} are constrained by ggF and ttH. Due to the high correlation between them, it is necessary to perform a rotation. The rotation is close to an identity matrix because parameter space contains sensitivities with a different order of magnitude[23].

- e_{ttH}: The four fermion operators ($c_{tq^{(8)}}$, $c_{Qq^{(1,8)}}$, $c_{Qu^{(8)}}$, $c_{tu^{(8)}}$, $c_{Qq^{(3,1)}}$, $c_{Qd^{(8)}}$, $c_{td^{(8)}}$, $c_{Qq^{(1,1)}}$, $c_{tq^{(1)}}$, $c_{Qu^{(1)}}$, $c_{Qd^{(1)}}$) involving the top-quark, and the trilinear gluon coupling (c_G) affect $t\bar{t}H$ and the tH production modes and are grouped as having a similar impact with p_H^T. These operators are constrained by the $t\bar{t}H$ spectrum measured in $H \to \gamma\gamma$ and $H \to b\bar{b}$ channels and the separation of the tH production mode in $H \to \gamma\gamma$ also allows to constrain one direction in this operators group.

- $e_{H\gamma\gamma,Z\gamma}$: The operators c_{HW}, c_{HWB}, c_{HB}, c_{tW}, c_{tB} are constrained by the branching ratio modification of $H \to \gamma\gamma$ and $H \to Z\gamma$. There is also some residual sensitivity from VBF and VH to constrain a third direction in this group.

- e_{ZH}: The operators c_{Hu},$c_{Hq^{(1)}}$,c_{Hd},c_{Ht},$c_{Hl_{33}^{(1)}}$,$c_{He_{33}}$,$c_{Hl_{33}^{(3)}}$,c_{Hb} mainly affect the Higgs-neutral current interaction and also the propagator correction to Z-decay. These operators are grouped together and are mainly constrained by the $VH(bb)$ analysis.

- e_{Hll}: The operators $c_{Hl_{11}^{(1)}}$,$c_{Hl_{22}^{(1)}}$,$c_{He_{11}}$,$c_{He_{22}}$ mainly affect $H \to ZZ^* \to 4l$. The operator c_{HDD} affects both the Higgs normalisation as $(c_{H\Box} - c_{HDD}/4)$ and has a dedicate impact on the HZZ coupling. The operators $c_{HQ^{(3)}}$ and c_{HQ^1} affects both $H \to ZZ^* \to 4l$, $H \to WW^* \to l\nu l\nu$ and also VH production as propagator corrections to W and Z. It is grouped in the $H \to 4\ell$ channel as it has the highest correlation with this group.

Illustration of the transfer matrix from the Warsaw basis to the fit-basis is given by Fig. 5.7.

[23] Same effect can be seen in the eigenvectors decomposition in the differential cross-section analysis.

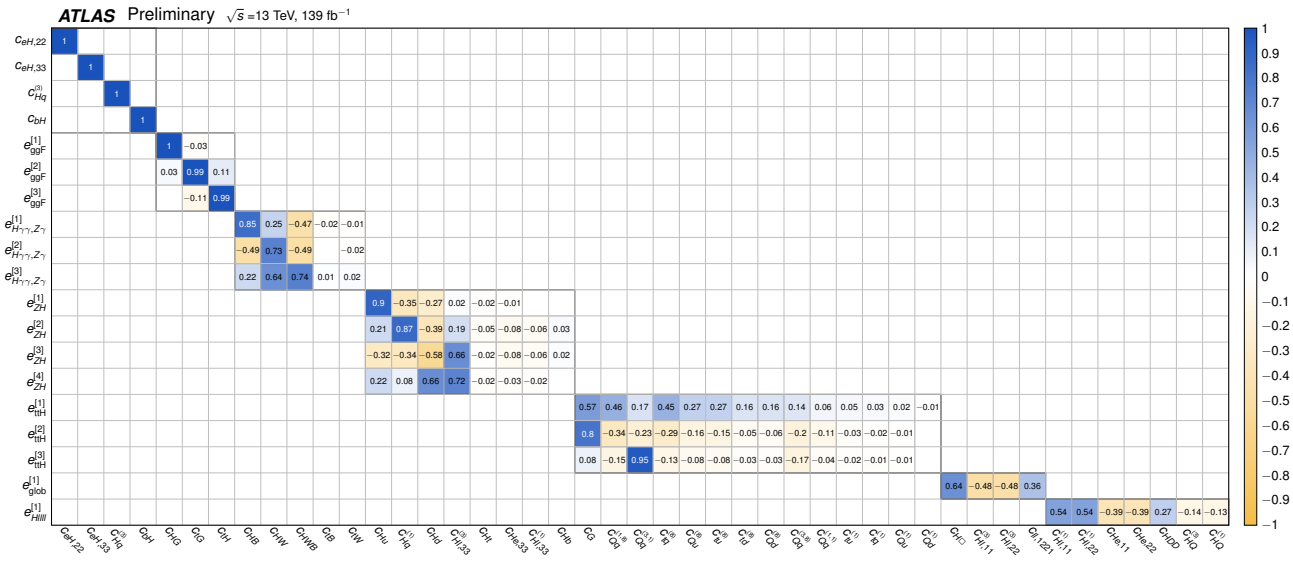

Figure 5.7: Transfer matrix to the fit-basis. Source: [117].

Impacts of these groups of parameters, that we denote as $\mathcal{C}'_j$, on the STXS cross-sections and the branching ratios are shown on Fig. C.6. On this plot, values of the Wilson coefficient groups are set to match their expected uncertainty in the linear SMEFT model.

5.5 SMEFT DIFF XS interpretations

For the differential cross-section EFT interpretation, only the available $H \to \gamma\gamma$ and $H \to ZZ^*$ channels are combined. Among various kinematic variables, it was found that the p_T^H spectrum is the most sensitive to the EFT effects. Particularly, the differential cross-section measurements are sensitive at high p_T^H regions, where impacts of the three following operators can be measured[24]:

- $\mathcal{O}_{tH} = (H^\dagger H)(\bar{Q}\widetilde{H}t)$ is top-Higgs Yukawa coupling modifier, with an impact on the total cross-section for the ggH and $t\bar{t}H$ processes.
- $\mathcal{O}_{HG} = H^\dagger H\, G^A_{\mu\nu} G^{A\mu\nu}$ is Higgs-gluon point-like contact term, with a shape impact that becomes significant at $p_{\mathrm{T}}^H \gtrsim 300$ GeV as well as overall normalisation effects.
- $\mathcal{O}_{tG} = (\bar{Q}\sigma^{\mu\nu}T^A t)\widetilde{H}\, G^A_{\mu\nu}$ is top-gluon coupling modifier, also known as a chromomagnetic dipole operator, with a substantial shape impact in the regime of $p_{\mathrm{T}}^H \gtrsim 500$ GeV and overall normalisation effects in the entire spectrum.

Since the p_T^H spectrum is the only observable, the three Wilson coefficients are highly correlated, they cannot be reliably constrained simultaneously. To reduce the correlation, it is possible to use the PCA eigenvectors:

$$\begin{aligned} ev^{[1]} &= \quad 0.999c_{HG} - 0.035c_{tG} - 0.003c_{tH}, \\ ev^{[2]} &= \quad 0.035c_{HG} + 0.978c_{tG} + 0.205c_{tH}, \\ ev^{[3]} &= -0.005c_{HG} - 0.205c_{tG} + 0.979c_{tH}. \end{aligned}$$

[24] Since in this analysis only the real parts are probed, it deals with $ctGRe$ and $ctHRe$ coefficients, which are real parts of ctG and ctH, respectively.

The obtained eigenvectors are close to the initial directions of the Wilson coefficients, since they all have different orders of impact. However, the rotation is still useful to reduce the correlations.

Illustration of the p_T^H spectrum observed in the $\gamma\gamma$ and 4ℓ final states predicted by the SM and the post-fit in the PCA basis is shown on Fig. 5.8.

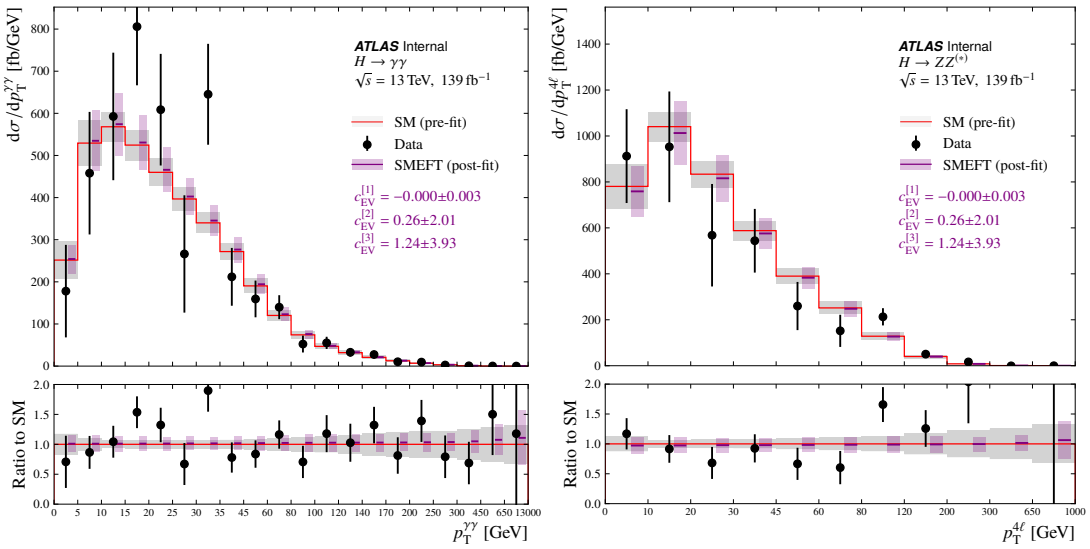

(a) (b)

Figure 5.8: Illustration of the observed (a) $p_T^{H\to\gamma\gamma}$ and (b) $p_T^{H\to 4\ell}$ spectrum along with the SM expected (pre-fit) and the SMEFT expected (post-fit) in the PCA basis (eq. 5.26). Source: [135].

Performance of the decorrelation of the PCA is shown on Fig. 5.9, which compares the observed correlation matrices in the Warsaw basis and in the eigenbasis.

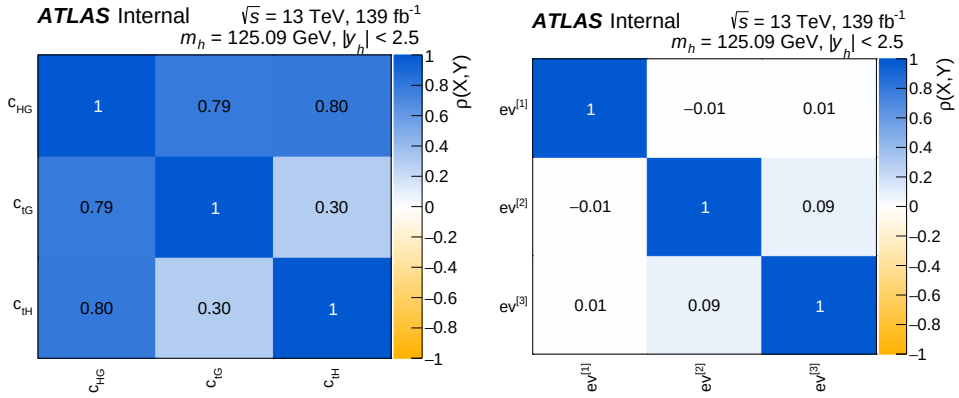

(a) Warsaw basis (b) Eigen-vector basis

Figure 5.9: Observed correlation matrices for the measurements in the (a) Warsaw basis and (b) corresponding eigen-vector basis, obtained with PCA (eq. 5.26). Source: [135].

The impact of the rotated coefficients on the p_T^H spectrum observed in the $\gamma\gamma$ and 4ℓ final states is shown on Fig. 5.10.

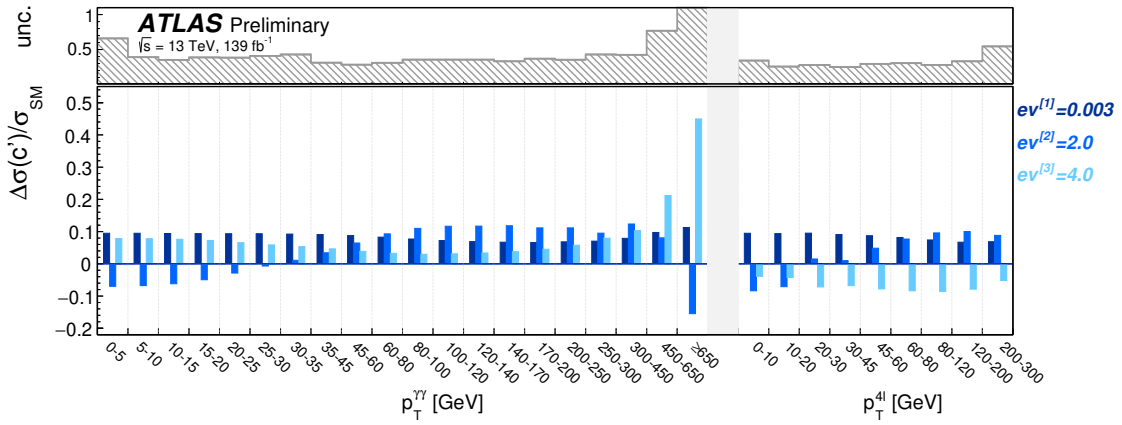

Figure 5.10: Ratio of the SM-BSM interference cross-section to the one predicted by the SM for each of the p_T^H spectrum in $H \to \gamma\gamma$ and $H \to ZZ^{(*)}$. SM-BSM term contains only the contributions from the operators in the PCA basis, defined by eq. 5.26. Source: [117].

5.5.1 Differential cross-section parametrisation

To obtain the EFT parametrisation, signal strength in each differential bin (independently for the $H \to \gamma\gamma$ and $H \to ZZ^*$ channels) is parametrised as:

$$\mu_{bin} = \frac{1}{\sum\limits_{i \in prod} \sigma_{i,bin}^{best-known,SM}} \left(\sum_{i \in prod} \frac{\sigma_{i,bin}^{SMEFT}(\mathcal{C}_j)}{\sigma_{i,bin}^{SMEFT}(\mathcal{C}_j = 0)} \times \sigma_{i,bin}^{best-known,SM} \right), \tag{5.26}$$

where normalisation on the best-known SM predictions allows to profit from their high accuracy, similarly to what is done for the STXS case.

The differential interpretation can benefit from a finer p_T^H binning with respect to the STXS one, but it does not separate out various production modes.

5.5.2 Differential cross-section measurements

To perform measurements of the three remaining Wilson coefficients (or PCA EV), a few possible fit strategies could be used:

- Simultaneous, where all the three Wilson coefficients are fit at the same time;
- One-at-a-time, where the Wilson coefficients are fit one-by-one, leaving the remaining ones at their SM values (zero).

Summary of the fit results for the Wilson coefficients and the PCA eigenvectors in the simultaneous and the one-at-a-time strategies are given in Tables 5.3, 5.4 and 5.5.

Corresponding NLL (negative log-likelihood) scans for the eigenvectors for the simultaneous fit case are shown on Fig. 5.11.

WC	Best-fit value $\pm1\sigma$ (obs)	Stat only (obs)	Best-fit value $\pm1\sigma$ (exp)	Stat only (exp)
c_{HG}	$0.000^{+0.003}_{-0.003}$	$0.000^{+0.002}_{-0.002}$	$0.000^{+0.003}_{-0.003}$	$0.000^{+0.002}_{-0.002}$
c_{tG}	$0.00^{+0.08}_{-0.09}$	$0.00^{+0.05}_{-0.05}$	$0.00^{+0.08}_{-0.09}$	$0.00^{+0.05}_{-0.05}$
c_{tH}	$0.1^{+1.0}_{-1.1}$	$0.1^{+0.7}_{-0.7}$	$0.0^{+1.0}_{-1.1}$	$0.0^{+0.7}_{-0.7}$

Table 5.3: Best-fit values and uncertainties for the three Wilson coefficients studied in the differential cross-section analyses. The Wilson coefficients which are not scanned are fixed to their SM value (zero). Both the total and the statistical only uncertainties are reported. Source: [117].

WC	Best-fit value $\pm1\sigma$ (obs)	Stat only (obs)	Best-fit value $\pm1\sigma$ (exp)	Stat only (exp)
$ev^{[1]}$	$0.000^{+0.003}_{-0.003}$	$0.000^{+0.002}_{-0.002}$	$0.000\ ^{+0.003}_{-0.003}$	$0.000\ ^{+0.002}_{-0.002}$
$ev^{[2]}$	$0.3^{+2.1}_{-1.9}$	$0.3^{+1.4}_{-1.3}$	$0.0\ ^{+2.2}_{-1.9}$	$0.0\ ^{+1.4}_{-1.4}$
$ev^{[3]}$	$1.2^{+3.9}_{-3.9}$	$1.2^{+3.0}_{-3.2}$	$0.0\ ^{+3.8}_{-3.9}$	$0.0\ ^{+3.0}_{-3.1}$

Table 5.4: Best-fit values and uncertainties for the three eigen-vectors studied in the differential cross-section analyses. The remaining two eigen-vectors are profiled in the fit. Both the total and the statistical only uncertainties are reported. Source: [117].

WC	Best-fit value $\pm1\sigma$ (obs)	Stat only (obs)	Best-fit value $\pm1\sigma$ (exp)	Stat only (exp)
$ev^{[1]}$	$0.000^{+0.003}_{-0.003}$	$0.000^{+0.002}_{-0.002}$	$0.000^{+0.003}_{-0.003}$	$0.000^{+0.002}_{-0.002}$
$ev^{[2]}$	$0.212^{+2.026}_{-1.789}$	$0.212^{+1.268}_{-1.236}$	$0.002^{+2.174}_{-1.973}$	$0.002^{+1.330}_{-1.295}$
$ev^{[3]}$	$1.200^{+3.809}_{-3.878}$	$1.190^{+3.096}_{-3.145}$	$0.000^{+3.819}_{-3.855}$	$0.000^{+3.159}_{-3.205}$

Table 5.5: Best-fit values and uncertainties for the three eigen-vectors studied in the differential cross-section analyses. The contributions of the Wilson Coefficients to the non-scanned eigen-vectors are fixed to zero (in the fit, not scanned eigen-vectors are non profiled and fixed at zero). Both the total and the statistical only uncertainties are reported. Source: [135].

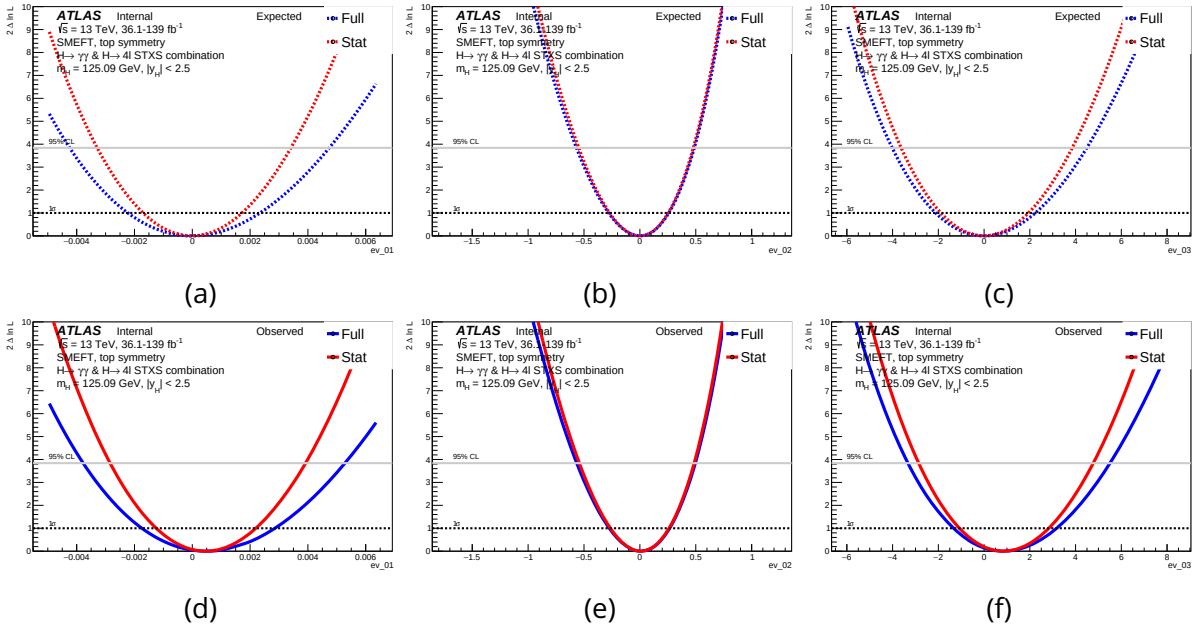

Figure 5.11: Single-parameter expected and observed likelihood scans from STXS $H \rightarrow \gamma\gamma$ and $H \rightarrow 4l$ for (a-d) $ev^{[1]}$, (b-e) $ev^{[2]}$ and (c-f) $ev^{[3]}$. The remaining two directions which are not scanned are fixed to the SM values (zero). The likelihood, obtained with all nuisance parameters being fixed at their best-fit-values are shown in red. The full likelihood, with floating all the parameters are shown in blue. Source: [135].

5.6 SMEFT Comparison of STXS and Diff XS interpretations

To compare the performance on probing EFT of the STXS and differential cross-section analyses, the same final states are used: $H \to \gamma\gamma$ and $H \to 4\ell$. The results of the simultaneous fit are shown on Fig. 5.12.

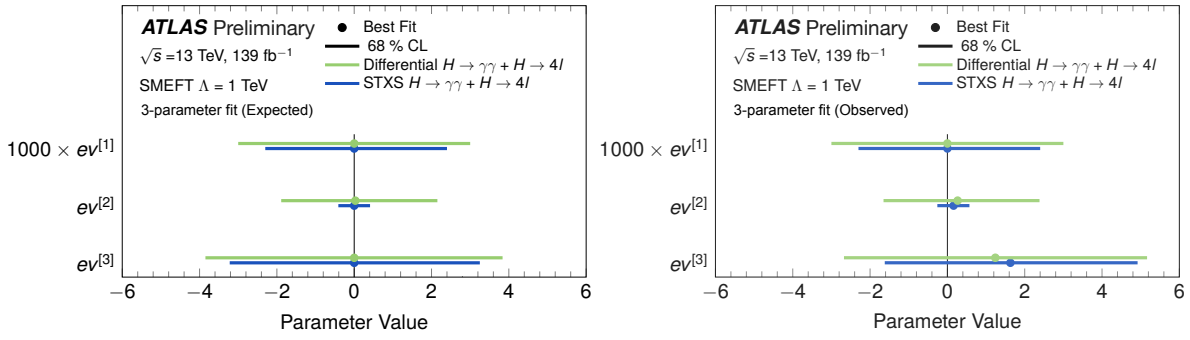

(a) (b)

Figure 5.12: Comparison of the (a) expected and (b) observed simultaneous fit results for the STXS (blue) and the differential cross-section (green) $H \to \gamma\gamma$ and $H \to 4\ell$, using the eigen-basis of the differential cross-sections. Source: [117].

In the one-at-a-time case, the constraining performance of the two approaches are similar, while in the simultaneous fit case, the STXS approach shows better results. It may come from by the design of the STXS measurements, which distinguishes the various production modes and probes in multi-dimension the kinematic phase space (Section 4.2), optimised to enhance sensitivity to BSM physics.

5.6.1 Systematics

Ranking plot for the simultaneous fit results with the combined $H \to \gamma\gamma$ and $H \to 4\ell$ STXS datasets are shown on Fig. 5.13. The most important systematics are from the theoretical modelling of UEPS (underlying event parton shower).

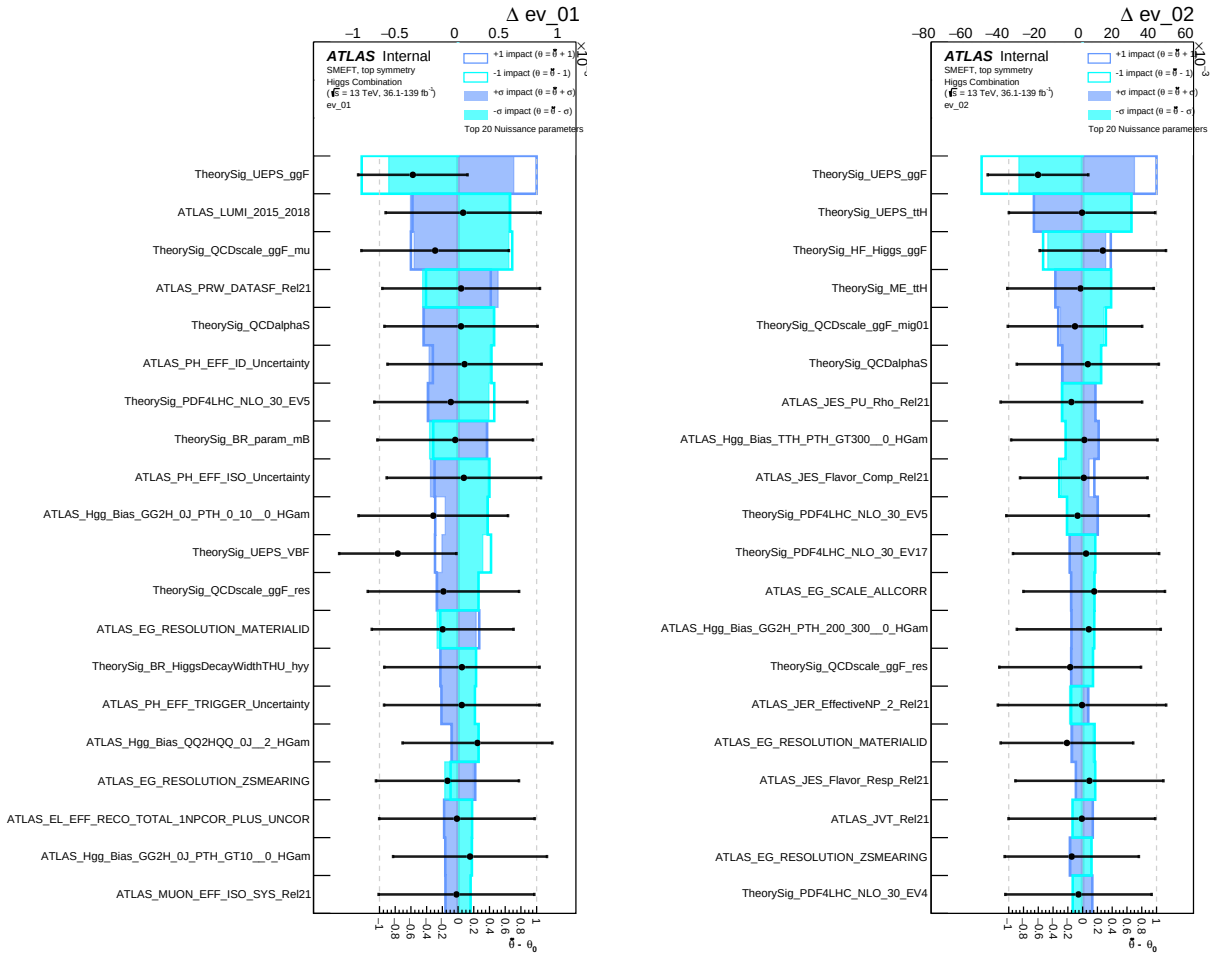

(a) (b)

Figure 5.13: Ranking plots for the STXS dataset in the basis two leading eigenvectors defined in the differential cross-section analysis. Empty (shaded) histograms show the pre-fit (post-fit) impact of the nuisance parameter value on the given POI. Source: [135].

5.7 SMEFT fit results with the STXS combination

5.7.1 Linear results

The results of a simultaneous fit of the Wilson coefficients in the fit-basis in the linear model are shown by Fig. 5.14. Potential difference between the sensitivities of the expected and observed results may come from the non-linearity of the parametrisation and is discussed in Section 5.7.3.

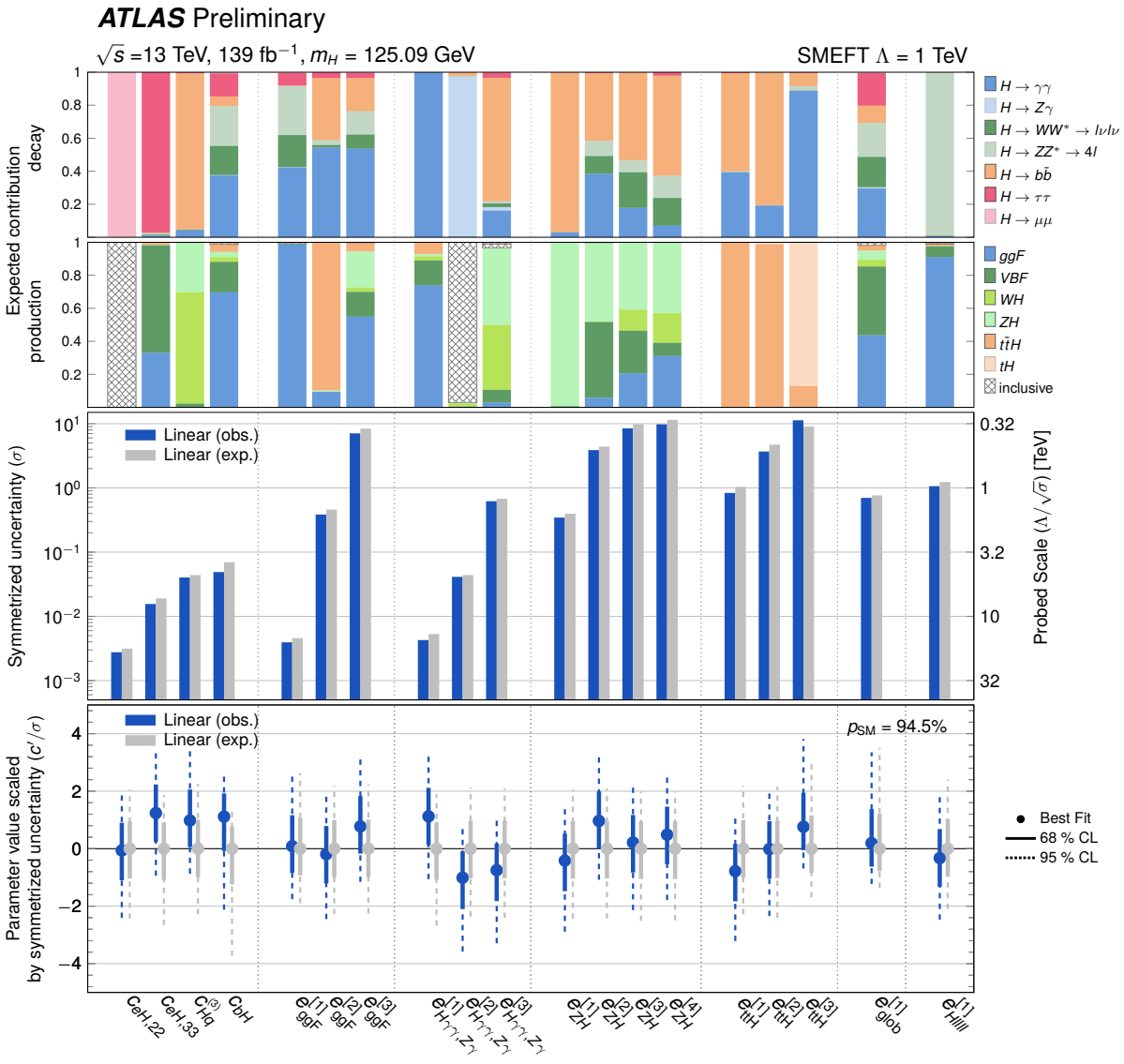

Figure 5.14: Expected (grey) and observe (blue) pull of central values of the Wilson coefficients in the fit-basis (bottom plot), their uncertainties (middle) and relative contributions from each input channel and production mode (top) to the precision of the measurements. The results are obtained under the linear parametrisation. Source: [117].

From these results, one could see how individual analyses of the Higgs boson decaying to leptons ($\mu\mu$ and $\tau\tau$) significantly improve constraining power on $\mathcal{C}_{eH}^{22}$ and $\mathcal{C}_{eH}^{33}$, which affect the corresponding Higgs couplings. Correlation matrices of the measurement are shown on Fig. 5.15.

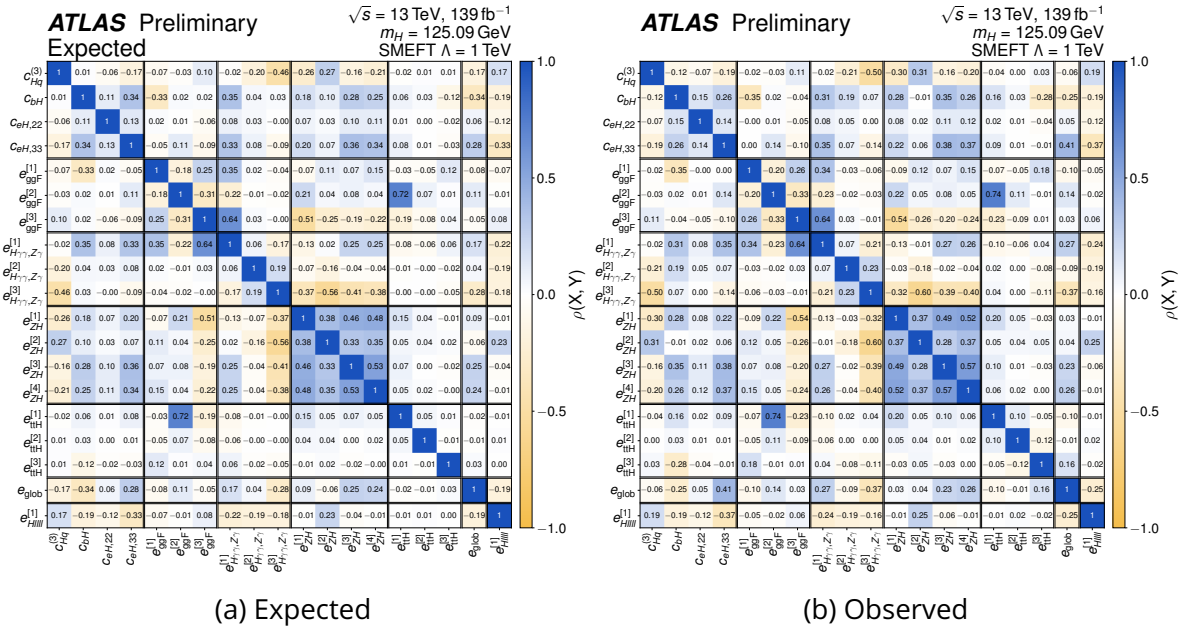

(a) Expected (b) Observed

Figure 5.15: (a) Expected and (b) observed covariance matrices for the simultaneous fit of the Wilson coefficients in the fit basis for the linear parametrisation. Source: [117].

The largest correlations occur between e_{ttH}^{1} (4-fermion operator, mainly affecting ttH) and e_{ggH}^{2} (mostly, $\mathcal{C}_{tG}$) and may come due to the overlap of impacts: e_{ttH}^{1} is mainly constrained from the ttH process, which is highly sensitive to the ggH production mode (which is affected by e_{ggH}^{2}).

Remnant correlations between the Wilson coefficients of the same group occur due to the residual correlations with other parameters, outside of the given group.

Breakdown of uncertainties into statistical and systematic components is given by Fig. C.7, which shows that most of the Wilson coefficients are statistically dominated[25].

5.7.2 Quadratic results

The fit results in the case of the quadratic parametrisation are shown on Fig. 5.16 and the comparison with the linear results are given by Fig. 5.17.

[25]The corresponding NII scans for various components of systematic uncertainties are given by Fig. C.9 and Fig. C.10.

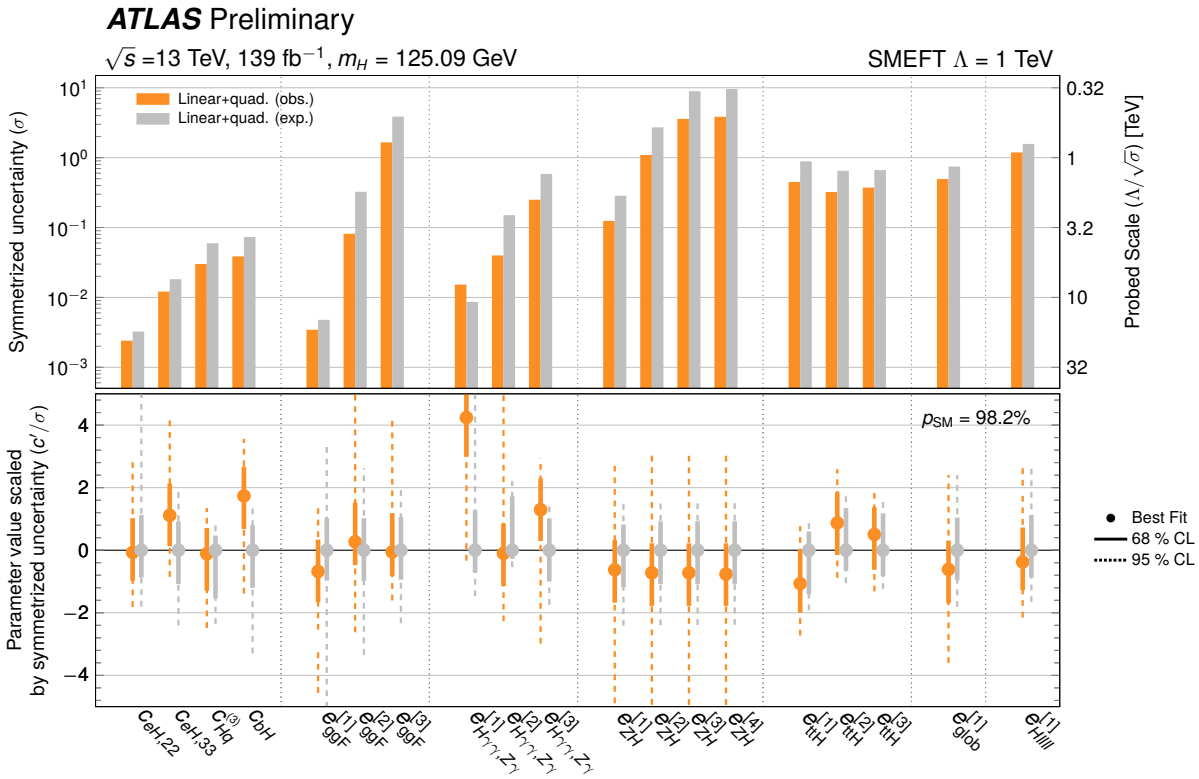

Figure 5.16: Expected (grey) and observed (yellow) pull of values of the Wilson coefficients in the fit-basis (bottom) and the total uncertainty (top sub-plot) in the case of the quadratic parametrisation. Source: [117].

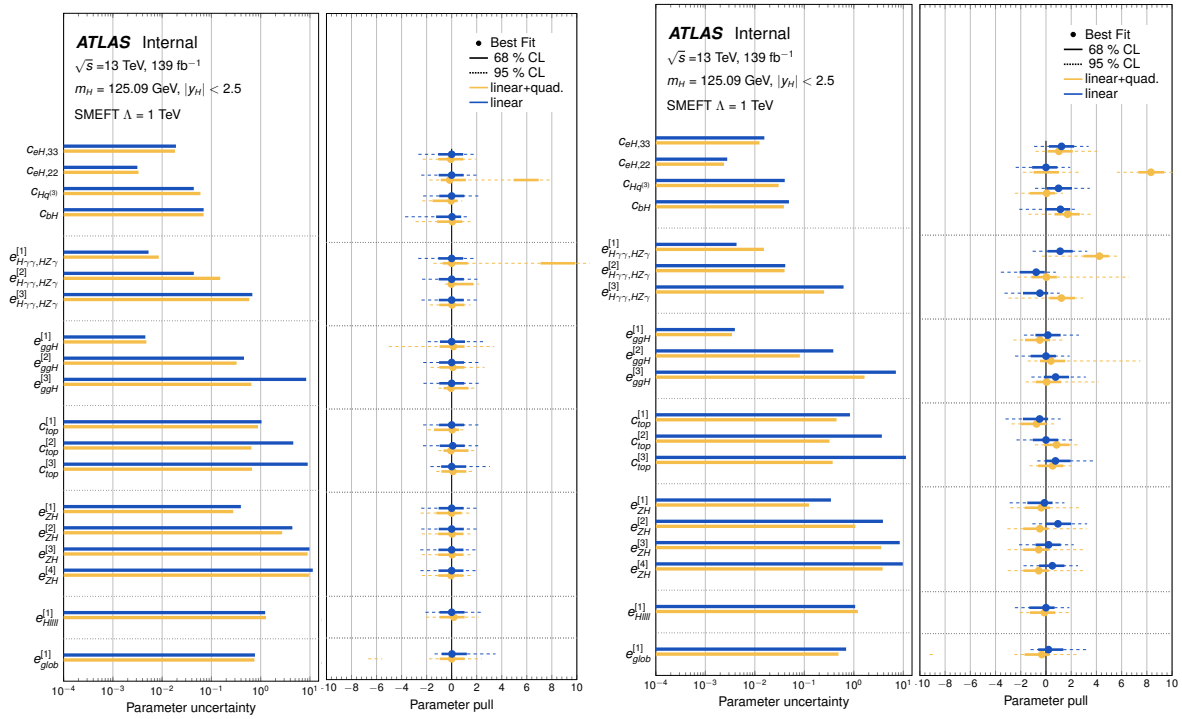

(a) Expected (b) Observed

Figure 5.17: Comparison of the fit results between the case of the linear parametrisation (blue) and the quadratic one (yellow) for (a) expected and (b) observed cases. Left sub-plots show total uncertainty on a given Wilson coefficient and the right ones illustrate the pull of best-fit values and their uncertainties (68% and 95% CL). Source: [135].

For some Wilson coefficients, the difference in uncertainties between the quadratic and linear parametrisations can reach an order of a magnitude (for example, $e^1_{H\to\gamma\gamma,H\to 4\ell}$). This difference indicates a potential importance of including the dimension-8 terms in the parametrisation and a necessity to use the quadratic parametrisation.

At the results shown by Fig. 5.17, some CI are disconnected (for example, $\mathcal{C}^{22}_{eH}$). Explanation is given by the likelihood scan, depicted on Fig. 5.18.

5.7.3 Likelihood shape for the quadratic results

The quadratic fit results show some potential problems with the estimation of the CI for specific Wilson coefficients. To understand it, a series of likelihood scans (Fig. 5.18) have been performed.

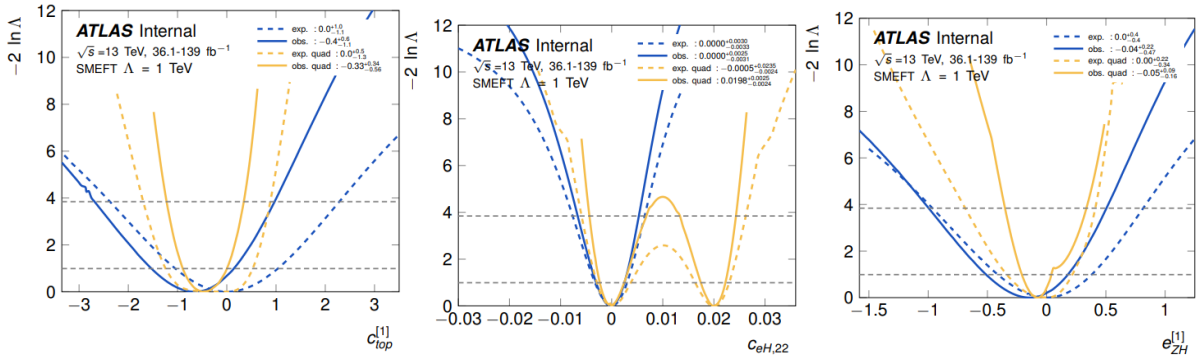

(a) normal (b) Double minimum (c) Non-differentiable

Figure 5.18: Examples of the likelihood scans with linear (blue) and quadratic (yellow) parametrisations for representative cases: (a) normal behaviour, (b) double minimum and (c) non-differentiable behaviour of likelihood. The observed results are shown with a solid line and the expected are drawn with a dotted one. Source: [136].

Double-well structure

Origin of the double-well structure could be explained with a toy study, illustrated by Fig. 5.19: in a case when linear effects[26] are as important as quadratic[27], the log-likelihood behaves as a quartic function and therefore exhibits a double-well structure. Contrary, if the quadratic effects are the dominant ones, the behaviour of the likelihood manifests in a U-shape with a flat area around the SM-value.

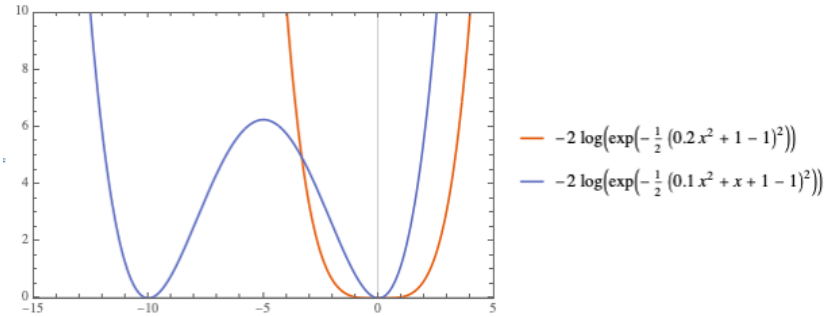

(a)

Figure 5.19: Illustration of a toy study for quartic Nll for a case of similar contributions from the linear and quadratic terms (blue) and for a case of dominant contribution from the quadratic ones (red). Source: [136].

[26] Effects coming from the SM-D6 interference terms in the squared matrix element.
[27] Effects originating from the pure BSM terms from the D6-D6 terms in the squared matrix element.

Non-differentiable behaviour (Multiple minima)

To solve the issue with a non-differentiable behaviour of likelihood, a different method (Fig. 5.20[28]) to construct it has been adopted:

- To construct a likelihood shape for a given Wilson coefficient $\mathcal{C}_i$:
  - For each other $\mathcal{C}_j$ $(i \neq j)$ perform a series of Nll scans and for each value $\mathcal{C}_j^{\alpha}$ of $\mathcal{C}_j$ probed, find the best-fit-value $\hat{\mathcal{C}}_i^{j|\alpha}$ of $\mathcal{C}_i$ and likelihood.
  - Plot all points $\mathcal{C}_i$ and the corresponding Nll.
  - Consider an envelope of the points as a truth Nll shape for a given $\mathcal{C}_i$;

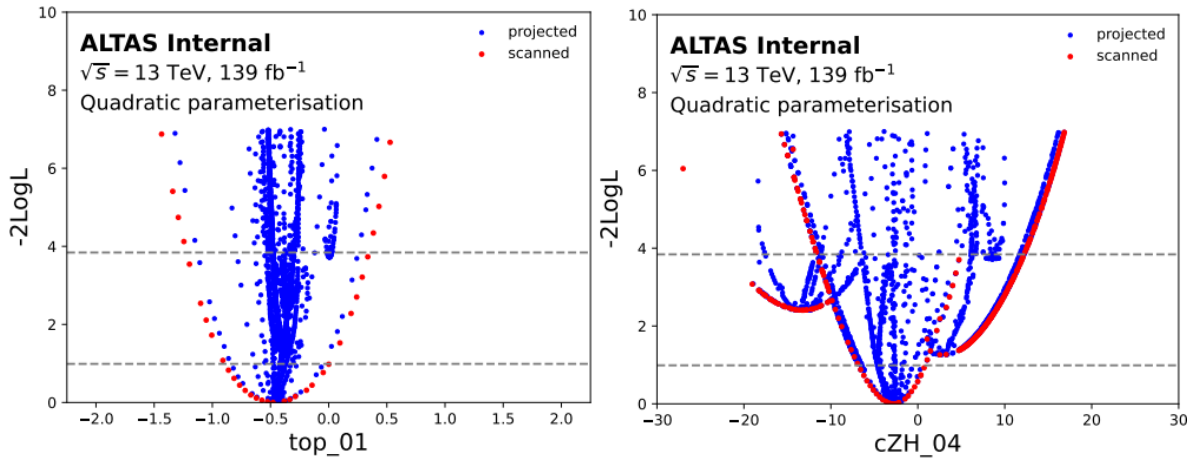

(a) Normal behaviour (b) Multiple wings

Figure 5.20: Illustration of constructing an envelope for a given Wilson coefficient $\mathcal{C}_i$: each blue point is constructed from an NII scan for another Wilson coefficient $\mathcal{C}_j$ with plotting of the best-fit-value for the probed one and the corresponding NII value. The red dots show a traditional NII scan for $\mathcal{C}_i$. Source: [136].

Presence of multiple wings in the NII scan may explain the non-differentiable behaviour of the NII shape obtained in a classical method.

Difference between the expected and observed sensitivities

Non-linear[29] nature of the parametrisation leads to a non-Gaussian likelihood (Fig. 5.21). In this case, a slight variation of the central value (minimum of NII) can significantly change the CI.

[28] Plots for all Wilson coefficients probed are in appendix: (expected) Fig. C.11 and (observed) Fig. C.12

[29] Here, non-linear refers to the ratio of polynomials (Section 5.3) and should not be confused with the linear and quadratic parametrisations, expressing the inclusion of only SM-D6 interference and D6-D6 terms in the squared matrix element

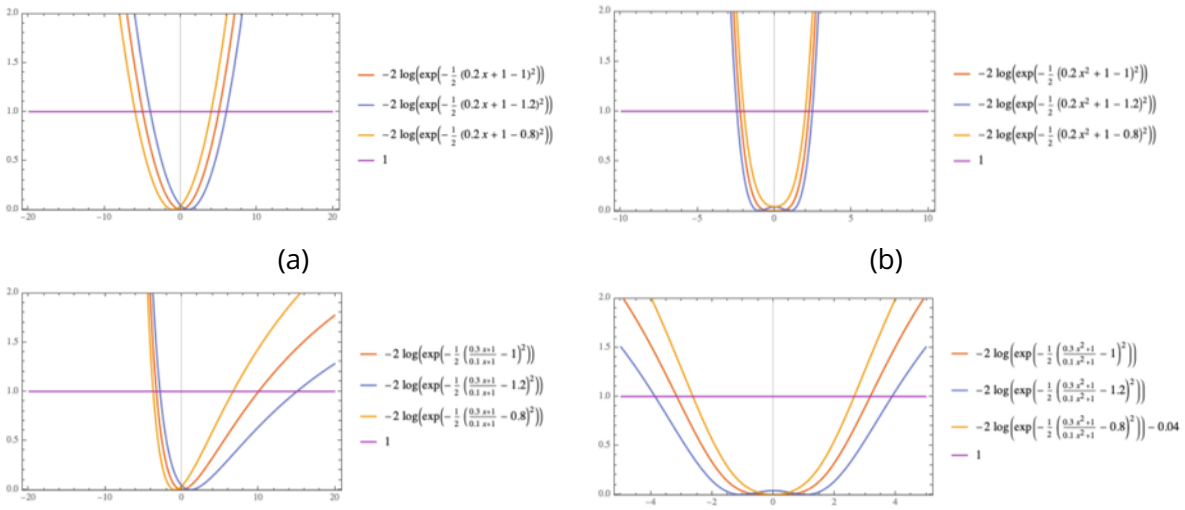

Figure 5.21: Illustration of toy likelihoods for the case of (a, c) linear parametrisation and (b, d) quadratic one. (a) shows fully linear log-likelihood, (c) illustrates a case when no Taylor-expansion is used for the polynomial ratio. (b) shows a quartic likelihood with a Taylor-expanded ratio of polynomials. On (d) no Taylor-expansion is used and the likekihood is a quartic function (which corresponds to the quadratic parametrisation). Source: [136].

5.8 Two-Higgs-doublet model

5.8.1 Introduction

In 2HDM (Two Higgs Doublet Model), the Higgs sector is extended by an additional complex doublet Φ with the vacuum expectation value v_2 [137, 138, 139]. For this analysis, the CP conservation and a Z_2 symmetric potential[30] is assumed. In this case, after electroweak symmetry breaking, five Higgs bosons appear[31]:

- 2 neutral CP-even (h and H)
- 1 neutral CP-odd (A)
- 2 charged $H^{\pm}$

The masses of additional Higgs bosons are assumed to be heavier than the SM Higgs, hence causing no additional decay channels of the observed Higgs boson. Given the Z_2 symmetry, there is no flavour changing neutral currents at the tree level [140, 141], therefore all right-handed quarks must couple only to a single Higgs multiplet.

All remaining possible scenarios of 2HDM can be classified in the four types, depending on the couplings of the additional doublets to quarks and leptons:

- *Type I*: One Higgs doublet is coupled to charged fermions. If the doublets do not mix, the first one has no couplings to fermions (is *fermiophobic*).
- *Type II*: One Higgs doublet couples to up-type quarks and the other to down-type quarks and charged leptons. This scenario is also called *MSSM-like*, since it is realised in the MSSM (Minimal Supersymmetric Standard Model).
- *Lepton-specific*: One Higgs doublet couples to leptons and the other one to up- and down-type quarks. As a result, the Higgs bosons have the same couplings to quarks as in *Type I* and to charged leptons as in *Type II*.
- *Flipped*: One Higgs doublet couples to down-type quarks and the other one to up-type quarks and leptons. As a result, the Higgs bosons have the same couplings to quarks as in the *Type II* and to charged leptons as in *Type I*:

In 2HDM models, the Higgs sector is described by seven parameters:

- 4 masses (m_h, m_H, m_A, $m_{H^{\pm}}$).
- $\tan\beta$ (ratio of the vacuum expectation values of the Higgs doublets: $\tan\beta = v_2/v_1$, with a constrain: $v_1^2 + v_2^2 \approx 246$ GeV).
- $\cos(\beta - \alpha)$. With α being mixing angle between h and H.
- m_{12} (Higgs potential parameter)

Existence of these models can be probed via the SM Higgs boson couplings, which are usually exploited via the κ-framework. Manifestation of the couplings change depending on the model is given in Table 5.6.

[30] A Z_2 symmetric potential is one for which (ϕ) and ($-/phi$) are undistinguishable.
[31] which is the observed Higgs with a mass of 125 GeV.

Coupling scale factor	Type I	Type II	Lepton-specific	Flipped
κ_V	$\sin(\beta-\alpha)$			
κ_u	$s(\beta-\alpha)$+$c(\beta-\alpha)$/tanβ	$s(\beta-\alpha)$+$c(\beta-\alpha)$/tanβ	$s(\beta-\alpha)$+$c(\beta-\alpha)$/tanβ	$s(\beta-\alpha)$+$c(\beta-\alpha)$/tanβ
κ_d	$s(\beta-\alpha)$+$c(\beta-\alpha)$/tanβ	$s(\beta-\alpha)$-tanβ $c(\beta-\alpha)$	$s(\beta-\alpha)$+$c(\beta-\alpha)$/tanβ	$s(\beta-\alpha)$-tanβ $c(\beta-\alpha)$
κ_l	$s(\beta-\alpha)$+$c(\beta-\alpha)$/tanβ	$s(\beta-\alpha)$-tanβ $c(\beta-\alpha)$	$s(\beta-\alpha)$-tanβ $c(\beta-\alpha)$	$s(\beta-\alpha)$+$c(\beta-\alpha)$/tanβ

Table 5.6: Mapping between the kappa-modifiers at the lowest order for the SM Higgs boson h to vector bosons κ_V, up-type quarks κ_u, down-type quarks κ_d, and charged leptons κ_l, parametrised by $\tan\beta$ and $\cos(\beta-\alpha)$ in the 4 2HDMs types. $c(\beta-\alpha)$ stands for $\cos(\beta-\alpha)$ and $s(\beta-\alpha)$ for $\sin(\beta-\alpha)$. Source: [135].

5.8.2 Results from κ-measurements

The results for the four models are given by Fig. 5.22, where the parameters α and β are required to satisfy $0 \leq \beta \leq \pi/2$ and $0 \leq \beta - \alpha \leq \pi$ without loss of generality.

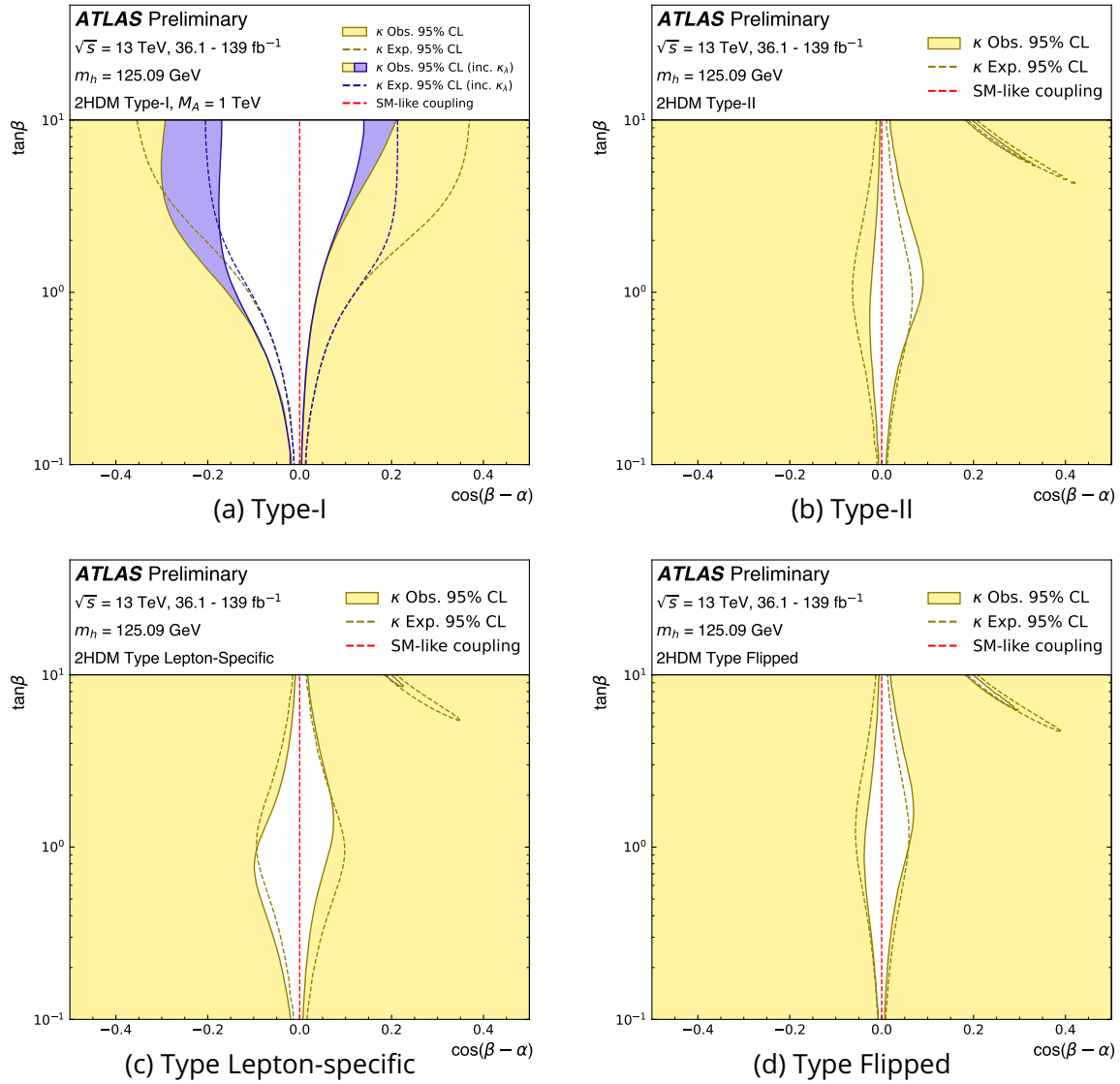

Figure 5.22: Exclusion contours for the four 2HDM models in the ($\tan\beta$, $\cos(\beta-\alpha)$): (a) Type I, (b) Type II, (c) Lepton specific and (d) Flipped scenarios. Source: [117].

For some models, there is a small petal-like additional allowed region at the top-right part of the plots. It corresponds to the wrong-sign Yukawa case (limit of $\cos(\beta+\alpha)=0$), where at least one of the Higgs bosons couplings to down-type quarks and leptons is at the opposite with respect to the SM sign. Another source of information to constrain the 2HDM models is the SM Higgs boson self-coupling κ_λ, which is parametrised in the 2HDM models as:

$$\kappa_\lambda = \sin^3(\beta-\alpha)+\left(3-2\frac{\bar{m}^2}{m_h^2}\right)\cos^2(\beta-\alpha)\sin(\beta-\alpha)+2\cot 2\beta\left(1-\frac{\bar{m}^2}{m_h^2}\right)\cdot\cos^3(\beta-\alpha), \quad (5.27)$$

with $\bar{m}$ defined as:

$$\bar{m}^2 = \frac{m_{12}^2}{\sin\beta\cos\beta} \quad (5.28)$$

Since the m_{12} parameter is related to the mass of the heavy Higgs m_A as:

$$m_{12}^2 = \frac{m_A^2}{1+\tan^2\beta}, \quad (5.29)$$

it is possible re-express $\bar{m}$ as:

$$\bar{m}^2 = \frac{m_A^2\tan\beta}{(\sin\beta\cos\beta)(1+\tan^2\beta)} = m_A^2, \quad (5.30)$$

hence, they coincide.

Therefore, one can see, including the κ_λ dependency, introduces an additional dependence of the heavy Higgs mass. Since it is not directly probed, it is fixed to $m_A = 1$ TeV. Dependence of the constrain power on m_A is given by Fig. 5.23.

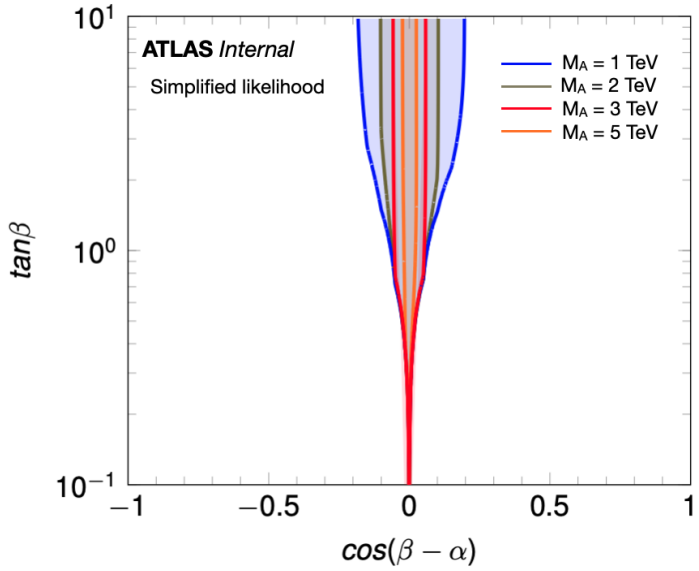

Figure 5.23: Exclusion contour in the $(\cos(\beta-\alpha,\ \tan\beta)$ plane for various masses of the heavy Higgs m_A. Source: [135].

Impact on the constraining power after adding the κ_λ measurements is illustrated by Fig. 5.24. Inclusion of the κ_λ into the parametrisation allows significantly shrink the high $\tan\beta$ region.

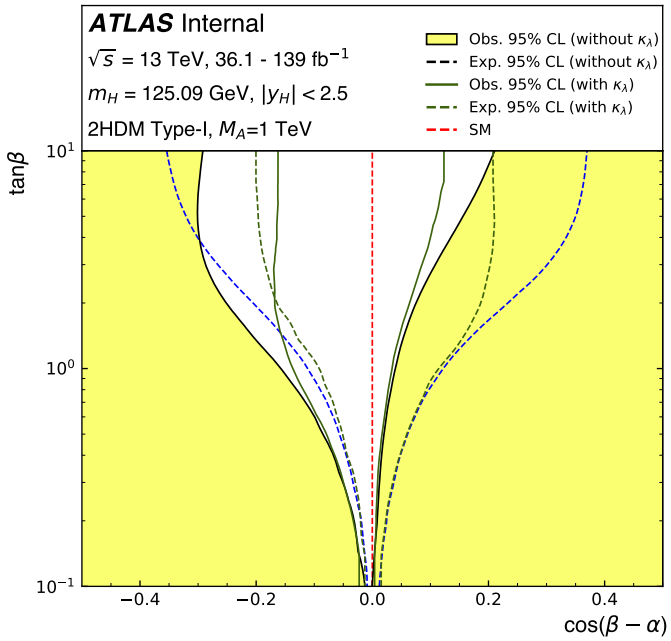

Figure 5.24: Exclusion contours in the $(\cos(\beta-\alpha,\ \tan\beta)$ plane with and without including the κ_λ parametrisation in the 2HDM *Type I* scenario. Mass of the heavy Higgs is fixed to 1 TeV. Source: [135].

5.8.3 SMEFT - 2HDM matching

Given that any EFT theory serves as an intermediate model-independent representation of BSM models, it can be directly mapped to a given dedicated BSM model, transferring the constrains on the Wilson coefficients into constrains for a given UV model. This procedure is called matching.

The SMEFT matching of the 2HDM model is valid in the decoupling limit of the 2HDM (the heavy fields decouples from the light ones). Hence, masses of the heavy Higgs bosons are related to the New Physics scale Λ:

$$m_a^2 \approx m_{H_0}^2 \approx m_{H^\pm}^2 \equiv M^2 \gg v^2, m_h^2 \approx v^2. \tag{5.31}$$

In the exact alignment limit ($\cos(\beta-\alpha) \to 0$), the SMEFT operators appear only at 1-loop. In contrary, away from this limit, Higgs Yukawa couplings appear (along with the κ_λ correction).

Only the following Wilson coefficients have a non-zero impact: $c_{tH}, c_{bH}, c_{eH22}, c_{eH33}$ and therefore must be re-expressed in terms of $\cos(\beta-\alpha)$, $\tan\beta$ and SM Yukawa coupling. In the linear case, it yields the parametrisation given by Table 5.7.

SMEFT parameters	Type I	Type II	Lepton-specific	Flipped
$\frac{v^2 c_{tH}}{\Lambda^2}$	$-Y_t c_{\beta-\alpha}/\tan\beta$	$-Y_t c_{\beta-\alpha}/\tan\beta$	$-Y_t c_{\beta-\alpha}/\tan\beta$	$-Y_t c_{\beta-\alpha}/\tan\beta$
$\frac{v^2 c_{bH}}{\Lambda^2}$	$-Y_b c_{\beta-\alpha}/\tan\beta$	$Y_b c_{\beta-\alpha}\tan\beta$	$-Y_b c_{\beta-\alpha}/\tan\beta$	$Y_b c_{\beta-\alpha}\tan\beta$
$\frac{v^2 c_{eH,22}}{\Lambda^2}$	$-Y_\mu c_{\beta-\alpha}/\tan\beta$	$Y_\mu c_{\beta-\alpha}\tan\beta$	$Y_\mu c_{\beta-\alpha}\tan\beta$	$-Y_\mu c_{\beta-\alpha}/\tan\beta$
$\frac{v^2 c_{eH,33}}{\Lambda^2}$	$-Y_\tau c_{\beta-\alpha}/\tan\beta$	$-Y_\tau c_{\beta-\alpha}\tan\beta$	$Y_\tau c_{\beta-\alpha}\tan\beta$	$-Y_\tau c_{\beta-\alpha}/\tan\beta$
$\frac{v^2 c_H}{\Lambda^2}$	$c^2_{\beta-\alpha} M_A^2/v^2$	$c^2_{\beta-\alpha} M_A^2/v^2$	$c^2_{\beta-\alpha} M_A^2/v^2$	$c^2_{\beta-\alpha} M_A^2/v^2$

Table 5.7: Wilson coefficients at lowest order for SMEFT, modifying the Yukawa couplings c_{tH}, c_{bH}, $c_{eH,33}$, and $c_{eH,22}$ for the top quark, bottom quark, τ, and μ parametrised by $\tan\beta$ and $\cos(\beta-\alpha)$ in 2HDMs 4 different types where $c_{\beta-\alpha}$ stands for $\cos(\beta-\alpha)$. c_H corresponds to modification to the self-coupling of the Higgs and M corresponds to the mass of the Heavy Higgs bosons in 2HDM. Y_i corresponds to $\sqrt{(2)}m_i/v$. For the purposes of this analysis, $M_A = \Lambda = 1$ TeV is considered. The parametrisation is taken from [142]. Source: [135].

To include the self-coupling modifier κ_λ in the fit, it needs to be expressed in terms of the SMEFT operators:

$$\kappa_\lambda = 1 + \frac{v^2 c_{H\Box}}{\Lambda^2} - \frac{v^2 c_{HDD}}{4\Lambda^2} - \frac{c_{Hl^{(3)},11}}{2\Lambda^2} - \frac{c_{Hl^{(3)},22}}{2\Lambda^2} + \frac{v^2 c_{ll,1221}}{2\Lambda^2} - \frac{v^2 c_H}{\lambda\Lambda^2}, \tag{5.32}$$

with $\lambda = (G_f * m_h^2)/\sqrt{2}$.

This parametrisation uses the Taylor-expanded version of the full parametrisation from [143] cut at Λ^{-2} terms. Impact from using the exact parametrisation and its linear (in Λ^{-2}) version is shown in Fig. 5.25.

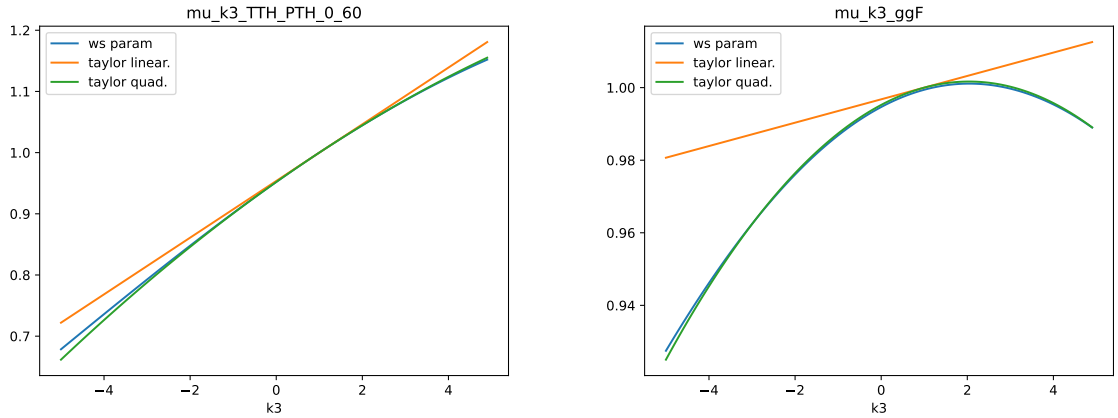

(a) (b)

Figure 5.25: Comparison of the exact parametrisation of κ_λ (the blue curve) and its Taylor expansion in Λ^{-2} cut at linear (the red curve) and quadratic (the green curve) terms for selected production bins and branching ratio. Source: [135].

From the figure, it can be seen that for large values of κ_λ, the expansion can significantly deviate from the exact parametrisation.

The Wilson coefficients $c_{H\Box}$ and c_{HDD} in the equation 5.32 cannot be directly mapped to κ_λ, since they significantly disturb kinematic distributions, therefore in the 2HDM case, they were omitted. The resulting constrains (expected and observed) are shown in Fig. 5.26.

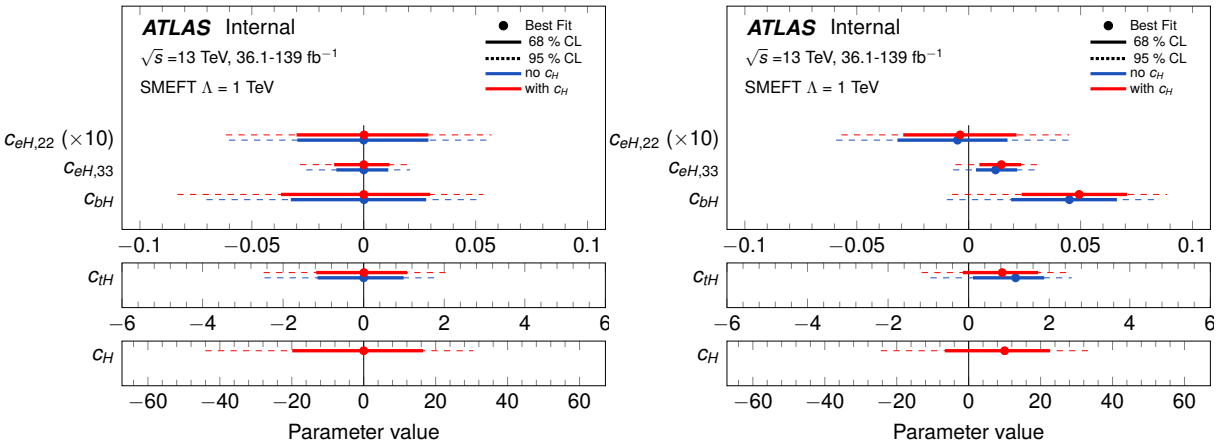

Figure 5.26: The expected (a) and observed (b) constraints for the 2HDM matching. The red and blue lines shown the constraints obtained separately for the scenarios with and without c_H, respectively. Source: [135].

5.8.4 Comparison on SMEFT-based and κ-based 2HDM constrains

The exclusion contours in the 2HDM models obtained from the SMEFT-matching and the κ-bases re-interpretation of the results is shown in Fig. 5.27, 5.28.

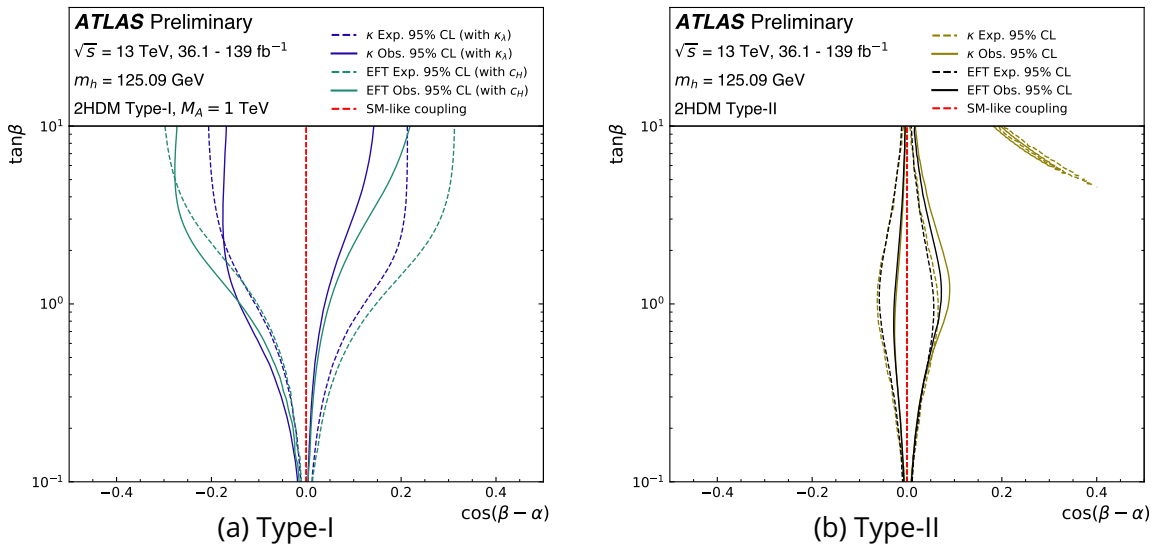

Figure 5.27: Comparison of the exclusion contours from the approaches based on the $\kappa-$ (yellow) and EFT-frameworks (black) for the four 2HDM models in the ($\tan\beta$, $\cos(\beta-\alpha)$): (a) Type I, (b) Type II scenarios. Source: [117].

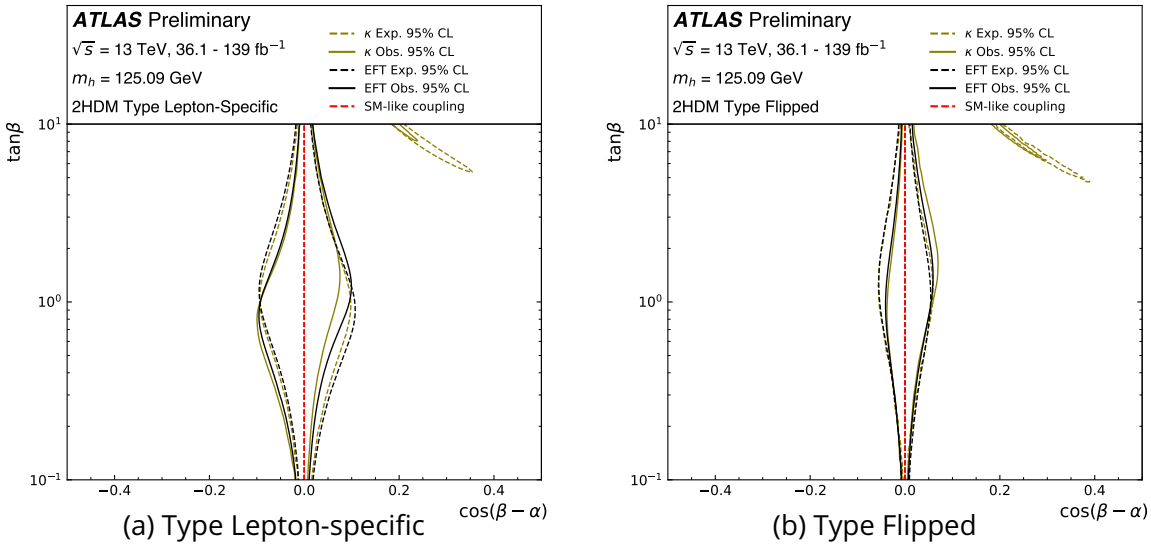

(a) Type Lepton-specific (b) Type Flipped

Figure 5.28: Comparison of the exclusion contours from the approaches based on the $\kappa-$ (yellow) and EFT-frameworks (black) for the four 2HDM models in the ($\tan\beta$, $\cos(\beta-\alpha)$): (a) Type Lepton-specific, (b) Type Flipped scenarios. Source: [117].

The potential difference may come from the treatment of the $\cos(\beta-\alpha)$ term: the κ-framework uses all its orders as is to re-interpret the results, while in the SMEFT framework, the matching is accurate to $O(\frac{\nu^2}{\Lambda^2})$, hence only to $\cos(\beta-\alpha)$. Since, coupling of the Higgs boson to the electro-weak bosons $\kappa_V$is proportional to $\sin(\beta-\alpha) \sim \cos(\beta-\alpha)^2$, it is suppressed.

5.9 MSSM

MSSM stands for the Minimal Supersymmetric Standard Model, a theoretical extension of the Standard Model of particle physics that introduces supersymmetry (SUSY) as a solution to several open problems in the Standard Model. In the MSSM, every Standard Model particle has a supersymmetric partner particle called sparticle with a spin that differs by 1/2. For example, it introduces spin-zero partners of the SM fermions, called sfermions, spin-half gluinos (partners of the SM gluons). In the EW sector, MSSM describes eight spin-half partners of the EW gauge bosons (including Higgs boson):

- 1 neutral bino (partner of the B_μ $\mathrm{U}(1)$ gauge field);
- 2 charged and 1 neutral winos (partners of the W_μ $\mathrm{SU}(2)$ gauge field);
- 4 higgsinos: 2 neutral and a charged pair, which all are superpartners of the Higgs fields.

which exactly match the 2HDM spectrum with type-II Yukawa couplings. The bino, neutral wino and the neutral higgsinos are mixed into four neutralinos. The charged winos and higgsinos form charginos.

Assuming CP-conservation, at the tree-level, all masses and couplings of the Higgs boson sector in MSSM can be parametrised in terms of only two parameters. Usually, these parameters are chosen to be $\tan\beta$ and m_A, which is the mass of the pseudo-scalar Higgs boson A.

Since MSSM has over a hundred parameters, they cannot be probed simultaneously. Hence, comparison of the theoretical predictions with the observed data is usually done via a set of

benchmark scenarios, which make some assumptions on all the MSSM parameters, fixing them to a certain value. The only remaining parameters are $\tan\beta$ and m_A.

5.9.1 Benchmark scenarios

In this study it is assumed that the observed Higgs boson ($m_H = 125$ GeV) is the light CP-even Higgs boson. In the most of the scenarios described below (except, the $M_H^{125}(alignment)$), the masses of the other Higgs bosons are assumed much larger than 125 GeV due to the mass split, hence there is no interference between them and the observed Higgs. In the $M_H^{125}(alignment)$ scenario, the interference effect is also very small.

The seven probed scenarios are:

- $\boldsymbol{M_h^{125}}$. All super-particles are assumed to be so heavy that loop-induced SUSY corrections contributions to the couplings of the light CP-even scalar (SM Higgs) is small and the heavy Higgs bosons (with a mass up to 2 TeV) decay only to the SM particles.
- $\boldsymbol{M_h^{125}(\tilde{\tau})}$. This scenario differs from the previous one by the parameters of the soft SUSY-breaking (masses and trilinear interaction term for the staus) are significantly smaller. Hence, light staus and light gaugino-like charginos can affect the decay width of the SM-Higgs to photons. At low m_A, the Hbb coupling is enhanced, significantly suppressing decay rates of other channels.
- $\boldsymbol{M_h^{125}(\tilde{\chi})}$. In this scenario, all charginos and neutralinos are relatively light, higgsino-gaugino mixing is enhanced and the electroweakino mass spectrum is compressed. At low $\tan\beta$, the SM-Higgs decay to photons is significantly altered.
- $\boldsymbol{M_h^{125}(alignment)}$ (alignment without decoupling) scenario, where for a given value of $\tan\beta$, one of the two neutral CP-even Higgses has the SM-like couplings, regardless masses of the remaining Higgs bosons.
- $\boldsymbol{M_{h_1}^{125}(\mathrm{CPV})}$. In this scenario, there is a CP-violation in the Higgs sector, induced by a non-zero phase ϕ_τ (Section 1.7.4). The relevant parameters are chosen such that the mass of the SM-Higgs matches the observed value.
- $\boldsymbol{M_{h,\,\mathrm{EFT}}^{125}}$ is characterised by a flexible SUSY scale, which may vary in the range 6 TeV $-$ 10^{16} TeV to ensure matching of the Higgs boson mass to the observed one and to prevent parameter region of low $\tan\beta$. Contribution to the Higgs properties is computed wit the EFT approach. Masses of all the super-particles are chosen to be so heavy to have a low impact on the MSSM Higgs bosons properties (as in the $\boldsymbol{M_h^{125}}$ scenario)
- $\boldsymbol{M_{h,\,\mathrm{EFT}}^{125}(\tilde{\chi})}$. In contrary to the previous case, neutralinos and charginos are allowed to be relatively light, hence significantly affecting Higgs properties.

5.9.2 MSSM results

The results for the different benchmark scenarios are shown in Fig. 5.29 .

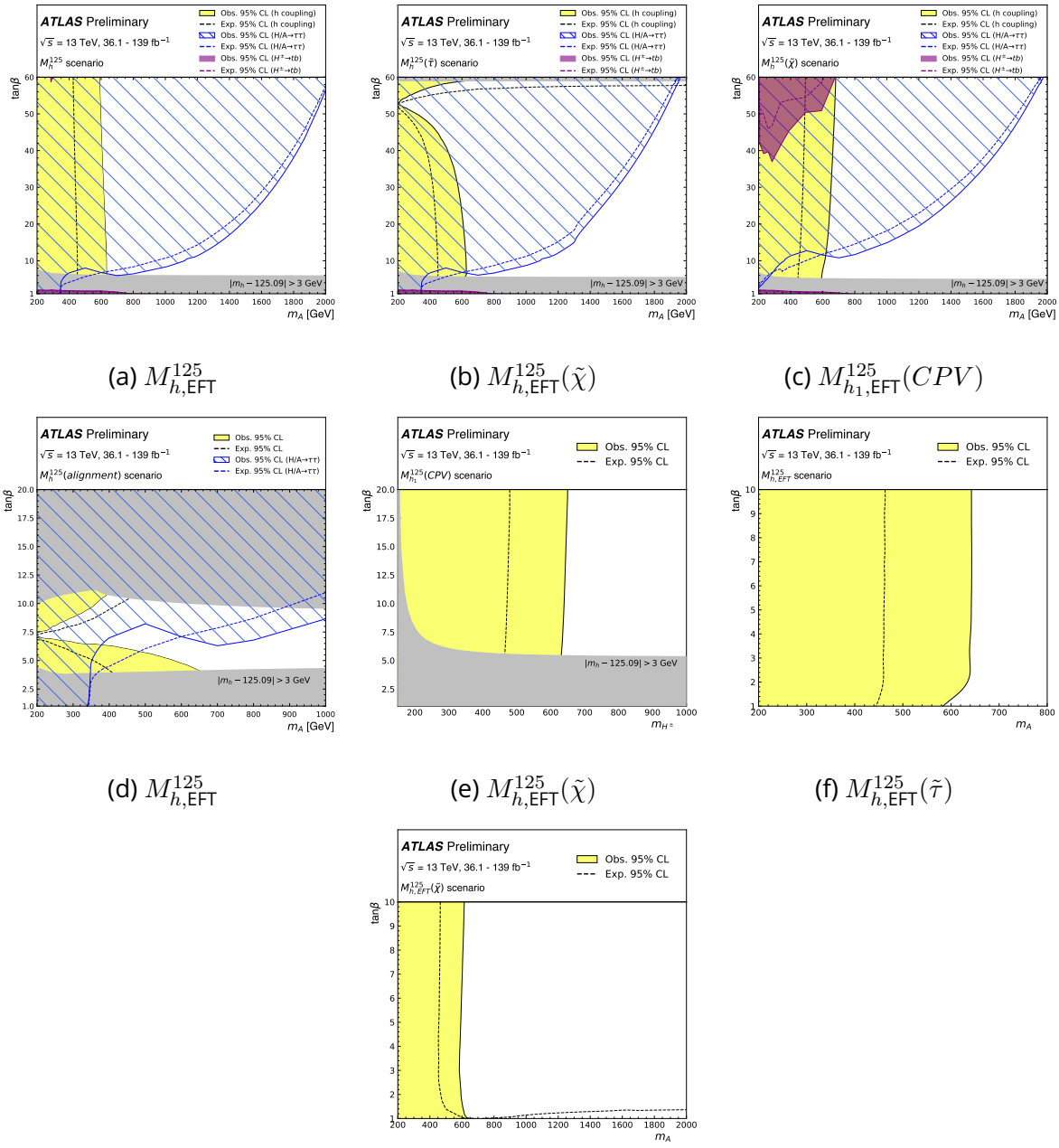

(a) $M_{h,\text{EFT}}^{125}$ (b) $M_{h,\text{EFT}}^{125}(\tilde{\chi})$ (c) $M_{h_1,\text{EFT}}^{125}(CPV)$

(d) $M_{h,\text{EFT}}^{125}$ (e) $M_{h,\text{EFT}}^{125}(\tilde{\chi})$ (f) $M_{h,\text{EFT}}^{125}(\tilde{\tau})$

(g) $M_{h,\text{EFT}}^{125}(alignment)$

Figure 5.29: Preliminary results for the seven scenarios. Source: [117].

5.9.3 hMSSM

The hMSSM scenario is a special case of MSSM, where all superpartners (apart from the Higgs sector) are very heavy. This scenario is not valid for the $\tan\beta$ values lower than 1 (to maintain mass-relations in the Higgs sector) and larger than 10 (for the validity of the radiative corrections). In this scenario, the Higgs boson couplings to vector bosons (κ_V), up-type fermions (κ_u) and down-type fermions (κ_d) can be expressed as functions of only two parameters: m_A and $\tan\beta$ as:

$$\begin{aligned} \kappa_V &= \frac{s_d(m_A,\tan\beta)+\tan\beta\ s_u(m_A,\tan\beta)}{\sqrt{1+\tan^2\beta}} \\ \kappa_u &= s_u(m_A,\tan\beta)\frac{\sqrt{1+\tan^2\beta}}{\tan\beta} \\ \kappa_d &= s_d(m_A,\tan\beta)\sqrt{1+\tan^2\beta}, \end{aligned} \tag{5.33}$$

where the functions s_u and s_d are given by:

$$\begin{aligned} s_u &= \frac{1}{\sqrt{1+\frac{\left(m_A^2+m_Z^2\right)^2\tan^2\beta}{\left(m_Z^2+m_A^2\tan^2\beta-m_h^2(1+\tan^2\beta)\right)^2}}} \\ s_d &= \frac{\left(m_A^2+m_Z^2\right)\tan\beta}{m_Z^2+m_A^2\tan^2\beta-m_h^2(1+\tan^2\beta)}\ s_u. \end{aligned} \tag{5.34}$$

The results of the 2-dimensional likelihood scan in the $(m_A,\tan\beta)$ plane are shown by Fig. 5.30.

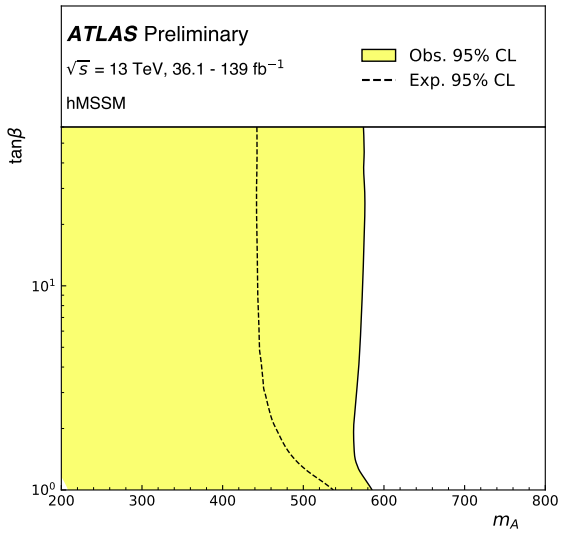

Figure 5.30: Exclusion contours: observed (solid) and expected (dashed) results on the hMSSM $(m_A,\tan\beta)$ parameter space. Source: [117].

5.10 Conclusion

STXS combination of various Higgs boson decay channels is interpreted in SMEFT framework. The results are presented as 68% and 95% confidence intervals for the Wilson coefficients in the Warsaw basis in top-scheme and PCA eigenvectors. MSSM and 2HDM interpretation of this results is obtained.

Independently of the STXS combination, performance of the differential cross-section interpretation is compared to the one of STXS using the $H \to \gamma\gamma$ and $H \to 4\ell$ combination.

Conclusion

The thesis presents the E_T/p_T method as an alternative to the classical m_{ee} method for the calibration of the electromagnetic calorimeter. In the central region of the detector (barrel, $|\eta| < 1.0$) both results show similar tendency for the linearity measurements. Using the $p_T^Z - y^Z$ reweighting, which corrects the Z-boson kinematic distributions, improves the overall agreement between the methods. With more statistics and improved calibration of the tracker, this new method may become a more solid cross-check for the nominally used m_{ee} method even outside of the barrel.

Measurements of the Higgs boson STXS couplings are made with the $H \to \gamma\gamma$ channel in the thesis over 28 truth-bins. No deviation from the SM is found. Cross-section of the $pp \to H \to \gamma\gamma$ process is measured to be $121 \pm 10\ fb$, which corresponds to the inclusive signal strength of 1.045 ± 0.10. Contribution from the statistical and systematic uncertainties are at the same level. This analysis establishes the most strict limit on the tH production cross-section ($8.41\times$SM) from a single channel measurement. Results are interpreted within the kappa-framework and a general EFT. The $H \to \gamma\gamma$ only EFT results are not described in the thesis, to avoid overlapping with the material of the combined Higgs EFT interpretation.

Combined Run 2 Higgs dataset is used for an EFT and BSM (2HDM and MSSM) interpretations. The results are presented in the form of 68% and 95% CI on the Wilson coefficients in the Warsaw basis and in the PCA-transformed ones. Independently, a comparison on the constraint power of the EFT measurements with the STXS and differential cross-section approaches is done using the same final states: $H \to \gamma\gamma$ and $H \to 4\ell$ combination. In the case of the simultaneous fit of all three probed Wilson coefficients, the STXS approach shows better constraining power, which might be explained by the STXS design, which separates production modes and uses an optimised phase-space binning for BSM measurements.

2HDM and MSSM results are obtained using a combined STXS Run 2 dataset. For the MSSM, 7 benchmark scenarios are probed. 2HDM results include constrains with and without including the Higgs-self-coupling parameter κ_λ. Direct results on the confidence intervals on the 2HDM models are compared with the ones obtained with the EFT interpretation via matching. Results are similar.

A - Statistics

A.1 Introduction

The limited knowledge on the detailed genuine configuration of the analyses (limited performance of the subdetectors, intrinsic stochastic behaviour of the interaction of particles with matter, limited knowledge on the theory, etc.) conducted at the LHC naturally drives to the usage of statistics to extract information from data. Two main interpretations are commonly used:

- frequentist, which interprets probability as a relative frequency of observing a given result if the experiment is repeated.
- Bayesian, which interprets probability as a degree of belief in a certain hypothesis (theory or value of a parameter) based on the observed data. The so-called Bayes theorem relates the probability to observe an event under a certain hypothesis to the probability of the hypothesis if an event is observed:

$$P(hyp|event) = \frac{P(event|hyp) \times P(hyp)}{P(event)}, \tag{A.1}$$

  where $P(hyp)$ means the prior (unconditional) probability of the hypothesis, $P(event)$ is the probability of an event to occur, $P(hyp|event)$ is the a posteriori probability of the hypothesis, if the event has occurred, $P(event|hyp)$ is the probability of the event to happen if the hypothesis is true.

The statistical procedure aims to extract information on some parameters from a given set of data x[1], which may rule out our current paradigm of theory. Traditionally, the frequentist interpretation is used in the domain of particle physics.

Firstly, the construction of the model is reviewed. Then, the extraction of information on these parameters is explained, as well as how to check the validity of the model.

A.2 Fundamental Concepts

The fundamental object is the Probability Density Function (pdf) $f(x)$. For a given continuous variable x defined over a phase space Ω, it gives the probability that x belongs to the infinitesimal interval $[x, x + \mathrm{d}x]$. Hence, it is normalised over the phase space to have a total probability of unity:

$$\int_{\Omega} f(y)\,\mathrm{d}y = 1. \tag{A.2}$$

A typical example is the Gaussian function (Fig. A.1), also called Normal Distribution defined by:

$$f(x) = \frac{1}{\sigma\sqrt{2\pi}} e^{-\frac{1}{2}\frac{(x-\mu)^2}{\sigma^2}}, \tag{A.3}$$

[1] Later on, by x it will be also denoted a set of observations $\{x\}$.

where μ is the central position and σ is the spread of the function. The formula can be naturally generalised to higher dimension x, y, ... as:

$$\text{probability } x \in [x, x + \mathrm{d}x] \text{ and } y \in [y, y + \mathrm{d}y] \text{ and } \ldots \; = f(x, y, \ldots)\, \mathrm{d}x\, \mathrm{d}y \ldots \tag{A.4}$$

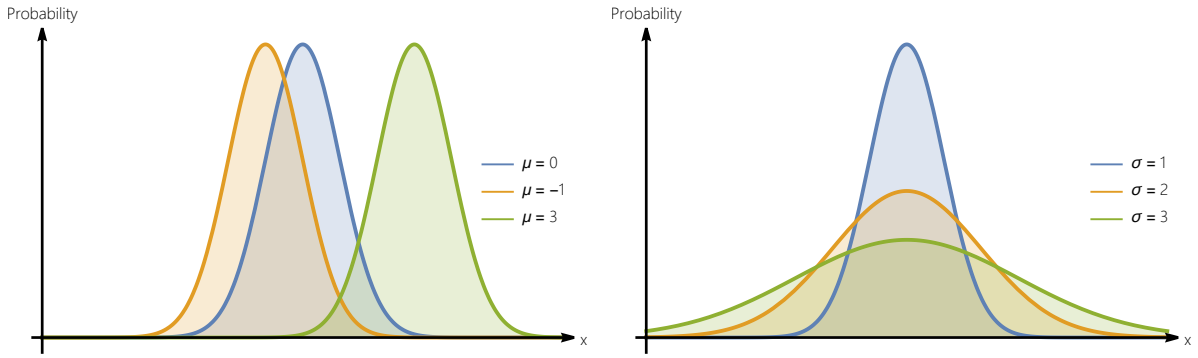

Figure A.1: Examples of Gaussian Distributions with various mean (μ) and spread (σ).

The integral of the pdf, so-called Cumulative Distribution Function (cdf, Fig. A.2), labelled as F, is often used to extract various properties on a random variable, in particular to establish the probability to have a value greater than a certain threshold (Section A.5.2). It is defined as:

$$F(x) = \int_{-\infty}^{x} f(x)\, \mathrm{d}x. \tag{A.5}$$

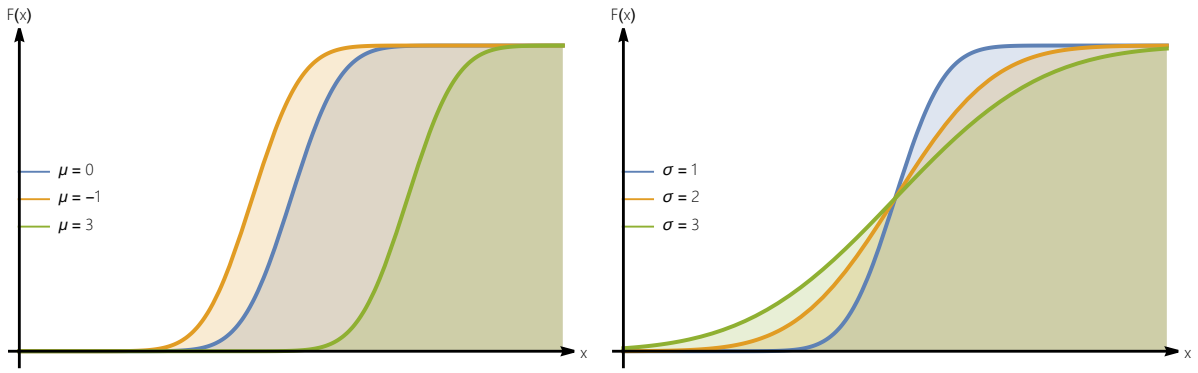

Figure A.2: Examples of cdf of various Gaussian functions.

A.3 Building of the Statistical Model

A.3.1 Random variable

Given the statistical nature of variables, any random variable x is fully characterised by its pdf $f(x|params)$, where $params$ is a set of parameters. This is written as:

$$x \sim f(x|params). \tag{A.6}$$

Often, observed quantities follow Gaussian distribution, which is a consequence of the Central-limit theorem, stating that if a variable value results from a large number of independent factors, its distribution is asymptotically approaching the Gaussian function.

A.3.2 Likelihood

For a given set of measurements, it is possible to construct a pdf. Before a measurement, a joint pdf of obtaining a set of data x described by a set of parameters is $f(x|params)$. With data already observed, one may regard it as a function of the parameters. This function is called likelihood:

$$\mathcal{L}(params) = f(x|params) \tag{A.7}$$

For a given fixed data set, it states a likelihood value for each possible value of the useful parameters. The likelihood function can be used to estimate the best value of these parameters in order to accommodate with the data using the Maximum Likelihood estimator method (Section A.4).

To increase the flexibility of a model with a given data, the model may require some additional parameters, so-called nuisance parameters, labelled θ in the following, which are not parameters of interest, but may reflect some additional properties of data. They are classified in two types:

- *Unconstrained*. This is the case for parameters with no constraint from a prior knowledge, such as normalisation and slope of background.
- *Constrained*, also called systematic nuisance parameters. This is the case for parameters which serve to represent a level of the systematic uncertainty (called also shortly systematic) on the model itself, based on a prior value of the systematic. To reflect that precise values of such parameters is not known, their values follow a given pdf, so-called constraint pdf or penalty function.

A.3.3 Nuisance Parameters

To reflect that the parameters entering the likelihood (cross-sections, branching ratios, efficiencies, etc.) could depend on some systematics, nuisance parameters are introduced:

$$param(\vec{\theta}) = param_{nominal} \times \mathcal{F}(\vec{\theta}), \tag{A.8}$$

where $\mathcal{F}$ is the response function, carrying information on the nuisance parameter influence on a given parameter x. Usually, any nuisance parameter may lead to a small effect on a parameter of interest (POI), hence the response function is usually linear. There are few usual choices on the response function:

- Gaussian constraint $\mathcal{F}_G(\delta, \theta) = (1 + \delta\theta)$, where δ is the systematic. For example, it could be used for the Higgs mass or the Photon Energy Scale in the $H \to \gamma\gamma$ analysis.
- Log-normal constraint $\mathcal{F}_{LN}(\delta, \theta) = \mathrm{e}^{\sqrt{\ln(1+\delta^2)}\theta}$. It is used whenever a negative model parameter has no physical sense (luminosity, branching ratio, trigger response, etc.).

- Asymmetric constraint $\mathcal{F}_A(\delta,\theta) = \begin{cases} \mathcal{F}_{LN}(\delta^{up},\theta) & \text{up variation} \\ \mathcal{F}_{LN}(\delta^{down},\theta) & \text{down variation} \end{cases}$

  This is the case when a potential impact from an up- and down-variation can have different magnitude. Some examples are: Photon Isolation, α_s (strong coupling), pileup, where δ is the relative uncertainty amplitude.

The pull θ is defined as the difference between the best-fit-value $\hat{\theta}$, and the central value of the corresponding global observable θ_0, divided on the pre-fit error σ_θ:

$$\theta = \frac{\hat{\theta} - \theta_0}{\sigma_\theta}. \tag{A.9}$$

Usually the nuisance parameters themselves are gaussian-distributed[2], hence their own pdf $G(\theta)$ must be included in the total likelihood via the following form:

$$G(\theta) = \frac{1}{\sqrt{2}} \mathrm{e}^{-\frac{(\theta-\theta_0)^2}{2}}. \tag{A.10}$$

Such nuisance parameters are usually referred as α-*type*[3] systematic.

In recent works [144] it was found that a fit may be improved after accommodating to the fact that errors on the nuisance parameters (which are defined in an additional external experiment) have their own uncertainties. Hence, the errors on the nuisance parameters are not numbers, but follow a statistical distribution. Due to the fact that they follow a Γ-distribution, such nuisance parameters are called γ-type ones. For example, such a modification is useful to describe a predicted number of events in a background-only bin in a control region of the analysis. Usually, the prediction is based on the MC simulation which have finite statistics and might be also affected by some intrinsic nuisance parameters of the generator used.

A.3.4 Example of likelihood

In particle physics, there are three main basic types of analysis depending on the way to construct the likelihood:

- *Counting experiment*. The observable is the total number of events n composed of signal s and background events b. The likelihood follows a Poisson distribution:

  $$\mathcal{L}(n|s,b) = \exp^{-(s+b)} \frac{(s+b)^n}{n!}, \tag{A.11}$$

  In this case, the shape of the distribution is not exploited.

- *Binned shape analysis*. The observables are the number of events n_i in each bin i. In this case, the likelihood is:

  $$\mathcal{L}(n_i|s,b) = \prod_{i \in bins} \exp^{-\left(sf_i^{sig}+bf_i^{bkg}\right)} \frac{\left(sf_i^{sig}+bf_i^{bkg}\right)^{n_i}}{n_i!}, \tag{A.12}$$

[2] Or log-normal, as it is discussed in the text above. Here, Gaussian distribution is discussed for simplicity.

[3] This notation of α-*type* systematic should not be confused with the α-type error from statistics.

with sf_i^{sig} and bf_i^{bkg} being the fitted signal and background number of events in the bin i.

- *Unbinned shape extended analysis*. The likelihood takes a similar form to the binned one expression, except that the total number of events is irrelevant and the likelihood is constructed as a product of likelihoods of single events:

$$\mathcal{L}(n|s,b) = \frac{\exp^{-(s+b)}}{n!} \prod_{i \in events} (s\ pdf(x_i) + b\ pdf(x_i)) \tag{A.13}$$

where x_i is the discriminant variable used to distinguish between signal and background.

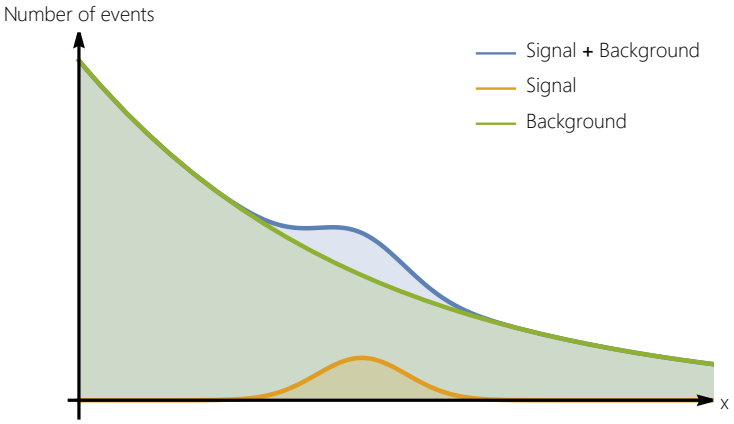

Figure A.3: Illustration of a model (total pdf normalised to the number of events) and its components: signal (orange) and background (green).

A.4 Parameter estimation

Given a set of data x, it is possible to infer a confidence interval of values for a parameter μ used in a statistical model describing this data. An estimator is a function of the observed data used to estimate some property of a pdf which can be computed in a unique way. Often, an estimator, denoted as $\hat{\mu}$, is introduced to evaluate the value of the parameter μ of a given model (pdf). Practically, an estimator must obey a few properties:

- *consistent*: accuracy of the estimator increases with an increase of statistics. If $\hat{\theta}_n$ is an estimator for a dataset of size n:

$$P\left(|\hat{\theta}_n - \theta| > \epsilon\right) \xrightarrow[n\to\infty, \forall\epsilon]{} 0 \tag{A.14}$$

- *unbiased*: bias defined as $b = E[\hat{\theta}] - \theta$, must be zero;
- *efficient*: estimator variance must asymptomatically converge to the Rao-Cramer-Frecher bound (eq. A.16) i.e. there is no other estimator with a smaller variance.

Value of an efficient estimator $\hat{\theta}$ is usually obtained by the Maximum Likelihood criterium:

$$\begin{aligned} \frac{\partial \mathcal{L}}{\partial \theta_i} &= 0 \\ \hat{\theta} &= \underset{\theta}{\operatorname{argmax}}\, \mathcal{L}\left(\theta\right) \end{aligned} \tag{A.15}$$

Such an estimator is called ML estimator (Maximum Likelihood estimator).

The error on an efficient estimator $\hat{\theta}$ can be obtained from the RCF bound (eq. A.16):

$$V[\hat{\theta}] \geqslant \left(1 + \frac{\partial b}{\partial \theta}\right)^2 / E\Big[-\frac{\partial^2 \ln(\mathcal{L})}{\partial \theta^2}\Big] \tag{A.16}$$

In a case of an unbiased estimator, the error is just an element of the inverse information matrix:

$$\mathcal{I}_{ij} = E\left[-\frac{\partial^2 \ln(\mathcal{L})}{\partial \theta_i \partial \theta_j}\right] \tag{A.17}$$

A.4.1 Graphical method of uncertainties estimation

In a case of one parameter, in the vicinity of the best-fit value $\hat{\theta}$ of a parameter θ (ML estimate), one can perform a Taylor expansion:

$$\ln\, \mathcal{L}(\theta) = \ln\, \mathcal{L}(\hat{\theta}) + \left[\frac{\partial \ln \mathcal{L}}{\partial \theta}\right]_{\theta=\hat{\theta}} (\theta - \hat{\theta}) + \frac{1}{2!}\left[\frac{\partial^2 \ln\, \mathcal{L}}{\partial \theta^2}\right]_{\theta=\hat{\theta}} (\theta - \hat{\theta})^2 + \cdots, \tag{A.18}$$

Given that $\hat{\theta}$ is the local minimum, the following relations hold:

$$\begin{aligned} &\frac{\partial \ln \mathcal{L}}{\partial \theta}|_{\theta=\hat{\theta}} = 0 \\ &\ln\, \mathcal{L}(\theta)|_{\theta=\hat{\theta}} = \ln\, \mathcal{L}(\theta)_{max} \\ &\frac{\partial^2 \ln\, \mathcal{L}(\theta)}{\partial \theta^2} = -\hat{\sigma^2}_{\hat{\theta}} \end{aligned} \tag{A.19}$$

where the latest relationship is a consequence of eq. (A.17).

Hence, ignoring higher terms in the expansion (considering Gaussian case), the following relation can be derived:

$$\ln\, \mathcal{L}(\theta) = \ln\, \mathcal{L}_{max} - \frac{(\theta - \hat{\theta})^2}{2\hat{\sigma^2}_{\hat{\theta}}}. \tag{A.20}$$

In a case of one standard deviation $\hat{\sigma}_{\hat{\theta}}$:

$$\ln\, \mathcal{L}(\hat{\theta} \pm \hat{\sigma}_{\hat{\theta}}) = \ln\, \mathcal{L}_{max} - \frac{1}{2}, \tag{A.21}$$

Hence, the error on a parameter θ can be obtained graphically on a plot of the log-likelihood $\ln \mathcal{L}(\theta)$ as a function of θ by finding such values of θ, where the likelihood varies on 1/2. An illustration is shown at Fig. A.4 for a 1-D scenario.

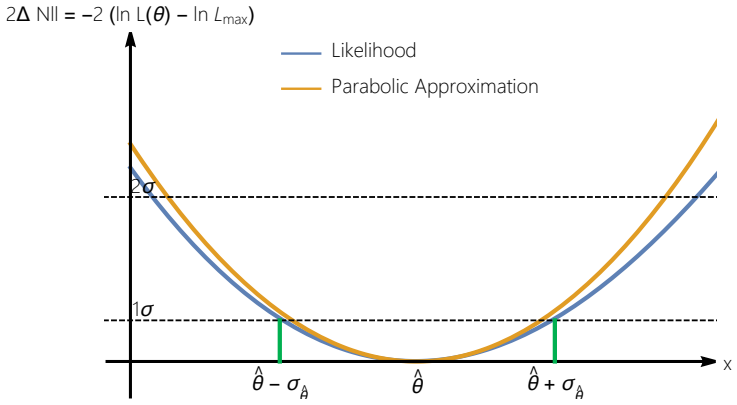

Figure A.4: Illustration of a likelihood scan in 1D (blue) and its parabolic extrapolation (orange). Dashed line show one variation of likelihood corresponding to the level of uncertainty on $\hat{\theta}$ of $1(1^2 = 1)$ and 2σ ($2^2 = 4$) respectively. ML best-fit-value $\hat{\theta}$ is at the position of the minimum of $-2 \ln \mathcal{L}$ (maximum of likelihood).

In the 2D case, relation A.20 becomes:

$$\ln \mathcal{L}(\alpha, \beta) = \ln \mathcal{L}_{max} - \frac{1}{2(1-\rho^2)} \left[\left(\frac{\alpha - \hat{\alpha}}{\sigma_{\hat{\alpha}}} \right)^2 + \left(\frac{\beta - \hat{\beta}}{\sigma_{\hat{\beta}}} \right)^2 - 2\rho \left(\frac{\alpha - \hat{\alpha}}{\sigma_{\hat{\alpha}}} \right) \left(\frac{\beta - \hat{\beta}}{\sigma_{\hat{\beta}}} \right) \right], \tag{A.22}$$

with $\rho = cov[\alpha, \beta]/(\sigma_{\hat{\alpha}} \sigma_{\hat{\beta}})$. 2D likelihood contours are illustrated in Fig. A.5. From such 2D contours in a $\theta_1 \times \theta_2$ plane, one may get a hint of errors on both θ_1 and θ_2 and on their correlation ρ:

$$\rho = \mathrm{tg}\,(2\phi)\, \frac{\sigma_{\hat{\alpha}}^2 - \sigma_{\hat{\beta}}^2}{\sigma_{\hat{\alpha}} \sigma_{\hat{\beta}}} \tag{A.23}$$

A.5 Hypothesis testing

It is possible to reformulate the purpose of statistics as a tool to distinguish between two hypotheses: $\mathcal{H}_0$ (null-hypothesis) and $\mathcal{H}_1$ (alternative hypothesis) via the observed set of data x depending on a value of a quantity called test-statistic t. For example, to compute a significance of presence a signal, the null-hypothesis $\mathcal{H}_0$ usually assumes presence of only background, while the alternative hypothesis $\mathcal{H}_1$ assumes presence of a signal at its predicted rate.

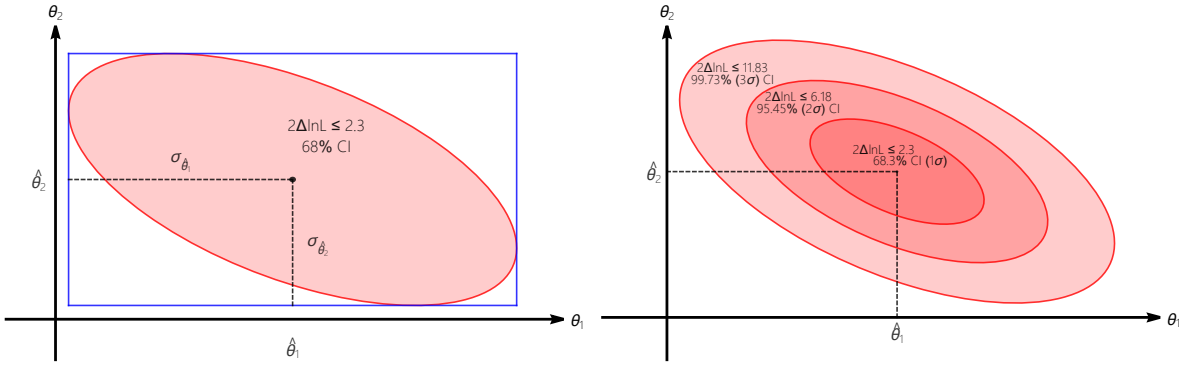

(a) (b)

Figure A.5: Illustration of a 2D likelihood contour (a) fulfilling the condition of $2\Delta \ln \mathcal{L} \leq 2.3$, giving 68% CI (confidence interval). The maximum likelihood point (black dot in the center of the ellipse) gives ML (minimum likelihood) best-fit-value $\hat{\theta}_1$ and $\hat{\theta}_2$ for the parameters θ_1 and θ_2, respectively. Blue surrounding lines give 68% CI for the parameters independently, which is the level of 1σ error. Figure (b) shows 1, 2 and 3σ uncertainty levels and the corresponding thresholds for the likelihood contours.

A.5.1 Test Statistic t

A test-statistic t is a numerical quantity computed on a dataset x. It is used to make a decision on rejecting a given nominal $\mathcal{H}_0$ hypothesis with respect to an alternative hypothesis $\mathcal{H}_1$. Each statistics is quantified by its *power*: probability to correctly reject the null-hypothesis $\mathcal{H}_0$ when it is false. Another important quantities in statistics are α- and β-Type errors, representing probability to mistakenly reject the null (alternative) hypothesis, when it is not the case and the power of a test, respectively.

According to the Neyman–Pearson lemma [145], for two simple[4] hypotheses $\mathcal{H}_0$ and $\mathcal{H}_1$, the optimal statistics is given by the likelihoods ratio:

$$t = \frac{\mathcal{L}(\mathcal{H}_0)}{\mathcal{L}(\mathcal{H}_1)}, \tag{A.24}$$

which minimises the β-type errors for a given α. Though in particle physics non-parameter-free hypothesis are utilised, similar test statistic still commonly used.

A.5.2 p-value

For each test statistic, it is possible to compute the $p-value$, which is the probability that the test statistic is more extreme than a given value if $\mathcal{H}_0$ is true. In a nutshell, $p-value$ is a probability to get a larger value of the test statistics t then the observed t_{observed}, under $\mathcal{H}_0$. It is basically, the α-type error. Therefore, it can be computed as:

$$p_0 = \int_{t_{\text{observed}}}^{\infty} f(t|\mathcal{H}_0)\,\mathrm{d}t = p\left(t > t_{\text{observed}}|\mathcal{H}_0\right), \tag{A.25}$$

[4] with no free parameters.

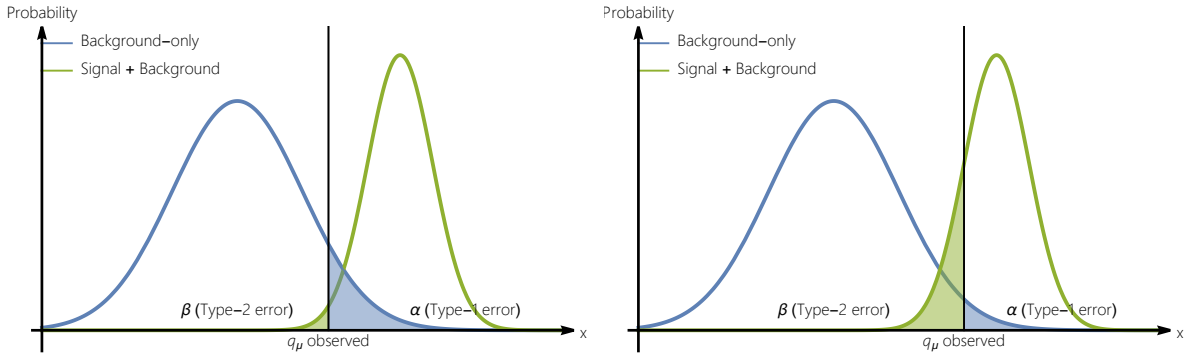

(a) (b)

Figure A.6: Distribution of a test statistics q_μ for two hypotheses: a null-hypothesis $\mathcal{H}_0$ (here, with a scenario where the data contains only background) and an alternative $\mathcal{H}_1$ (there is a signal present in the data). At each picture, the green shaded area shows the β-Type error: probability to reject the baseline hypothesis $\mathcal{H}_0$, when it is true. The blue shaded are is the α-Type error: probability to reject the baseline hypothesis $\mathcal{H}_0$, when it is true. For the scenario (a) the $\mathcal{H}_1$ should be rejected since the probability that it is true (given by the β-Type error) is small. In contrary, for the scenario (b), the null hypothesis should be rejected.

where $t_{observed}$ is the value of the test statistics in a probed dataset and $f(t|\mathcal{H}_0)$ is the distribution of t under the null-hypothesis $\mathcal{H}_0$ (see Section A.6.5).

The $p-value$ is usually translated into an equivalent quantity, the significance Z:

$$Z = \Phi^{-1}(1-p), \tag{A.26}$$

where Φ^{-1} is the inverse of Gaussian cdf (quantile). Such definition allows to express the observed $p-value$ in units of standard deviations of Gaussian (Fig. A.7).

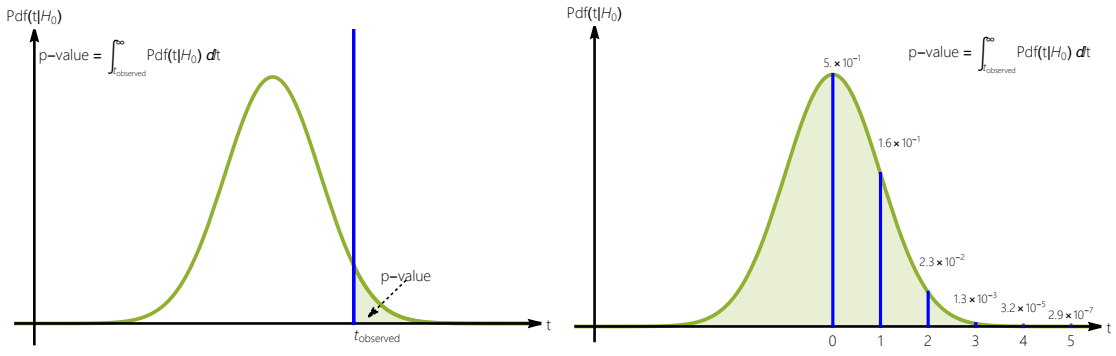

(a) (b)

Figure A.7: Figure (a) shows what for a given observed value of a test statistic t is the $p-value$ (green shaded area). Figure (b) Illustrates $p-value$ for various levels of the significance.

In particle physics, the threshold value of $p-value$ used to make a decision on disregarding the null-hypothesis $\mathcal{H}_0$ with respect to the alternative $\mathcal{H}_1$ and to claim a discovery, is 5σ significance ($Z = 5$). The corresponding $p-value$ is $2.87\ 10^{-7}$. For establishing an upper limit (section A.6.4), 95% confidence interval is used, corresponding to $p-value = 0.05$ and $Z = 1.64$. An example of the $p-value$ for the Higgs boson depending on its mass is shown in Fig. A.11.

A.6 Framework for a search

A.6.1 Signal strength

In particle physics, a measurement of a signal is often conducted in terms of the signal strength μ which is the ratio of the observed cross-section of a process to the predicted value:

$$\mu = \frac{\sigma_{obs}}{\sigma_{SM}}. \tag{A.27}$$

Normalisation of this parameter to the SM allows to have a unit-less quantity, with a value around unity for any physical process, therefore preventing having problems with various scales (for example, the neutrino scattering cross-section is many orders lower than the Z-boson di-electron decay). In this way, one can construct a general statistical test to probe the signal strength on its deviation from unity. An example of a scan of the Higgs boson signal strength depending on its mass is shown in Fig. A.8.

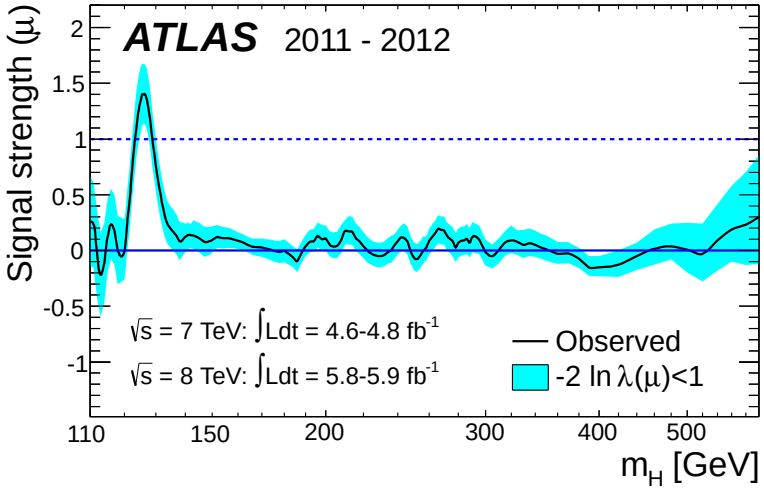

Figure A.8: Observed signal strength of the Higgs boson signal. Based on the ATLAS dataset of 2011 and 2012 data-taking years at the centre-of-mass energy $\sqrt{s} = 7, 8$ TeV. The cyan contour illustrates the 68% confidence interval. Source: [146].

In real statistical models used in analyses, there are additional free parameters such as nuisance parameters (Section A.3.3). Hence, the optimal statistic defined by (eq. A.24) needs to be modified to accommodate for these parameters. It is done by defining $\lambda(\mu)$ as:

$$\lambda(\mu) = \frac{\mathcal{L}(\mu, \hat{\hat{\theta}})}{\mathcal{L}(\hat{\mu}, \hat{\theta})}, \tag{A.28}$$

where μ is the signal strength (POI[5]) as a function of which the likelihood ratio is constructed, $\hat{\mu}$ and $\hat{\theta}$ are respectively the best-fit-values ML for the signal strength (POI) and the nuisance parameters. $\hat{\hat{\theta}}$ is the best-fit-value ML for θ maximising the likelihood for specified μ. Therefore, the numerator represents the maximal value of the likelihood achievable for a given μ and denominator is the global maximum of the likelihood function. Hence, $\lambda(\mu)$ spans values from zero to unity.

It is often more convenient to use the following static based on $\lambda(\mu)$:

$$t_\mu = -2 \ln \lambda(\mu), \tag{A.29}$$

with the corresponding p_μ:

$$p_\mu = \int_{t_\mu^{\text{observed}}}^{\infty} f(t_\mu|\mu)\, \mathrm{d}t_\mu, \tag{A.30}$$

A.6.2 Confidence Interval (CI) and Confidence Level (CL)

In a case where one has no sensitivity to discover a signal, one could establish upper limits on its rate. Otherwise, it is possible to compute a confidence interval (CI) for a given parameter at a given confidence level (CL) α. For a given measurement $\hat{\mu}$ of a variable μ and a confidence level (expressed in percent) CL_α it is possible to establish a confidence interval Ω. In the frequentist approach, it is related to the series of observations $\hat{\mu}$: in CL_α % of cases, the observed values $\hat{\mu}$ would belong to the established range Ω. Mathematically speaking, from the dataset x, one could deduce interval bounds $a(x)$ and $b(x)$, such as:

$$p\left([a(x), b(x)] \ni \mu\right) = 68\% \tag{A.31}$$

where μ is the true value.

In the Bayesian approach, the *credible interval* is used instead: for a series of observations yielding a range Ω, the real value of the parameter μ would be covered by these intervals in CL_α of the cases:

$$\int_a^b p\left(\mu\right) = 68\% \tag{A.32}$$

where $p(\mu)$ is the posterior distribution of μ.

Practically, the confidence intervals are often used to define the so-called CL_s statistics:

$$CL_s = \frac{CL_{s+b}}{CL_b}, \tag{A.33}$$

where CL_{s+b} and CL_b are the confidence levels for the *signal and background* and *pure background* hypotheses. In fact, this definition of CL_s modifies the $p-value$ p_μ as:

$$p'_\mu = \frac{p_\mu}{1-p_b}, \tag{A.34}$$

where p_μ is the $p-value$ of presence of a signal with a signal strength μ (which is preferred by data) and p_b is the $p-value$ of the *background-only* hypothesis.

[5]Parameter-of-interest

A.6.3 Alternative statistic $\tilde{t}_\mu$

In a case when it is a priori known that the signal may only lead to additional events (therefore, the signal strength $\mu \geqslant 0$), then a better agreement between data and a model is achieved by trimming the eq. A.28 ratio for negative μ. The modified likelihood ratio is defined as:

$$\tilde{\lambda}(\mu) = \begin{cases} \dfrac{\mathcal{L}(\mu, \hat{\hat{\theta}})}{\mathcal{L}(\hat{\mu}, \hat{\theta})}, & \hat{\mu} \geqslant 0 \\ \dfrac{\mathcal{L}(\mu, \hat{\hat{\theta}})}{\mathcal{L}(0, \hat{\theta}(0))}, & \hat{\mu} < 0, \end{cases} \tag{A.35}$$

which yields to the corresponding modified test statistic $\tilde{t}_\mu$:

$$\tilde{t}_\mu = \begin{cases} -2 \ln \dfrac{\mathcal{L}(\mu, \hat{\hat{\theta}})}{\mathcal{L}(\hat{\mu}, \hat{\theta})}, & \hat{\mu} \geqslant 0 \\ -2 \ln \dfrac{\mathcal{L}(\mu, \hat{\hat{\theta}})}{\mathcal{L}(0, \hat{\theta}(0))}, & \hat{\mu} < 0 \end{cases} \tag{A.36}$$

A.6.4 Limits

For defining an upper limit on a signal strength μ, one is usually interested in existence of a positive signal, therefore it is convenient to modify the general expression for the test statistic described by the equation A.29 in the following way (the statistic used for an upper-limit is denoted as q_μ):

$$q_\mu = \begin{cases} -2 \ln \lambda(\mu) & \hat{\mu} \leq \mu, \\ 0 & \hat{\mu} > \mu, \end{cases} \tag{A.37}$$

In a case of only positive signal allowed (where $\tilde{\lambda}$ statistic is used, defined by eq. A.35), it is possible to define in a similar way an alternative test statistic $\tilde{q}_\mu$:

$$\tilde{q}_\mu = \begin{cases} -2 \ln \tilde{\lambda}(\mu) & \hat{\mu} \leq \mu, \\ 0 & \hat{\mu} > \mu, \end{cases} = \begin{cases} -2 \ln \dfrac{\mathcal{L}(\mu, \hat{\theta}(\mu))}{\mathcal{L}(0, \hat{\hat{\theta}}(0))} & \hat{\mu} < 0, \\ -2 \ln \dfrac{\mathcal{L}(\mu, \hat{\theta}(\mu))}{\mathcal{L}(\hat{\mu}, \hat{\hat{\theta}})} & 0 \leq \hat{\mu} \leq \mu, \\ 0 & \hat{\mu} > \mu. \end{cases} \tag{A.38}$$

with the corresponding $p - value$:

$$p_\mu = \int_{q_\mu^{\text{obs}}}^{\infty} f(\tilde{q}_\mu | \mu) \, \mathrm{d}\tilde{q}_\mu \tag{A.39}$$

An example of a limit on the signal strength as a function of a parameter is given in Fig. A.9.

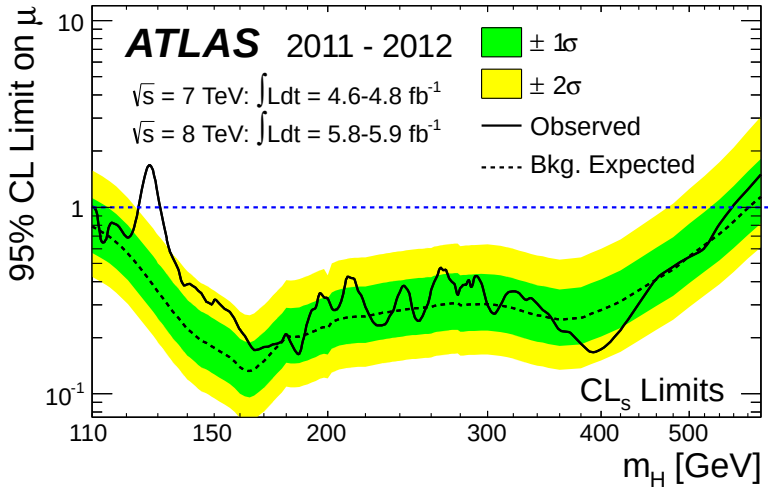

Figure A.9: Example of limits on the Higgs boson rate depending on its mass. Significant deviation of the observed and expected results around 125 GeV show a potential presence of the Higgs boson at this mass. Source: [146].

A.6.5 Approximate distribution of the profile likelihood ratio

Computing $p-value$ from a given observed value of the test statistic q_μ requires knowledge of its pdf. In a simple case with a large statistics, it can be approximated using the Wald results [147]:

$$-2\ \ln\ \lambda(\mu) = \frac{(\mu-\hat{\mu})^2}{\sigma^2} + \mathcal{O}\left(\frac{1}{\sqrt{N}}\right), \tag{A.40}$$

where $\hat{\mu}$ is the best-fit-value, since $\hat{\mu}$ follows a Gaussian distribution with a mean μ' and a standard deviation σ. N is the data-sample size, hence in a large-sample-limit, the last term can be safely neglected. μ' is the alternative hypothesis value of μ. In general, the test statistic t_μ follows a non-central chi-square distribution with a non-centrality parameter Λ given by:

$$\Lambda = \frac{(\mu-\mu')}{\sigma^2}. \tag{A.41}$$

In a special case of $\mu' = \mu$, $-2\ \ln\ \lambda(\mu)$ approaches a chi-square for one degree of freedom [148].

If statistical model contains n POIs, then the t_μ is described by the chi-square distribution for n-degree of freedom (illustration given by Fig. A.10).

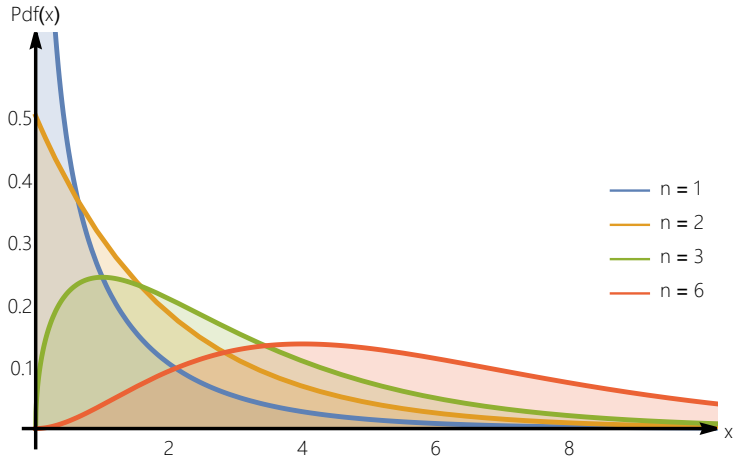

Figure A.10: Example of χ^2 distributions for a various number degrees of freedom.

Approximate distribution of the alternative test statistic $\tilde{q}_\mu$

The alternative test statistic $\tilde{q}_\mu$ defined by eq. A.38 may be approximated as [144]:

$$f(\tilde{q}_\mu|\mu) = \frac{1}{2}\delta(\tilde{q}_\mu) + \begin{cases} \frac{1}{2}\frac{1}{\sqrt{2\pi}}\frac{1}{\sqrt{\tilde{q}_\mu}}e^{-\tilde{q}_\mu/2} & if\ 0 < \tilde{q}_\mu \leq \mu^2/\sigma^2, \\ \frac{1}{\sqrt{2\pi}(2\mu/\sigma)}exp\left[-\frac{1}{2}\frac{(\tilde{q}_\mu+\mu^2/\sigma^2)^2}{(2\mu/\sigma)^2}\right] & if\ \tilde{q}_\mu > \mu^2/\sigma^2 \end{cases} \tag{A.42}$$

with $\sigma^2 = \frac{\mu^2}{q_{\mu,A}}$ where $q_{\mu,A}$ is the corresponding Asimov test statistic[6].

A.6.6 Significance

In order to claim a discovery of a new signal or phenomenon it is natural to test the hypothesis of the absence of signal, with respect to the presence of a signal. Hence, the profiled likelihood ratio should be used with signal strength μ equal to zero, representing pure-background hypothesis. Therefore, one ends up with the following test statistic q_0:

$$q_0 = \begin{cases} -2\ \ln\ \lambda(0) = -2\ \ln\ \dfrac{\mathcal{L}(0,\hat{\hat{\theta}})}{\mathcal{L}(\hat{\mu},\hat{\theta})} & \hat{\mu} \geqslant 0 \\ 0 & \hat{\mu} < 0, \end{cases} \tag{A.43}$$

which in the large sample limit yields the following expression for the significance:

$$Z = \sqrt{q_0}. \tag{A.44}$$

In a counting experiment with an observable n (number of detected events) expressed as:

$$n = \mu s + b, \tag{A.45}$$

Significance Z may be approximately determined via:

$$Z = \sqrt{2\left((s+b)\ln\left(1+\frac{s}{b}\right) - s\right)}, \tag{A.46}$$

[6]Asimov test statistic is defined using the Asimov dataset (Section A.7.1)

which for a low s/b reduces to:

$$Z = \frac{s}{\sqrt{b}}. \tag{A.47}$$

An example of a significance scan (and the corresponding $p-value$) depending on a parameter (here, mass of the Higgs boson) is given by Fig. A.11.

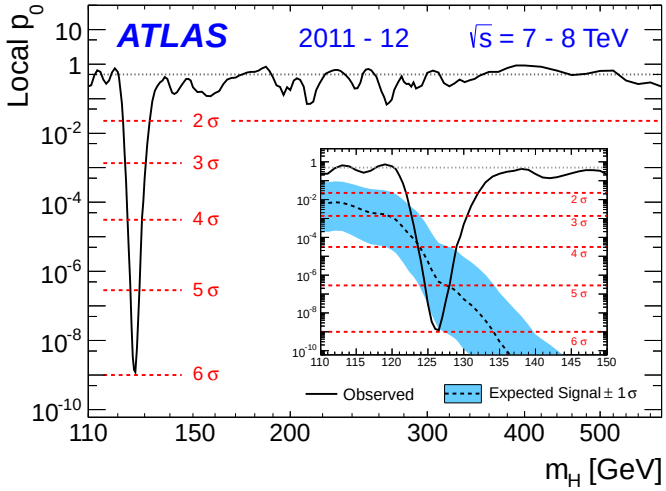

Figure A.11: $p-value$ and the corresponding significance in the historical scan for the search by ATLAS of the Higgs boson signal as a function of its mass. Based on the ATLAS 2011-2012 dataset at $\sqrt{s} = 7$ and 8 TeV. Source: [146].

A.7 Diagnostic of the results

A.7.1 Asimov dataset

To examine the sensitivity of a measurement (errors on the parameters, CL, others), one often conducts the measurement over a special dataset, called Asimov dataset. It is defined as the one which exactly follows a given model, hence all estimators $\hat{\theta}$ must give the truth values θ^{truth}. An example is given by Fig. A.12.

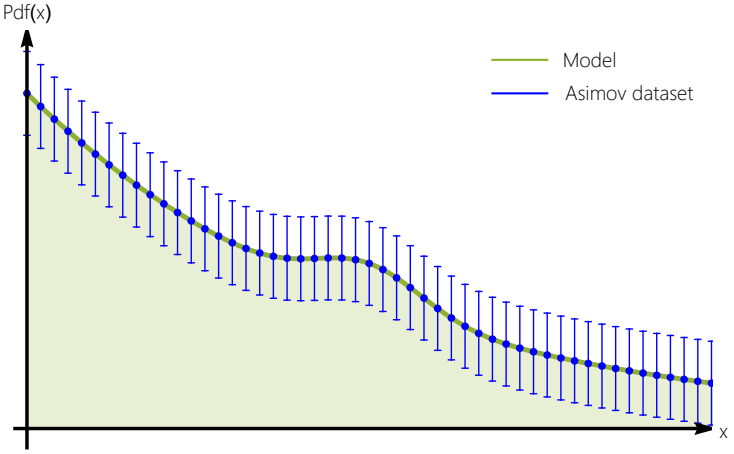

Figure A.12: Example of an Asimov dataset. Generated data (blue) follows exactly the model (green).

Commonly used terms

- **Observed** and **expected** (**pre-fit** and **post-fit**). Statistical results obtained with Asimov dataset are referred to as expected, while the ones from the real data are referred to as observed. For example, 1D likelihoods for the observed and expected branching fraction of the Higgs boson decaying into invisible final states are given in Fig. A.13.

  Among the expected results, one traditionally distinguishes between the **pre-fit** and **post-fit** ones. The difference between them is in the values of the nuisance parameters used in the generation of a dataset: for the pre-fit one, the nuisance parameters have zero value[7] and for the post-fit ones, they take their best-fit-values obtained from the real data.

- **Stat-only** and **full uncertainty** on a measured value consists of contributions from the statistical uncertainty and the systematic one. To compute only the statistical uncertainty, one needs to fix all the systematics at their best-fit value.

- **Profiled** (nuisance) parameters: if in a fit, one allows a parameter to float (its value is not fixed), then this parameter is said to be profiled. Otherwise, it is fixed.

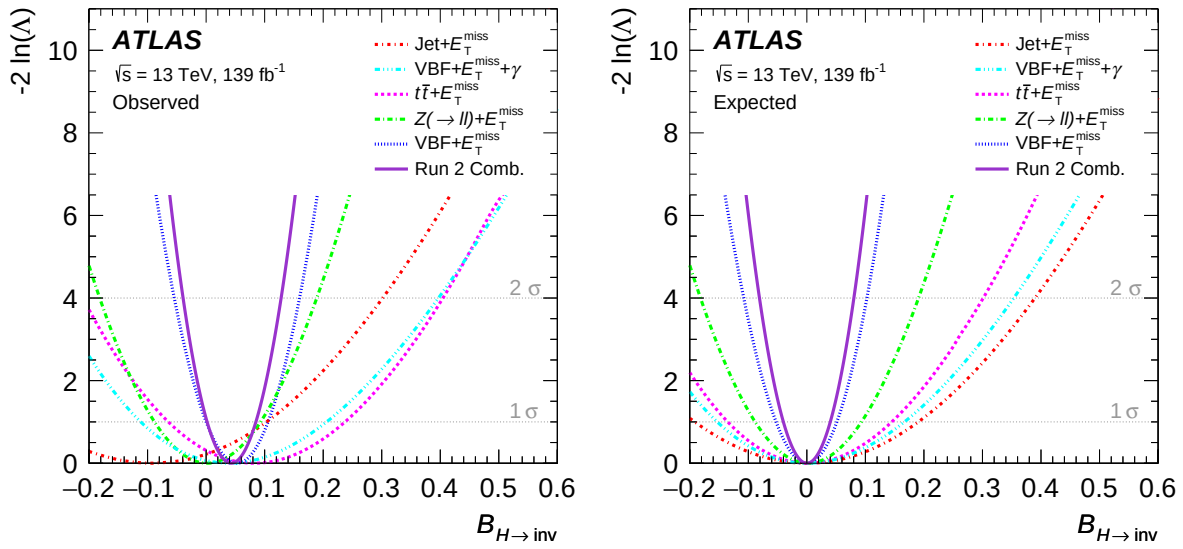

Figure A.13: Likelihoods for $\mathcal{B}\ (H_{inv})$ from the combined Run 2 dataset measured at ATLAS. (a) shows observed one and (b) - expected. Similarity of the likelihood curves is a cross-check of the method consistency. Source: [149].

[7] The nuisance parameters for the pre-fit case should have the same value, as the corresponding global observable θ_0. By convention, it is zero.

A.7.2 Nuisance parameters ranking

Another important aspect of verifying a model is to check the consistency of the nuisances model. The test concerns the central values of the nuisances obtained in a final analysis: their pull values should be within one sigma range. A significant deviation of a pull value for one systematic from unity is a hint of a problem in the nuisance model. An example of a nuisance parameter plot is given in Fig. A.14.

To obtain such a plot, one needs to study how the central value of a POI changes under varying systematic uncertainties one-by-one at-a-time.

If in an unconditional fit used to get a result on a analysis a POI μ is found to have a central value $\hat{\mu}$ with an error $\sigma_{\hat{\mu}}$ and a set of systematics $\vec{\hat{\theta}}$ is found with their errors $\vec{\hat{\sigma}}_{\theta_i}$, a set of fits must be done to construct a nuisance parameter ranking plot:

- $\sigma_i = \hat{\sigma}_i \pm 1$: pre-fit variations
- $\sigma_i = \hat{\sigma}_i \pm \sigma_{\hat{\theta}}$: post-fit variations.

Denoting best-fit-value in each case as $\hat{\mu}_{cond}$, impact in each case is the difference: $\hat{\mu} - \hat{\mu}_{cond}$. All other nuisance parameters are profiled (floated).

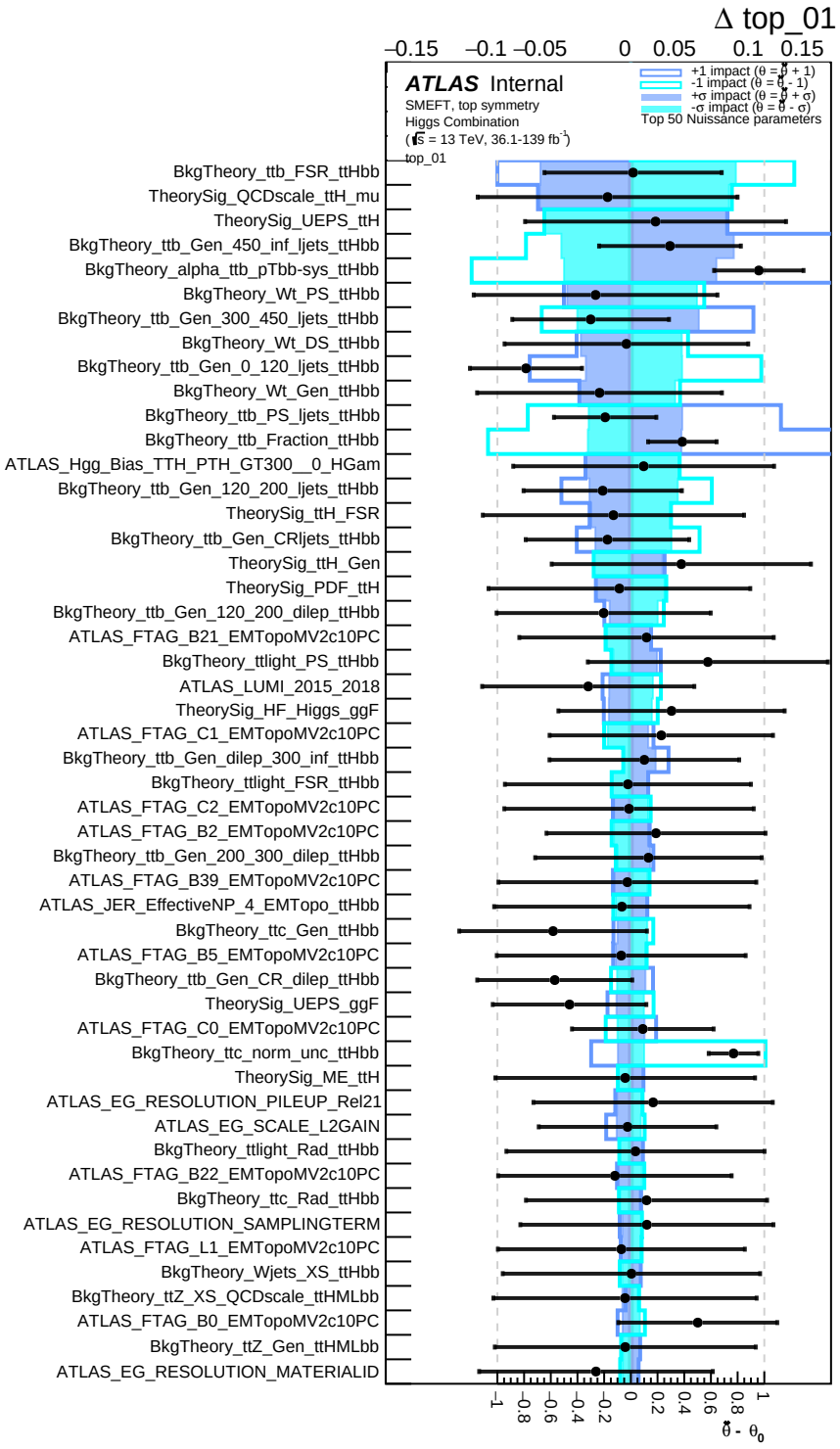

Figure A.14: Example of nuisance parameters ranking for a combined Higgs EFT measurement for the top_01 Wilson coefficient. Rows are ranked according to the sum of the squares of post-fit impacts on the POI. Transparent (shaded) areas show the pre-fit (post-fit) impact: change in the POI central value after changing the nuisance parameter value to its best-fit-value ± 1 ($\pm\sigma$). The corresponding axis is on the top of the plot. Black dots show best-fit-values of the nuisances and their errors. Values are encoded in the bottom axis. The colours represent the results of positive and negative variations of the systematics.

A.8 Conclusion

Statistical methods are widely used in particle physics for a variety of measurements: from observation of a new particle to establishing a limit on allowed values of parameters. Usually, in particle physics the frequentist interpretation is used to present the results. The statistical framework treats various physical quantities as mathematical functions, describing their pdfs and allowed values. Neumann-Pearson lemma is used to define a test statistics. This formalism is used in the analyses made in this PhD thesis.

B - Gamma matrices and Dirac bilinear forms

B.1 Gamma matrices

B.1.1 Definition

The set of γ^μ objects with $\mu \in \{0, 4\}$ is called gamma-matrices, which span a matrix representation of a Clifford algebra $\mathfrak{sl}_{1,3}(\mathbb{R})$ with the following properties:

$$\{\gamma_\mu, \gamma_\nu\} = 2g_{\mu\nu} \tag{B.1}$$

It is often defined the γ^5 matrix as:

$$\gamma^5 = \frac{i}{4}\epsilon_{\mu\nu\rho\sigma}\gamma^\mu\gamma^\nu\gamma^\rho\gamma^\sigma \tag{B.2}$$

There exists a couple of representations of the gamma-matrices:

Dirac representation

$$\begin{aligned}\gamma^0 &= \begin{pmatrix} 1 & 0 \\ 0 & -1 \end{pmatrix} \\ \gamma^\alpha &= \begin{pmatrix} 0 & \sigma^i \\ -\sigma^i & 0 \end{pmatrix} \\ \gamma^5 &= \begin{pmatrix} 0 & 1 \\ 1 & 0 \end{pmatrix}\end{aligned} \tag{B.3}$$

In this representation, the charge conjugation operator is real and anti-symmetric:

$$C = i\gamma^2\gamma^0 = \begin{pmatrix} 0 & 0 & 0 & -1 \\ 0 & 0 & 1 & 0 \\ 0 & -1 & 0 & 0 \\ 1 & 0 & 0 & 0 \end{pmatrix} \tag{B.4}$$

Weyl (chiral) basis Often, for analytical computations, it is more convenient to deal independently with the left and right parts of a Dirac bispinor ψ, by working in a basis where:

$$\psi = \begin{pmatrix} \psi_L \\ \psi_R \end{pmatrix} \tag{B.5}$$

In this basis, the gamma-matrices are defined as:

$$\begin{aligned}\gamma^0 &= \begin{pmatrix} 0 & 1 \\ 1 & 0 \end{pmatrix} \\ \gamma^\alpha &= \begin{pmatrix} 0 & \sigma^i \\ -\sigma^i & 0 \end{pmatrix} \\ \gamma^5 &= \begin{pmatrix} -1 & 0 \\ 0 & 1 \end{pmatrix}\end{aligned} \tag{B.6}$$

In this representation, the chiral projectors $P_L(R)$ take a simple form:

$$\begin{aligned} \mathcal{P}_L &= \frac{1}{2}\left(1-\gamma_5\right) = \begin{pmatrix} 1 & 0 \\ 0 & 0 \end{pmatrix} \\ \mathcal{P}_R &= \frac{1}{2}\left(1+\gamma_5\right) = \begin{pmatrix} 0 & 0 \\ 0 & 1 \end{pmatrix} \end{aligned} \tag{B.7}$$

B.1.2 Properties

$$\begin{aligned} \gamma^{\mu\dagger} &= \gamma^0\gamma^\mu\gamma^0 \\ \gamma^{5\dagger} &= \gamma^5 \\ \left(\gamma^5\right)^2 &= 1 \\ \{\gamma^5, \gamma^\mu\} &= 0 \\ \gamma_\mu\gamma^\mu &= 4 \\ \gamma_\mu\gamma^\nu\gamma^\mu &= -2\gamma^\nu \\ \gamma_\mu\gamma^\nu\gamma^\rho\gamma^\mu &= 4g^{\nu\rho} \end{aligned} \tag{B.8}$$

B.1.3 Root, rank and weights of a group

Rank

All the $\mathrm{SU}(N)$ generators are classified into two types:

- H_i: hermit diagonal operators (for $\mathrm{SU}(2)$, J_3). $i \in \{1, ..., m\}$.
- E_α: operators of creation and destruction (for $\mathrm{SU}(2)$, $J_\pm$).

The amount of hermit diagonal operators H_i given by m is called rank of a representation. It has a physical meaning of a maximal amount of quantum numbers required to describe quantum state. For example, $rang(\mathrm{SU}(2)) = 1$, so only one quantum number (*spin*) is enough to distinguish between all possible quantum states.

The ensemble of H_i forms the *Cartan sub-algebra*.

Weight

Eigenvalues μ_i of the hermitian operators H_i (introduced above in B.1.3) are called weights:

$$H_i|\vec{\mu}, D\rangle = \mu_i|\vec{\mu}, D\rangle \tag{B.9}$$

For $\mathrm{SU}(2)$, which has rang 1, there exists only one hermit diagonal operator J_3. Depending on the representation (singlet, doublet, triplet, ...), the weight takes the following values:

$$\mu = -J, -J-1, ..., J-1, J. \tag{B.10}$$

allowing $2J+1$ independent states.

Root

In the adjoint representation, there is a direct correspondance between a generator T_a and a state $|T_a\rangle$, represented by a matrix: $(T_a)_{bc} = -if_{abc}$. Hence, it can be written as:

$$T_a \to |T_a\rangle, \tag{B.11}$$

with a scalar product:

$$\langle T_a|T_b\rangle = \lambda^{-1}\mathrm{Tr}(T_a^\dagger T_b) \tag{B.12}$$

The action of an operator T_a on another generator T_b is defined as their commutator $[T_a, T_b]$. Hence, action of the operator T_a leads to a state:

$$T_a|T_b\rangle = |\,[T_a, T_b]\rangle \tag{B.13}$$

Since the H_i are hermit and diagonal, the commutators are:

$$\begin{aligned} H_i|H_j\rangle &= 0 \\ H_i|E_\alpha\rangle &= \alpha_i E_\alpha \\ H_i|E_\alpha^\dagger\rangle &= -\alpha_i E_\alpha^\dagger \end{aligned} \tag{B.14}$$

With the normalisation:

$$\begin{aligned} \langle E_\alpha|E_\beta\rangle &\equiv \lambda^{-1}\mathrm{Tr}\left(E_\alpha^\dagger E_\beta\right) = \delta_{\alpha\beta} \\ \langle H_\alpha|H_\beta\rangle &\equiv \langle H_\alpha|H_\beta\rangle = \delta_{\alpha\beta} \end{aligned} \tag{B.15}$$

By definition, the vector of weights in the adjoint representation is called roots. Since, the creation (destruction) operator increases (decreases) a quantum number of a state:

$$E_{\pm\alpha}|\vec{\mu}, D\rangle = N_{\pm\alpha,\mu}|\vec{\mu} \pm \vec{\alpha}, D\rangle \tag{B.16}$$

It can be shown that the scalar product of $\vec{\alpha}$ and $\vec{\mu}$ is:

$$\vec{\alpha} \cdot \vec{\mu} = -\frac{p-q}{2}\vec{\alpha}^2, \tag{B.17}$$

with p and q being real. Therefore, for two weights $\vec{\alpha}$ and $\vec{\beta}$, one can deduce:

$$\begin{aligned} \vec{\alpha} \cdot \vec{\beta} &= -\frac{m}{2}\vec{\alpha}^2 \\ \vec{\alpha} \cdot \vec{\beta} &= -\frac{m'}{2}\vec{\beta}^2 \end{aligned} \tag{B.18}$$

where m and m' are real numbers. Taking into account that the angle between two vectors $\vec{\alpha}$ and $\vec{\beta}$ is:

$$\cos^2\theta \equiv \frac{\left(\vec{\alpha} \cdot \vec{\beta}\right)^2}{\vec{\alpha}^2\vec{\beta}^2} = \frac{mm'}{4} \tag{B.19}$$

the allowed values of m and m' are shown in Tab. B.1:

(m, m')	mm'	θ
$(0, m')$, $(m, 0)$	0	$\pi/2$
$(1, 1)$	1	$\pi/3, 2\pi/3$
$(1, 2)$, $(2, 1)$	2	$\pi/4, 3\pi/4$
$(1, 3)$, $(3, 1)$	3	$\pi/6, 5\pi/6$
$(1, 4)$, $(2, 2)$, $(4, 1)$	4	$0, \pi$

Table B.1: Allowed pair of values for m and m', defined by eq. B.19.

B.1.4 Lorentz transformation

A Lorentz transformation matrix $\Lambda^{\mu}{}_{\nu}$ describing a Lorentz boost along a given x axis is:

$$\Lambda^{\mu}{}_{\nu} = \begin{pmatrix} \gamma & -\gamma\beta & 0 & 0 \\ \gamma\beta & \gamma & 0 & 0 \\ 0 & 0 & 1 & 0 \\ 0 & 0 & 0 & 1 \end{pmatrix}, \tag{B.20}$$

where β is a velocity in the units on the speed of light $\beta = v/c$ and γ is the gamma-factor[1] $\gamma \equiv \frac{1}{\sqrt{1-\beta^2}}$.

For a spinor field ψ_σ with a spinor index ψ, Lorentz transformation matrix $L_{\sigma\rho}$ from a state $\psi_\rho(x)$ to a boosted by momentum $\vec{p}$ state $\psi'_\sigma(x')$:

$$\psi'_\sigma(x') = L_{\sigma\rho}\psi_\rho(x) \tag{B.21}$$

can be expressed as:

$$L(\vec{p}) = \sqrt{\frac{E+m}{2m}}\left(1 - \gamma^0 \frac{\vec{\gamma}\vec{p}}{E+m}\right) \tag{B.22}$$

[1] It should not be confused with γ-matrices. Throughout the text, the matrices always carry an index.

C - EFT auxiliary material

C.1 STXS measurements

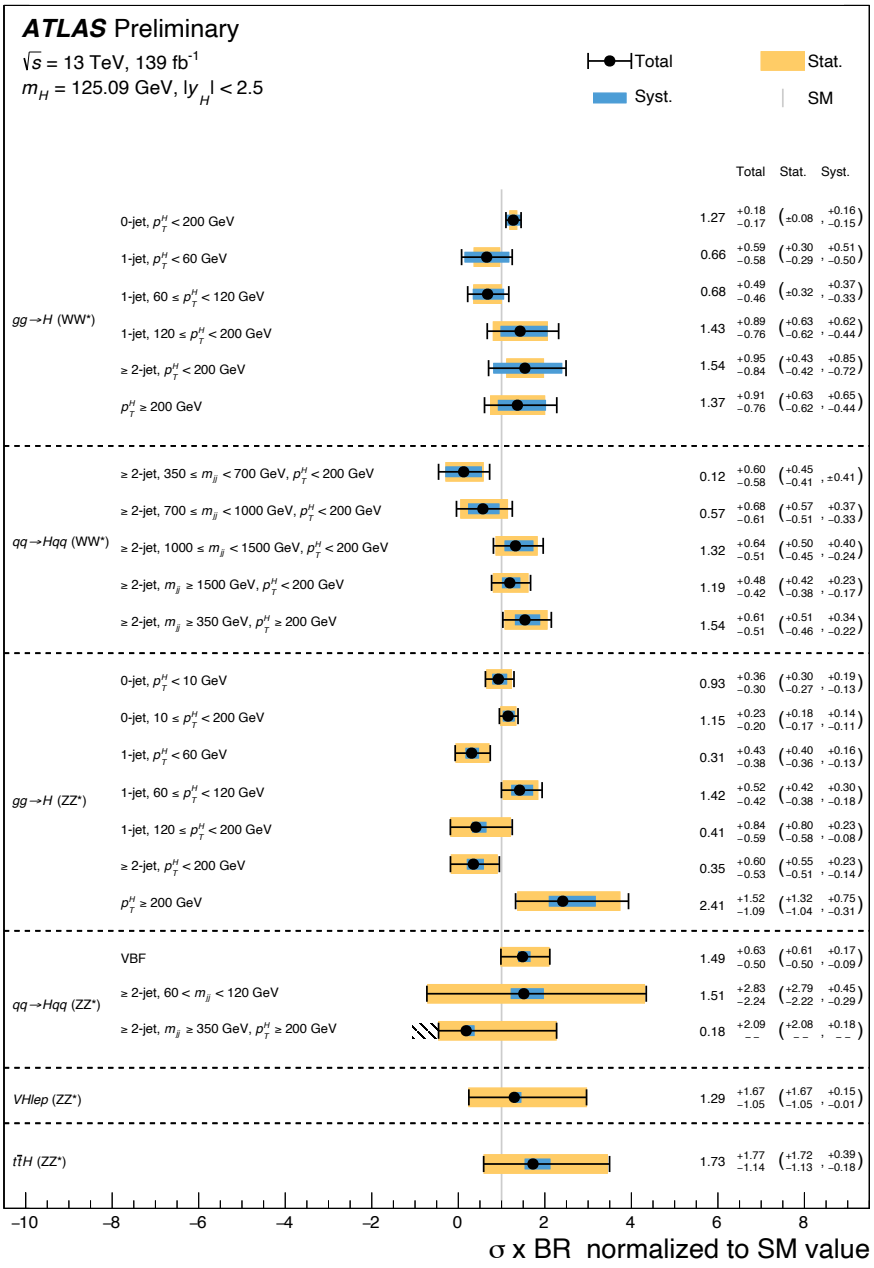

Figure C.1: Observed STXS signal strength in the WW and ZZ-related categories. Source: [117].

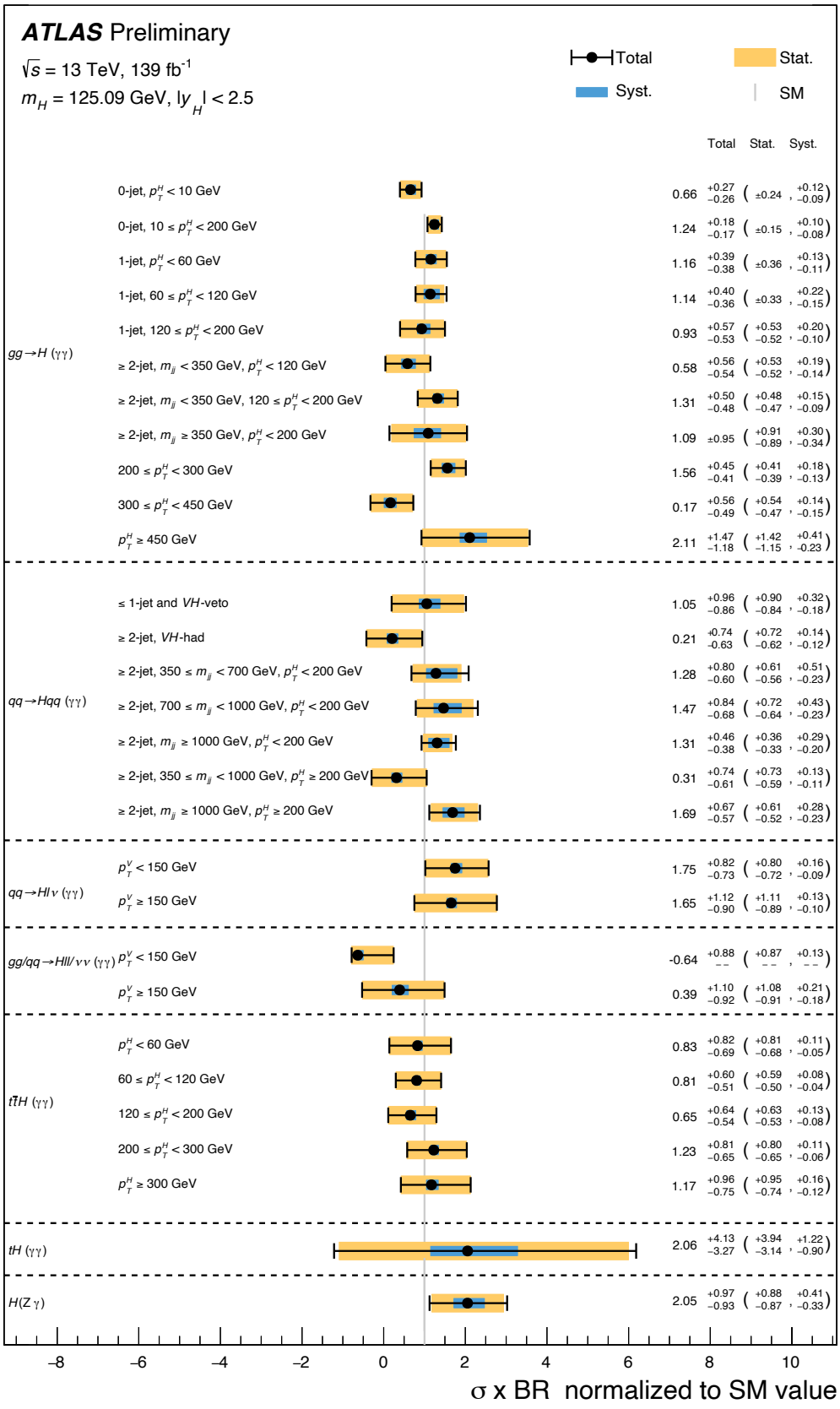

Figure C.2: Observed STXS signal strength in the $\gamma\gamma$- and $Z\gamma$-related categories. Source: [117].

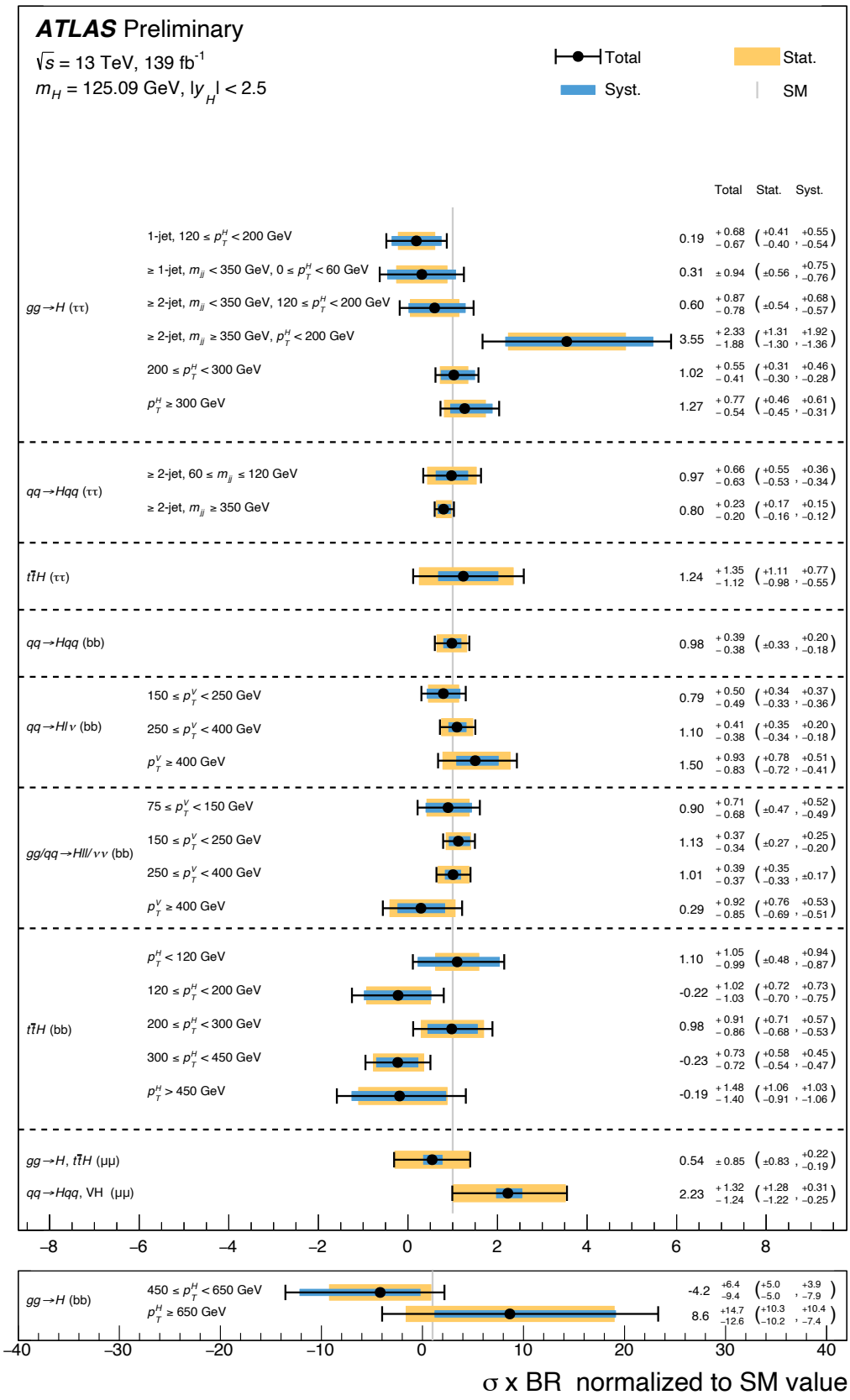

Figure C.3: Observed STXS signal strength in the $\tau\tau$, bb, $\mu\mu$ and cc-related categories. Source: [117].

C.2 Impact plots

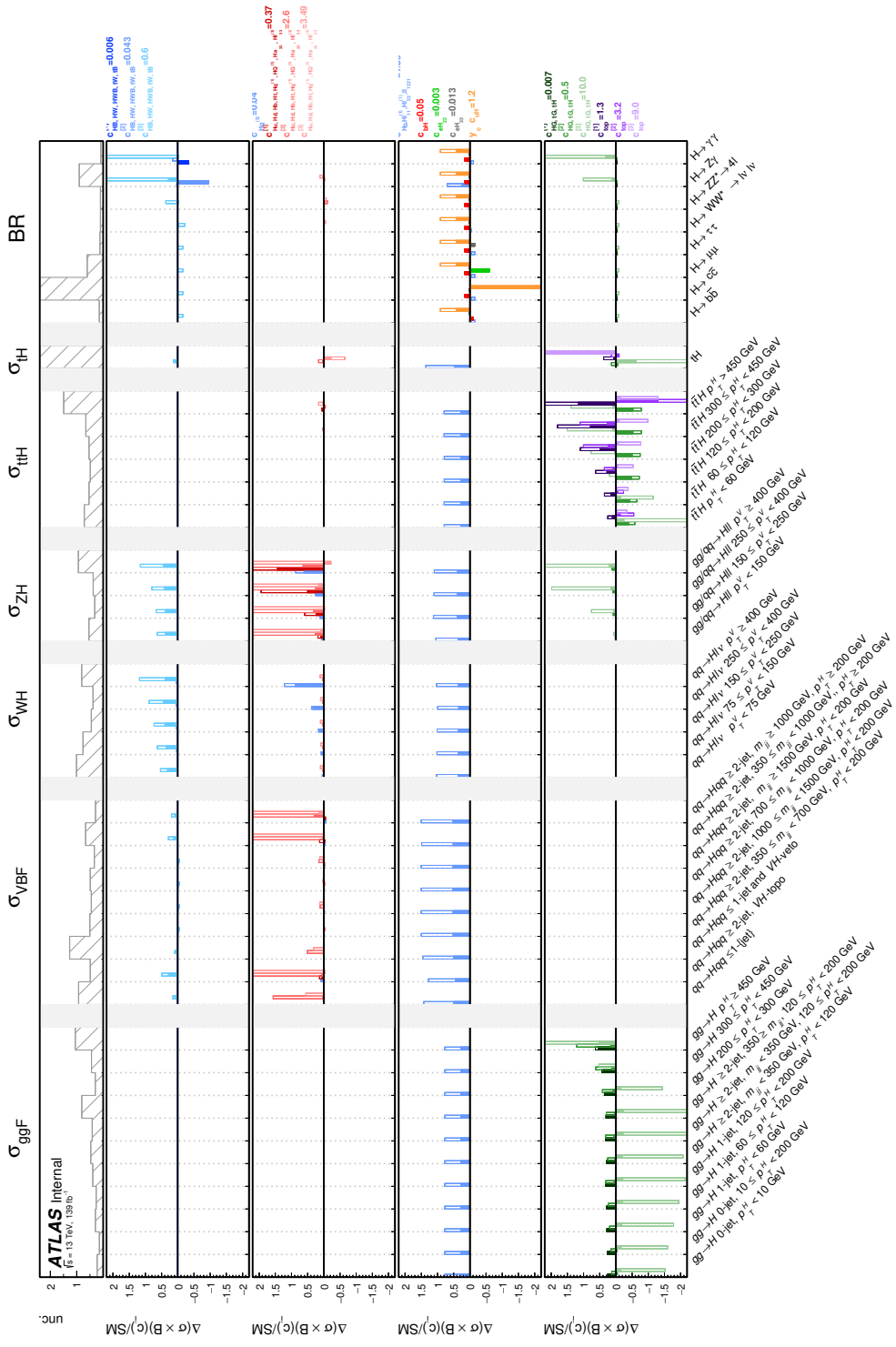

Figure C.4: Impact of various Wilson coefficients in the case of only linear (solid) and linear + quadratic (transparent) on the STXS cross-section. Source: [135].

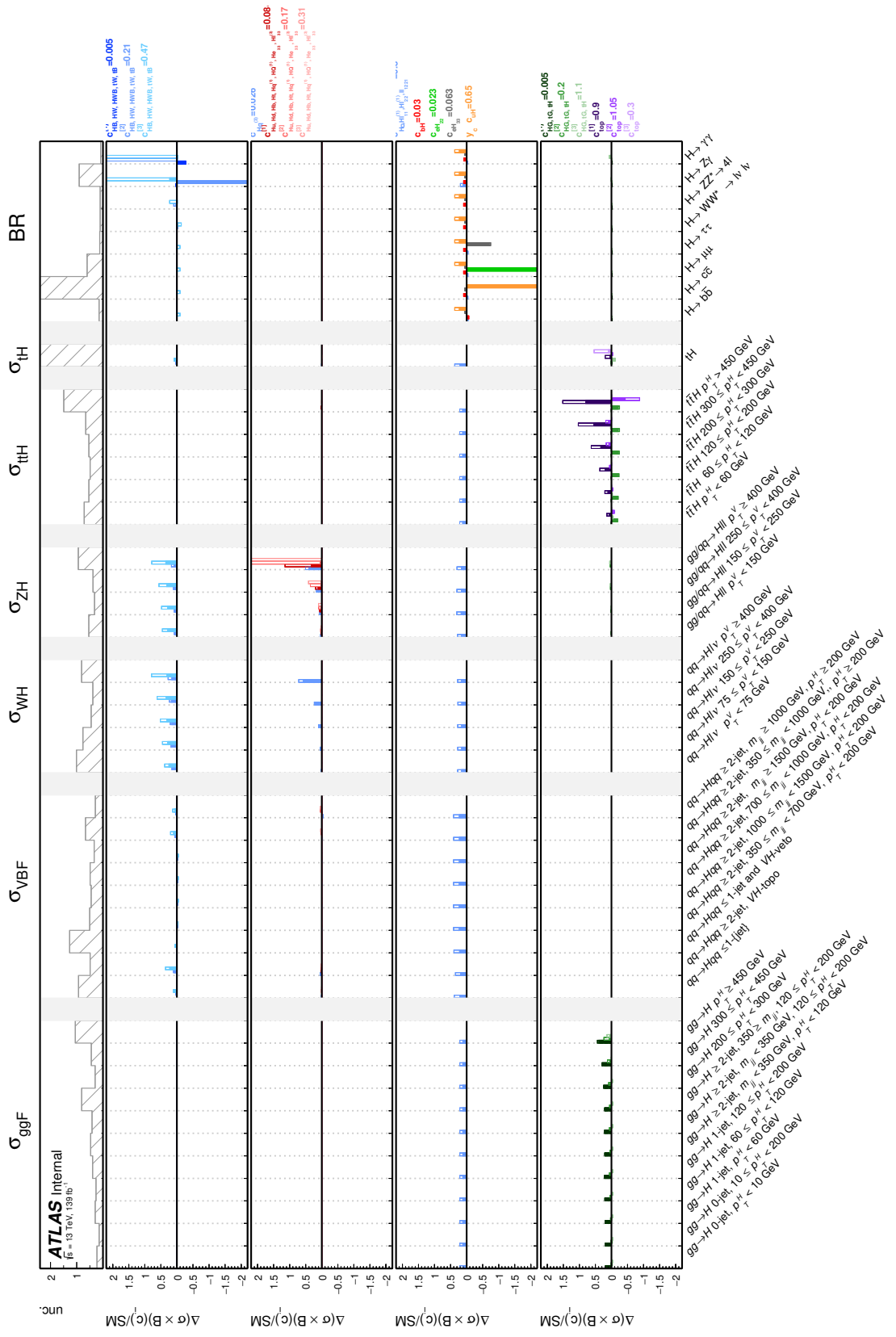

Figure C.5: Observed STXS signal strength in the WW and ZZ-related categories. Source: [135].

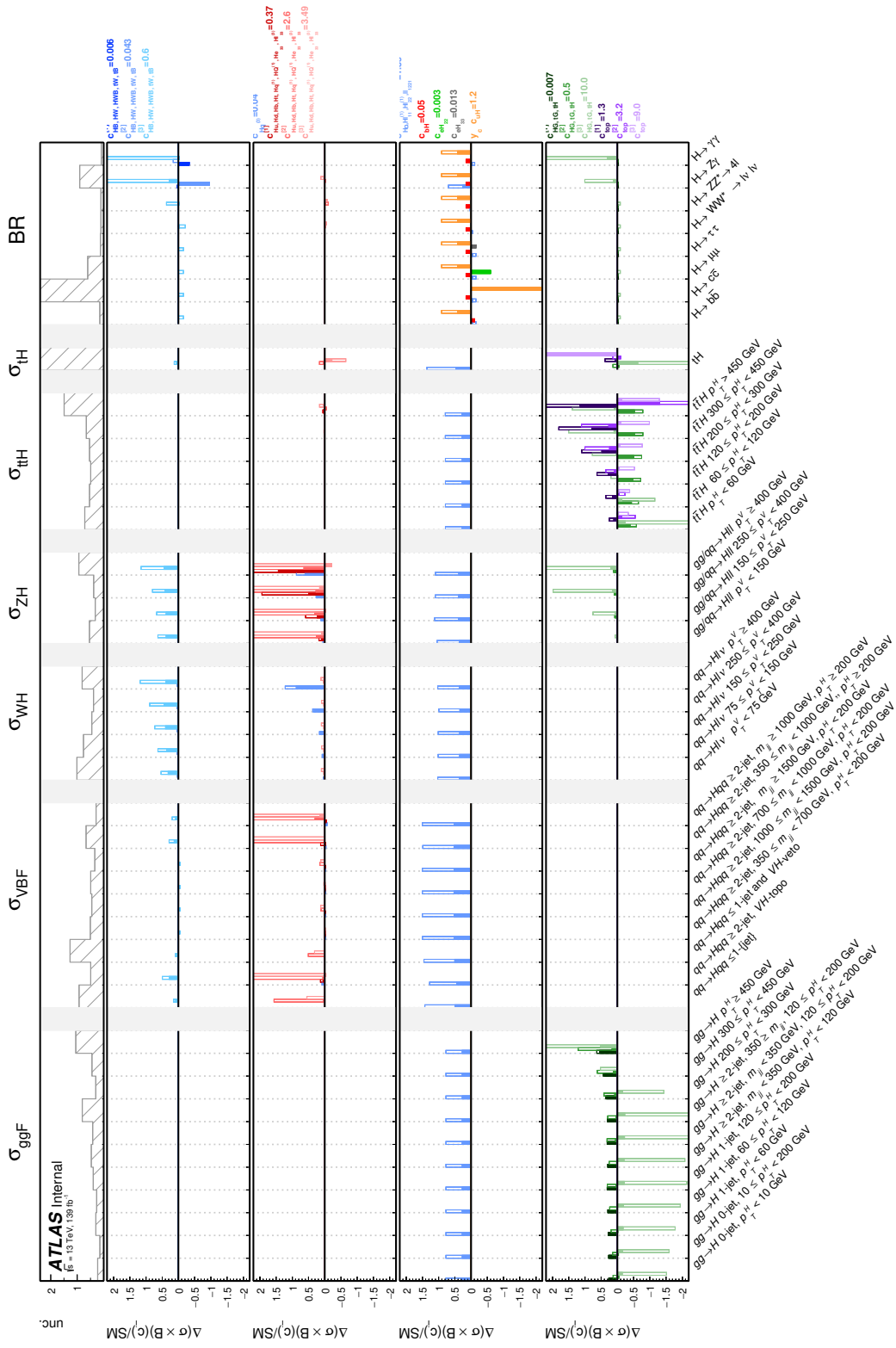

Figure C.6: Impact of the operators in the fit-basis on the cross-sections of various truth-bins. Filled histograms represent contributions of the linear terms and the open ones show impact of the quadratic parametrisation. Impact is defined as the ratio of the induced cross-section to the SM one. Source: [135].

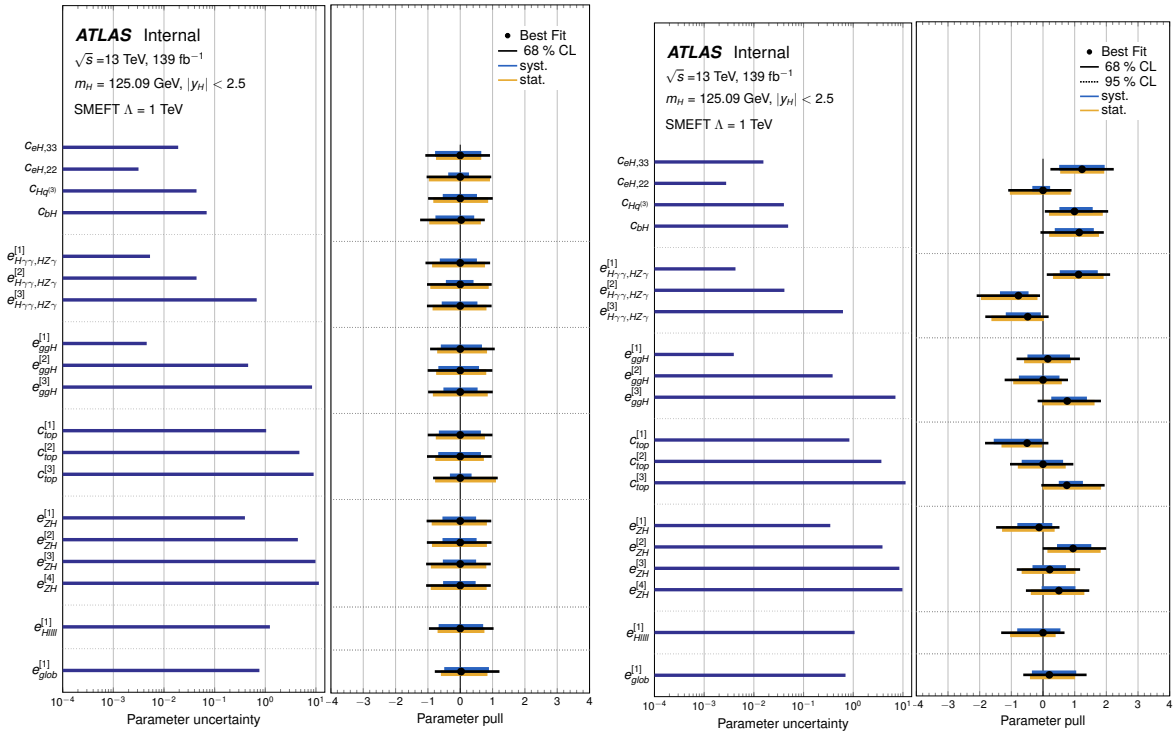

(a) Expected (b) Observed

Figure C.7: Expected (left) and observed (right) measurements of central values and breakdown of uncertainties on the Wilson coefficients in the fit-basis. Individual contributions of the systematic and statistical uncertainties are shown in blue and yellow, respectively. On each plot, the left sub-plot shows total uncertainty on a given coefficient. The results are obtained under the linear parametrisation. Source: [135].

C.3 Likelihood scans for the linear and quadratic parametrisations

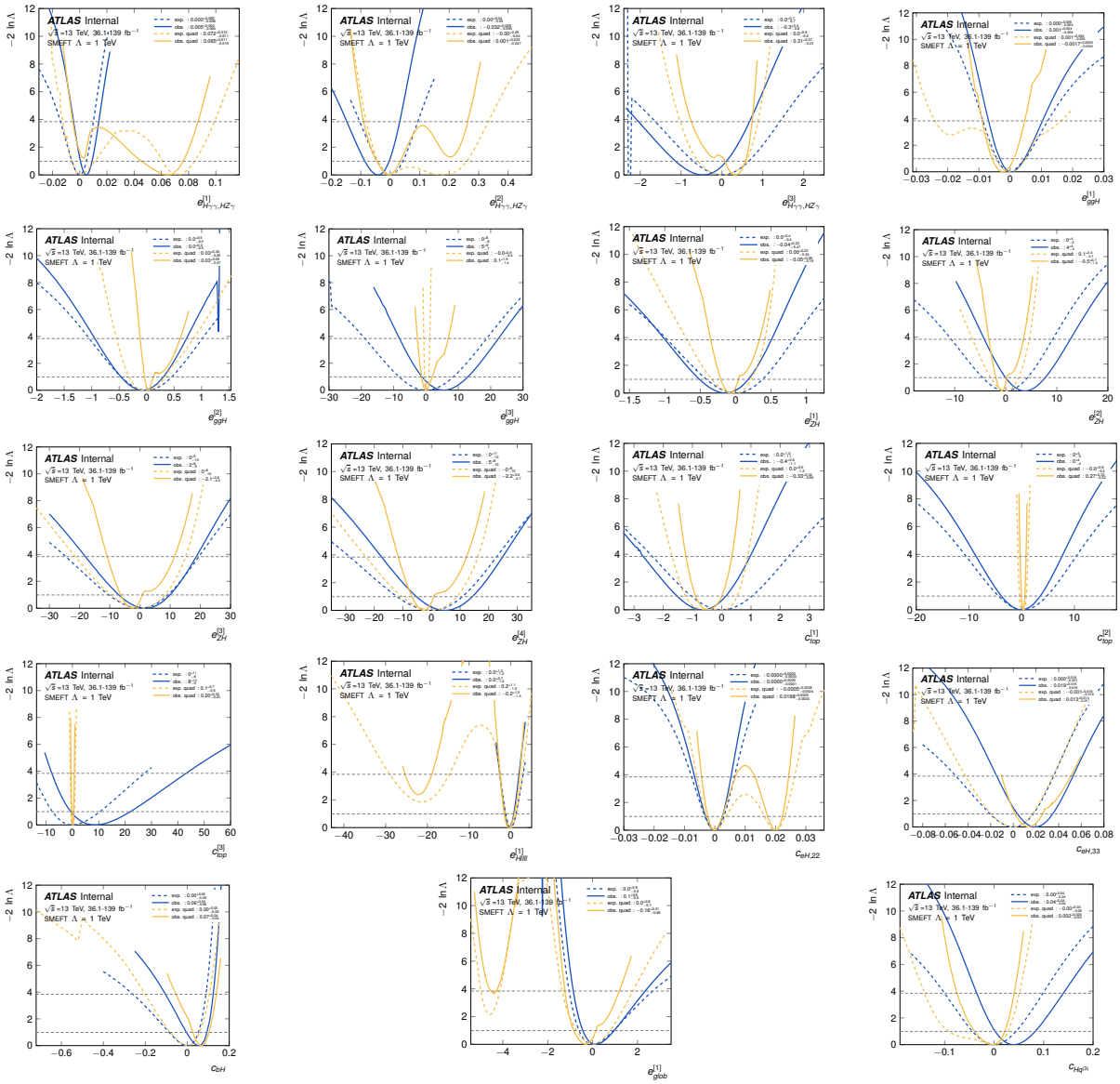

Figure C.8: Expected (dashed) and observed (solid) Nll scans for the linear (blue) and linear + quadratic (yellow) parametrisation for the eigenvectors in the fit basis. Source: [135].

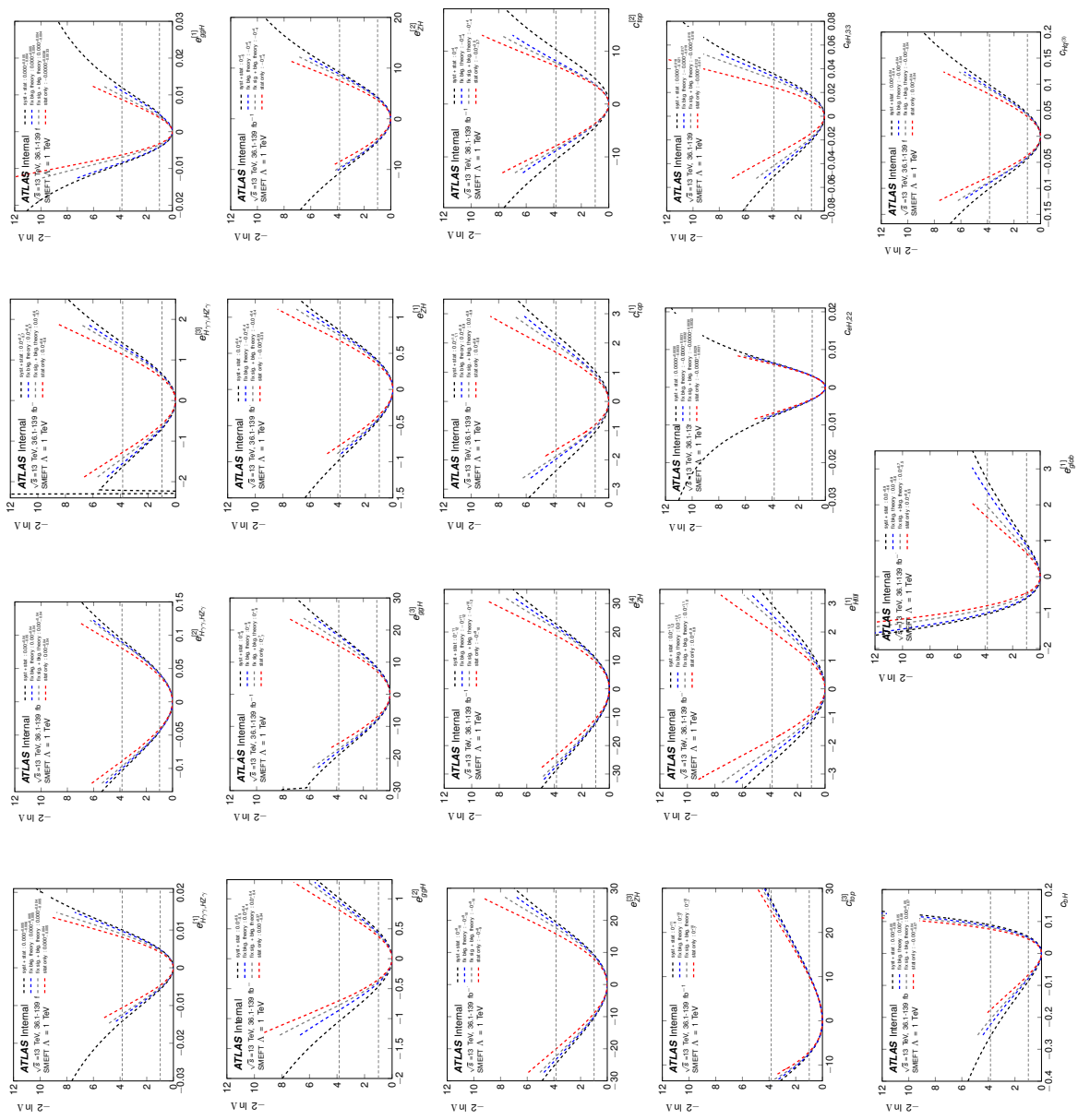

Figure C.9: Expected Nll scans (black) and the ones for the case of fixing given groups of systematics to the best-fit-values (blue for fixed background theoretical ones, grey for fixing signal theoretical ones on top to the previous and red is the stat-only). Source: [135].

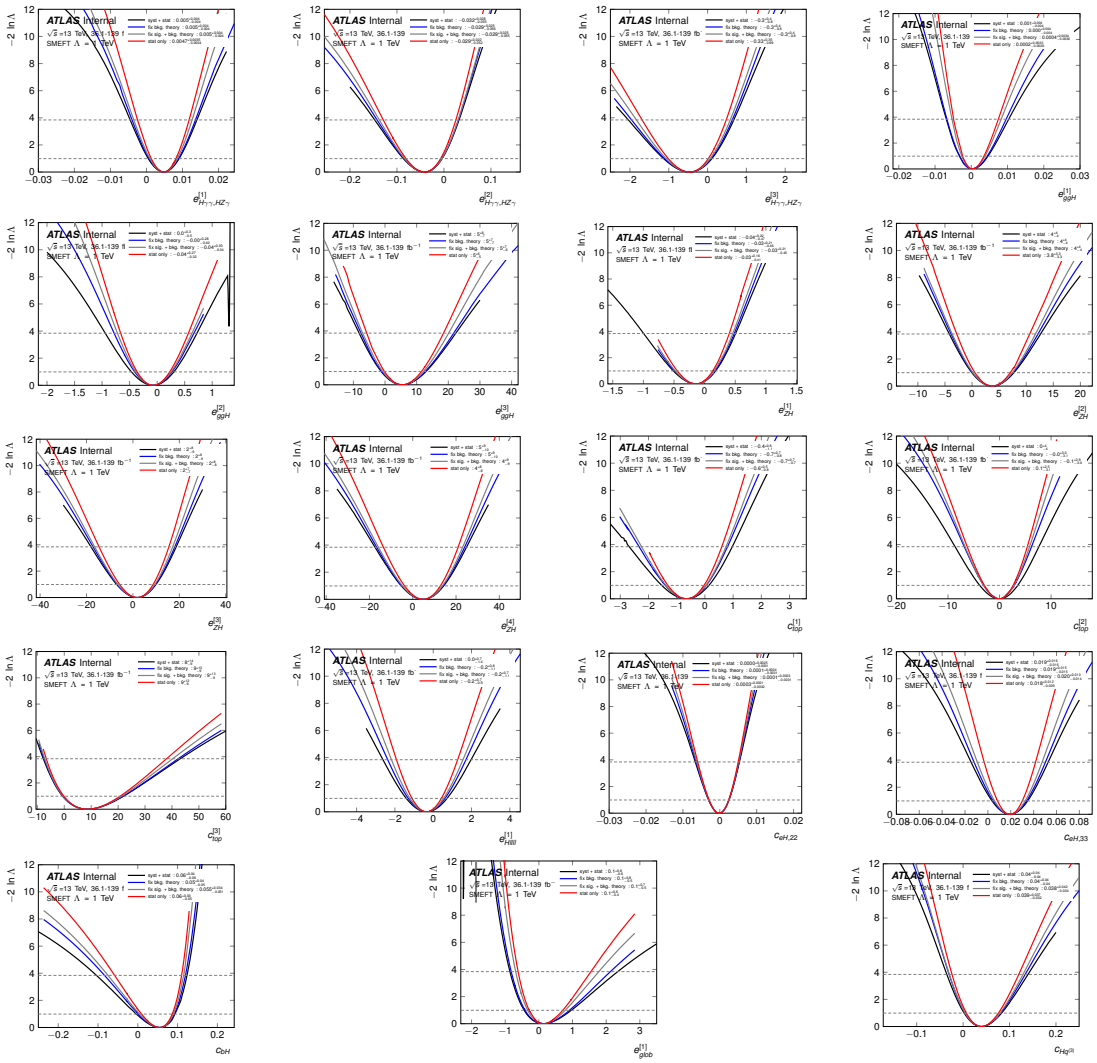

Figure C.10: Observed Nll scans (black) and the ones for the case of fixing given groups of systematics to the best-fit-values (blue for fixed background theoretical ones, grey for fixing signal theoretical ones on top to the previous and red is the stat-only).. Source: [135].

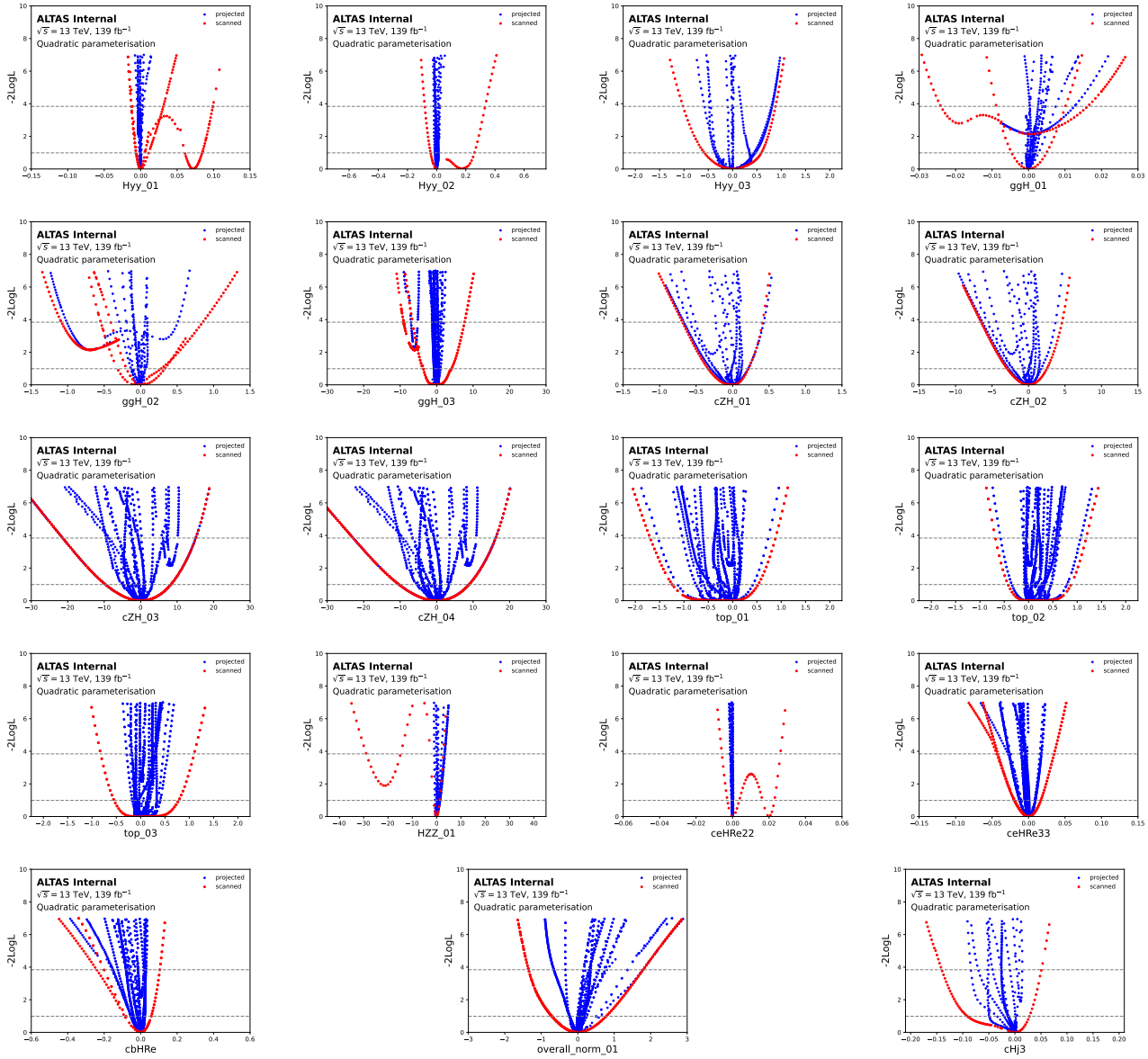

Figure C.11: Nll scans. Source: [135].

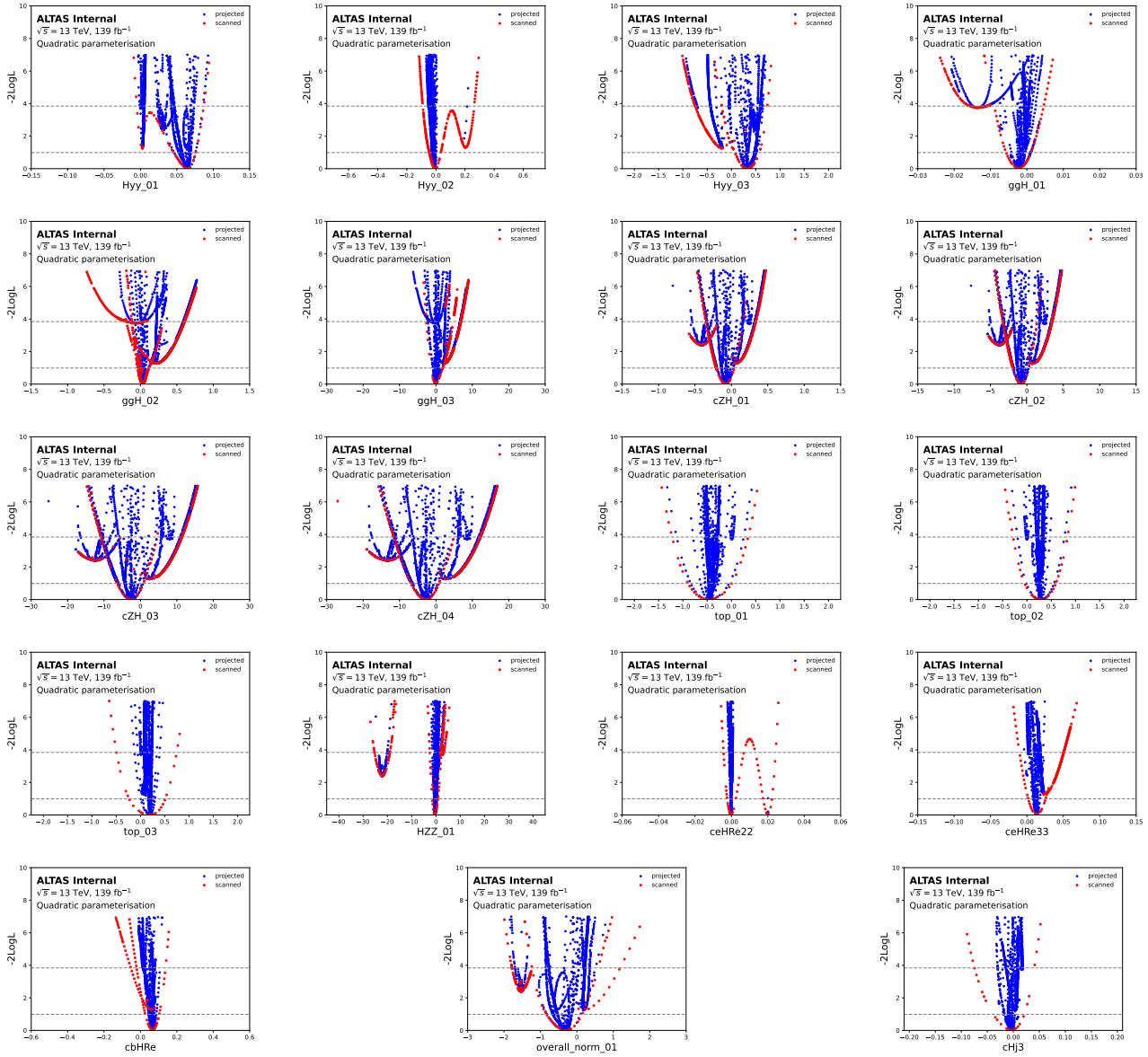

Figure C.12: Nll scans. Source: [135].

C.4 Back-propagated constraints on STXS

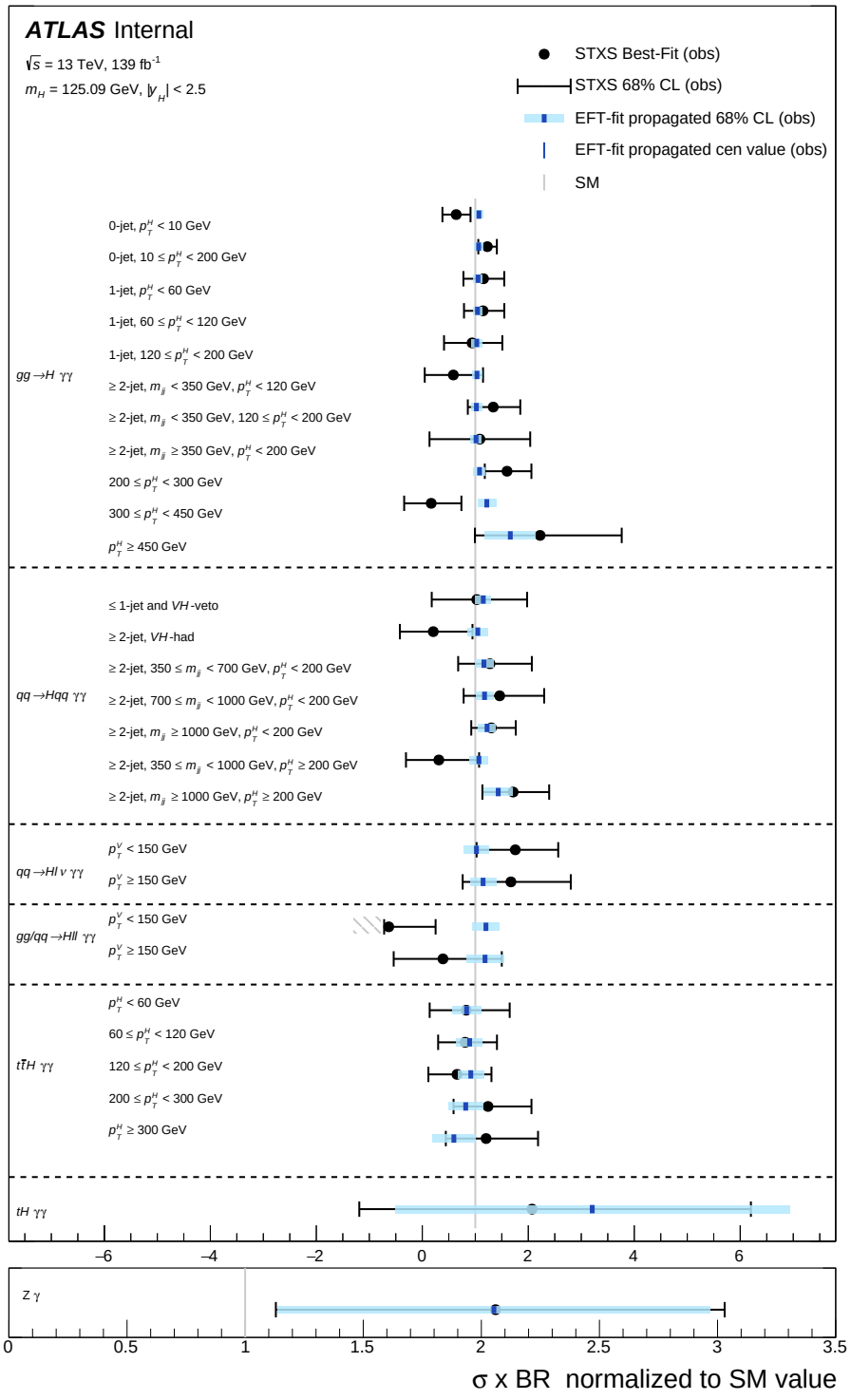

Figure C.13: Comparison between the best-fit-values of the STXS bins (black) and the values for the STXS signal strength back-propagated from the SMEFT fit (blue) for the $\gamma\gamma$ and $Z\gamma$ channels. Source: [135].

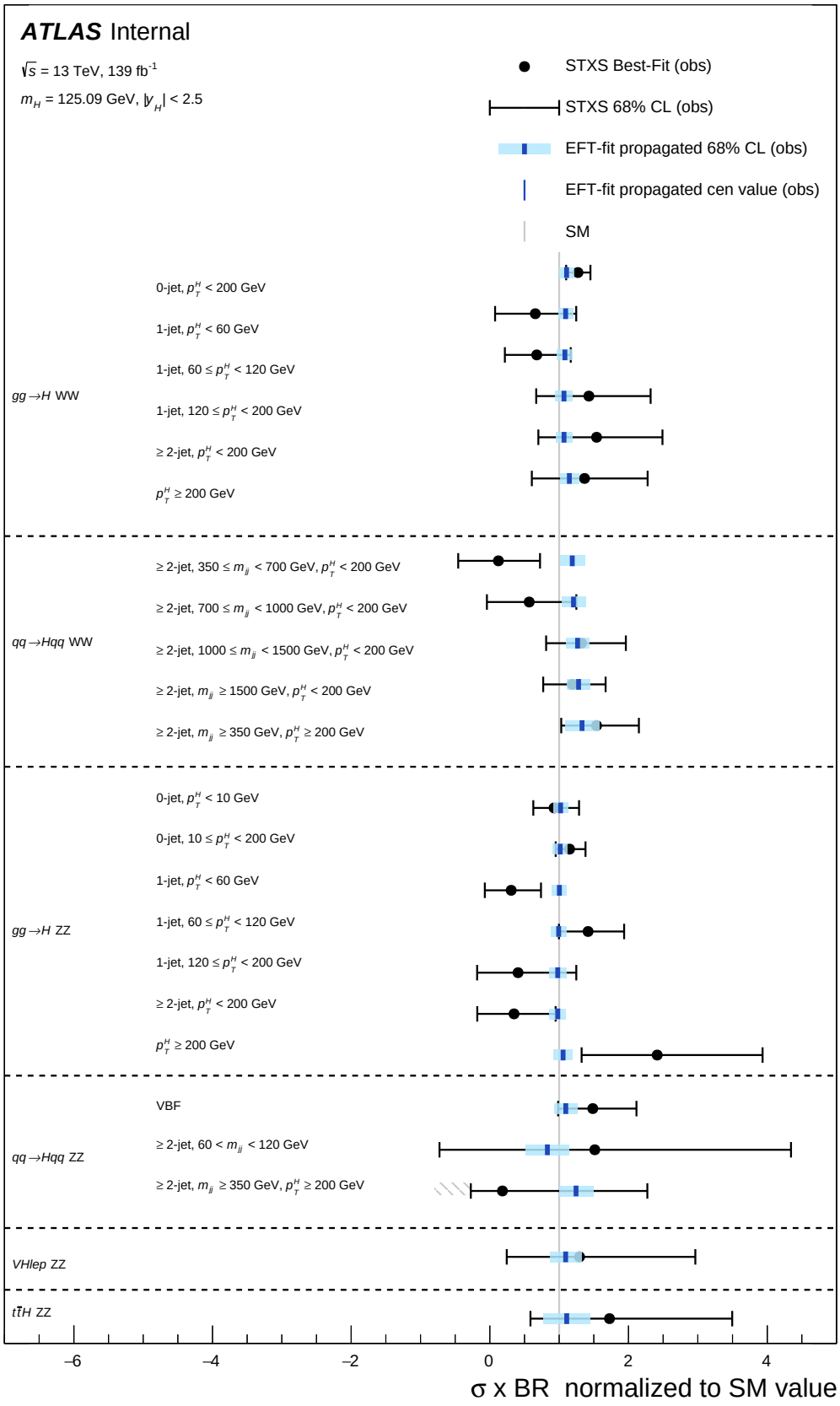

Figure C.14: Comparison between the best-fit-values of the STXS bins (black) and the values for the STXS signal strength back-propagated from the SMEFT fit (blue) for the WW and ZZ channels. Source: [135].

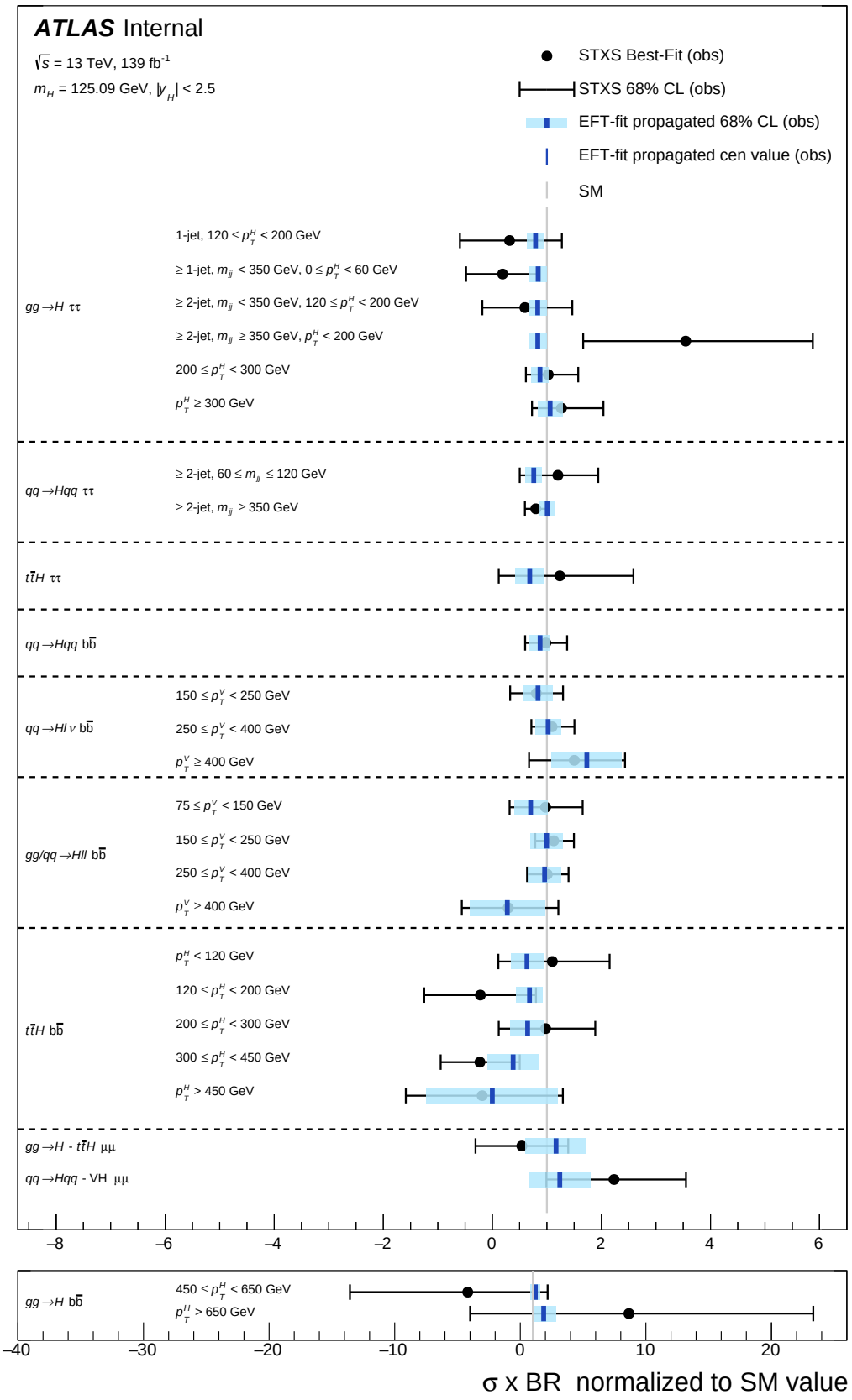

Figure C.15: Comparison between the best-fit-values of the STXS bins (black) and the values for the STXS signal strength back-propagated from the SMEFT fit (blue) for the remaining channels. Source: [135].

C.5 Simplified likelihood

Instead of using the full likelihood, one may consider a simplified version, which is based on a Gaussian approximation, allowing significant simplification of the computational complexity:

$$\mathcal{L}(\vec{\mu}) = \frac{1}{\sqrt{(2\pi)^{n_{\text{dof}}}\det\left(V_\mu\right)}} \exp\left(-\frac{1}{2}\Delta\vec{\mu}V_\mu^{-1}\Delta\vec{\mu}\right) \tag{C.1}$$

with $\vec{\mu}$ being observables (POIs), $\Delta\vec{\mu} = \vec{\mu} - \hat{\vec{\mu}}$, where $\hat{\vec{\mu}}$ is a set of the best-fit-values for the observables and V_μ is their covariance. Comparison of the results with the simplified likelihood and the full one for a linear parametrisation is given on Fig. C.16.

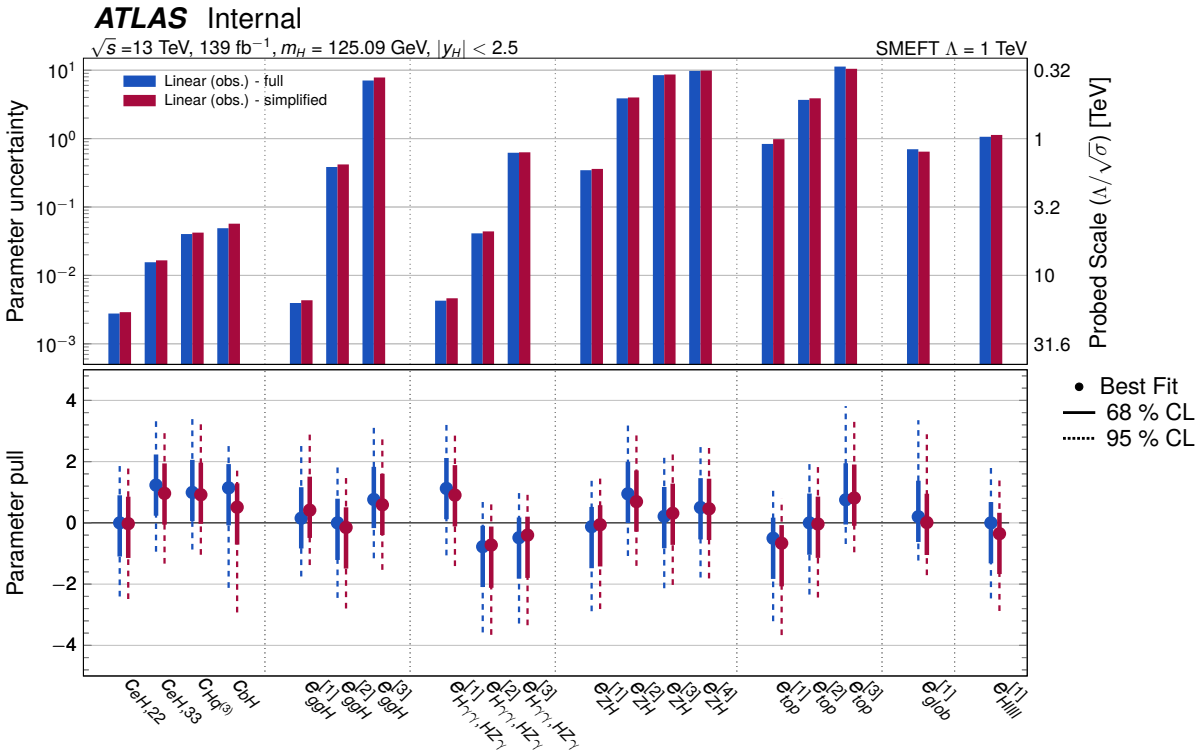

Figure C.16: Comparison of the fit results between the full likelihood (blue) and the simplified one (purple) for the linear parametrisation. Source: [135].

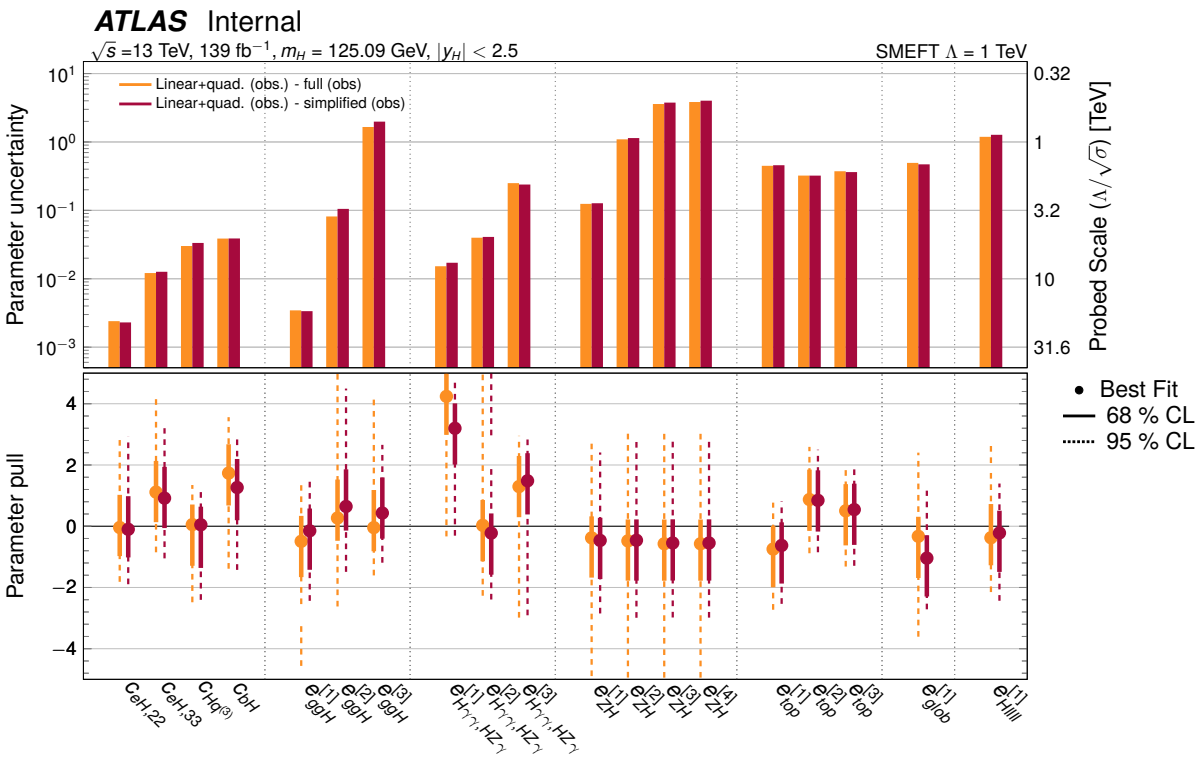

Figure C.17: Comparison of the fit results between the full likelihood (blue) and the simplified one (purple) for the quadratic parametrisation. Source: [135].

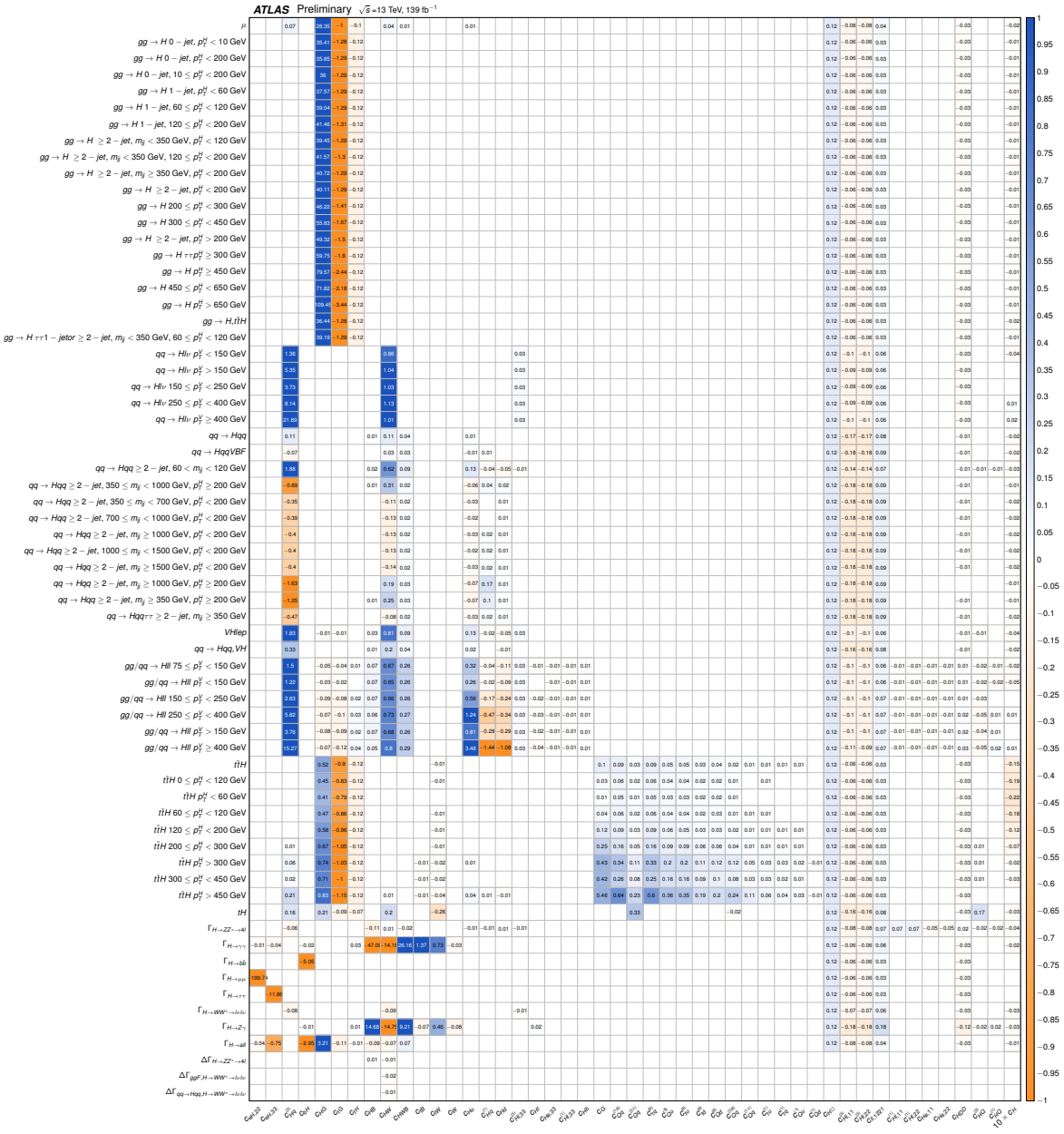

Figure C.18: Liner coefficients $\mathcal{A}^t_{kj}$, $\mathcal{A}^f_{kj}$ and $\mathcal{A}^H_{kj}$ of the SMEFT parametrisation. The estimated correction factors needed to account for the non-negligible experimental acceptance effects in $H \to ZZ^*$ and $H \to WW^*$ decay modes and that affect the impact of certain SMEFT operators are separately provided and labelled as $\Delta\Gamma$. These correction factors should be added to the corresponding Γ term to obtain the parametrisation including acceptance effects. Source: [117].

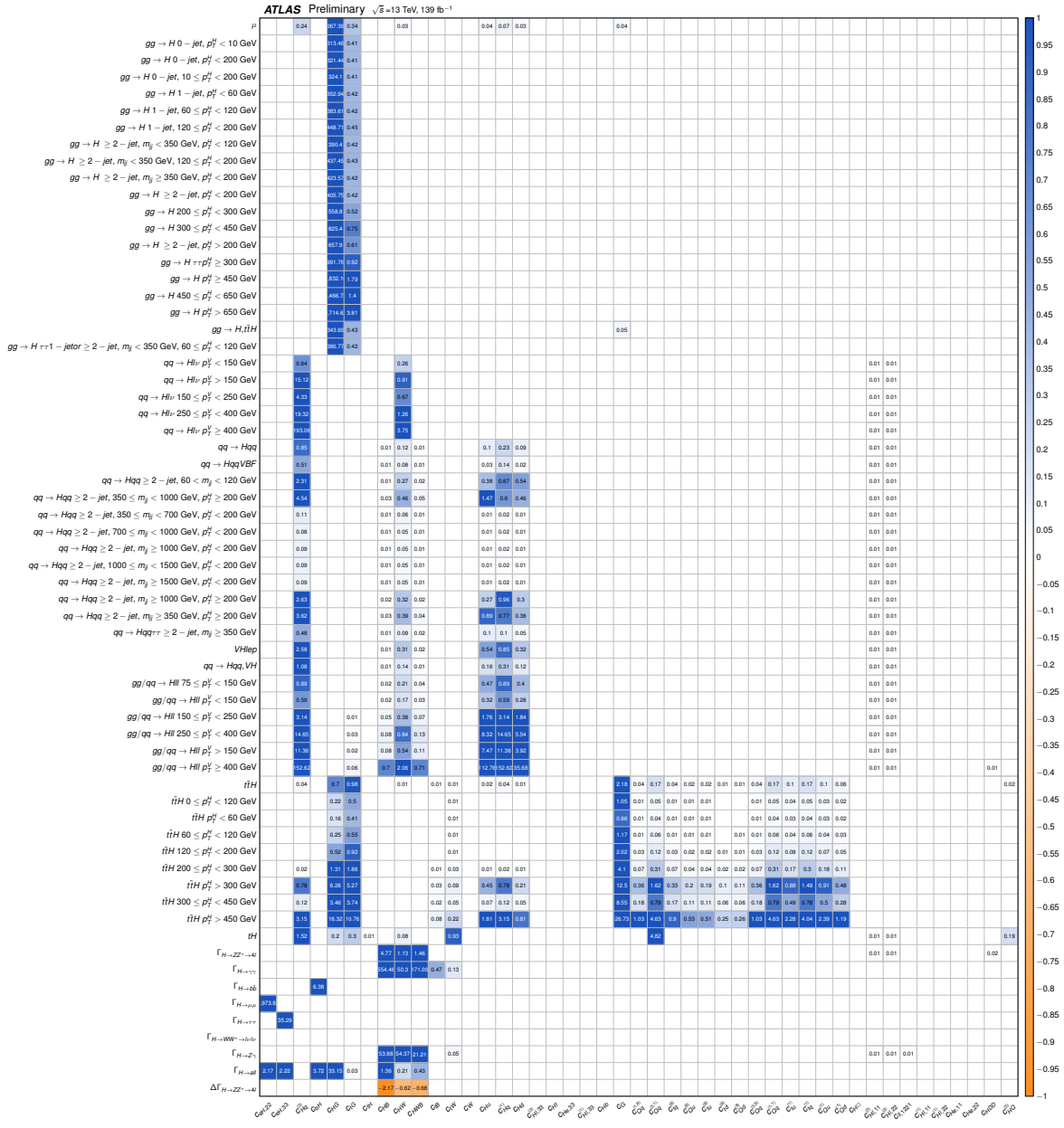

Figure C.19: Diagonal terms of quadratic coefficients $\mathcal{B}^t_{kj}$, $\mathcal{B}^f_{kj}$ and $\mathcal{B}^H_{kj}$ of the SMEFT parametrisation. The estimated correction factors needed to account for the non-negligible experimental acceptance effects in $H \to ZZ^*$ and $H \to WW^*$ decay modes and that affect the impact of certain SMEFT operators are separately provided and labelled as $\Delta\Gamma$. These correction factors should be added to the corresponding Γ term to obtain the parametrisation including acceptance effects. Source: [117].

C.6 Simulation of SMEFT impacts

Two UFO models are used to compute SMEFT predictions: SMEFTsim [129], [150], and SMEFTatNLO [151].
For the $H \to \gamma\gamma$ and $H \to Z\gamma$ decays, analytical calculations including one-loop electroweak SMEFT impacts are used [152], [153].

ggF+bbH	generate p p > h QED=1 [QCD] add process p p > h j QED=1 [QCD] add process p p > h j j QED=1 [QCD] add process p p > h b b~QED=1 [QCD]
VBF+VHhad	generate p p > h j j QCD=0
ZHlep	generate p p > h l+ l- add process p p > h ta+ ta- add process p p > h vl vl~
WHlep	generate p p > h l+ vl add process p p > h l- vl~
ttH	generate p p > h t t~
tHjb	generate p p > h t b~j add process p p > h t~b j
tHW (5FS)	define p = p b b~ generate p p > h t w- add process p p > h t~w+

$H \to 4\ell$	generate h > l+ l- l+ l-
$H \to \ell\nu\ell\nu$	generate h > e+ vl mu- vl~ h > e- vl mu+ vl~
$H \to b\bar{b}$	generate h > b b~
$H \to \mu^+\mu^-$	generate h > mu+ mu-
$H \to \gamma\gamma$	generate h > a a
$H \to c\bar{c}$	generate h > c c
$H \to Z\gamma$	generate h > z a
$H \to \tau^+\tau^-$	generate h > ta+ ta-
Additional channels entering total width	
$H \to \tau^+\nu_\tau\tau^-\bar{\nu}_\tau$	generate h > ta+ vt ta- vt
$H \to \ell\nu_\ell\tau\nu_\tau$	generate h > l+ vl ta- vt add process h > ta+ vt l- vl
$H \to jj\ell(\tau)\nu$	generate h > l+ vl j j add process h > j j l- vl add process h > ta+ vt j j add process h > j j ta- vt
$H \to 4j$	generate h > j j j j
$H \to 4\tau$	generate h > ta+ ta- ta+ ta-
$H \to 4\nu$	generate h > vl vl vl vl add process h > vt vt vt vt add process h > vt vt vl vl
$H \to \ell^+\ell^-\tau^+\tau^-$	generate h > l+ l- ta+ ta-
$H \to 2\nu 2\ell(\tau)$	generate h > vl vl ta+ ta- add process h > vt vt l+ l-
$H \to 2j2\ell(\tau)$	generate h > j j l+ l- add process h > j j ta+ ta-
$H \to 2j2\nu$	generate h > j j vl vl add process h > j j vt vt
$H \to s\bar{s}$	generate h > s s
$H \to e^+e^-$	generate h > e+ e-
$H \to gg$	generate h > g g

Table C.1: Definition of the Higgs boson production modes (L) used for the simulation of events using MadGraph. Definition of the Higgs boson decay modes used for the simulation of events using MadGraph. For the two-body decays into light fermions, the massive scheme is used to obtain a non-zero decay width. Here "p" defines the proton in the 4FS, "j" includes the up-, down-, strange- and charm-quark, "l" is a massless lepton (e or μ) and "vl" is a neutrino of any flavour. "~" denominates the anti-particle. SMEFT modifications can be targetted specifically by using the matrix-element squared order syntax `NP^2==1(2)` and `NP^2==2(4)` for `SMEFTsim(SMEFTatNLO)`. Source: [117]

Bibliography

[1] S. Bilenky, *Basics of Introduction to Feynman Diagrams and Electroweak Interactions Physics*, Basics of, Editions Frontières, 1994. [Cited on page 19.]

[2] M. E. Peskin and D. V. Schroeder, *An Introduction to Quantum Field Theory*, Westview Press, 1995, Reading, USA: Addison-Wesley (1995) 842 p. [Cited on pages 19, 28, and 31.]

[3] M. Maggiore, *A Modern introduction to quantum field theory*, Oxford Master Series in Physics, 2005. [Cited on pages 19 and 25.]

[4] W. Greiner and J. Reinhardt, *Quantum Electrodynamics*, Physics and astronomy online library, Springer, 2003. [Cited on page 19.]

[5] T.-P. Cheng and L.-F. Li, *Gauge Theory of Elementary Particle Physics*, Oxford University Press, Oxford, UK, 1984. [Cited on page 19.]

[6] V. Berestetskii, E.M.Lifshitz and L. Pitaevskii, *Quantum Electrodynamics (Second Edition)*, Butterworth-Heinemann, Oxford, second edition edition, 1982. [Cited on pages 19 and 27.]

[7] L. D. Landau and E. M. Lifshits, *Mechanics*, volume v.1 of *Course of Theoretical Physics*, Butterworth-Heinemann, Oxford, 1976. [Cited on page 19.]

[8] E. Cartan, *Œuvres complètes*, Number v. 1, pt. 2 in Œuvres complètes, Gauthier-Villars, 1952. [Cited on page 21.]

[9] Wikipedia: Standard Model of Particles physics, `https://en.wikipedia.org/wiki/Standard_Model`, Accessed: 2023-04-13. [Cited on page 26.]

[10] F. J. Hasert et al. (Gargamelle Neutrino Collaboration), *Observation of Neutrino Like Interactions Without Muon Or Electron in the Gargamelle Neutrino Experiment*, Phys. Lett. B **46**, 138–140 (1973). [Cited on page 32.]

[11] G. Arnison et al. (UA1 Collaboration), *Experimental Observation of Isolated Large Transverse Energy Electrons with Associated Missing Energy at* $\sqrt{s} = 540$ *GeV*, Phys. Lett. B **122**, 103–116 (1983), `CERN-EP-83-13`. [Cited on page 32.]

[12] M. Banner et al. (UA2 Collaboration), *Observation of Single Isolated Electrons of High Transverse Momentum in Events with Missing Transverse Energy at the CERN anti-p p Collider*, Phys. Lett. B **122**, 476–485 (1983), `CERN-EP-83-25`. [Cited on page 32.]

[13] G. Arnison et al. (UA1 Collaboration), *Experimental Observation of Lepton Pairs of Invariant Mass Around 95-GeV/c**2 at the CERN SPS Collider*, Phys. Lett. B **126**, 398–410 (1983), `CERN-EP-83-73`. [Cited on page 32.]

[14] P. Bagnaia et al. (UA2 Collaboration), *Evidence for* $Z^0 \to e^+e^-$ *at the CERN* $\bar{p}p$ *Collider*, Phys. Lett. B **129**, 130–140 (1983), `CERN-EP-83-112`. [Cited on page 32.]

[15] P. W. Higgs, *Broken symmetries, massless particles and gauge fields*, Phys. Lett. **12**, 132–133 (1964). [Cited on page 33.]

[16] P. W. Higgs, *Broken Symmetries and the Masses of Gauge Bosons*, Phys. Rev. Lett. **13**, 508–509 (1964). [Cited on page 33.]

[17] P. W. Higgs, *Spontaneous Symmetry Breakdown without Massless Bosons*, Phys. Rev. **145**, 1156–1163 (1966). [Cited on page 33.]

[18] F. Englert and R. Brout, *Broken Symmetry and the Mass of Gauge Vector Mesons*, Phys. Rev. Lett. **13**, 321–323 (1964). [Cited on page 33.]

[19] J. Goldstone, *Field theories with "superconductor" solutions*, Nuovo Cimento **19**, 154–164 (1961), CERN-TH-118. [Cited on page 41.]

[20] Y. Nambu, *Quasi-Particles and Gauge Invariance in the Theory of Superconductivity*, Phys. Rev. **117**, 648–663 (Feb 1960). [Cited on page 41.]

[21] N. Cabibbo, *Unitary Symmetry and Leptonic Decays*, Phys. Rev. Lett. **10**, 531–533 (Jun 1963). [Cited on page 41.]

[22] M. Kobayashi and T. Maskawa, *CP-Violation in the Renormalizable Theory of Weak Interaction*, Progress of Theoretical Physics **49**(2), 652–657 (02 1973), https://academic.oup.com/ptp/article-pdf/49/2/652/5257692/49-2-652.pdf. [Cited on pages 41 and 42.]

[23] Z. Maki, M. Nakagawa and S. Sakata, *Remarks on the Unified Model of Elementary Particles*, Progress of Theoretical Physics **28**(5), 870–880 (11 1962), https://academic.oup.com/ptp/article-pdf/28/5/870/5258750/28-5-870.pdf. [Cited on pages 41 and 42.]

[24] R. L. Workman and Others (Particle Data Group Collaboration), *Review of Particle Physics*, PTEP **2022**, 083C01 (2022). [Cited on page 42.]

[25] G. Aad et al. (ATLAS Collaboration), *Determination of the parton distribution functions of the proton from ATLAS measurements of differential W and Z boson production in association with jets*, JHEP **07**, 223 (2021), arXiv:2101.05095 [hep-ex], CERN-EP-2020-237. [Cited on page 43.]

[26] *A detailed map of Higgs boson interactions by the ATLAS experiment ten years after the discovery*, Nature **607**(7917), 52–59 (2022), arXiv:2207.00092 [hep-ex], CERN-EP-2022-057, [Erratum: Nature 612, E24 (2022)]. [Cited on pages 44, 47, 48, and 49.]

[27] *Measurement of the Higgs boson mass with $H \to \gamma\gamma$ decays in 140 fb^{-1} of $\sqrt{s} = 13$ TeV pp collisions with the ATLAS detector*, (2023), ATLAS-CONF-2023-036. [Cited on pages 44 and 45.]

[28] S. Dittmaier et al. (LHC Higgs Cross Section Working Group Collaboration), *Handbook of LHC Higgs Cross Sections: 1. Inclusive Observables*, (1 2011), arXiv:1101.0593 [hep-ph], CERN-2011-002. [Cited on page 44.]

[29] D. de Florian et al. (LHC Higgs Cross Section Working Group Collaboration), *Handbook of LHC Higgs Cross Sections: 4. Deciphering the Nature of the Higgs Sector*, **2/2017** (10 2016), arXiv:1610.07922 [hep-ph], CERN-2017-002-M, CERN-2017-002. [Cited on page 45.]

[30] *Combined measurement of the Higgs boson mass from the $H \to \gamma\gamma$ and $H \to ZZ^* \to 4\ell$ decay channels with the ATLAS detector using $\sqrt{s}$ = 7, 8 and 13 TeV pp collision data*, (2023), ATLAS-CONF-2023-037. [Cited on page 45.]

[31] A. M. Sirunyan et al. (CMS Collaboration), *A measurement of the Higgs boson mass in the diphoton decay channel*, Phys. Lett. B **805**, 135425 (2020), arXiv:2002.06398 [hep-ex], CMS-HIG-19-004, CERN-EP-2020-004. [Cited on page 45.]

[32] G. Aad et al. (ATLAS, CMS Collaboration), *Combined Measurement of the Higgs Boson Mass in pp Collisions at $\sqrt{s} = 7$ and 8 TeV with the ATLAS and CMS Experiments*, Phys. Rev. Lett. **114**, 191803 (2015), arXiv:1503.07589 [hep-ex], ATLAS-HIGG-2014-14, CMS-HIG-14-042, CERN-PH-EP-2015-075. [Cited on page 45.]

[33] Evidence of off-shell Higgs boson production and constraints on the total width of the Higgs boson in the $ZZ \to 4\ell$ and $ZZ \to 2\ell 2\nu$ decay channels with the ATLAS detector, Technical report, CERN, Geneva, 2022, All figures including auxiliary figures are available at https://atlas.web.cern.ch/Atlas/GROUPS/PHYSICS/CONFNOTES/ATLAS-CONF-2022-068. [Cited on page 45.]

[34] G. Aad et al. (ATLAS Collaboration), *Evidence of off-shell Higgs boson production from ZZ leptonic decay channels and constraints on its total width with the ATLAS detector*, (4 2023), arXiv:2304.01532 [hep-ex], CERN-EP-2023-023. [Cited on page 45.]

[35] G. Aad et al. (ATLAS Collaboration), *Measurements of the Higgs boson inclusive and differential fiducial cross sections in the 4ℓ decay channel at $\sqrt{s}$ = 13 TeV*, Eur. Phys. J. C **80**(10), 942 (2020), arXiv:2004.03969 [hep-ex], CERN-EP-2020-035. [Cited on pages 45 and 142.]

[36] A. Tumasyan et al. (CMS Collaboration), *Measurement of the Higgs boson width and evidence of its off-shell contributions to ZZ production*, Nature Phys. **18**(11), 1329–1334 (2022), arXiv:2202.06923 [hep-ex], CMS-HIG-21-013, CERN-EP-2021-272. [Cited on page 45.]

[37] G. Aad et al. (ATLAS Collaboration), *Measurements of WH and ZH production in the $H \to b\bar{b}$ decay channel in pp collisions at 13 TeV with the ATLAS detector*, Eur. Phys. J. C **81**(2), 178 (2021), arXiv:2007.02873 [hep-ex], CERN-EP-2020-087. [Cited on pages 46 and 47.]

[38] A. M. Sirunyan et al. (CMS Collaboration), *Evidence for Higgs boson decay to a pair of muons*, JHEP **01**, 148 (2021), arXiv:2009.04363 [hep-ex], CMS-HIG-19-006, CERN-EP-2020-164. [Cited on page 46.]

[39] G. Aad et al. (ATLAS Collaboration), *Measurement of the properties of Higgs boson production at $\sqrt{s} = 13$ TeV in the $H \to \gamma\gamma$ channel using 139 fb^{-1} of pp collision data with the ATLAS experiment*, JHEP **07**, 088 (2023), arXiv:2207.00348 [hep-ex],

CERN-EP-2022-094. [Cited on pages 46, 97, 98, 99, 100, 101, 110, 112, 113, 114, 116, 117, 118, 124, 128, 129, 130, 131, 133, 134, 135, 137, and 142.]

[40] *Measurement of the Higgs boson mass in the $H \to ZZ^* \to 4\ell$ decay channel using 139 fb^{-1} of $\sqrt{s} = 13$ TeV pp collisions recorded by the ATLAS detector at the LHC*, (7 2022), arXiv:2207.00320 [hep-ex], CERN-EP-2022-135. [Cited on page 46.]

[41] G. Aad et al. (ATLAS Collaboration), *A search for the dimuon decay of the Standard Model Higgs boson with the ATLAS detector*, Phys. Lett. B **812**, 135980 (2021), arXiv:2007.07830 [hep-ex], CERN-EP-2020-117. [Cited on page 47.]

[42] *Measurements of Higgs boson production by gluon−gluon fusion and vector-boson fusion using $H \to WW^* \to e\nu\mu\nu$ decays in pp collisions at $\sqrt{s} = 13$ TeV with the ATLAS detector*, (7 2022), arXiv:2207.00338 [hep-ex], CERN-EP-2022-078. [Cited on pages 47 and 142.]

[43] G. Aad et al. (ATLAS Collaboration), *Evidence for the spin-0 nature of the Higgs boson using ATLAS data*, Phys. Lett. B **726**, 120–144 (2013), arXiv:1307.1432 [hep-ex], CERN-PH-EP-2013-102. [Cited on page 50.]

[44] *Measurement of the CP properties of Higgs boson interactions with τ-leptons with the ATLAS detector*, (12 2022), arXiv:2212.05833 [hep-ex], CERN-EP-2022-244. [Cited on page 50.]

[45] L. R. Evans and P. Bryant, *LHC Machine*, JINST **3**, S08001 (2008), This report is an abridged version of the LHC Design Report (CERN-2004-003). [Cited on page 51.]

[46] B. A. et al., The Tevatron Control System, Technical Report FERMILAB-TM-0763, Fermi National Accelerator Laboratory, 1979. [Cited on page 53.]

[47] ATLAS Collaboration, *Luminosity determination in pp collisions at $\sqrt{s} = 13$ TeV using the ATLAS detector at the LHC*, (6 2019), ATLAS-CONF-2019-021. [Cited on pages 53, 66, and 100.]

[48] P. Zyla et al. (Particle Data Group Collaboration), *Review of Particle Physics*, PTEP **2020**(8), 083C01 (2020). [Cited on pages 54 and 108.]

[49] J. Pequenao and P. Schaffner, How ATLAS detects particles: diagram of particle paths in the detector, 2013. [Cited on page 54.]

[50] G. Aad et al. (ATLAS Collaboration), *The ATLAS Experiment at the CERN Large Hadron Collider*, JINST **3**, S08003 (2008). [Cited on page 54.]

[51] M. Aaboud et al. (ATLAS Collaboration), *Evidence for the associated production of the Higgs boson and a top quark pair with the ATLAS detector*, Phys. Rev. D **97**(7), 072003 (2018), arXiv:1712.08891 [hep-ex], CERN-EP-2017-281. [Cited on page 55.]

[52] G. Aad et al. (ATLAS Collaboration), *The ATLAS Experiment at the CERN Large Hadron Collider*, JINST **3**, S08003 (2008). [Cited on pages 56 and 62.]

[53] ATLAS Collaboration, *ATLAS Insertable B-Layer Technical Design Report*, (9 2010), CERN-LHCC-2010-013, ATLAS-TDR-19. [Cited on page 56.]

[54] G. Aad et al. (ATLAS Collaboration), *Alignment of the ATLAS Inner Detector in Run-2*, Eur. Phys. J. C **80**(12), 1194 (2020), arXiv:2007.07624 [hep-ex], CERN-EP-2020-108. [Cited on page 56.]

[55] *ATLAS calorimeter performance: Technical Design Report*, Technical design report. ATLAS, CERN, Geneva, 1996. [Cited on pages 57, 58, and 59.]

[56] CERN, *Large Hadron Collider Workshop: Aachen, Germany 4 - 9 Oct 1990. Large Hadron Collider Workshop*, Geneva, 1990, CERN. [Cited on page 58.]

[57] G. Aad et al. (ATLAS Collaboration), *Search for displaced photons produced in exotic decays of the Higgs boson using 13 TeV pp collisions with the ATLAS detector*, Phys. Rev. D **108**(3), 032016 (2023), arXiv:2209.01029 [hep-ex], CERN-EP-2022-096. [Cited on page 59.]

[58] J. Colas et al. (ATLAS Liquid Argon Calorimeter Collaboration), *Position resolution and particle identification with the ATLAS EM calorimeter*, Nucl. Instrum. Meth. A **550**, 96–115 (2005), arXiv:physics/0505127. [Cited on page 59.]

[59] G. Aad et al. (ATLAS Collaboration), *Commissioning of the ATLAS Muon Spectrometer with Cosmic Rays*, Eur. Phys. J. C **70**, 875–916 (2010), arXiv:1006.4384 [physics.ins-det]. [Cited on page 60.]

[60] G. Aad et al. (ATLAS Collaboration), *Operation of the ATLAS trigger system in Run 2*, JINST **15**(10), P10004 (2020), arXiv:2007.12539 [physics.ins-det], CERN-EP-2020-109. [Cited on page 61.]

[61] M. Aaboud et al. (ATLAS Collaboration), *Measurement of the Higgs boson mass in the $H \to ZZ^* \to 4\ell$ and $H \to \gamma\gamma$ channels with $\sqrt{s} = 13$ TeV pp collisions using the ATLAS detector*, Phys. Lett. B **784**, 345–366 (2018), arXiv:1806.00242 [hep-ex], CERN-EP-2018-085. [Cited on page 63.]

[62] L. e. a. Aperio Bella, Electron and photon energy calibration with the ATLAS detector using LHC Run 2 data, Technical report, CERN, Geneva, 2022. [Cited on page 64.]

[63] G. Aad et al. (ATLAS Collaboration), *Electron and photon energy calibration with the ATLAS detector using LHC Run 1 data*, Eur. Phys. J. **C74**(10), 3071 (2014), arXiv:1407.5063 [hep-ex], CERN-PH-EP-2014-153. [Cited on page 64.]

[64] M. Aaboud et al. (ATLAS Collaboration), *Electron and photon energy calibration with the ATLAS detector using 2015–2016 LHC proton-proton collision data*, JINST **14**(03), P03017 (2019), arXiv:1812.03848 [hep-ex], CERN-EP-2018-296. [Cited on page 64.]

[65] G. Aad et al. (ATLAS Collaboration), *Topological cell clustering in the ATLAS calorimeters and its performance in LHC Run 1*, Eur. Phys. J. C **77**, 490 (2017), arXiv:1603.02934 [hep-ex], CERN-PH-EP-2015-304. [Cited on page 64.]

[66] G. Aad et al. (ATLAS Collaboration), *Electron and photon performance measurements with the ATLAS detector using the 2015–2017 LHC proton-proton collision data*, JINST **14**(12), P12006 (2019), arXiv:1908.00005 [hep-ex], CERN-EP-2019-145. [Cited on page 64.]

[67] S. Schael et al. (ALEPH, DELPHI, L3, OPAL, SLD, LEP Electroweak Working Group, SLD Electroweak Group, SLD Heavy Flavour Group Collaboration), *Precision electroweak measurements on the Z resonance*, Phys. Rept. **427**, 257–454 (2006), arXiv:hep-ex/0509008, SLAC-R-774. [Cited on page 64.]

[68] C. Goudet, *Etalonnage du calorimètre électromagnétique de l'expérience ATLAS et application à la mesure des couplages du boson de (Brout-Englert-)Higgs dans le canal diphoton dans le cadre du Run 2 du LHC.*, PhD thesis, Saclay, 2017. [Cited on page 65.]

[69] H. Atmani, *Calibration of the ATLAS Electromagnetic Calorimeter and Measurement of W Boson Properties at $\sqrt{s}$ = 5 and 13 TeV with the ATLAS Detector at the LHC.*, PhD thesis, Université Paris-Saclay, U. Paris-Saclay, 2020. [Cited on page 65.]

[70] L. Guo, *Improvement on the $H \to \gamma\gamma$ mass measurement by constraining the photon energy scale uncertainty and search for Higgs boson pair production in the $b\bar{b}\gamma\gamma$ final state with the ATLAS experiment using the full Run 2 at $\sqrt{s}$=13 TeV pp collision of LHC*, PhD thesis, IJCLab, Orsay, 2022. [Cited on page 65.]

[71] L. Guo, *Electron energy in-situ calibration and linearity measurements from $Z \to ee$ events.*, (2020), ATL-COM-PHYS-2020-757. [Cited on pages 65, 66, 73, 74, 80, 81, 84, 94, and 95.]

[72] G. Aad et al. (ATLAS Collaboration), *Measurement of $W^{\pm}$ and Z-boson production cross sections in pp collisions at $\sqrt{s} = 13$ TeV with the ATLAS detector*, Phys. Lett. B **759**, 601–621 (2016), arXiv:1603.09222 [hep-ex], CERN-EP-2016-069. [Cited on page 67.]

[73] G. Aad et al. (ATLAS Collaboration), *Electron and photon performance measurements with the ATLAS detector using the 2015–2017 LHC proton-proton collision data*, JINST **14**(12), P12006 (2019), arXiv:1908.00005 [hep-ex], CERN-EP-2019-145. [Cited on pages 67 and 105.]

[74] G. Aad et al. (ATLAS Collaboration), *Electron reconstruction and identification in the ATLAS experiment using the 2015 and 2016 LHC proton-proton collision data at $\sqrt{s}$ = 13 TeV*, Eur. Phys. J. C **79**(8), 639 (2019), arXiv:1902.04655 [physics.ins-det], CERN-EP-2018-273. [Cited on pages 67, 68, 105, and 106.]

[75] Anastopoulos et al., *Electron identification and efficiency measurements in 2017 data*, (Jan 2019), ATL-COM-PHYS-2018-1727. [Cited on pages 67 and 105.]

[76] O. Lukianchuk, *In-situ calibration of the liquid argon electromagnetic calorimeter with E/p method using 2018 LHC proton-proton collision data*, (Oct 2021), ATL-COM-PHYS-2021-897, Qualification task report. [Cited on pages 68, 69, 70, 71, 72, 74, 75, 77, 78, 81, 82, 84, 85, 86, 87, 88, 89, 90, 91, 92, 94, and 95.]

[77] G. Aad et al. (ATLAS Collaboration), *Alignment of the ATLAS Inner Detector in Run-2*, Eur. Phys. J. C **80**(12), 1194 (2020), arXiv:2007.07624 [hep-ex], CERN-EP-2020-108. [Cited on pages 79, 80, 91, and 92.]

[78] *Studies of the muon momentum calibration and performance of the ATLAS detector with pp collisions at $\sqrt{s}$=13 TeV*, (12 2022), arXiv:2212.07338 [hep-ex], CERN-EP-2022-274. [Cited on page 79.]

[79] G. Artoni, private communication. [Cited on pages 81 and 82.]

[80] G. Aad et al. (ATLAS Collaboration), *Muon reconstruction performance of the ATLAS detector in proton–proton collision data at $\sqrt{s}$ =13 TeV*, Eur. Phys. J. C **76**(5), 292 (2016), arXiv:1603.05598 [hep-ex], CERN-EP-2016-033. [Cited on pages 82 and 91.]

[81] M. Aaboud et al. (ATLAS Collaboration), *Measurements of Higgs boson properties in the decay channel with $36\ \mathrm{fb}^{-1}$ of pp collision data at $\sqrt{s} = 13\ \mathrm{TeV}$ with the ATLAS detector*, Phys. Rev. D **98**, 052005 (Sep 2018). [Cited on page 97.]

[82] ATLAS Collaboration, *Measurements of Higgs boson properties in the diphoton decay channel using 80 fb^{-1} of pp collision data at $\sqrt{s}$ = 13 TeV with the ATLAS detector*, (7 2018), ATLAS-CONF-2018-028. [Cited on page 97.]

[83] G. Aad et al. (ATLAS, CMS Collaboration), *Measurements of the Higgs boson production and decay rates and constraints on its couplings from a combined ATLAS and CMS analysis of the LHC pp collision data at $\sqrt{s} = 7$ and 8 TeV*, JHEP **08**, 045 (2016), arXiv:1606.02266 [hep-ex], CERN-EP-2016-100, ATLAS-HIGG-2015-07, CMS-HIG-15-002. [Cited on page 97.]

[84] G. Aad et al. (ATLAS, CMS Collaboration), *Combined Measurement of the Higgs Boson Mass in pp Collisions at $\sqrt{s} = 7$ and 8 TeV with the ATLAS and CMS Experiments*, Phys. Rev. Lett. **114**, 191803 (2015), arXiv:1503.07589 [hep-ex], ATLAS-HIGG-2014-14, CMS-HIG-14-042, CERN-PH-EP-2015-075. [Cited on page 98.]

[85] G. Aad et al., *ATLAS data quality operations and performance for 2015–2018 data-taking*, Journal of Instrumentation **15**(04), P04003–P04003 (Apr 2020). [Cited on page 100.]

[86] G. Avoni et al. (ATLAS Collaboration), *The new LUCID-2 detector for luminosity measurement and monitoring in ATLAS*, JINST **13**(07), P07017 (2018). [Cited on page 100.]

[87] J. R. Andersen et al. (LHC Higgs Cross Section Working Group Collaboration), *Handbook of LHC Higgs Cross Sections: 3. Higgs Properties*, (7 2013), arXiv:1307.1347 [hep-ph], CERN-2013-004. [Cited on page 100.]

[88] S. Alioli, P. Nason, C. Oleari and E. Re, *A general framework for implementing NLO calculations in shower Monte Carlo programs: the POWHEG BOX*, JHEP **06**, 043 (2010), arXiv:1002.2581 [hep-ph], DESY-10-018, SFB-CPP-10-22, IPPP-10-11, DCPT-10-22. [Cited on page 100.]

[89] H. B. Hartanto, B. Jager, L. Reina and D. Wackeroth, *Higgs boson production in association with top quarks in the POWHEG BOX*, Phys. Rev. D **91**(9), 094003 (2015), arXiv:1501.04498 [hep-ph]. [Cited on page 100.]

[90] S. Frixione, P. Nason and C. Oleari, *Matching NLO QCD computations with Parton Shower simulations: the POWHEG method*, JHEP **11**, 070 (2007), arXiv:0709.2092 [hep-ph], BICOCCA-FT-07-9, GEF-TH-21-2007. [Cited on page 100.]

[91] P. Nason, *A New method for combining NLO QCD with shower Monte Carlo algorithms*, JHEP **11**, 040 (2004), arXiv:hep-ph/0409146, BICOCCA-FT-04-11. [Cited on page 100.]

[92] J. Alwall et al., *The automated computation of tree-level and next-to-leading order differential cross sections, and their matching to parton shower simulations*, JHEP **07**, 079 (2014), arXiv:1405.0301 [hep-ph], CERN-PH-TH-2014-064, CP3-14-18, LPN14-066, MCNET-14-09, ZU-TH-14-14. [Cited on page 100.]

[93] T. Sjostrand, S. Mrenna and P. Z. Skands, *A Brief Introduction to PYTHIA 8.1*, Comput. Phys. Commun. **178**, 852–867 (2008), arXiv:0710.3820 [hep-ph], CERN-LCGAPP-2007-04, LU-TP-07-28, FERMILAB-PUB-07-512-CD-T. [Cited on page 100.]

[94] Sjöstrand et al., *An introduction to PYTHIA 8.2*, Comput. Phys. Commun. **191**, 159–177 (2015), arXiv:1410.3012 [hep-ph], LU-TP-14-36, MCNET-14-22, CERN-PH-TH-2014-190, FERMILAB-PUB-14-316-CD, DESY-14-178, SLAC-PUB-16122. [Cited on page 100.]

[95] D. J. Lange, *The EvtGen particle decay simulation package*, Nuclear Instruments and Methods in Physics Research Section A: Accelerators, Spectrometers, Detectors and Associated Equipment **462**(1), 152–155 (2001), BEAUTY2000, Proceedings of the 7th Int. Conf. on B-Physics at Hadron Machines. [Cited on page 100.]

[96] J. Rojo, *PDF4LHC recommendations for Run II*, PoS **DIS2016**, 018 (2016), arXiv:1606.08243 [hep-ph]. [Cited on page 100.]

[97] E. Bothmann et al. (Sherpa Collaboration), *Event Generation with Sherpa 2.2*, SciPost Phys. **7**(3), 034 (2019), arXiv:1905.09127 [hep-ph], FERMILAB-PUB-19-218-T, SLAC-PUB-17433, IPPP/19/42, MCNET-19-11. [Cited on page 100.]

[98] R. D. Ball et al., *Parton distributions with LHC data*, Nucl. Phys. B **867**, 244–289 (2013), arXiv:1207.1303 [hep-ph], EDINBURGH-2012-08, IFUM-FT-997, FR-PHENO-2012-014, RWTH-TTK-12-25, CERN-PH-TH-2012-037, SFB-CPP-12-47. [Cited on page 100.]

[99] N. Berger et al. (ATLAS Collaboration), *Measurements of Higgs boson coupling properties in the diphoton decay channel using full Run 2 pp collision data at $\sqrt{s}$ = 13 TeV with the ATLAS detector*, (Apr 2021), ATL-COM-PHYS-2021-180. [Cited on pages 102, 120, 122, 125, 127, and 136.]

[100] ATLAS Collaboration, *Electron and photon reconstruction and performance in ATLAS using a dynamical, topological cell clustering-based approach*, (12 2017), ATL-PHYS-PUB-2017-022. [Cited on page 103.]

[101] N. e. a. Proklova, Measurements of Photon efficiencies in pp collision data collected in 2015, 2016 and 2017 at $\sqrt{s} = 13$ TeV with the ATLAS detector, Technical report, CERN, Geneva, 2018. [Cited on pages 103 and 104.]

[102] G. Aad et al. (ATLAS Collaboration), *Muon reconstruction performance of the ATLAS detector in proton–proton collision data at $\sqrt{s}$ =13 TeV*, Eur. Phys. J. C **76**(5), 292 (2016), arXiv:1603.05598 [hep-ex], CERN-EP-2016-033. [Cited on page 106.]

[103] M. Cacciari, G. P. Salam and G. Soyez, *The anti-ktjet clustering algorithm*, Journal of High Energy Physics **2008**(04), 063–063 (Apr 2008). [Cited on page 107.]

[104] ATLAS Collaboration, Optimisation and performance studies of the ATLAS b-tagging algorithms for the 18 LHC run, Technical report, CERN, Geneva, Jul 2017, All figures including auxiliary figures are available at https://atlas.web.cern.ch/Atlas/GROUPS/PHYSICS/PUBNOTES/ATL-PHYS-PUB-2017-013. [Cited on page 107.]

[105] *Measurement of the tau lepton reconstruction and identification performance in the ATLAS experiment using pp collisions at $\sqrt{s} = 13\,TeV$*, (5 2017), ATLAS-CONF-2017-029. [Cited on page 107.]

[106] ATLAS Collaboration, *Expected performance of missing transverse momentum reconstruction for the ATLAS detector at $\sqrt{s} = 13$ TeV*, (7 2015), ATL-PHYS-PUB-2015-023. [Cited on page 108.]

[107] *Object-based missing transverse momentum significance in the ATLAS detector*, (7 2018), ATLAS-CONF-2018-038. [Cited on page 108.]

[108] L. e. a. Carminati, Measurement of the isolated di-photon cross section in 4.9 fb-1 of pp collisions at sqrt(s) = 7 TeV with the ATLAS detector, Technical report, CERN, Geneva, 2012. [Cited on pages 109 and 120.]

[109] D. P. Mungo, Measurement of the SM Higgs boson properties in the diphoton decay channel with the ATLAS Run 2 dataset, 2022, Presented 11 Mar 2022. [Cited on page 111.]

[110] G. Aad et al. (ATLAS Collaboration), *Search for Scalar Diphoton Resonances in the Mass Range $65 - 600$ GeV with the ATLAS Detector in pp Collision Data at $\sqrt{s} = 8\,TeV$*, Phys. Rev. Lett. **113**(17), 171801 (2014), arXiv:1407.6583 [hep-ex], CERN-PH-EP-2014-142. [Cited on page 115.]

[111] M. Escalier, *Recherche et découverte du boson de Higgs avec son mode de désintégration en paire de photons avec l'expérience ATLAS au LHC : une introduction*, Habilitation à diriger des recherches, Université Paris Sud 11, March 2015. [Cited on page 119.]

[112] M. Ebden, Gaussian Processes: A Quick Introduction, 2015. [Cited on page 122.]

[113] D. de Florian et al. (LHC Higgs Cross Section Working Group Collaboration), *Handbook of LHC Higgs Cross Sections: 4. Deciphering the Nature of the Higgs Sector*, (2016), arXiv:1610.07922 [hep-ph], FERMILAB-FN-1025-T. [Cited on pages 130, 135, and 136.]

[114] I. Brivio and M. Trott, *The Standard Model as an Effective Field Theory*, Phys. Rept. **793**, 1–98 (2019), arXiv:1706.08945 [hep-ph]. [Cited on page 139.]

[115] B. Grzadkowski, M. Iskrzynski, M. Misiak and J. Rosiek, *Dimension-Six Terms in the Standard Model Lagrangian*, JHEP **10**, 085 (2010), arXiv:1008.4884 [hep-ph], IFT-9-2010, TTP10-35. [Cited on page 139.]

[116] D. Barducci et al., *Interpreting top-quark LHC measurements in the standard-model effective field theory*, (2 2018), arXiv:1802.07237 [hep-ph], CERN-LPCC-2018-01. [Cited on page 140.]

[117] ATLAS Collaboration, *Interpretations of the ATLAS measurements of Higgs boson production and decay rates and differential cross-sections in pp collisions at $\sqrt{s} = 13$ TeV*, (2023), ATLAS-CONF-2023-052. [Cited on pages 141, 142, 146, 147, 152, 154, 156, 157, 159, 161, 162, 163, 169, 173, 174, 176, 177, 207, 208, 209, 224, 225, and 226.]

[118] G. Aad et al. (ATLAS Collaboration), *Measurements of the Higgs boson inclusive and differential fiducial cross-sections in the diphoton decay channel with pp collisions at $\sqrt{s}$ = 13 TeV with the ATLAS detector*, JHEP **08**, 027 (2022), arXiv:2202.00487 [hep-ex], CERN-EP-2021-227. [Cited on page 142.]

[119] ATLAS Collaboration, *Higgs boson production cross-section measurements and their EFT interpretation in the 4ℓ decay channel at $\sqrt{s} = 13$ TeV with the ATLAS detector*, Eur. Phys. J. C **80**, 957 (2020), arXiv:2004.03447 [hep-ex], CERN-EP-2020-034. [Cited on page 142.]

[120] ATLAS Collaboration, *Evidence for the associated production of the Higgs boson and a top quark pair with the ATLAS detector*, Phys. Rev. D **97**, 072003 (2018), arXiv:1712.08891 [hep-ex], CERN-EP-2017-281. [Cited on page 142.]

[121] G. Aad et al. (ATLAS Collaboration), *Measurements of Higgs boson production cross-sections in the $H \to \tau^+\tau^-$ decay channel in pp collisions at $\sqrt{s}$ = 13 TeV with the ATLAS detector*, JHEP **08**, 175 (2022), arXiv:2201.08269 [hep-ex], CERN-EP-2021-217. [Cited on page 142.]

[122] G. Aad, B. Abbott, D. Abbott, O. Abdinov, A. Abed Abud, K. Abeling, D. Abhayasinghe, S. Abidi, O. AbouZeid, N. Abraham and et al., *Measurement of the production cross section for a Higgs boson in association with a vector boson in the $H \to WW^* \to l\nu l\nu$ channel in pp collisions at $\sqrt{s} = 13$ TeV with the ATLAS detector*, Physics Letters B **798**, 134949 (Nov 2019). [Cited on page 142.]

[123] ATLAS Collaboration, *Combination of measurements of Higgs boson production in association with a W or Z boson in the $b\bar{b}$ decay channel with the ATLAS experiment at $\sqrt{s} = 13$ TeV*, (2021), ATLAS-CONF-2021-051. [Cited on page 142.]

[124] G. Aad et al. (ATLAS Collaboration), *Measurements of Higgs bosons decaying to bottom quarks from vector boson fusion production with the ATLAS experiment at $\sqrt{s} = 13$ TeV*, Eur. Phys. J. C **81**(6), 537 (2021), arXiv:2011.08280 [hep-ex], CERN-EP-2020-195. [Cited on page 142.]

[125] ATLAS Collaboration, Measurement of Higgs boson decay into b-quarks in associated production with a top-quark pair in pp collisions at $\sqrt{s} = 13$ TeV with the ATLAS detector, 2021. [Cited on page 142.]

[126] ATLAS Collaboration, Constraints on Higgs boson production with large transverse momentum using $H \to b\bar{b}$ decays in the ATLAS detector, 2021. [Cited on page 142.]

[127] G. Aad et al. (ATLAS Collaboration), *A search for the $Z\gamma$ decay mode of the Higgs boson in pp collisions at $\sqrt{s}$ = 13 TeV with the ATLAS detector*, Phys. Lett. B **809**, 135754 (2020), arXiv:2005.05382 [hep-ex], CERN-EP-2020-052. [Cited on page 142.]

[128] ATLAS Collaboration, *A search for the dimuon decay of the Standard Model Higgs boson with the ATLAS detector*, Phys. Lett. B **812**, 135980 (2021), arXiv:2007.07830 [hep-ex], CERN-EP-2020-117. [Cited on page 142.]

[129] I. Brivio, Y. Jiang and M. Trott, *The SMEFTsim package, theory and tools*, JHEP **12**, 070 (2017), arXiv:1709.06492 [hep-ph]. [Cited on pages 143 and 226.]

[130] N. Castro, K. Cranmer, A. V. Gritsan, J. Howarth, G. Magni, K. Mimasu, J. Rojo, J. Roskes, E. Vryonidou and T. You, *LHC EFT WG Report: Experimental Measurements and Observables*, (11 2022), arXiv:2211.08353 [hep-ph], CERN-LHCEFTWG-2022-001, CERN-LPCC-2022-05. [Cited on page 143.]

[131] P. A. Zyla et al., *Review of Particle Physics*, Progress of Theoretical and Experimental Physics **2020**(8) (08 2020), https://academic.oup.com/ptep/article-pdf/2020/8/083C01/34673740/rpp2020-vol2-2015-2092_18.pdf, 083C01. [Cited on page 143.]

[132] T. A. Aaltonen et al. (CDF, D0 Collaboration), *Combination of CDF and D0 W-Boson Mass Measurements*, Phys. Rev. D **88**(5), 052018 (2013), arXiv:1307.7627 [hep-ex], FERMILAB-PUB-13-289-E. [Cited on page 143.]

[133] G. Aad et al. (ATLAS Collaboration), *Higgs boson production cross-section measurements and their EFT interpretation in the 4ℓ decay channel at $\sqrt{s}$ =13 TeV with the ATLAS detector*, Eur. Phys. J. C **80**(10), 957 (2020), arXiv:2004.03447 [hep-ex], CERN-EP-2020-034, [Erratum: Eur.Phys.J.C 81, 29 (2021), Erratum: Eur.Phys.J.C 81, 398 (2021)]. [Cited on page 147.]

[134] I. Jolliffe, *Principal Component Analysis*, Springer Verlag, 1986. [Cited on page 149.]

[135] E. Rossi et al. (ATLAS Collaboration), *SMEFT and BSM interpretation of combined Higgs boson measurements*, (2022), ATL-COM-PHYS-2022-890. [Cited on pages 151, 155, 157, 158, 160, 164, 169, 170, 171, 172, 173, 210, 211, 212, 213, 214, 215, 216, 217, 218, 219, 220, 221, 222, and 223.]

[136] R. Balasabramanian, private communication. [Cited on pages 165, 166, and 167.]

[137] T. D. Lee, *A Theory of Spontaneous T Violation*, Phys. Rev. D **8**, 1226–1239 (Aug 1973). [Cited on page 168.]

[138] J. F. Gunion and H. E. Haber, *The CP conserving two Higgs doublet model: The Approach to the decoupling limit*, Phys. Rev. D **67**, 075019 (2003), arXiv:hep-ph/0207010, SCIPP-02-10. [Cited on page 168.]

[139] G. C. Branco, P. M. Ferreira, L. Lavoura, M. N. Rebelo, M. Sher and J. P. Silva, *Theory and phenomenology of two-Higgs-doublet models*, Phys. Rept. **516**, 1–102 (2012), arXiv:1106.0034 [hep-ph]. [Cited on page 168.]

[140] S. L. Glashow and S. Weinberg, *Natural conservation laws for neutral currents*, Phys. Rev. D **15**, 1958–1965 (Apr 1977). [Cited on page 168.]

[141] E. A. Paschos, *Diagonal neutral currents*, Phys. Rev. D **15**, 1966–1972 (Apr 1977). [Cited on page 168.]

[142] S. Dawson, S. Homiller and S. D. Lane, *Putting standard model EFT fits to work*, Phys. Rev. D **102**, 055012 (Sep 2020). [Cited on page 172.]

[143] F. Monti et al., *Modelling of the single-Higgs simplified template cross-sections (STXS 1.2) for the determination of the Higgs boson trilinear self-coupling*, (2022), LHCHWG-2022-002. [Cited on page 172.]

[144] G. Cowan, *Statistical Models with Uncertain Error Parameters*, Eur. Phys. J. C **79**(2), 133 (2019), arXiv:1809.05778 [physics.data-an]. [Cited on pages 184 and 194.]

[145] J. Neyman and E. S. Pearson, *On the Problem of the Most Efficient Tests of Statistical Hypotheses*, Phil. Trans. Roy. Soc. Lond. A **231**(694-706), 289–337 (1933). [Cited on page 188.]

[146] *Observation of a new particle in the search for the Standard Model Higgs boson with the ATLAS detector at the LHC*. [Cited on pages 190, 193, and 195.]

[147] A. Wald, *Tests of Statistical Hypotheses Concerning Several Parameters When the Number of Observations is Large*, Transactions of the American Mathematical Society **54**(3), 426–482 (1943). [Cited on page 193.]

[148] S. S. Wilks, *The Large-Sample Distribution of the Likelihood Ratio for Testing Composite Hypotheses*, Annals Math. Statist. **9**(1), 60–62 (1938). [Cited on page 193.]

[149] ATLAS Collaboration, *Combination of searches for invisible decays of the Higgs boson using 139 fb^{-1} of proton-proton collision data at $\sqrt{s} = 13$ TeV collected with the ATLAS experiment*, (1 2023), arXiv:2301.10731 [hep-ex], CERN-EP-2022-289. [Cited on page 196.]

[150] I. Brivio, *SMEFTsim 3.0 — a practical guide*, JHEP **04**, 073 (2021), arXiv:2012.11343 [hep-ph]. [Cited on page 226.]

[151] C. Degrande, G. Durieux, F. Maltoni, K. Mimasu, E. Vryonidou and C. Zhang, *Automated one-loop computations in the standard model effective field theory*, Phys. Rev. D **103**(9), 096024 (2021), arXiv:2008.11743 [hep-ph], CERN-TH-2020-140, CP3-20-42. [Cited on page 226.]

[152] S. Actis, G. Passarino, C. Sturm and S. Uccirati, *NLO Electroweak Corrections to Higgs Boson Production at Hadron Colliders*, Phys. Lett. B **670**, 12–17 (2008), arXiv:0809.1301 [hep-ph], PITHA-08-20, SFB-CPP-08-62, TTP08-38. [Cited on page 226.]

[153] A. Bredenstein, A. Denner, S. Dittmaier and M. M. Weber, *Precision calculations for the Higgs decays H —> ZZ/WW —> 4 leptons*, Nucl. Phys. B Proc. Suppl. **160**, 131–135 (2006), arXiv:hep-ph/0607060, PSI-PR-06-09. [Cited on page 226.]